

Global Investigation of Large Earthquakes Using InSAR and Long-Period Seismic Data

A thesis submitted to the School of Environmental Sciences of the
University of East Anglia in partial fulfilment of the requirements for the
degree of Doctor of Philosophy

By Jennifer Weston

July 2013

© This copy of the thesis has been supplied on condition that anyone who consults it is understood to recognise that its copyright rests with the author and that no quotation from the thesis, nor any information derived therefrom, may be published without the author's prior, written consent.

© Copyright 2013

by

Jennifer Weston

Abstract

Earthquake source models are vital for enhancing our understanding of tectonic processes and for reliably assessing seismic hazard. The spatial and temporal resolution of InSAR and seismic data, respectively, make them powerful tools for studying earthquake sources.

In this thesis I present the first comprehensive global archive of InSAR-determined source models (ICMT database) compiled from the literature, which I use to independently assess source parameters reported in global and regional seismic catalogues. In general there is good agreement between InSAR and seismic source models, but there are some large discrepancies, particularly in location and seismic moment. There is a large intra-event variability in source parameters in the ICMT database, which highlights the uncertainties introduced by errors in the data and by simplified assumptions used in the modelling. Large discrepancies for five earthquakes with magnitudes M_w 6.0 - M_w 8.1 are investigated in detail by comparing seismic data with theoretical seismograms calculated using two forward modelling techniques and 1-D and 3-D Earth models. For moderate magnitude events the InSAR location improves the fit to the seismic data, but this is not the case for the larger earthquakes, which is partly due to errors in the Earth models used.

These findings motivated the development of a new seismo-geodesy joint source inversion technique that takes into account the effects of 3-D Earth structure when modelling the seismic data. It is tested on three synthetic events with different faulting mechanisms and for three real earthquakes in various tectonic settings (M_w 6.0 Eureka Valley, M_w 6.6 Aiquile and M_w 6.5 Zarand events). These tests clearly show the advantages of taking into account 3-D Earth structure in the modelling, and the combination of InSAR and seismic datasets reduces parameter tradeoffs and enables the robust characterisation of the earthquake source.

Acknowledgements

Firstly, I would like to thank Ana Ferreira who without her guidance and support over the past four years I would not have started on this path, let alone got to this point. So a huge thank you Ana for all your help, advice, and for sharing what seems to be your endless seismological knowledge! Secondly, thank you to Gareth Funning, an InSAR guru, without your help I would still be staring at interferograms with a very confused look on my face. Also thanks for the opportunities to visit California multiple times and the chance to see some real sunshine throughout this PhD. And thank you to Adrian Matthews whose outside view on this research was refreshing and definitely appreciated. Also thank you to the Natural Environment Research Council for funding this project in the first place.

Thank you to Martin Vallée for sharing your valuable source time function knowledge! Thanks to the small but mighty seismology group at UEA; Kostas, Sung-Joon, Laura, Ana, and Hannah. Also thank you to all the authors of the various studies which make up the database on which most of thesis is based on. Thank you for taking the time to reply to my many questions, in particular, Rowena Lohman, Matt Pritchard, Roland Bürgmann, and Martin Mai.

Now onto the people who have been through the highs and lows of the past few years with me. Firstly a shout out to all the various inhabitants (past and present) of the 'rocks office'. An especially big thank you to Katie and Mel, who I started this 'journey' with and without having you guys to laugh about everything with and willingly put up with me has made it a lot easier and a lot more fun to make it to this stage! Chris, Lucy, and Amy, the coffee and cake breaks definitely played a vital role in getting this far, so cheers guys. Also Sam, Ro and Suze thanks for the constant reminders that I can do this and that it will be worth it in the end! Thanks to all the guys at Riverside for making me feel so welcome in the strange and sunny land that is California.

And last but definitely by no means least, my parents. Thanks Mum, Dad, you have probably had to put up the most with the lows of my PhD, but without your support I wouldn't even have got as far as university to even begin to think about a PhD. So a massive thank you and here are 200 odd pages of proof that it wasn't all for nothing :)

Contents

Abstract	v
Acknowledgements	vii
1 Introduction	1
1.1 Global tectonics and the earthquake cycle	1
1.2 Quantifying global earthquakes	4
1.2.1 Seismological methods	5
1.2.2 Geodetic observations	8
1.3 Current challenges	11
1.4 Motivation and thesis outline	13
2 Construction of the ICMT catalogue	15
2.1 Introduction	15
2.2 Processing and modelling InSAR data	15
2.3 Earthquake source inversions using seismic data	20
2.4 Existing seismic source model catalogues	24
2.5 Compilation of InSAR Centroid Moment Tensor (ICMT) catalogue	27
2.5.1 Centroid Moment Tensor parameter calculations	29
2.6 Intraevent variability within the database	32
2.6.1 Seismic moment	32
2.6.2 Fault geometry and mechanism	32
2.6.3 Centroid spatial location	33
2.7 Conclusions	33

3	Systematic comparisons between InSAR and seismically-determined source models	41
3.1	Introduction	41
3.2	Seismic Moment and moment magnitude	42
3.2.1	Comparing ICMT and GCMT estimates	42
3.2.2	Cases of large discrepancies between ICMT and GCMT estimates	44
3.2.3	Trends due to geographical location and thrusting mechanism	45
3.3	Centroid Epicentral Location	49
3.3.1	Comparisons with global seismic catalogues	49
3.3.2	Comparisons with regional catalogues	54
3.3.3	Comparisons with geological information	54
3.3.4	Source directivity	59
3.4	Depth	63
3.5	Fault Geometry	69
3.6	Distributed Slip Models	74
3.6.1	Intraevent variability	74
3.6.2	Earthquake location	76
3.7	Discussion	78
3.7.1	Source parameter validation	78
3.7.2	Earth structure models	78
3.8	Conclusions	79
4	Testing InSAR and seismically-determined source models using 1-D and 3-D seismic forward modelling	81
4.1	Introduction	81
4.2	Data and methodology	83
4.2.1	Data selection and processing	83
4.2.2	Normal mode summation	84
4.2.3	Spectral element method	85
4.2.4	Quantifying phase, amplitude and waveform misfits	86
4.3	Results	86
4.3.1	Normal faulting event: Eureka Valley, M_w 6.1, 17 th May 1993	86

4.3.2	Large strike-slip event: Landers, M_w 7.3, 28 th June 1992	95
4.3.3	Multiple InSAR Models: Izmit, M_w 7.5, 17 th August 1999	99
4.3.4	Large Subduction Zone event: Pisco, M_w 8.1, 15 th August 2007	105
4.3.5	Small Subduction Zone Event: North Chile Subduction Zone, M_w 6.6, 19 th April 1996	110
4.4	Discussion and Conclusions	114
5	A joint inversion technique for earthquake source parameters	117
5.1	Introduction	117
5.2	Existing techniques	118
5.3	Method	120
5.3.1	Optimisation scheme	120
5.3.2	Theoretical seismograms and kernels	122
5.4	Data	125
5.4.1	Teleseismic waveform data	125
5.4.2	InSAR data	125
5.5	Synthetic Tests	126
5.5.1	Importance of 3-D Earth structure	129
5.5.2	Effect of data noise	130
5.6	Case Study: Eureka Valley, M_w 6.1, 17 th May 1993	138
5.7	Case Study: Aiquile, Bolivia, M_w 6.5, 22 nd May 1998	146
5.8	Case Study: Zarand, Iran, M_w 6.5, 22 nd February 2005	154
5.9	Discussion	162
5.10	Conclusions	167
6	Discussion and Conclusions	169
6.1	Spatial and temporal resolution	169
6.2	Weighting the data	170
6.3	Data and source parameter uncertainties	171
6.4	Importance of realistic Earth structures	173
6.5	Conclusions	174
6.6	Future Work	176

6.6.1	ICMT database	178
6.6.2	Development of the joint inversion approach	178
6.6.3	Further applications of the joint inversion technique	179
A	Additional ICMT and GCMT source parameter comparisons	181
B	Additional forward modelling waveform comparisons	189
C	Technical notes	197

List of tables

2.1	Summary of past and present radar satellites.	18
2.2	ICMT database for earthquakes between 1992 and 1997	34
4.1	Existing source models for the M_w 6.1 Eureka Valley, California, earthquake	89
4.2	Summary of misfit results from forward modelling tests for Eureka Valley	91
4.3	Existing source models for the M_w 7.3 Landers, California, earthquake . .	95
4.4	Summary of misfit results from forward modelling tests for the Landers earthquake	97
4.5	Existing source models for the M_w 7.5 Izmit, Turkey, earthquake	101
4.6	Summary of misfit results for the forward modelling tests of the Izmit earthquake	104
4.7	Existing source models for the M_w 8.1 Pisco, Peru, earthquake	107
4.8	Summary of misfit results for the forward modelling tests of the Pisco earthquake	108
4.9	Existing source models for the M_w 6.6 Northern Chile earthquake	110
4.10	Summary of misfit results for the forward modelling tests of the Northern Chile earthquake	112
5.1	Summary of source inversion results for the synthetic normal faulting earthquake	131
5.2	Summary of source parameters from joint source inversions for three ar- tificial earthquakes	134
5.3	Source inversion results for the M_w 6.1 Eureka Valley, California, earth- quake	141
5.4	Source inversion results for the M_w 6.6 Aiquile, Bolivia, earthquake . . .	149
5.5	Source inversion results for the M_w 6.5 Zarand, Iran, earthquake	157

List of figures

1.1	Map illustrating the global seismicity between 2002 and 2012	2
1.2	Photograph of surface offset on the Calaveras fault due to creeping	4
1.3	Map illustrating the coverage of the Global Seismic Network	6
1.4	Interferogram showing signal from the M_w 6.1 Eureka Valley earthquake	11
2.1	Geometry of an elastic dislocation model.	20
2.2	Example seismogram filtered for surface and body waves.	21
2.3	Fault geometry conventions used in this thesis.	23
2.4	Geographical locations of the 67 earthquakes in the ICMT database	29
2.5	Distribution of M_w of the earthquakes in the database	30
2.6	Example of the calculation of overall CMT source parameters for the 2003 Bam earthquake	31
3.1	Histogram illustrating the distribution of differences between the ICMT and GCMT moment estimates	43
3.2	Comparison of ICMT and GCMT M_w estimates with respect to location and fault mechanism	46
3.3	Comparison of ICMT and GCMT M_w estimates with respect to postseis- mic activity.	48
3.4	Distribution of epicentral distance between ICMT and seismic catalogue locations	49
3.5	Maps comparing differences in locations from InSAR and those reported in global seismic catalogues	52
3.6	Regional maps comparing InSAR and global seismic catalogue earth- quake locations	53

3.7	Maps comparing differences in ICMT and regional seismic catalogue locations	55
3.8	Comparison of InSAR and seismic locations with respect to known fault locations for the M_w 7.1 Hector Mine earthquake	57
3.9	Comparison of InSAR and seismic locations with respect to known fault locations for the M_w 7.3 Landers earthquake	58
3.10	Plot of fault trace and distributed slip model for the Landers earthquake.	59
3.11	Comparison of ICMT and GCMT centroid locations with EHB hypocentre locations.	61
3.12	Distributed slip model for Izmit earthquake with respect to InSAR and seismic locations.	62
3.13	Comparison of ICMT centroid depths and EHB hypocentre depths.	65
3.14	Comparing ICMT centroid and EHB hypocentre with respect to assumed half-space model.	66
3.15	Comparison of ICMT centroid and EHB hypocentre depths with respect to location and fault mechanism.	68
3.16	Distribution of difference between ICMT and GCMT strike, dip and rake estimates	72
3.17	Comparison of ICMT and GCMT strike, dip and rake estimates with respect to location and fault mechanism	73
3.18	Comparison of three distributed slip models for the M_w 7.1 Hector Mine earthquake.	75
3.19	Comparison of two distributed slip models for the M_w 7.9 Wenchuan, China earthquake.	77
4.1	Global map with the location and mechanisms of the five earthquakes studied.	83
4.2	Tectonic setting and topography of southern California.	87
4.3	Tectonic setting in Eureka Valley, California.	88
4.4	Distribution of seismic stations used for the Eureka Valley comparisons	89
4.5	Comparisons of synthetic and observed long period surface waves for the Eureka Valley earthquake.	92

4.6	Comparison of synthetic and observed long period body waves for the Eureka Valley earthquake.	94
4.7	Distribution of seismic stations used for the Landers earthquake comparisons.	96
4.8	Comparison of synthetic and observed long period surface waves for the Landers earthquake.	98
4.9	Topography and tectonic setting of the North Anatolian Fault.	100
4.10	Distribution of seismic stations used for the Izmit earthquake comparisons	101
4.11	Comparison of synthetic and observed long period surface waves for the Izmit earthquake.	103
4.12	Topography and tectonic setting of the south American subduction zone. .	106
4.13	Distribution of seismic stations used for the Pisco earthquake.	107
4.14	Comparison of synthetic and observed long period surface waves for the Pisco comparisons	109
4.15	Distribution of seismic stations used for the Northern Chile earthquake . .	111
4.16	Comparison of synthetic and observed long period surface waves for the Northern Chile earthquake.	113
5.1	Flowchart of joint inversion technique.	121
5.2	Velocity perturbation maps of S40RTS and CRUST2.0	123
5.3	Excitation kernels calculated assuming both 1-D and 3-D Earth structures	124
5.4	Locations and focal mechanisms of the three artificial earthquakes tested. .	126
5.5	Examples of synthetic InSAR and seismic data for a normal faulting event.	128
5.6	Comparison of results from inversions assuming a 1D and 3D Earth structure.	132
5.7	Tradeoff scatterplots for 1-D and 3-D Earth test joint inversions	133
5.8	Tradeoff scatterplots for InSAR, seismic and joint inversions for an artificial normal faulting earthquake.	135
5.9	Tradeoff scatterplots for InSAR, seismic and joint inversions for an artificial strike-slip faulting earthquake.	136
5.10	Tradeoff scatterplots for InSAR, seismic and joint inversions for an artificial thrust faulting earthquake.	137

5.11	Tectonic setting in Eureka Valley, California.	139
5.12	Fit of Eureka Valley joint inversion result to the InSAR data.	142
5.13	Fit of Eureka Valley joint inversion result to the long period surface waves.	143
5.14	Fit of the Eureka Valley joint inversion result to the long period body waves.	144
5.15	Tradeoff scatterplots of InSAR, seismic and joint inversions for the Eureka Valley earthquake.	145
5.16	Tectonic setting in the Aiquile region, Bolivia	147
5.17	Fit of the Aiquile joint inversion result to the long period surface waves .	150
5.18	Fit of the Aiquile joint inversion result to the long period surface waves. .	151
5.19	Fit of the Aiquile joint inversion result to the InSAR data	152
5.20	Tradeoff scatterplots for the InSAR, seismic and joint inversions for the Aiquile earthquake.	153
5.21	Tectonic setting of south-central Iran	155
5.22	Fit of joint inversion result to the InSAR data for the Zarand earthquake. .	158
5.23	Fit of the joint inversion result to the long period surface waves for the Zarand earthquake.	159
5.24	Fit of the joint inversion result to the long period body waves for the Zarand earthquake.	160
5.25	Tradeoff scatterplots for InSAR, seismic and joint inversion results for the Zarand earthquake.	161
A.1	Comparisons between ICMT and GCMT seismic moment estimates with respect to other source parameters.	182
A.2	Comparisons between ICMT and GCMT moment estimates with respect to slip assumption.	183
A.3	Comparisons between ICMT and GCMT centroid locations with respect to other source parameters.	184
A.4	Comparisons between ICMT and EHB depth estimates with respect to other source parameters.	185
A.5	Comparisons between ICMT and GCMT strike estimates with respect to other source parameters.	186

A.6	Comparisons between ICMT and GCMT dip estimates with respect to other source parameters.	187
A.7	Comparisons between ICMT and GCMT rake estimates with respect to other source parameters.	188
B.1	Comparison of synthetic and observed long period surface waves for the M_w 7.3 Landers earthquake.	190
B.2	Comparison of synthetic and observed long period surface waves for the M_w 7.5 Izmit earthquake.	191
B.3	Comparison of synthetic and observed long period surface waves for the M_w 7.5 Izmit earthquake.	192
B.4	Comparison of synthetic and observed long period surface waves for the M_w 8.1 Pisco earthquake.	193
B.5	Comparison of synthetic and observed long period surface waves for the M_w 8.1 Pisco earthquake.	194
B.6	Comparison of synthetic and observed long period surface waves for the M_w 6.6 Northern Chile earthquake.	195

Chapter 1

Introduction

Recent large, complex, and destructive earthquakes such as Haiti (M_w 7.0, 12th January 2010) and Tohoku, Japan (M_w 9.0 11th March 2011) have highlighted the importance of prior knowledge of the tectonic regime of a region. The robust characterisation of earthquakes provides key information for this purpose. Initially seismic and geodetic data (*e.g.* trilateration, levelling) were the few data sources available for the determination of earthquake source models. The development of GPS and radar interferometry marked the beginning of the rapid expansion of geodetic data to measure all aspects of the earthquake cycle around the world. Since the first observation of a coseismic event in 1992 (M_w 7.3, Landers, California), Interferometric Synthetic Aperture Radar (InSAR) has proven a powerful tool and over the past two decades there have been significant developments in the techniques used to exploit this InSAR data. Moreover, the fine spatial resolution of InSAR data complements the high temporal resolution of seismic data, which when combined into a single analysis can robustly constrain the earthquake source. However, the assumed Earth structure model is an important consideration when modelling the seismic data and further improvements in joint seismo-geodetic inversion techniques will be beneficial for investigating large earthquakes, and consequently better understanding the earthquake cycle.

1.1 Global tectonics and the earthquake cycle

The majority of global seismicity occurs at, and within, narrow zones surrounding plate boundaries (Figure 1.1), but the influence of the motion at plate boundaries can extend

thousands of kilometres into the plate interior (*e.g.* Range and Basin Province, North America, Parsons and Thatcher, 2011). The build up of strain due to plate motions either at the boundaries or within the plate interiors is the key driver for the earthquake cycle, a concept based on elastic rebound theory. It was first proposed by Harry Reid (1910) after the M_w 7.8 San Francisco earthquake in 1906. Elastic strain builds up due to the relative motions of the plates either side of a fault, referred to as the interseismic phase. When the strain overcomes the frictional resistance on the fault the built up strain energy is released in a sudden movement on the fault, which is the earthquake (coseismic phase). This results in a change in the stress state in the region and the activities relating to the adjustment of the region to this change occur in the postseismic phase.

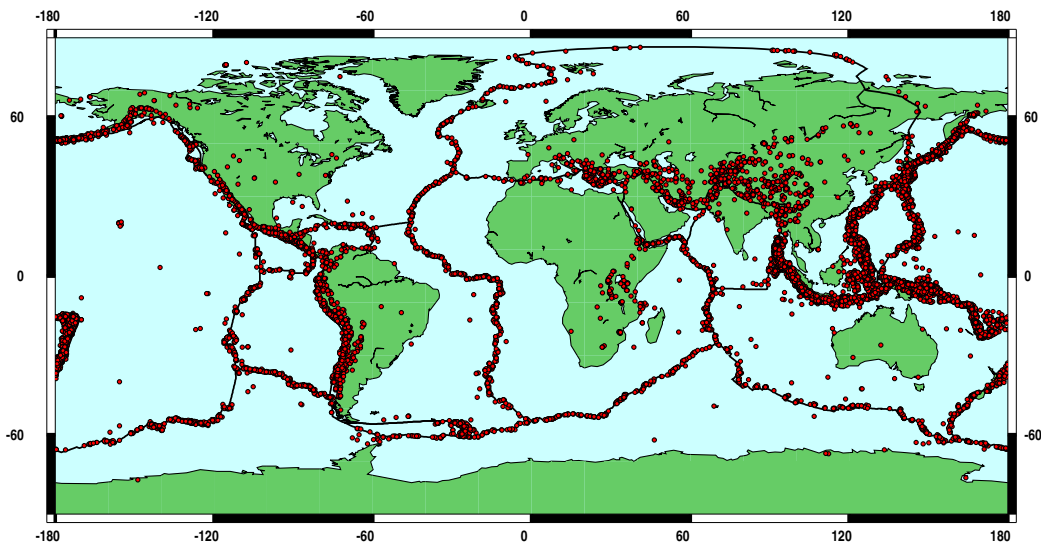


Figure 1.1: Global map showing earthquakes (red circles) with $M \geq 5.0$ that occurred between 2002–2012 at depths less than 100 km. Based on data downloaded from the National Earthquake Information Center. Plate boundaries are shown in black.

The whole cycle typically lasts tens to hundreds of years and it has been observed in full in a few places, such as the Parkfield section of the San Andreas fault (Murray and Langbein, 2006), the Sumatra subduction zone (Prawirodirdjo *et al.*, 2010) and the East Pacific Rise (McGuire, 2008). The advent of geodetic data has proven a particularly useful tool for observing each aspect of the cycle. For example, slow slip events, which refer to periods of slip which last for days and don't produce damaging seismic waves (*e.g.* Meade and Loveless, 2009) have been observed with continuous GPS in various subduction zones including Cascadia, North America (Dragert *et al.*, 2001) and Hikurangi, New

Zealand (Wallace and Beavan, 2006). The build up of interseismic strain across large continental fault systems has been measured using InSAR and GPS data (*e.g.* Wright *et al.*, 2001b; Biggs *et al.*, 2007; Walters *et al.*, 2011; Pezzo *et al.*, 2012) and geodetic measurements have revealed significant postseismic deformation following the 2004 Parkfield earthquake in California (Freed, 2005; Johanson *et al.*, 2006).

Postseismic deformation can be explained by a variety of mechanisms, including; afterslip on the fault or neighbouring structures (*e.g.* 2005, M_w 7.5, Kashmir, Pakistan earthquake, Jouanne *et al.*, 2011), viscoelastic relaxation in the lower crust and upper mantle following large subduction zone earthquakes (*e.g.* 2001, M_w 8.5, Arequipa, Peru, Hergert and Heidbach, 2006) or large strike slip events (*e.g.* 2001, M_w 7.6, Kokoxili, Tibet, Ryder *et al.*, 2007) and poroelastic relaxation in the upper crust (*e.g.* Gahalaut *et al.*, 2008) or a combination of mechanisms (*e.g.* Fialko, 2004a; Árnadóttir *et al.*, 2005; Lubis *et al.*, 2013).

Regarding the coseismic part of the cycle, recent attention has been paid to extreme rupture behaviours, for example the afore-mentioned slow slip events and at the opposite end of the scale, supershear ruptures. These are events which involve the propagation of the rupture at speeds faster than shear wave velocity and have been observed for recent large strike-slip events, (*e.g.* Izmit M_w 7.5, 17th August 1999; Bouchon *et al.*, 2002). Investigations of the coseismic part of the earthquake cycle also include the reliable estimation of the magnitude, location and fault geometry of an earthquake, which are useful for a variety of purposes. On a short timescale following an earthquake, robust earthquake source models are key to the successful implementation of the National Earthquake Information Centre's PAGER system (Prompt Assessment of Global Earthquakes for Response) which relies on accurate parameters to determine the extent of ground shaking and consequently the number of potential fatalities, usually within 30 minutes of the event. Thus, accurate source models provide information critical to coordinating effective relief efforts. On a longer timescale, compilations of source models for earthquakes in a given region allow the investigation of the tectonic regime (*e.g.* Jackson and McKenzie, 1984; Dewey and Lamb, 1992; Ambraseys and Jackson, 1998; Devlin *et al.*, 2012), which is important for understanding the seismic hazard. Moreover, source models can be used as inputs for Coulomb stress calculations (*e.g.* King *et al.*, 1994; Astiz *et al.*, 2000; Enescu

et al., 2012; Serpelloni *et al.*, 2012), another key tool for assessing the risk of future events in a region. Understanding the uncertainties in source models is particularly important for the correct interpretation of potential stress triggering in a region (Woessner *et al.*, 2012) and treatment of how the fault network is connected based on geological observations and models for previous earthquakes can significantly change the resulting calculations (Parsons *et al.*, 2012). Therefore earthquake source models play an important role in understanding the tectonic processes, which is important for the many populations that live on or near faults (Figure 1.2).



Figure 1.2: Image taken in Hollister, northern California, the slight bend in the pavement in the middle of the picture indicates the influence of the right lateral motion of the Calaveras fault (yellow arrows) which runs underneath the houses to the left. A large event is considered unlikely to occur in this particular section as it is creeping.

1.2 Quantifying global earthquakes

Many of the fault systems that are discussed in this thesis have been active for millions of years (*e.g.* San Andreas Fault, California) and the detection of historic events on these structures, prior to the development of seismic and geodetic techniques, relied on field observations. Measurements of the instantaneous deformation of landforms and sediments as a result of the earthquake, in combination with the dating of rocks can be used to determine the location, timing and magnitude of large (usually $M > 6.5$) historic earthquakes

— a field known as paleoseismology. This includes the measurement of fault scarps (*e.g.*, Bonilla *et al.*, 1984), offsets of river terraces (*e.g.*, Lensen, 1968), uplift of marine terraces (*e.g.*, Berryman *et al.*, 1989) and the excavation of trenches across faults to map and date the sediments (*e.g.*, Sieh, 1978). Further details and an excellent overview of paleoseismology are given in McCalpin (1996).

Some of the afore-mentioned techniques are used to investigate present-day earthquakes. For example, measurements of coral uplift along the coast as a result of the Haiti earthquake were used as a further constraint when modelling the event (Hayes *et al.*, 2010). Offsets along the fault are also valuable information and are complementary to GPS and InSAR data, (*e.g.*, Wenchuan, China, M_w 7.9, 12th May 2008 Hao *et al.*, 2009). As well as offset measurements, observations of the surface rupture are also useful to identify the faults that were involved in the earthquake, and the strike and dip of these faults provide further constraints when trying to model the event (*e.g.*, Zarand, Iran, M_w 6.5, Talebian *et al.*, 2006). These type of data are useful additions to the data collected through various seismological and geodetic techniques, which will now be discussed.

1.2.1 Seismological methods

Seismologists have been using the measurements of displacements, velocities and accelerations due to seismic waves generated by earthquakes to gain insight into their source mechanism since the 1880's (Byerly, 1960). But it was the in-depth study of the 1906 San Francisco event (*e.g.* Lawson, 1908; Reid, 1910) which was the first landmark in measuring and recognising that earthquakes are due to slip on faults. The substantial deployment of seismic stations since then, particularly global networks throughout the 1960s and 1970s such as the World Wide Standard Seismograph Network (WWSSN), and later in 1986 the Global Seismograph Network (GSN, shown in Figure 1.3), lead to the explosion of source studies of earthquakes (*e.g.* Ben-Menahem and Toksoz, 1963; Tsai and Aki, 1970; Kanamori, 1970; Randall and Knopoff, 1970; Fitch *et al.*, 1980; Dziewonski *et al.*, 1981). During this period, the vast improvement in the volume, quality and availability of seismic data also sparked the routine reporting of earthquake locations and magnitudes, on a global scale. This includes the activities of the International Seismological Centre (ISC) in the UK (ISC Bulletin, <http://www.isc.ac.uk/iscbulletin/search>) and the National

Earthquake Information Centre (NEIC) in the United States (NEIC Global Earthquake Search, <http://earthquake.usgs.gov/earthquakes/eqarchives/epic>). It also led to the development of numerous inversion techniques for the rapid determination of the earthquake source mechanism, as well as the location and magnitude.

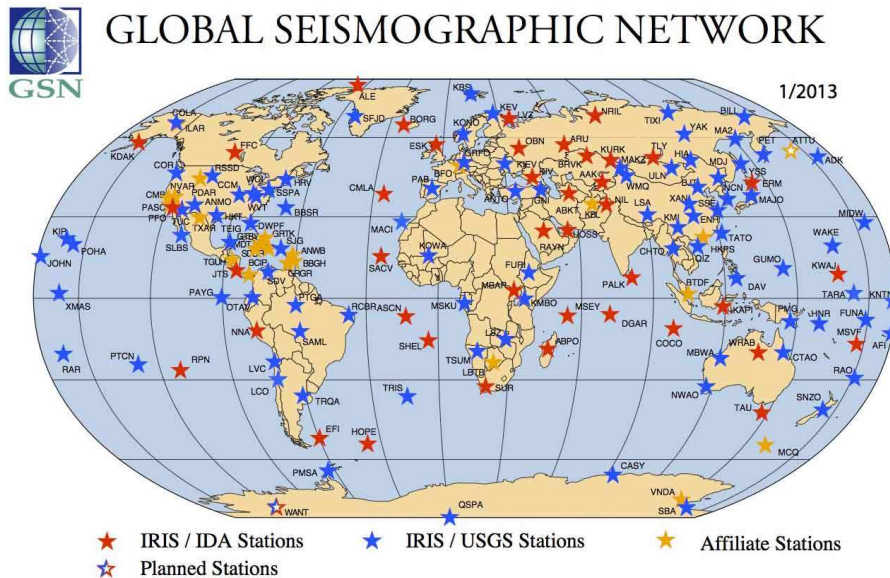


Figure 1.3: Map of the 150 plus stations included in the GSN network, which is a partnership between Incorporated Research Institutions for Seismology (IRIS) and the United States Geological Survey (USGS). Figure downloaded from IRIS (<http://www.iris.edu/hq/programs/gsn>).

One way to model an earthquake is to treat it as a point source and Gilbert (1970) was the first to suggest that it can be represented as a three-by-three matrix of force couples, known as a moment tensor. The components of this tensor are linearly related to the velocities observed in seismograms, if the latter are assumed to be a sum of the normal modes excited by the earthquake (Gilbert and Dziewonski, 1975). This is the approach behind the Centroid Moment Tensor (CMT) method (Dziewonski *et al.*, 1981), which was one of the first techniques implemented on a global scale for the rapid and routine determination of the location, magnitude and focal mechanism for earthquakes with $M_w \geq 5.5$ (Dziewonski and Woodhouse, 1983). Solutions calculated using this approach for thousands of events since the early 1980s to the present day are reported in the Global CMT (GCMT) catalogue, one of the most widely used seismic catalogues (Ekström *et al.*, 2012).

The GCMT catalogue uses long period surface and body waves, but due to the large

volume of information contained in a seismogram there are many other ways in which it can be exploited. For example the ISC Bulletin uses multiple P and S phase arrivals based on the 1-D velocity model, ak135 (Kennett *et al.*, 1995), and a linear least squares approach, to determine the hypocentral location. Measurements of the maximum amplitude of P and surface wave ($T \sim 18 - 22$ s) arrivals are used to determine body (m_b) and surface wave (M_s) magnitudes, respectively. Teleseismic bodywaves are one of the first recordings of an earthquake available, arriving within the first few minutes, and they are useful for the quick yet robust characterisation of an event. For example, a recently developed bodywave deconvolution method, SCARDEC (Vallée *et al.*, 2011), is able to determine, a depth, focal mechanism and source time function (STF) for earthquakes generally larger than M_w 6.0, within 45 minutes of an event occurring.

For studies of individual earthquakes, particularly for moderate to large events, a more detailed description of the spatial complexity of the source can be determined, where the event is modelled as varying slip across one or more planar surfaces. The fault geometry and location are usually fixed and the surface is split up into a grid, where the slip amplitude and rupture time for each subfault are solved for. There are numerous techniques for such an inversion; which vary depending on the type of seismic data used and the approach taken to solve the problem. Early studies used strong motion data (*e.g.* Trifunac, 1974; Olson and Apsel, 1982), and teleseismic bodywaves (P and SH) have also been used (*e.g.* Das and Kostrov, 1990; Hartzell *et al.*, 1991), as has a combination of the two datasets (*e.g.* Mendoza and Hartzell, 1989). A linear approach can be taken to solve for the slip amplitude (*e.g.* Trifunac, 1974; Das and Kostrov, 1990; Hartzell *et al.*, 1991). Alternatively the slip amplitude and rupture time can be simultaneously solved in a linear iterative fashion (*e.g.* Beroza and Spudich, 1988).

Strong motion data are able to record the higher amplitude seismic waves more robustly than teleseismic observations. Recordings from large strike-slip events in the past decade or so, such as the M_w 7.3 Izmit earthquake in 1999 in Turkey and the M_w 7.9, Wenchuan earthquake in China in 2008 have enabled in-depth studies into not only the distribution of slip, but also the propagation of the rupture (*e.g.* Delouis *et al.*, 2002; Zhang *et al.*, 2012). This includes the observation of supershear rupture, for Izmit (*e.g.* Bouchon *et al.*, 2002) and a slightly smaller event which also ruptured part of the North

Anatolian fault only three months later, M_w 7.1 Duzce, (Konca *et al.*, 2010). Moreover, ocean-bottom seismometers (OBS) have proven particularly useful for recording large subduction events (*e.g.* Romano *et al.*, 2010) and dense OBS deployments recording local events enables the identification of the tectonic mechanisms driving the deformation in plate boundary settings (*e.g.* Geissler *et al.*, 2010; Sumy *et al.*, 2013). Another current focus in inversion techniques is how the fault surface is modelled. Rather than assuming it to be planar, meshes of triangular elements have been used to simulate more realistic irregular shaped representations of active faults (*e.g.* Southern California Community Fault Model, Plesch *et al.*, 2002, 2007), and also to take into account the plate geometry in subduction zones (*e.g.* Slab1.0, Hayes *et al.*, 2012).

1.2.2 Geodetic observations

Geodetic measurements of crustal deformation were conducted as early as the late 1800s. For example, triangulation surveys were carried out along the Hayward fault in the San Francisco Bay area to measure displacements due to the M_w 7.0 event in 1868 (Yu and Segall, 1996). Trilateration is an alternative to triangulation, for the determination of the absolute horizontal position, and the development of Electronic Distance Meters (EDMs) improved the accuracy of this technique, which was used to measure coseismic displacements due to the Landers earthquake (M_w 7.3, 28th June 1992, Murray *et al.*, 1993). Triangulation and trilateration can accurately determine horizontal displacements but for more precise vertical measurements levelling surveys are used (*e.g.*, M 7.1 Imperial Valley earthquake, 18th May 1940, Relinger, 1984). Initially these were the main techniques available but the development of Very Long Baseline Interferometry (VLBI) for precision geodesy in the late 1970s provided another means for measuring crustal deformation, such as displacements along the San Andreas fault (Clark *et al.*, 1987). However, it was the development of GPS (Global Positioning System) which marked the expansion of geodetic data for measuring all aspects of earthquake cycle. The Loma Prieta earthquake (M_w 6.9, 17th October 1989) was one of the first events to be measured using GPS (Williams *et al.*, 1993), and also using VLBI (Clark *et al.*, 1990).

Then in 1991 the launch of the satellite ERS-1 heralded the beginning of an era of global coverage of synthetic aperture radar (SAR) observations. As geodesists learned

how to exploit this data source and additional SAR satellites were launched by multiple agencies, an alternative, non-seismological, method for study of shallow earthquakes was established. An active radar signal is emitted by a satellite and the phase of the signal reflected back from a target and recorded by the antenna, is a function of the distance between the radar antenna (in this case, the satellite) and the radar target (in this case, the ground). Therefore, by differencing the phase of the SAR images acquired at different times we can in principle detect changes in the distance that are due to the movement of the ground toward or away from the satellite between acquisitions. If one SAR image is acquired before, and another after, a process that generates surface deformation, a fine resolution map of the displacement can be generated. This technique is interferometric SAR (InSAR), and is a powerful Earth observation tool for investigating varying sources of crustal deformation, which include; sub-surface fluid movement (*e.g.* subsidence due to groundwater abstraction, Gonzalez and Fernandez, 2011), landslides (*e.g.* Roering *et al.*, 2009), glacier movement (*e.g.* Gray, 2011), and volcanic deformation (*e.g.* Amelung and Day, 2002; Pritchard and Simons, 2004; Parks *et al.*, 2012).

A further application is the detection and measurement of earthquakes, an example interferogram for a moderate magnitude earthquake in California is shown in Figure 1.4. Here one fringe (one cycle of pink to red) corresponds to displacement in the line of sight (LOS) of the satellite that is equal to half a wavelength of the radar signal, which in this case is equivalent to 2.8 cm away from the satellite. Elastic dislocation modelling of the surface displacements measured by InSAR can then be used to estimate the source parameters of the earthquake, information that is independent from seismology.

Unlike seismic data, InSAR data have poor temporal resolution, and other geodetic techniques such as GPS, trilateration and triangulation have a slight advantage, as surveys can be conducted relatively quickly after an earthquake, and are less likely to be contaminated by postseismic deformation. Also these data are a direct measurement of the surface displacement whereas InSAR measures a component of the deformation, but interferograms record displacements for many points (millions) over a large area (usually ~ 100 km), whereas much fewer measurements for the same area are possible with techniques such as GPS. Consequently, InSAR and geodetic measurements acquired in the field are complementary as the data can be used to cross-verify each other and fill in gaps

where the quality of either dataset is poor.

One significant advantage of InSAR is that the data can be acquired remotely and can cover inaccessible regions, where geodetic and seismic networks are limited. There are, however, only a limited number of satellites, and the SAR images have to be acquired before and after the event of interest and ideally with the same acquisition geometry and as small a time period as possible between the two images, to minimize decorrelation. Since the first earthquake (Landers, M_w 7.3, 26th June 1992, Massonnet *et al.*, 1993) was measured, the volume and accessibility of SAR data has steadily increased and consequently the number of earthquakes studied using this type of data and the modelling approaches used has increased also.

The first source models for earthquakes observed by InSAR in the early 1990s (*e.g.* M_w 6.1 Eureka Valley 17th May 1993) were calculated assuming uniform slip on a finite fault in a homogeneous elastic half-space (*e.g.* Peltzer and Rosen, 1995; Massonnet and Feigl, 1995). These calculations are based on the solutions of Okada (1985), which show that the fault size, geometry, and location are non-linearly related to the surface displacements, and almost all InSAR studies of earthquakes use the Okada solutions and a non-linear optimisation algorithm. However, for larger events, such as the Landers earthquake, the spatial complexity of the source ideally needs to be taken into account, in a similar way to models based on seismic data. The high spatial resolution of InSAR data has proven to be a powerful tool for mapping this complexity, especially for large continental strike-slip events such as Hector Mine, California (M_w 7.1, 16th October 1999, Simons *et al.*, 2002), Denali, Alaska (M_w 7.9, 3rd November 2002, Wright *et al.*, 2004a) and Kokoxili, Tibet (M_w 7.8, 14th November 2001, Lasserre *et al.*, 2005). As slip is linearly related to the observed surface displacements, once the fault geometry and location are determined, the spatial distribution of slip can be inverted for using simple inverse methods (*e.g.* Salichon *et al.*, 2004; Funning *et al.*, 2007; Tong *et al.*, 2010).

A homogeneous half-space is a simple approximation of a potentially highly heterogeneous crust, and although this has been found to be a reasonable assumption (*e.g.* Wald and Heaton, 2001), it can introduce biases in the source parameters, such as depth (*e.g.* Savage, 1998; Cattin *et al.*, 1999). Therefore, layered half-spaces are increasingly being used instead (*e.g.* Lohman *et al.*, 2002; Pritchard *et al.*, 2006; Pritchard and Fielding,

2008; Baer *et al.*, 2008) and in one case the 3-D Earth structure has also been considered (Bustin *et al.*, 2004). The trend over the past decade or so regarding InSAR and other geodetic data, such as GPS, has been the development of techniques which jointly invert these data with seismic data, an issue discussed next.

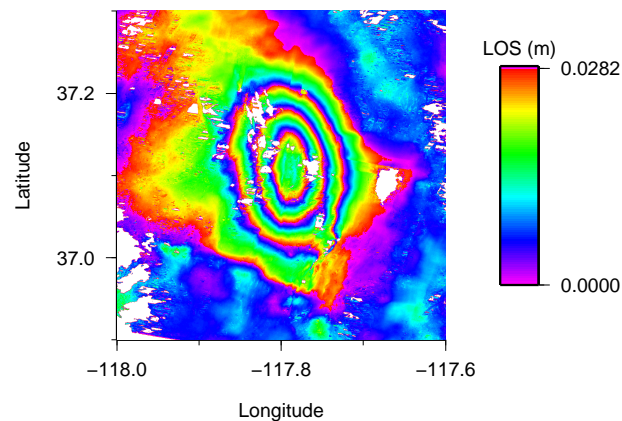


Figure 1.4: Unwrapped interferogram showing a signal from the Eureka Valley earthquake (M_w 6.1, 17th May 1993). This was produced using two SAR images from 01/06/92 and 08/11/93 by ERS-1, here 1 interferometric fringe corresponds to 2.8 cm displacement in the LOS of the satellite, adding all the fringes results in a total of 8cm of range increase which is consistent with subsidence from normal faulting.

1.3 Current challenges

There are several well established techniques for the determination of earthquake source parameters which use a variety of different seismic data, and there are several global seismic catalogues which routinely report these parameters. This includes the aforementioned GCMT catalogue, the ISC and Engdahl-van der Hilst-Buland (EHB) Bulletins run by the ISC, and also the NEIC. The NEIC have several different catalogues and are usually the first to report a location and magnitude for an earthquake. In recent years there have been focused efforts on the compilation of regional catalogues such as the RCMT for events in the Mediterranean (Pondrelli *et al.*, 2002). These catalogues tend to use local velocity structures to model the seismic data, which are more accurate than the Earth models used in global seismic catalogues, because the data used are more sensitive to the crustal structure. Errors in the assumed Earth model can lead to biases in source parameters, for example systematic mislocations of events in the south American subduction zone by the GCMT catalogue (*e.g.* Syracuse and Abers, 2009).

Seismic catalogues are valuable tools in the field of seismology and no equivalent catalogue exists for source models derived from geodetic data. Yet, considering the independent nature of the two datasets, a compilation of geodetically-determined source models would be useful for assessing those reported in seismic catalogues, and vice versa. Not many studies have compared source models calculated using the two different datasets, most consider events on an individual or regional scale (*e.g.*, Wright *et al.*, 1999; Lohman *et al.*, 2002; Mellors *et al.*, 2004; Pritchard *et al.*, 2006). One study has considered global events but mainly in the context of the seismic moment and earthquake scaling laws (Funning, 2005). These comparisons have highlighted some key issues though, particularly regarding the assumed Earth structure and the quality of the data (*e.g.* Feigl, 2002; Pritchard *et al.*, 2006).

The complementary strong spatial and high temporal resolution of InSAR data and seismic data, respectively, is also evident from these comparisons. Over the past decade there has been an increasing trend for the development of inversion techniques which combine and exploit the strengths of the two datasets. There are numerous approaches which differ mainly in the methods used to model the seismic data and to search the parameter space. Strong motion data (*e.g.* Hernandez *et al.*, 1999), regional network data (*e.g.* Lohman *et al.*, 2002), teleseismic data (*e.g.* Delouis *et al.*, 2000, 2002) or a combination of these (*e.g.* Ji *et al.*, 2002b; Kaverina *et al.*, 2002) have been jointly used with InSAR data. To search the parameter space genetic algorithms (*e.g.* Hernandez *et al.*, 1999), simulated annealing methods (*e.g.* Ji *et al.*, 2002a; Delouis *et al.*, 2002), or the Neighbourhood Algorithm (*e.g.* Lohman *et al.*, 2002) have all been employed, as well as a hybrid downhill Powell-Monte Carlo approach (*e.g.* Wright *et al.*, 1999; Funning *et al.*, 2007). One common feature amongst all these joint inversion techniques is that when modelling the seismic data they all assume a 1-D Earth structure. The study of Wald and Graves (2001) is the only study, to the writer's knowledge, to consider the effect of a 3-D structure, suggesting that the addition of geodetic data to seismic source inversions leads to more robust results as seismic data are very sensitive to the assumed Earth structure but geodetic data are much less so.

Both InSAR and seismic data are vital for the robust characterisation of the earthquake source process and this is evident through the continued investment in future satellites and

denser seismic networks. In 2013 the ESA plans to launch the first of two satellites with SARs (Sentinel 1A), with the specific purpose of acquiring SAR images for natural hazard applications. The second satellite (Sentinel 1B) is planned in the next few years, and once launched it will work in tandem with the first so that a SAR image of anywhere on Earth can theoretically be acquired every 6 days and the revisit time will be even shorter, compared with 35 days for the previous ESA missions. With regard to seismic data, the USArray is just one example of the expansion of portable and temporary networks. It is part of the 15 year-long Earthscope program and consists of 400 portable seismometers which are gradually being moved across the continental US to record local and global seismic activity, with the aim of improving the understanding of continental tectonics, lithospheric structure, and deep Earth structure (*e.g.* Meltzer *et al.*, 1999). Significant developments in high performance computing have also enabled advances in the forward modelling of seismic wave fields on a global scale (*e.g.* Komatitsch and Tromp, 1999; Jahnke *et al.*, 2008), and local scale (*e.g.* simulation of broadband ground motions, Graves *et al.*, 2008), and the modelling of the Earth structure (*e.g.* Schaefer *et al.*, 2011), with increasing accuracy and efficiency. Also the launch of further satellites, such as Sentinel 1A and 1B, will result in a significant expansion in the volume of InSAR data, and increasing computing capacity will be extremely useful for processing this large amount of data. All these improvements in data quality and availability, and modelling capability are extremely promising for the future development of techniques which characterise the earthquake source robustly.

1.4 Motivation and thesis outline

The goal of this thesis is to study large global earthquakes using InSAR and long period seismic data by investigating the differences between the two datasets to understand their relative strengths and weaknesses. This information will then be used to develop a new seismo-geodetic point source inversion technique to constrain the source in a robust way for these large events.

In Chapter 2 the first global catalogue of InSAR-determined source models, based on studies published in the scientific literature, is presented. This catalogue is subsequently

used in Chapter 3 as an independent means for verifying source models reported in seismic catalogues and cross-verifying InSAR source models for the same earthquake. The seismic moment, centroid location and fault geometry are all considered, and the centroid locations are also compared with the known geology and hypocentral locations. In addition, variations between source models (uniform and distributed slip) for the same earthquakes are used to assess the uncertainties.

Five earthquakes (M_w 6.0 - 8.1) which showed large discrepancies in these comparisons are investigated in Chapter 4 by forward modelling the source parameters to calculate seismic synthetics for comparison with the observed data. Two forward modelling techniques and Earth models are used; (i) Normal mode summation using the 1-D Earth model, PREM (Preliminary Reference Earth Model, Dziewonski and Anderson, 1981) and (ii) the Spectral element method using the 3-D shear wave mantle model, S20RTS (Ritsema *et al.*, 1999), combined with the crustal model CRUST2.0 (Bassin *et al.*, 2000).

These tests highlight the importance of the assumed Earth structure when modelling the seismic data and is one of the motivations behind the joint inversion technique presented in Chapter 5. This method is tested using three synthetic earthquakes and is then applied to three real events that could benefit from the joint inversion of InSAR and long period seismic data: Eureka Valley (M_w 6.1, 17th May 1993), Aiquile, Bolivia (M_w 6.6, 22nd February 1998) and Zarand, Iran (M_w 6.5, 22nd May 2005). Finally in Chapter 6 the key issues highlighted in this thesis are discussed and the main conclusions summarised.

Chapter 2

Construction of the ICMT catalogue

2.1 Introduction

Seismic data are routinely used to determine earthquake source models and, increasingly, Interferometric Synthetic Aperture Radar (InSAR) data are also being used. There are numerous seismic catalogues which provide locations and source mechanisms. However, currently there is not a homogeneous catalogue of InSAR-determined earthquake source parameters, where the source models have been determined using consistent modelling techniques and Earth models.

In this chapter I summarise the basic principles behind InSAR and seismic data for earthquake observation and the modelling approaches used to determine earthquake source parameters. A summary of existing seismic catalogues is then given. This is followed by a description of the compilation of the first global archive of InSAR derived source models, which is used in Chapter 3 for comparisons with estimates reported in global and regional seismic catalogues. The current version of the InSAR archive has been published in Weston *et al.* (2011, 2012).

2.2 Processing and modelling InSAR data

There are many studies that have reviewed the principles of InSAR (*e.g.*, Massonnet and Feigl, 1998; Bürgmann *et al.*, 2000; Feigl, 2002; Funning, 2005) which should be referred to for further details, but an outline of the technique will now be summarised. Synthetic Aperture Radar (SAR) involves a moving side-looking radar emitting pulses of microwave

radiation towards the ground and measuring the amplitude and phase of the radiation that is scattered back to the radar. By combining responses from multiple observation points as the radar platform moves, a high resolution SAR image is obtained (a comprehensive overview of SAR imaging can be found in e.g., Curlander and McDonough, 1991). This image is referred to as a Single Look Complex (SLC) image which contains the phase and amplitude information for each pixel as a complex number:

$$Z = Ae^{i\phi} \quad (2.1)$$

where A refers to the amplitude and ϕ the phase. InSAR is based on the difference in phase ($\Delta\phi$) between two SAR images; if these two SAR images are acquired before and after an earthquake, part of the phase difference corresponds to one component of the surface displacement caused by the event ($\Delta\phi_{def.}$). However, atmospheric delay ($\Delta\phi_{atmos.}$), topography ($\Delta\phi_{top.}$) and the difference in satellite position ($\Delta\phi_{pos.}$) and pixel properties ($\Delta\phi_{pixel}$) in the SAR image at the two image acquisition times can also cause phase changes:

$$\Delta\phi = \Delta\phi_{def.} + \Delta\phi_{atmos.} + \Delta\phi_{top.} + \Delta\phi_{pos.} + \Delta\phi_{pixel} \quad (2.2)$$

In order to isolate the phase change due to the earthquake surface displacement several methods have been developed to remove the other contributing factors, which are usually carried out during the processing stage of the data. Interferometric fringes due to topography are removed using a Digital Elevation Model (DEM) and the phase shift due to a change in satellite position can be corrected by using knowledge of the satellite orbits (e.g. Scharroo and Visser, 1998). However, the phase delay due to the atmosphere is more difficult to remove and, unlike topography and orbital changes, is not routinely removed. In recent years there has been an increased focus on developing techniques for removing this remaining, and potentially major, source of error in radar interferometry. Approaches to calculate the delay include using meteorological or atmospheric models and observed data to calculate the potential contribution of the atmosphere, particularly water vapour (e.g., Wadge *et al.*, 2006; Puysegur *et al.*, 2007; Doin *et al.*, 2009; Wadge *et al.*, 2010). Few studies have tried to integrate a method of removal into a processing

routine for InSAR data, but Li *et al.* (2005) successfully integrated water vapour correction models into the ROIPAC (Rosen *et al.*, 2004) software, a free and popular SAR data processing package.

Even in situations when such error sources are mitigated, noise from temporal decorrelation (changes to the radar scattering characteristics of the ground) can still remain in the interferogram. Changes in land use, land cover (*e.g.*, snow) or vegetation can be responsible for decorrelation, and the probability of change, and thus decorrelation, increases with time. Decorrelation can be mitigated by using a longer radar wavelength (*e.g.*, the ALOS satellite, $\lambda = 235$ mm) which is able to penetrate the canopies of trees and scatter off their more stable trunks, and is less sensitive in general to changes in small scatterers on the ground.

Once phase changes due to sources other than surface deformation are removed, then the surface displacement (\mathbf{u}) in the line of sight (LOS) of the radar is equal to the change in distance (or range) between the satellite and the ground:

$$\Delta\phi = \left(\frac{4\pi}{\lambda}\right) \mathbf{u} \cdot \hat{\mathbf{p}} \quad (2.3)$$

where, $\hat{\mathbf{p}}$ is a unit vector pointing from the ground towards the satellite antenna and λ refers to the wavelength of the radiation emitted by the satellite. Following equation 2.3, surface displacement equal to one half wavelength of the radar signal, corresponds to one fringe in an interferogram (1 cycle of pink to red in Figure 1.4). Wavelengths range from 31 mm to 235 mm (Table 2.1), consequently, surface displacements at millimetre level can potentially be detected by InSAR.

The 1990s saw the launch of various radar satellites and there are a few currently in operation which provide radar images that can be used to produce interferograms (Table 2.1). The ERS-1 from the ESA was the first C-band satellite, and the first to provide data that were used to measure the surface displacement from an earthquake. An L-band satellite, JERS-1, was launched by the Japanese Aerospace Exploration Agency (JAXA) a year later and over the following decade three further C-band satellites were launched. This included two from the ESA (ERS-2 and ENVISAT) and the Canadian Space Agency's first commercial earth observation satellite, RADARSAT-1. The ALOS was a follow-up L-band satellite to JERS-1, but this, and all the afore-mentioned satellites

have since been decommissioned. However, missions launched in 2007, by the Canadian, Italian and German space agencies are still in operation, which includes RADARSAT-2 and two X-band satellites, COSMO-SkyMed and TerraSAR-X. Moreover, the ESA plans to launch two new C-band satellites, with the first satellite (Sentinel-1A) to be launched in 2013 (ESA, 2007, 2011). Also JAXA are currently developing their next L-band satellite, ALOS-2.

Table 2.1: Summary of past and present satellites that provide SAR data for the measurement of earthquakes. Note that COSMO-SkyMed is not one satellite but a constellation of four satellites.

Satellite	Operation Period	Wavelength (mm)	Band
European Remote Sensing Satellite 1 (ERS-1)	1991 – 2000	56.7	C
European Remote Sensing Satellite 2 (ERS-2)	1995 – 2011	56.7	C
RADARSAT-1	1995 – 2013	56.0	C
ENVISAT	2002 – 2012	56.3	C
Japanese Earth Resource Satellite (JERS-1)	1992 – 1998	235.0	L
Advanced Land Observation Satellite (ALOS)	2006 – 2011	235.0	L
COSMO-SkyMed	2007 –	31.0	X
TerraSAR-X	2007 –	31.0	X
RADARSAT-2	2007 –	56.0	C

There are various packages available for the processing of SAR data to produce interferograms, with one of the most widely used packages being ROI_PAC (Rosen *et al.*, 2004). Detailed overviews of the processing stages used in the programme are available in several other studies (*e.g.*, Rosen *et al.*, 2000, 2004; Funning, 2005) but the process will be briefly summarised here. The two SAR images are preprocessed to produce Single-Look Complex images (SLC) which are high resolution images that contain both the phase and amplitude information. Then, using orbital information and estimated offsets between the images, the SLC images are resampled into the same geometry and the image acquired before the earthquake is multiplied by the complex conjugate of the ‘after’ image to form the interferogram. The signal from topography is then removed by calculating a synthetic interferogram using orbital information and the Digital Elevation Model (DEM, 3 Arc second Shuttle Radar Topography Mission (SRTM) in most cases). The interferogram is then filtered to enhance the strongest signals and the phase part of the signal is unwrapped from its modulo 2π value into the difference in phase between two neighbouring pixels. This difference is then adjusted up to a multiple of 2π to give the total change in range between the ground and the satellite. This unwrapped interferogram is then used to refine the

viewing geometry and any further topographic corrections and, finally the interferogram is geocoded to produce an image, such as the one seen in Figure 1.4.

The next step is to downsample the highly spatially correlated data because with a small subset of the data it is still possible to model the key features of the data. Down-sampling methods such as quadtree decomposition (*e.g.*, Jónsson *et al.*, 2002; Simons *et al.*, 2002), focused near-field sampling (*e.g.*, Funning *et al.*, 2005b), and resolution-based sampling (*e.g.*, Lohman and Simons, 2005b) have all been successfully used to reduce the number of data points to model from millions to hundreds or thousands.

Once down-sampled, static elastic dislocation theory can be used to model the displacement field seen in an interferogram. Steketee (1958) was the first to demonstrate that the dislocation $\delta u_j(\xi_1, \xi_2, \xi_3)$ across a planar surface, Σ , in an isotropic medium (*i.e.* an earthquake) will result in the following displacement field, $u_i(x_1, x_2, x_3)$:

$$u_i = \frac{1}{F} \int \int_{\Sigma} \delta u_j \left[\lambda \delta_{jk} \frac{\delta u_i^n}{\delta \xi_n} + \mu \left(\frac{\delta u_i^j}{\delta \xi_k} + \frac{\delta u_i^k}{\delta \xi_j} \right) \right] v_k d\Sigma \quad (2.4)$$

Each u_i^j refers to the i^{th} component of displacement at (x_1, x_2, x_3) due to a point force at (ξ_1, ξ_2, ξ_3) in the j^{th} direction with magnitude F , where δ_{jk} is the Kronecker delta, λ and μ refer to Lamé elastic parameters and v_k is the direction cosine of the normal to the surface element $d\Sigma$.

Analytical solutions to this equation for shear and tensile motions on a fault are given by Okada (1985), based on the cartesian coordinate system and conventions shown in Figure 2.1. Following these solutions it is evident that the fault geometry (strike, dip, rake), location and length are non-linearly related to the surface displacement field. Thus, while the forward modelling of displacement fields (and, interferograms) is a simple process, the inverse problem of determining the optimal source parameters from interferograms is not as straightforward. A number of algorithms have been adopted to solve this non-linear inverse problem; genetic (*e.g.* Hernandez *et al.*, 1999), simulated annealing (*e.g.* Delouis *et al.*, 2002; Ji *et al.*, 2002a), the Neighbourhood Algorithm (*e.g.* Lohman and Simons, 2005a) and a downhill Powell-Monte Carlo approach (*e.g.* Clarke *et al.*, 1997; Wright *et al.*, 1999).

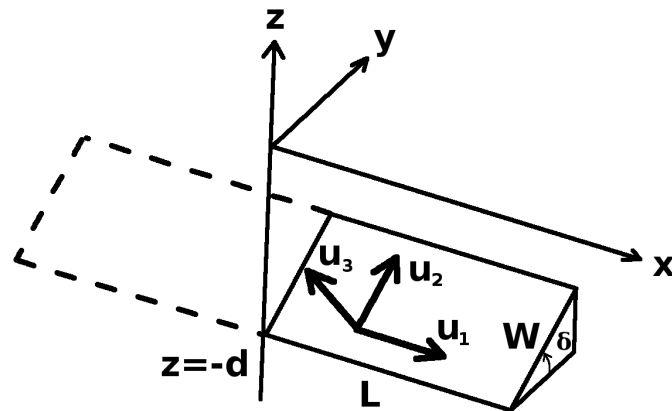


Figure 2.1: Coordinate system and source geometry assumed, after Okada (1985), for a fault of length L , width W , and dipping at an angle of δ . U_1 , U_2 , and U_3 are elementary dislocations and correspond to strike-slip (U_1), dip-slip (U_2) and tensile (U_3) components of an arbitrary dislocation, respectively.

2.3 Earthquake source inversions using seismic data

Measurements of displacements caused by seismic waves generated by earthquakes is the traditional approach for observing earthquakes. In this study, data recorded on the global seismic networks (*e.g.* Global Seismic Network, GSN) at teleseismic distances are used, which includes body waves (P and S) and surface waves (Rayleigh and Love), see Figure 2.2. Body waves are the fastest, the P waves arrive first, followed by S waves. Surface waves are the last to arrive, which despite circumnavigating the Earth several times, due to their lower rates of geometrical spreading are usually the highest amplitude arrivals at teleseismic distances. Rayleigh waves are created by the interaction of P and SV waves and are observed on the vertical and longitudinal components of a seismogram (Figure 2.2 a & b). Love waves are the result of the constructive interference of SH waves trapped at the surface and are seen on the transverse component (Figure 2.2 c).

The displacements due to an earthquake observed at seismometers can be uniquely described using body forces and the response of the assumed Earth structure to these forces. Based on the uniqueness theorem and various representation theorems (see Aki and Richards, 1980), and omitting the effects of traction and displacement discontinuities (Julian, 1998), then the displacement field, $u(x,t)$ due to a shear dislocation in a volume,

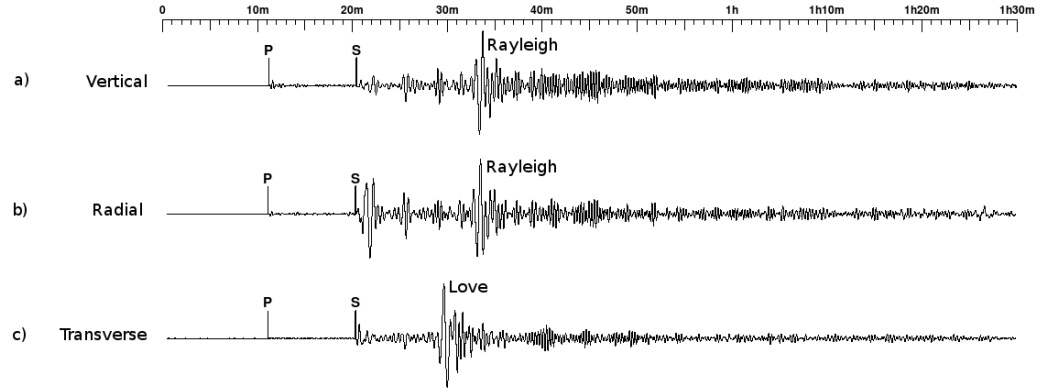


Figure 2.2: Example seismogram showing the displacements due to the Haiti earthquake (M_w 7.0, January 12th January 2010) recorded at the BFO station in Germany at an epicentral distance 70° and 44° azimuth. P, S, Rayleigh and Love wave arrivals are highlighted on the vertical, longitudinal and transverse components. The record spans an hour and a half following the occurrence time of the earthquake (21:53:10, GMT), as shown along the top of the figure. The amplitude corresponds to ground velocity in ms^{-1} .

V , due to a body force, f , at position ξ can be written as:

$$u_i(x, t) = \int \int \int_V G_{ij}(x, \xi, t) * f_j(\xi, t) d^3\xi \quad (2.5)$$

where $G_{ij}(x, \xi, t)$ is the elastodynamic Green's function which describes the i th component of displacement due to a unit force applied in the j th direction at position ξ and time zero and '*' indicates temporal convolution. If the Green's function is expanded using a Taylor series then equation 2.5 becomes

$$u_i(x, t) = G_{ij}(x, 0, t) * F_j(t) + G_{ij,k}(x, 0, t) * M_{jk}(t) + \dots \quad (2.6)$$

where F is the total force exerted by the source:

$$F_j(t) = \int \int \int_V f_j(\xi, t) d^3\xi \quad (2.7)$$

and M is the seismic moment tensor:

$$M_{jk}(t) = \int \int \int_V \xi_k f_j(\xi, t) d^3\xi \quad (2.8)$$

which describes the earthquake as a combination of nine force couples, and was first introduced by Gilbert (1970). The seismic moment tensor can be expressed using spherical coordinates in matrix form:

$$M = \begin{pmatrix} M_{rr} & M_{r\theta} & M_{r\phi} \\ M_{\theta r} & M_{\theta\theta} & M_{\theta\phi} \\ M_{\phi r} & M_{\phi\theta} & M_{\phi\phi} \end{pmatrix} \quad (2.9)$$

where (r, ϕ, θ) are the orthogonal axes (up, E, S). The moment tensor is symmetric, hence there are only six independent elements, where the eigenvectors and eigenvalues of this matrix describe the source type, moment and orientation. The moment tensor can be decomposed into three parts; isotropic, double-couple and compensated linear vector dipole (CLVD). If a pure double-couple source is assumed (*i.e.* no volume change, such as shear fracture) then the trace and the determinant of the moment tensor is zero, $\lambda_1 + \lambda_2 + \lambda_3 = 0$, whereas for a purely isotropic source (*e.g.* an explosion) $\lambda_1 = \lambda_2 = \lambda_3$. Consequently, the ratio of the minimum and maximum eigenvalues of the trace of the tensor can be used to quantify the percentage of the non-double-couple component. For most earthquakes the double-couple is the dominant mechanism however, the CLVD is a special case where the moment tensor is traceless but one of the eigenvalues is twice that of the other two, which are equal. Moment tensors with this kind of behaviour have been observed for earthquakes in volcanic settings (*e.g.* Julian, 1983; Shuler and Ekström, 2009), or for earthquakes which involve two subevents occurring almost simultaneously (*e.g.* Stich *et al.*, 2005).

Assuming a pure double couple the moment tensor can be expressed in terms of fault geometry, strike (Φ), dip (δ) and rake (λ) and seismic moment (M_0), where Figure 2.3 shows the conventions followed throughout the thesis for these parameters, and following the notation of Aki and Richards (1980):

$$M = M_0 \begin{pmatrix} \sin 2\delta \sin \lambda \\ -(\sin \delta \cos \lambda \sin 2\Phi + \sin 2\delta \sin \lambda \sin^2 \Phi) \\ \sin \delta \cos \lambda \sin 2\Phi - \sin 2\delta \sin \lambda \cos^2 \Phi \\ -(\cos \delta \cos \lambda \sin \Phi + \cos 2\delta \sin \lambda \sin \Phi) \\ \cos \delta \cos \lambda \sin \Phi - \cos 2\delta \sin \lambda \cos \Phi \\ -(\sin \delta \cos \lambda \cos 2\Phi + \frac{1}{2} \sin 2\delta \sin \lambda \sin 2) \end{pmatrix} = \begin{pmatrix} M_{rr} \\ M_{\theta\theta} \\ M_{\phi\phi} \\ M_{r\theta} \\ M_{r\phi} \\ M_{\theta\phi} \end{pmatrix} \quad (2.10)$$

The moment tensor is linearly related to the displacements recorded at seismometers Gilbert and Dziewonski (1975) and this is part of the basis behind the approach used in the seismic catalogue, the Global Centroid Moment Tensor catalogue, (GCMT) which routinely reports focal mechanisms for earthquakes of M_w 5.5 or greater.

For the fast inversion of seismic data, a point source can be assumed such as in the GCMT catalogue, or, if more information on the source is desired, a finite fault model can be determined (*e.g.*, Wald and Heaton, 1994). There are strengths and weaknesses to each method, and the inversion methods employed in the seismic catalogues used here will be outlined in the following section.

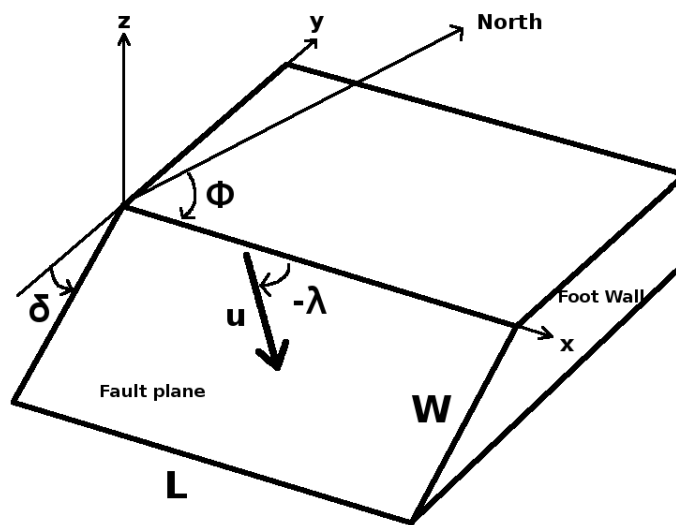


Figure 2.3: The strike (Φ), dip (δ) and rake (λ) conventions followed throughout this thesis for a fault of length L , and width W , where u refers to the slip vector that describes the movement of the hanging wall with respect to the foot wall.

2.4 Existing seismic source model catalogues

With extensive global seismic networks deployed worldwide and vast data analysis and inversion techniques available, seismology is a well-established and reliable technique for determining earthquake source parameters. The GCMT catalogue is one of the most frequently used seismic catalogues and has calculated focal mechanisms for moderate to large events ($M \geq 5.0$) since 1976. Long-period body and surface waves are used in inversions for the six moment tensor components. Synthetic seismograms for each moment tensor component at each seismometer location, otherwise known as excitation kernels, are calculated using normal mode summation (e.g., Gilbert, 1976) in a 3D Earth model (SH8/U4L8, Dziewonski and Woodward, 1992). Originally, a 1D Earth model was used instead (PREM, Dziewonski *et al.*, 1981). The observed seismograms can be expressed as a multiplication between the matrix of excitation kernels and the vector of six moment tensor components. To solve for the moment tensor this linear relationship is solved using a least-squares procedure, where for the 0th iteration of the inversion the kernels are calculated using the location from the Preliminary Determination of Epicenters (PDE) catalogue published by the NEIC. Once there is an initial estimate of the moment tensor, then excitation kernels are recalculated for all ten source parameters (centroid location, origin time and moment tensor) and an iterative least-squares inversion is carried out until an optimal agreement is reached between the observed and theoretical seismograms (Dziewonski *et al.*, 1981; Dziewonski and Woodhouse, 1983).

The International Seismological Centre (ISC) has two global catalogues; the ISC and EHB (Engdahl-van der Hilst - Buland) Bulletins. The agency uses data from the monthly listing of events produced by the National Earthquake Information Centre (NEIC) and data submitted from various agencies around the world. These data are associated to an event and a least-squares procedure is used to determine four source parameters: hypocentral depth, location, and origin time. These parameters are reported in the ISC Bulletin along with magnitude values m_b and M_s (Adams *et al.*, 1982). To reduce the observed bias in ISC focal depths the methodology above was modified and a more recent Earth model, the ak135 model (Kennett *et al.*, 1995) was used instead of the Jeffreys and Bullen travel time tables (Jeffreys and Bullen, 1940). Station patch corrections and later phase arrivals were also incorporated into the procedure (Engdahl *et al.*, 1998) and the resulting

parameters are published in the EHB bulletin. More recently the ISC has implemented a new location algorithm which used the Neighbourhood Algorithm (Sambridge, 1998) to obtain an initial guess for the hypocentre location and has the capability to include regional traveltime predictions for certain phase arrivals (Pg, Lg, Pn, Sn), based on a 3-D velocity model, for more details see Bondar and Storchak (2011). This was implemented at the beginning of 2011 and so applies to events from 2009 onwards reported in the ISC Bulletin (ISC, 2011).

In addition to these global catalogues, there are numerous catalogues based on data from local or regional seismic networks, which focus on events in regions including central Europe or individual countries, such as Japan. The following regional catalogues are used in this chapter:

- **Regional Centroid Moment Tensor Catalogue (RCMT)** – This reports source mechanisms for $4.5 < M < 5.5$ events in the Mediterranean region from 1977, with the most recently published catalogue including events up to 2008 (Pondrelli *et al.*, 2011). The method used is the same as in the GCMT catalogue, except that in order to account for smaller magnitude events, the data are low-pass filtered at 35 s to include shorter period fundamental mode surface waves. Synthetic seismograms for these waves are calculated using global, laterally-varying, phase velocity models and propagating a source pulse through them (Pondrelli *et al.*, 2002), instead of a classical normal mode summation approach in a 1D Earth model.
- **Euro-Med Bulletin** – This has been developed, and is run by, the Euro-Mediterranean Seismological Centre (EMSC). The current database covers events in the Euro-Mediterranean region in the period 1998–2008. Data are collected from over 60 networks in 53 countries and the gathered phase and location information are processed in a three-step procedure to produce the bulletin. For a local event the associated phases are collected and a location is determined iteratively by computing travel times using a local velocity model until the least-square travel time residual is minimized. The location is then tested against the initial reported location, the variation in the travel time residual and the RMS, and the defining phases (Godey *et al.*, 2006).

- **National Research Institute for Earth Science and Disaster Prevention (NEID) Catalogue** – There are several regional networks in Japan run by the Japan Meteorological Agency (JMA) and the NEID. The data are archived by JMA and NEID and made available for public use (Okada *et al.*, 2004). For earthquakes since 1997 the data recorded on the regional broadband seismic network (F-net) have been used by the NEID to calculate focal mechanisms based on the polarities of the first P-wave arrivals (Kubo *et al.*, 2002).
- **India Meteorological Department (IMD) Catalogue** – Similar to Japan, regional data from their National Seismological Network (NSN) are used for the calculation of location and magnitude; the agency also submits the solutions to the ISC (IMD, 2011).
- **Earthquake Mechanisms of the Mediterranean Area (EMMA)** – This is a database of focal mechanisms for earthquakes that have occurred in the Mediterranean area between 1905 and 2003. The mechanisms and the related source parameters reported in the literature are collected as well as the data that were used to calculate them. The focal mechanisms were recomputed using these data and compared with the mechanism published in the study. Errors, such as rotations in strike or rake values as a result of the formulation used, are corrected for. Multiple solutions for each event are reported, but one is suggested as the best solution using a list of four criteria, the foremost dependent on whether errors were reported with the original solution; for further details see Vannuccii and Gasperini (2003).
- **Advanced National Seismic System (ANSS) Composite Catalogue** – This is a world-wide catalogue run by the Northern California Earthquake Data Center including events since 1898 to the present day. It merges solutions from 15 contributing regional networks across North America, and the NEIC. Each regional network is assigned a geographic region and solutions from this network for events that occur in the region are always reported in the catalogue. If multiple solutions from various networks are reported for an event, the solution from the network whose geographic region covers the location of the event is considered the best solution. For events with more than one solution that occur outside the area covered by the

regional networks the solution with the largest magnitude is kept (ANSS, 2010).

- **Southern California Seismic Network (SCSN) catalogue** – Similar to ANSS, the Southern California Seismic Network (SCSN) collects data from regional seismic networks across North America, including its own network of over 160 stations. The origin time, date, location and magnitude along with uncertainties are determined using an automatic phase picking procedure and reviewed by a seismologist. There are currently over 470,000 events since 1932 to the present day included in the catalogue (Hutton *et al.*, 2010).

These seismic catalogues greatly outnumber the global or regional compilations of source models calculated from geodetic data. The SRCMOD database is one of the largest online resources to include finite-source rupture models obtained from the inversion of seismic and/or geodetic data. It began in 2004 and archives kinematic and static source models reported in the literature. Since 2012 it has been part of the earthquake research resources (equake-RC) project, which aims at providing data and resources for earthquake research. Consequently, as well as authors being able to upload models, there is also the option of downloading other models included in the database. Currently there are 159 source models for 85 earthquakes (SRCMOD, 2012).

2.5 Compilation of InSAR Centroid Moment Tensor (ICMT) catalogue

Since 1992 the number of InSAR derived models has grown rapidly, yet there was no catalogue similar to the various seismic catalogues described in the previous section. The absence of such a database prompted the compilation of CMT source parameters (spatial centroid location, seismic moment and fault's geometry) for global earthquakes occurring since 1992 studied using InSAR from nearly 100 studies published in the literature.

A total of 67 earthquakes that occurred between 1992 and 2010 from 96 studies are included in the database listed in Table 2.2 listed at the end of this chapter. For a given published study we use solution(s) in order of importance which are stated by the authors as their favourite solution and/or that fit the data better than the other solutions. Whenever uniform and variable slip inversions are carried out, both final inversion solutions are

included in the database, except if any of the models has a substantially lower misfit or if it is indicated by the authors as not being a preferred model. Whenever there are multiple studies of the same earthquake they are included in the database as they are valuable to assess uncertainties. Consequently for the 67 earthquakes there are a total of 131 source models. Only models for events that occurred before and including 2010 are used in this chapter as this was the most up to date version of the database at the time of comparisons. However, the database is constantly updated whenever new studies become available, and future work will include more earthquakes.

Figure 2.4 shows the geographical location of the 67 earthquakes listed in Table 2.2. As expected, most earthquakes are located within the continents, with depths shallower than 60 km (except for the 2005 Tarapaca, Chile, earthquake, which has a GCMT depth = 97.6 km). The magnitudes of the earthquakes studied are in the range M_w 5.0–8.5, with about half of the earthquakes having magnitudes M_w 6.0–6.5 (see Figure 2.5). This reflects the relative scarcity of large earthquakes ($M_w \geq 7.5$) in continental settings and the relative difficulty of studying small earthquakes ($M_w \leq 5$) using InSAR due to atmospheric noise, data incoherence or unfavourable earthquake depths. An additional factor limiting the number of small magnitude earthquakes used in this study is the absence of reported GCMT parameters for some of the small earthquakes studied using InSAR (*e.g.*, for the M_w 5.0, 18 September 1997 and 1 October 1998 Zagros mountains earthquakes studied by Lohman and Simons (2005a) and for the M_w 4.4, 21 September 2005, Kalan- nie and M_w 4.7, 10 October 2007, Katanning, Australia, earthquakes studied by Dawson *et al.* (2008)). Of the 67 earthquakes listed, 23 occurred on strike-slip faults, 28 thrust faults and 16 have normal fault movement.

Since InSAR data are commonly used in conjunction with other data types such as GPS, seismic and levelling, the events were classified according to the following criteria:

- I (InSAR data only)
- GI (GPS and InSAR data)
- SI (Seismic and InSAR data)
- OI (InSAR and other data, where three or more sources of information have been used, such as levelling, SPOT 5, *etc.*)

Studies with InSAR source models where multiple subevents are present that are clearly spatially discontinuous or the authors state as being strongly influence by substantial postseismic deformation, (*e.g.*, 2004 Parkfield earthquake), are not included in the database.

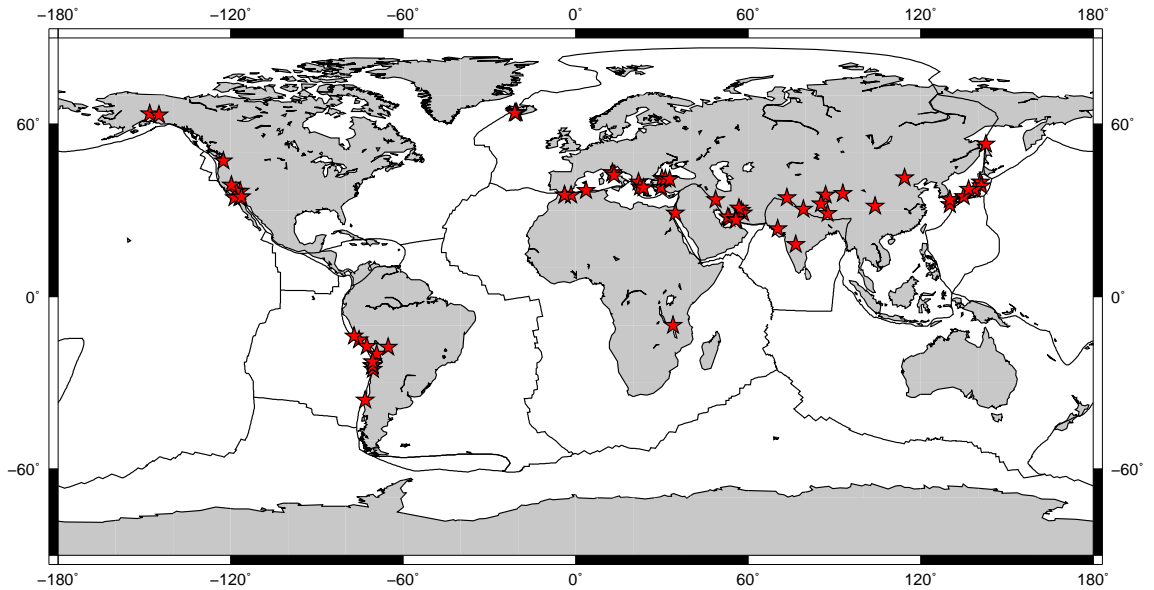


Figure 2.4: Geographical location of the 67 earthquakes (stars) studied with InSAR used in this study. All earthquakes have magnitudes between M_w 5.0–8.5 and are shallow (depth smaller than 60 km), except for the 2005 Tarapaca, Chile earthquake (GCMT depth=97.6 km).

2.5.1 Centroid Moment Tensor parameter calculations

Not all the required source parameters from InSAR studies were reported in the literature and in this instance the missing parameters were calculated with the information given in the study or using information provided on request from authors. For example, often the corner of the fault or the updip surface projection of the centroid were the only locations given. For uniform slip models this location is used along with additional geometrical information (*e.g.* fault strike, dip, width and length) to determine the centroid location. For the variable slip models that were obtained from several authors, the spatial distribution of slip and fault geometry are used to compute a centroid location. For uniform slip models which incorporate two or more faults a similar approach to the variable slip models is taken, whereby the parameters are weighted according to the seismic moment of each fault.

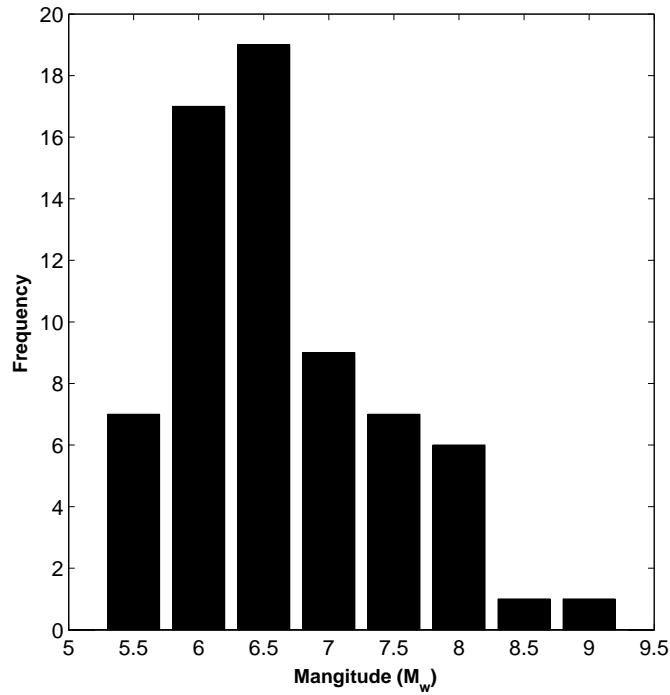


Figure 2.5: Distribution of earthquake moment magnitudes (M_w) of the earthquakes studied with InSAR used in this study. The distribution is skewed towards earthquakes in the magnitude range 6–6.5. This is probably due to the higher frequency of earthquakes of that magnitude compared to larger events and to a higher detectability of such earthquakes using InSAR than to smaller events. Also, in this study we do not use a number of small earthquakes studied using InSAR because of the absence of reported GCMT parameters for them (see main text for details).

To determine the seismic moment if the moment magnitude (M_w) was given it was converted using a simple relation (Kanamori, 1977):

$$M_w = \frac{2}{3} \log M_o - 6.03 \quad (2.11)$$

Alternatively, M_o was calculated if the area of the fault (A), the total slip (u) were known and an assumed rigidity modulus (μ) chosen:

$$M_o = \mu A u \quad (2.12)$$

We use the rigidity modulus quoted in the study but if it is not stated then a standard rigidity modulus of 32 GPa is assumed.

2.5.1.1 Example of ICMT parameter calculations

Figure 2.6 shows the two-fault, uniform slip model for the 2003 Bam, Iran, earthquake produced by Funning *et al.* (2005b). The primary fault released a seismic moment of 7.6×10^{18} N m, whereas the secondary fault has a seismic moment of 1.4×10^{18} N m. Figure 2.6 shows the focal mechanism (red beach ball) obtained from the total moment and the moment-weighted average strike, dip and rake of the two faults, assuming a pure, double-couple, source mechanism (see overall parameters in Table 2.2). As expected, the focal mechanism obtained from the overall parameters is similar to that of the primary fault, which has the larger moment. We also show the geometric centroid of each fault (black crosses) and the overall centroid obtained from a moment-weighted average of the centroids of the two faults (red cross). Again, as expected the overall centroid is close to that of the primary fault.

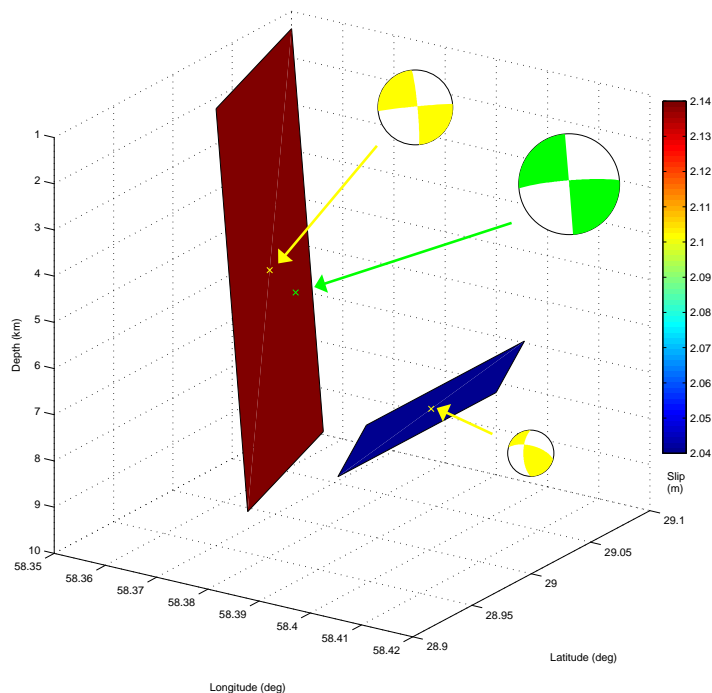


Figure 2.6: Example of the calculation of overall CMT source parameters for the 2003 Bam earthquake, using the two-fault, uniform slip model of Funning *et al.* (2005b) obtained using InSAR data. The model consists of a main fault plane with 2.14 m of slip and a smaller secondary fault with 2.04 m of slip, with estimated seismic moments of 7.6×10^{18} and 1.4×10^{18} N m, respectively. The corresponding focal mechanisms (yellow beach balls) and centroid locations (yellow crosses) are shown. The red beach ball represents the focal mechanism obtained from the total moment and from the moment-weighted average of strike, dip and rake of the two faults, assuming a pure double-couple mechanism. The average centroid location is also shown (green cross). The beach balls are not in absolute scale.

2.6 Intraevent variability within the database

Since the earthquakes used in this study span 17 years and the InSAR source models are generally built using different datasets and modelling strategies, the compilation is nonuniform in terms of reliability of various models. For some cases the compilation contains several source models for a given earthquake. The variability in such earthquake source models provides a means to assess qualitatively uncertainties of the source parameters, which are generally unknown.

2.6.1 Seismic moment

Among the earthquakes in our compilation with several InSAR-derived estimates of seismic moment, the intravent variability in moment between the smallest reported value and the others is below 20% for 19 earthquakes (median of $\sim 17\%$ and standard deviation, σ , 11%). Larger variabilities occur for the following seven earthquakes: 2003 Bam (44% difference between the moment estimated by Peyret *et al.* (2007) and that obtained by Funning *et al.* (2005b)); 1992 Little Skull Mountain (35% difference between “InSAR only” and “seismic and InSA” models determined by Lohman *et al.* (2002)); 1997 Manyi (35% difference between the moment from Funning *et al.* (2007) and that by Wang *et al.* (2007)); 1999 Duzce (37% difference between the moment obtained using a one-segment versus a multiple segment model by Wright (2000)); 1992 Fawnskin (27% difference between the moment given by Feigl and Thurber (2009) and that by Feigl *et al.* (1995)); and 1999 Izmit (25% difference between the moment given by Feigl (2002) and by Wright (2000)). The latter discrepancy may be due to the contamination by postseismic deformation (Feigl, 2002).

2.6.2 Fault geometry and mechanism

Differences in strike for a given earthquake are generally smaller than 20° (with a median variability over 18 earthquakes of $\sim 4^\circ$ and $\sigma=10^\circ$), except for the Al Hoceima 2004 earthquake, for which there is a difference of 44° between the strike determined by Tahayt *et al.* (2009) and that found by Biggs *et al.* (2006). For the 19 earthquakes in Table 2.2 with more than one value of fault dip reported, the variability in dip is smaller than 20° (with a median of $\sim 8^\circ$ and $\sigma=6^\circ$) except for the 2000 Cankiri earthquake, for which

there is a difference of 22° between the fault dip determined by Wright (2000) and that obtained by Çakir and Akoglu (2008). The variability in rake for a given earthquake is also generally smaller than 20° (with a median over 21 earthquakes of $\sim 7^\circ$ and $\sigma=11^\circ$), except for the following earthquakes: 1992 Little Skull Mountain (27° difference, see Table 2.2), 1999 Duzce (44° difference, see Table 2.2) and Noto Hanto (35° difference, see Table 2.2).

2.6.3 Centroid spatial location

Differences in epicentral location for a given earthquake are smaller than 10 km for 18 earthquakes (with a median over 20 earthquakes of ~ 3 km and $\sigma = 5$ km), with the following three earthquakes showing larger differences: 1996 Antofagasta (17 km difference between the studies of Pritchard *et al.* (2002, 2006)); 1997 Manyi (14 km difference between the results of Funning *et al.* (2007) and Wang *et al.* (2007)); and 1999 Izmit (14 km between the results of Wright (2000) and Delouis *et al.* (2000)). There is a very good agreement between the centroid depths in the various InSAR source models for a given earthquake, with a variability smaller than 5 km for most earthquakes (with the median of the variabilities for 20 earthquakes being ~ 2 km and $\sigma = 2$ km). The maximum variability in depth between source models obtained using layered 1-D and 3-D media by Bustin *et al.* (2004) is 9 km for the Nisqually earthquake.

2.7 Conclusions

While this study focuses on 67 earthquakes that occurred between 1992 and 2010, we are currently expanding our ICMT database by including InSAR source models that occurred since 2010 and will make it available to the wider community in the near future, thus contributing to ongoing earthquake source model validation efforts. Moreover, we anticipate that this database will also form the basis for future comparisons of other relevant parameters, such as average slip and stress drop. The compilation of the first global database of InSAR-determined source models from the scientific literature will now be used in the following chapter to assess the source parameters reported in seismic catalogues.

Table 2.2: CMT parameters from published InSAR studies for earthquakes that occurred between 1992 and 1997 **Date** and **Location** contain the earthquake’s date and geographical location. **M₀** is the seismic moment; **Lat.**, **Lon.**, **Depth** are the centroid’s latitude, longitude and depth, respectively; **Str.**, **Dip** and **Rake** are the fault’s strike, dip and rake angles, respectively. The type of faulting (column “**Type**”) is indicated by the symbols: ss (strike-slip fault), n (normal fault), and th (thrust fault). The type of data used for a given study is shown in the column “**Data**”: I (using InSAR data only), GI (using GPS and InSAR data), SI (using seismic and InSAR data) and OI (using InSAR data combined with two or more other types of data; see text for details). Whenever there are multiple models of the same earthquake produced in a given study, we distinguish them using the following symbols: “DS” (distributed slip model), “PS” (point source model), “FFP” (finite fault patches), “1 seg.” (fault model only with one segment), “mult. seg.” (fault model with multiple segments), “PM” (planar model) and “CM” (curved model). Any models in italics refer to inversions using a layered half-space. Any blank spaces mean that the parameter was not reported in the study and couldn’t be calculated using the available information, and any parameters in bold were fixed in the source inversion.

Date	Location	M₀ ($\times 10^{18} Nm$)	Lat. ($^{\circ}$)	Lon. ($^{\circ}$)	Depth (km)	Str. ($^{\circ}$)	Dip ($^{\circ}$)	Rake ($^{\circ}$)	Type	Data	Reference
28.06.92	Landers	103.00	34.45	243.48	5.53	154.1	89.9	173.9	ss	GI	Fialko (2004b)
29.06.92	<i>Little Skull Mountain</i>	<i>0.50</i>	<i>36.75</i>	<i>243.76</i>	<i>11.20</i>	<i>52.0</i>	<i>40.0</i>	<i>-51.0</i>	<i>n</i>	<i>I</i>	<i>Lohman et al. (2002)</i>
29.06.92	<i>Little Skull Mountain</i>	<i>0.32</i>	<i>36.75</i>	<i>243.72</i>	<i>9.40</i>	<i>36.0</i>	<i>58.0</i>	<i>-78.0</i>	<i>n</i>	<i>SI</i>	<i>Lohman et al. (2002)</i>
04.12.92	Fawnskin	0.15	34.35	243.09	2.60	106.0	28.0	93.0	th	I	Feigl <i>et al.</i> (1995)
			± 0.004	± 0.002	± 0.3	± 7.0	± 4.0	± 4.0			
04.12.92	Fawnskin	0.11	34.36	243.09	2.70	102.0	39.0	92.0	th	I	Feigl and Thurber (2009)
			± 0.001	± 0.009	± 0.15	± 7.0	± 4.0				
20.03.93	Ngamr. County, Tibet	1.48	29.06	87.48	7.00	4.3	49.7	-99.4	n	I	Funning (2005)
		± 0.02	± 0.002	± 0.003	± 0.1	± 1.0	± 3.2	± 3.0			
20.03.93	Ngamr. County, Tibet	1.57	26.06	87.49	7.00	4.2	46.5	-95.8	n	SI	Funning (2005)
		± 0.02	± 0.002	± 0.003	± 0.1	± 1.0	± 2.8	± 2.5			
17.05.93	Eureka Valley, California	1.70	37.11	242.21	9.20	173.0	54.0		n	I	Massonnet and Feigl (1995)
		± 0.3	± 0.004	± 0.005	± 0.2	± 2.0	± 2.0				
17.05.93	Eureka Valley, California (DS)				13.00	7.0	50.0		n	I	Peltzer and Rosen (1995)
11.07.93	<i>N. Chile</i>	<i>18.00</i>	<i>-25.20</i>	<i>289.97</i>	<i>54.00</i>	5.0	<i>30.0</i>	<i>104.0</i>	<i>th</i>	<i>SI</i>	<i>Pritchard et al. (2006)</i>
29.09.93	Killari, India	1.76			3.25	95.0	54.4	86.0	th	I	Satyabala and Bilham (2006)
						± 5.0		± 5.0			
17.01.94	Northridge	9.42				248.0	42.0		th	I	Massonnet <i>et al.</i> (1996)
26.05.94	Al Hoceima, Morocco	2.10	35.20	355.94	7.00	23.3	86.9	-1.2	ss	I	Biggs <i>et al.</i> (2006)
						± 4.5	± 2.3	± 2.6			

Continued on next page

Date	Location	M_0 ($\times 10^{18} Nm$)	Lat. ($^\circ$)	Lon. ($^\circ$)	Depth (km)	Str. ($^\circ$)	Dip ($^\circ$)	Rake ($^\circ$)	Type	Data	Reference
26.05.94	Al Hoceima, Morocco (DS)	2.00				23.0	77.0		ss	I	Akoglu <i>et al.</i> (2006)
12.09.94	Nevada	0.92	38.82	240.38	7.84	319.0	72.0	152.0	ss/n	I	Amelung and Bell (2003)
16.01.95	Kobe, Japan	19.30	34.62	135.06	6.22	229.1	89.9	-114.4	ss	I	Ozawa <i>et al.</i> (1997)
13.05.95	Kozani-Grevena	6.50				254.0	48.0	-96.0	n	SI	Resor <i>et al.</i> (2005, 2007)
13.05.95	Kozani-Grevena	6.90				257.8	38.2	-97.1	n	I	Rigo <i>et al.</i> (2004)
		± 0.5									
13.05.95	Kozani-Grevena	6.40							n	I	Meyer <i>et al.</i> (1996)
28.05.95	N. Sakhalin, Russia	73.73	52.89	142.90	7.29	197.5	84.2	173.7	ss	I	Tobita <i>et al.</i> (1998)
15.06.95	Aigion, Greece	3.90	38.33	22.22	5.10	275.0	35.0	-83.0	n	GI	Bernard <i>et al.</i> (1997)
30.07.95	Antofagasta, Chile (DS)	1600.00	-24.16	289.14	30.00	5.0	21.5	113.0	th	GI	Pritchard <i>et al.</i> (2002)
30.07.95	Antofagasta, Chile	1800.00	-24.16	289.31	27.00	5.0	30.0	105.0	th	OI	Pritchard <i>et al.</i> (2006)
01.10.95	Dinar, Turkey	4.55	38.10	30.08	6.42	145.0	49.0	-90.0	n	I	Wright <i>et al.</i> (1999)
		± 1.1			± 3.1	± 1.5	± 1.0				
01.10.95	Dinar, Turkey	4.30	38.10	30.09	4.60	135.0	49.8	-84.4	n	I	Funning (2005)
		± 0.2	± 0.009	± 0.009	± 0.1	± 0.5	± 0.9	± 3.6			
01.10.95	Dinar, Turkey	3.70	38.11	30.09	4.20	135.2	48.4	-95.7	n	SI	Funning (2005)
		± 0.1	± 0.009	± 0.009	± 0.1	± 0.9	± 0.9	± 2.3			
01.10.95	Dinar, Turkey (DS)	4.10				145.0	34.0		n	I	Fukahata and Wright (2008)
22.11.95	Nuweiba, Egypt	56.23	28.94	34.73	12.0	195.2	65.0	-15.5	ss/n	I	Klinger <i>et al.</i> (2000)
22.11.95	Nuweiba, Egypt	70.00				200.0	80.0		ss	SI	Shamir <i>et al.</i> 2003
22.11.95	Nuweiba, Egypt (DS)	65.00	28.88	34.75	11.25	197.5	67.0	-4.0	ss	SI	Baer <i>et al.</i> (2008)
19.04.96	N. Chile	14.00	-23.94	289.94	49.00	5.0	23.0	107.0	th	SI	Pritchard <i>et al.</i> (2006)
12.11.96	Nazca Ridge, Peru (DS)	440.00	-15.32	284.84	28.00	307.0	30.0	44.5	th	SI	Salichon <i>et al.</i> (2003)
12.11.96	Nazca Ridge, Peru (DS)	480.00	-15.40	284.80	30.00	312.0	15.0-30.0	50.0	th	OI	Pritchard <i>et al.</i> (2007)
26.03.97	Kagoshima, Japan	1.78				275.0	81.0	-19.0	ss	GI	Fujiwara <i>et al.</i> (1998)
						± 6.0	± 3.0	± 2.0			
05.05.97	Zagros Mts, Iran (PS)	0.16	27.13	53.88	5.20	120.0	80.0	-90.0	n	I	Lohman and Simons (2005a)
			± 0.003	± 0.003	± 3.0		± 4.0	± 6.0			
05.05.97	Zagros Mts, Iran (FFP)	0.16	27.13	53.88	4.40	120.0	80.0	-90.0	n	I	Lohman and Simons (2005a)
			± 0.003	± 0.003	± 3.0		± 4.0	± 5.0			
05.05.97	Zagros Mts, Iran (DS)	0.16	27.12	53.89	6.20	120.0	80.0	-83.0	n	I	Lohman and Simons (2005a)

Continued on next page

Date	Location	M_0 ($\times 10^{18} Nm$)	Lat. ($^\circ$)	Lon. ($^\circ$)	Depth (km)	Str. ($^\circ$)	Dip ($^\circ$)	Rake ($^\circ$)	Type	Data	Reference
26.09.97	Colfiorito, Italy, 00h33	0.48			4.50	154.0	46.0	-77.0	n	SI	Salvi <i>et al.</i> (2000)
26.09.97	Colfiorito, Italy, 09h40 (DS)	0.98				138.0	45.0	-75.0	n	SI	Salvi <i>et al.</i> (2000)
26.09.97	Colfiorito, Italy, 00h33 (DS)	0.43				144.0	45.0	-90.0	n	GI	Stramondo <i>et al.</i> (1999)
26.09.97	Colfiorito, Italy, 09h40 (DS)	1.05				144.0	45.0	-90.0	n	GI	Stramondo <i>et al.</i> (1999)
08.11.97	Manyi, Tibet	263.00	35.22	87.15	6.38	258.6	89.8	-5.4	ss	I	Funning <i>et al.</i> (2007)
08.11.97	Manyi, Tibet	171.90	35.26	87.21	4.85	257.7	89.1	-1.1	ss	I	Wang <i>et al.</i> (2007)
08.11.97	Manyi, Tibet (DS)	191.00	35.24	87.30	5.11	255.9	93.2	-5.7	ss	I	Wang <i>et al.</i> (2007)
10.01.98	Zhangbei, China	0.48	41.14	114.44	5.40	200.8	42.7	85.9	th	I	Li <i>et al.</i> (2008)
			± 0.004	± 0.004	± 0.3	± 6.4	± 3.6	± 10.2			
10.01.98	Zhangbei, China (DS)	0.47	41.13	114.51	5.00	200.8	42.7	85.9	th	I	Li <i>et al.</i> (2008)
30.01.98	<i>N. Chile</i>	<i>61.00</i>	<i>-23.96</i>	<i>289.83</i>	<i>45.00</i>	5.0	<i>23.0</i>	<i>102.0</i>	<i>th</i>	<i>SI</i>	<i>Pritchard et al. (2006)</i>
14.03.98	Fandoqa, Iran	8.90	30.03	57.64	3.50	145.2	63.2	-151.6	ss	I	Funning (2005)
		± 1.4	± 0.004	± 0.004	± 0.3	± 1.1	± 2.2	± 11.5			
14.03.98	Fandoqa, Iran	8.28	30.01	57.64	3.67	150.0	52.0	-146.0	ss	I	Berberian <i>et al.</i> (2001)
14.03.98	Fandoqa, Iran	8.40	30.02	57.65	3.50	147.3	65.1	-154.1	ss	SI	Funning (2005)
		± 0.4	± 0.004	± 0.002	± 0.2	± 1.1	± 3.2	± 3.44			
22.05.98	Aiquile, Bolivia (DS)	8.44	-17.89	294.82	7.30	7.0	79.0	171.0	ss	I	Funning <i>et al.</i> (2005a)
22.05.98	Aiquile, Bolivia	7.77	-17.90	294.84	7.40	7.0	79.0	171.0	ss	I	Funning <i>et al.</i> (2005a)
03.09.98	Mt Iwate, Japan (DS)	1.40	39.80	140.90	1.30	200.0	35.8	112.0	th	GI	Nishimura <i>et al.</i> (2001)
28.03.99	Chamoli, Himalaya	2.70	30.44	79.39		300.0	15.0	90.0	th	I	Satyabala and Bilham (2006)
30.04.99	Zagros Mts, Iran (PS)	0.112	27.87	53.63	4.10	110.0	42.0	-85.0	n	I	Lohman and Simons (2005a)
			± 0.002	± 0.002	± 0.18		± 6.0	± 7.0			
30.04.99	Zagros Mts, Iran (FFP)	0.112	27.87	53.63	3.20	110.0	53.0	-77.0	n	I	Lohman and Simons (2005a)
			± 0.002	± 0.002	± 0.15		± 5.0	± 13.0			
30.04.99	Zagros Mts, Iran (DS)	0.112	27.87	53.63	5.30	110.0	53.0	-79.0	n	I	Lohman and Simons (2005a)
17.08.99	Izmit, Turkey	253.59	40.73	30.05	10.80	271.2	89.7	-173.1	ss	I	Wright (2000)
17.08.99	Izmit, Turkey (DS)	184.00							ss	OI	Feigl (2002)
17.08.99	Izmit, Turkey						85.0		ss	OI	Delouis <i>et al.</i> (2000)
17.08.99	Izmit, Turkey (DS)	240.00	40.72	30.21	7.90	267.6	85.0	179.6	ss	OI	Delouis <i>et al.</i> (2002)
17.08.99	Izmit, Turkey (DS)	190.00	40.72	30.07	6.99	90.7	88.3	178.7	ss	I	Çakir <i>et al.</i> (2003)

Continued on next page

Date	Location	M_0 ($\times 10^{18} Nm$)	Lat. ($^\circ$)	Lon. ($^\circ$)	Depth (km)	Str. ($^\circ$)	Dip ($^\circ$)	Rake ($^\circ$)	Type	Data	Reference
07.09.99	Athens, Greece, Model 1	1.29	38.09	23.63	9.50	100.0	43.0		n	I	Kontoes <i>et al.</i> (2000)
07.09.99	Athens, Greece, Model 2	1.46	38.11	23.63	9.50	116.0	54.0		n	I	Kontoes <i>et al.</i> (2000)
16.10.99	Hector Mine (DS)	72.00	34.56	243.73	1.90	153.3	85.3	177.4	ss	GI	Simons <i>et al.</i> (2002)
16.10.99	Hector Mine (DS)	59.30	34.56	243.73	6.08	332.3	83.0	184.6	ss/th	GI	Jónsson <i>et al.</i> (2002)
16.10.99	Hector Mine (DS)	58.00	34.58	243.72	4.89	332.7	81.4	176.0	ss	OI	Salichon <i>et al.</i> (2004)
12.11.99	Duzce, Turkey	65.60	40.80	31.27	6.30	259.0	51.0	-178.0	ss	I	Wright (2000)
	1 seg.	± 3.4			± 1.0	± 1.0	± 4.0	± 3.0			
12.11.99	Duzce, Turkey	41.46	40.81	31.21	7.65	273.9	57.0	-134.0	ss	I	Wright (2000)
	Mult. seg.						± 4.0	± 17.0			
12.11.99	Duzce, Turkey	51.40	40.72	31.26	6.77	84.5	56.7	-174.0	ss/n	GI	Bürgmann <i>et al.</i> (2002)
12.11.99	Duzce, Turkey (DS)	56.60				86.7	54.0		ss/n	GI	Bürgmann <i>et al.</i> (2002)
22.12.99	Ain Temouchent, Algeria	0.47				57.0	32.0	90.0	th	I	Belabbes <i>et al.</i> (2009)
06.06.00	Cankiri, Turkey	1.40	40.63	32.99	5.50	357.0	55.0	-20.0	n	I	Wright (2000)
						± 15.0	± 19.0	± 15.0			
06.06.00	Cankiri, Turkey	1.38	40.63	32.99	4.0 - 6.6	2.0	33.0	-37.0	n	I	Çakir and Akoglu (2008)
17.06.00	S. Iceland	5.42	63.96	339.65	4.99	5.0	86.0	175.0	ss	I	Pedersen <i>et al.</i> (2001)
17.06.00	S. Iceland	4.40	63.97	339.66	3.94	1.0	87.0	180.0	ss	GI	Pedersen <i>et al.</i> (2003)
17.06.00	S. Iceland (DS)	4.50	63.97	339.66	3.09	2.0	87.0	180.0	ss	GI	Pedersen <i>et al.</i> (2003)
21.06.00	S. Iceland	5.06	63.99	339.30	4.50	359.0	90.0	180.0	ss	I	Pedersen <i>et al.</i> (2001)
21.06.00	S. Iceland	5.30	63.99	339.30	4.10	0.0	90.0	180.0	ss	GI	Pedersen <i>et al.</i> (2003)
21.06.00	S. Iceland (DS)	5.00	63.98	339.30	2.97	0.0	90.0	180.0	ss	GI	Pedersen <i>et al.</i> (2003)
26.01.01	Bhuj, India	190.00	23.51	70.27	13.00	82.0	51.0	77.0	th	I	Schmidt and Bürgmann (2006)
					± 1.1						
26.01.01	Bhuj, India (DS)	250.00				82.0	51.0		th	I	Schmidt and Bürgmann (2006)
28.02.01	Nisqually	20.00	47.10	237.33	51.00	180.0	20.0		n	GI	Bustin <i>et al.</i> (2004)
28.02.01	Nisqually				60.0	180.0	20.0		n	GI	Bustin <i>et al.</i> (2004)
23.06.01	Arequipa, Peru (DS)	6300.00	-17.36	287.39	27.00	316.0	11-25	69.0	th	OI	Pritchard <i>et al.</i> (2007)
14.11.01	Kokoxili, Tibet (DS)	710.00	35.84	92.45	11.00	97.6	90.0	0.0	ss	I	Lasserre <i>et al.</i> (2005)
23.10.02	Nenana Mountain	10.80	63.50	211.95	12.90	261.8	81.2	173.7	ss	I	Wright <i>et al.</i> (2003)
	Alaska	± 0.8	± 0.002	± 0.004	± 0.7	± 0.9	± 1.7	± 1.3			
03.11.02	Denali, Alaska	649.82	63.22	214.85	6.93	108.5	84.4	171.9	ss	GI	Wright <i>et al.</i> (2004a)

Continued on next page

Date	Location	M_0 ($\times 10^{18} Nm$)	Lat. ($^\circ$)	Lon. ($^\circ$)	Depth (km)	Str. ($^\circ$)	Dip ($^\circ$)	Rake ($^\circ$)	Type	Data	Reference
21.05.03	Zemmouri, Algeria (PM)	17.80			8.0 – 10.0	65.0	40.0	90.0	th	OI	Belabbes <i>et al.</i> (2009)
21.05.03	Zemmouri, Algeria (CM)	21.50			8.0 – 10.0	65.0	40.0	90.0	th	OI	Belabbes <i>et al.</i> (2009)
26.07.03	Miyagi, Japan	1.80	38.45	141.19	2.29	212.2	38.7	102.7	th	OI	Nishimura <i>et al.</i> (2003)
26.12.03	Bam, Iran	9.00 ± 0.3	29.03	58.36	5.69	355.4	89.9	-173.5	ss/th	I	Funning <i>et al.</i> (2005b)
26.12.03	Bam, Iran	6.20 ± 0.4	29.04	58.36	4.70 ± 0.4	355.2 ± 1.0	86.6 ± 3.6	173.7 ± 1.7	ss/th	SI	Funning <i>et al.</i> (2005b)
26.12.03	Bam, Iran	5.00	29.05	58.35	5.8	359.6	86.0	-179.8	ss	I	Peyret <i>et al.</i> (2007)
26.12.03	Bam, Iran		29.06	58.36	4.8	1.6	88.0	-170.9	ss	OI	Peyret <i>et al.</i> (2007)
26.12.03	Bam, Iran (DS)	6.79			5.60	358.2	88.8	180.0	ss	OI	Motagh <i>et al.</i> (2006)
24.02.04	Al Hoceima, Morocco	6.20	35.14	356.01	10.05	295.4	87.4	-179.2	ss	I	Biggs <i>et al.</i> (2006)
24.02.04	Al Hoceima, Morocco (DS)	7.40	35.14	356.00	8.80	295.0	88.0	-179.0	ss	I	Biggs <i>et al.</i> (2006)
24.02.04	Al Hoceima, Morocco	5.88	35.17	355.98	6.90	339.5	88.0	178.0	ss	OI	Tahayt <i>et al.</i> (2009)
24.02.04	Al Hoceima, Morocco (DS)	6.60							ss	I	Akoglu <i>et al.</i> (2006)
24.02.04	Al Hoceima, Morocco (DS)	6.80					88.0		ss	I	Çakir <i>et al.</i> (2006)
24.10.04	Niigata, Japan	13.99	37.30	138.83	4.70	200.0	45.0	72.0	th	I	Ozawa <i>et al.</i> (2005)
22.02.05	Zarand Iran	6.70 ± 0.2			4.65 ± 0.3	266.0 ± 1.0	67.0 ± 2.0	105.0 ± 2.0	th	I	Talebian <i>et al.</i> (2006)
20.03.05	Fukuoka-ken Seiho-oki, Japan	7.10				298.0	79.0	-18.0	ss	GI	Nishimura <i>et al.</i> (2006)
20.03.05	Fukuoka-ken (DS) Seiho-oki, Japan	8.70							ss	GI	Nishimura <i>et al.</i> (2006)
13.06.05	Tarapaca, Chile	580.00				189.0	24.0	-74.0	n	OI	Peyrat <i>et al.</i> (2006)
08.10.05	Kashmir (DS)	336.00	34.29	73.77		321.5	31.5		th	I	Pathier <i>et al.</i> (2006)
27.11.05	Qeshm Island, Iran	1.27 ± 0.07	26.77	55.92	6.00	267.0 ± 2.0	49.0 ± 4.0	105.0 ± 5.0	th	I	Nissen <i>et al.</i> (2007b)
27.11.05	Qeshm Island Iran	1.25 ± 0.01	26.88 ± 0.01	55.89 ± 0.004	5.80 ± 2.00	73.0 ± 3.0	36.0 ± 2.0	66. ± 5.0	th	I	Nissen <i>et al.</i> (2010)
31.03.06	Chalan-Chulan, Iran	1.70	33.67	48.88	4.80	320.0	60.0	180.0	ss	I	Peyret <i>et al.</i> (2008)
31.03.06	Chalan-Chulan, Iran (DS)	1.58				320.0	60.0	180.0	ss	I	Peyret <i>et al.</i> (2008)

Continued on next page

Date	Location	M_0 ($\times 10^{18} Nm$)	Lat. ($^\circ$)	Lon. ($^\circ$)	Depth (km)	Str. ($^\circ$)	Dip ($^\circ$)	Rake ($^\circ$)	Type	Data	Reference
28.06.06	Qeshm Island	1.35	26.91	55.89	8.50	25.0	46.0	65.0	th	I	Nissen <i>et al.</i> (2010)
	Iran	± 0.32	± 0.02	± 0.004	± 1.20	± 11.0	± 14.0	± 17.0			
25.03.07	Noto Hanto	14.52	37.22	136.66	6.00	50.7	53.5	150.0	th	GI	Ozawa <i>et al.</i> (2008)
25.03.07	Noto Hanto (DS)	11.09				50.7	48.0	115.0	th	GI	Fukushima <i>et al.</i> (2008)
15.08.07	Pisco, Peru	1900.00	-13.89	283.48	30.00	316.0	11–25	71.0	th	SI	Pritchard and Fielding (2008)
15.08.07	Pisco, Peru (DS)	2500.00							th	I	Biggs <i>et al.</i> (2009)
15.08.07	Pisco, Peru (DS)	1230.00	-13.89	-76.77	19.07		8.0 to 27.0	64.8	th	I	Motagh <i>et al.</i> (2008)
14.11.07	Tocopilla, Chile (DS)	501.00	-22.48	289.75	39.80	3.7	20.0	110.6	th	I	Motagh <i>et al.</i> (2010)
09.01.08	Nima, Tibet	2.57	32.44	85.33	7.65	217.3	60.0	86.4	n	I	Sun <i>et al.</i> (2008)
						± 1.4	± 1.9				
09.01.08	Nima, Tibet (DS)	5.40							n	I	Sun <i>et al.</i> (2008)
12.05.08	Wenchuan, China (DS)	891.25	31.67	104.04	10.29	226.4	53.2	129.7	th	GI	Feng <i>et al.</i> (2010)
12.05.08	Wenchuan, China (DS)	1536.24	31.77	104.23	7.47	228.2	48.7	156.0	th	OI	Hao <i>et al.</i> (2009)
29.05.08	Iceland (Doublet event)	1.46					90.0		ss	GI	Decriem <i>et al.</i> (2010)
10.09.08	Qeshm Island,	1.86	26.88	55.89	5.80	45.0	48.3	53.8	th	I	Nissen <i>et al.</i> 2010
	Iran	± 0.18	± 0.01	± 0.01	± 1.70		± 7.6	± 10.1			
06.04.09	L'Aquila,	2.90	42.32	13.43	7.06	133.0	47.0	-103.0	n	GI	Atzori <i>et al.</i> (2009)
	Italy					± 2.0	± 1.0	± 2.0			
06.04.09	L'Aquila, Italy (DS)	2.70	42.32	13.43	6.20	133.0	47.0	-103.5	n	GI	Atzori <i>et al.</i> (2009)
06.04.09	L'Aquila, Italy	2.80	42.33	13.45	7.30	144.0	54.0	-105.0	n	I	Walters <i>et al.</i> (2009)
	Italy	± 0.08	± 0.001	± 0.001	± 0.10	± 1.0	± 1.0	± 3.0			
06.04.09	L'Aquila, Italy (DS)	2.91	42.33	13.45	7.00	144.0	54.0	-105.0	n	I	Walters <i>et al.</i> (2009)
19.12.09	Karonga, Malawi	1.40	-9.89	33.90	3.20	155.0	41.0	-88.0	n	I	Biggs <i>et al.</i> (2010)
27.02.10	Maule, Chile (DS)	18000.00	-35.87	287.08	29.75	15.0	18.0	110.0	th	OI	Delouis <i>et al.</i> (2010)

Chapter 3

Systematic comparisons between InSAR and seismically-determined source models

3.1 Introduction

InSAR and seismic data have their own strengths and weaknesses, but few studies have previously compared the two datasets (*e.g.*, Wright *et al.*, 1999; Lohman *et al.*, 2002; Mellors *et al.*, 2004; Funning, 2005). Although there is generally good agreement between the source parameters for the majority of earthquakes previously studied, differences in location, seismic moment and fault geometry have highlighted issues including the Earth model used and the quality of the data (*e.g.* Pritchard *et al.*, 2006). Gaining an understanding of these issues enables the development of inversion techniques of both InSAR and seismic data for the calculation of more robust source models.

Robust earthquake source models are important for studying kinematic and dynamic processes at the fault scale all the way up to the tectonic scale. At the local and global scale, errors in source models affect the interpretation of stress regimes, seismogenic depth and fault structure in the area, all of which are important for seismic hazard assessment (Mellors *et al.*, 2004).

In this chapter the ICMT catalogue compiled in Chapter 2 is used to investigate the

compatibility between seismic and InSAR solutions. Source parameters, including; seismic moment, centroid location, strike, dip and rake are compared and the results provide insights into the parameter tradeoffs and uncertainties. The centroid location is investigated with regard to the known geology and rupture directivity, and the variation between multiple distributed slip models for the same earthquake is also considered. Finally this, and issues related to the data themselves and the processing and inversion techniques used will be discussed. The material presented in this chapter has been published in Weston *et al.* (2011, 2012).

3.2 Seismic Moment and moment magnitude

Seismic moment and moment magnitude are equivalent quantities related to the energy released in an earthquake. To investigate the overall trend and discrepancies for individual studies the comparisons are presented in terms of seismic moment rather than moment magnitude to illustrate better the difference in various estimates (sections 3.2.1 and 3.2.2). Trends due to geographical location and faulting mechanism are expressed as moment magnitude in section 3.2.3, as it is only the direction of the trend that is of interest (*i.e.* if the ICMT estimates are larger or smaller than those reported in the GCMT catalogue).

3.2.1 Comparing ICMT and GCMT estimates

Figure 3.1a compares seismic moment values from the GCMT catalogue with estimates from 114 InSAR source models in the ICMT database compiled in chapter 2. The differences between the two datasets are relatively small and follow a distribution close to Gaussian with a median of -2.96% ($\sigma = 36.93\%$). We find that the mean difference between InSAR and GCMT moment values is not statistically significantly different from zero at a 95% confidence interval (Students t test). This disagrees with previous studies using fewer earthquakes (*e.g.* Wright *et al.*, 1999; Lohman and Simons, 2005a; Funning *et al.*, 2007) and using simulations (Dawson *et al.*, 2008), which suggested that seismic moments determined using InSAR were larger than those obtained from seismic data. Feigl (2002) reported differences of up to 60% between geodetically-estimated and seismically-estimated moments, but solutions from other types of geodetic data such as levelling and GPS were also included. The inclusion of interseismic, triggered aseismic

and postseismic deformation in coseismic interferograms due to the longer measurement period of geodetic data, which can span years in some cases, were suggested as reasons for the trend. If anything, here it is found that there is a slight tendency for InSAR predicting smaller seismic moments than those reported in the GCMT catalogue.

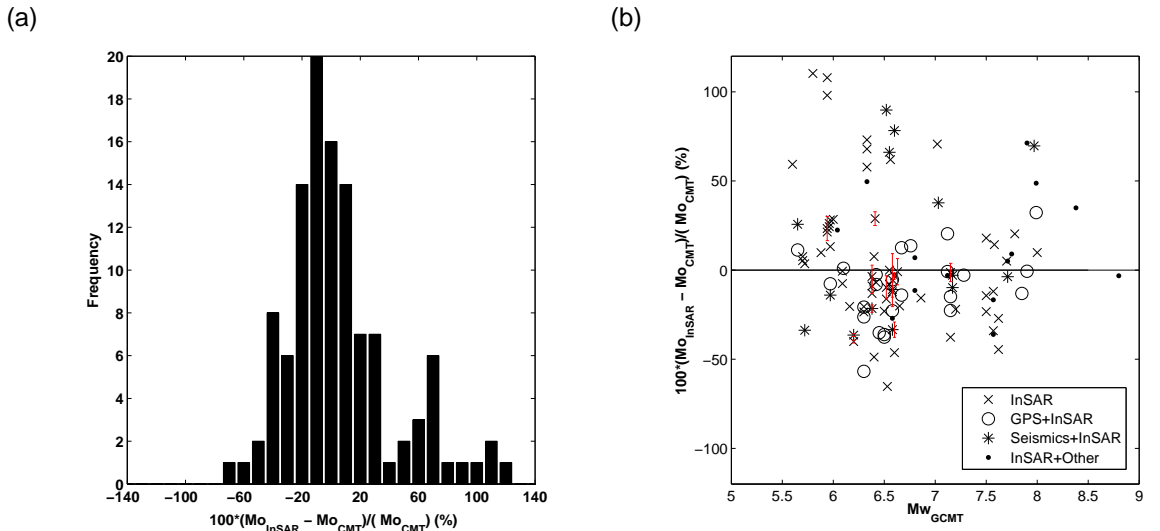


Figure 3.1: a) Distribution of the differences between the ICMT and GCMT seismic moment estimates. The median difference in estimates is -2.96% ($\sigma = 36.93\%$) for 114 source models. b) Scatterplot of the differences with respect to the type of data used to determine the ICMT source models. Black line represents the point where the ICMT and GCMT estimates are equal.

There is no relationship between differences in seismic moment and the specific combination of data used to determine the InSAR solutions: I, GI, SI, OI (see Figure 3.1b); likewise, there is no dependence of the differences of seismic moment on the size of the earthquake. Moreover, we examine the differences in seismic moment as a function of the non double-couple component of the earthquakes in the GCMT catalogue to investigate whether the discrepancies were larger for earthquakes with reported large non double-couple component but do not find any clear dependency (see Figure A.1 in Appendix A). In addition, we examine the differences in seismic moment as a function of strike, dip, rake and earthquake depth and do not find any clear trend. We also split the set of seismic moments into two subsets corresponding to InSAR determinations using uniform and distributed slip models (see Figure A.2 in Appendix A); there were similar tendencies in the comparisons between InSAR and GCMT moments for these two subsets to that found in Figure 3.1. Among all the InSAR models used here, only nineteen report uncertainties

for the estimated seismic moments (see Tables ?? to ??); the observed trend in the differences in seismic moment between InSAR and GCMT does not change when taking these uncertainties into account (Figure 3.1 b).

3.2.2 Cases of large discrepancies between ICMT and GCMT estimates

For some studies there are large differences between seismically and InSAR-determined moments. For example, for the 1994 Al Hoceima earthquake there are differences in moment of over 100% between the InSAR solutions of Biggs *et al.* (2006) and Akoglu *et al.* (2006) and the GCMT solution. A possible reason for this is that a substantial amount of surface deformation for this earthquake was offshore and the onshore deformation was relatively small, thus the signal-to-noise ratio in the interferogram was relatively low, which makes InSAR determinations more difficult. As a result, Biggs *et al.* (2006) report a strong tradeoff between slip and length, which might have affected moment estimations. Likewise, for the 1993 northern Chile earthquake the InSAR moment estimated by Pritchard *et al.* (2006) is 78% larger than that reported in the GCMT catalogue. Possible reasons for this discrepancy are that Pritchard *et al.* (2006) use a single interferogram, lacking offshore data coverage, and the signal-to-noise ratio is low for this relatively small and deep earthquake. Poor InSAR data due to dense vegetation and mountainous topography can also partly explain the substantially smaller InSAR-derived seismic moments for the 1999 Chamoli, Himalaya earthquake (the estimate of Satyabala and Bilham (2006) is 65% smaller than in the GCMT) and the 2001 Bhuj earthquake (the estimate of Schmidt and Bürgmann (2006) is 45% smaller than the GCMT). In addition, for the 2003 Bam earthquake, all InSAR studies (Funning, 2005; Motagh *et al.*, 2006; Peyret *et al.*, 2007) estimated a smaller magnitude than that reported by the GCMT catalog, with the estimate by Peyret *et al.* (2007) having the largest discrepancy, with a moment of 46% smaller than the GCMT, which corresponds to a difference in moment magnitude of ~ 0.18 . A potential source of error when estimating the horizontal motion close to the rupture is the angle at which the satellite acquired the data, combined with the fault's orientation. These under and overestimates are also considered in the context of the fault mechanism, an issue discussed with respect to moment magnitude in the following subsection Figure 3.3.

3.2.3 Trends due to geographical location and thrusting mechanism

I also compare moment magnitudes M_w calculated from the InSAR and GCMT seismic moments, using equation 2.11. The differences in M_w are small and are broadly normally distributed with a median of -0.009 magnitude units ($\sigma = 0.10$). Considering the difference in moment magnitude with respect to geographical location (Figure 3.2) there are no clear trends, thus indicating that GCMT seismic moment determinations are not biased by the Earth model used. There appears to be only a systematic overestimation of the moment magnitude by InSAR for subduction zone earthquakes off the coast of South America, an issue discussed subsequently.

If the mechanism of the event is considered (Figure 3.2 b-d), then strike-slip and thrust events show the largest outlier discrepancies. Interestingly the large outliers in the strike-slip category are due to poor quality InSAR data regardless of whether the InSAR moment estimate is an over or underestimate with respect to seismic data. For example, for the Al Hoceima event in 1994 the InSAR estimate, based on a uniform slip model, is ~ 0.2 moment magnitude units larger than the GCMT estimate (M_w 6.0). This is due to tradeoffs between several parameters in the inversion, including length and seismic moment, as a result of an incomplete pattern of surface deformation in the interferogram because most of the displacement occurred offshore (Biggs *et al.*, 2006). However, for thrust events, poor quality InSAR data can lead to substantially smaller InSAR-derived moments. Significant decorrelation in interferograms due to dense vegetation and mountainous topography lead to InSAR moment magnitudes -0.31 and -0.1 smaller than those in the GCMT catalogue, for the Chamoli (M_w 6.2, 28th March 1999) and Bhuj (M_w 7.6, 26th January 2001) earthquakes, respectively (Satyabala and Bilham, 2006; Schmidt and Bürgmann, 2006). In contrast, the ICMT moment magnitude is significantly larger than the GCMT estimate for two thrust events, Qeshm Island (M_w 5.8, 28th June 2006) and Pisco (M_w 8.0, 15th August 2007), which is likely due to the inclusion of additional, non-coseismic deformation in their associated interferograms.

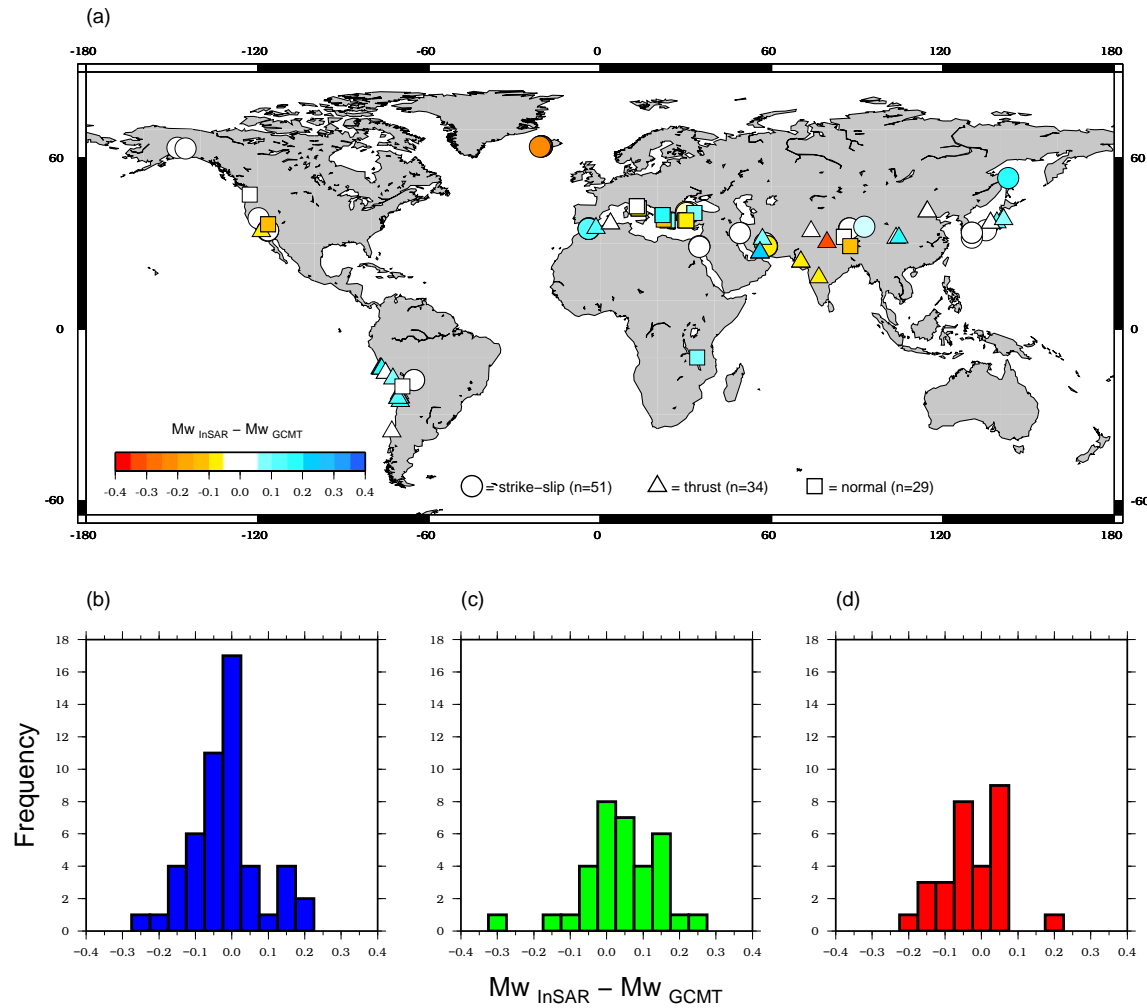


Figure 3.2: a) Comparisons between InSAR and GCMT moment magnitudes with respect to fault mechanism and location, where circles, triangles and squares represent strike-slip, thrust and normal faulting events, respectively. b) Distribution of difference in moment magnitude for 51 strike-slip models, median = -0.02 ($\sigma = 0.09$) c) Same as b) but for 34 thrust models, median = 0.04 ($\sigma = 0.17$) and d) 29 normal models, median = -0.03 ($\sigma = 0.08$).

Overall there is a slight trend for an overestimation of the moment magnitude for thrust events studied using InSAR (Figure 3.2c). It has been suggested that the moment magnitude estimate from InSAR increases with the measurement period (*e.g.* Feigl, 2002). However, considering the length of the time period between the event and the measurement of the second SAR image for thrust events (now referred to as the postseismic period) there is no clear trend (Figure 3.3a). For 24 earthquake source models the ICMT moment is larger than that reported in the GCMT but the difference in moment shows widespread variation. The two overestimates previously highlighted (Qeshm Island and Pisco) have significantly different postseismic periods; 659 days passed between the Qeshm Island earthquake and the acquisition of a second SAR image, whereas there was only a 65 day period between the Pisco earthquake and the post-earthquake SAR acquisition.

Considering this difference in measurement period we also investigate the influence of aftershocks. Figure 3.3b shows the total seismic moment contribution from aftershocks reported in the GCMT catalogue that occurred in the postseismic period covered by the interferogram, plotted as a fraction of the coseismic moment. There is no evident trend and the largest contribution from aftershocks ($\sim 86\%$) in fact corresponds to a normal faulting event for which the ICMT and GCMT moment are in relatively good agreement (Colfiorito, M_w 5.6, 27th September 1997). There are two thrust events for which the ICMT value is a significant overestimate with respect to that reported in the GCMT catalogue and there appears to be a significant contribution from aftershocks; $\sim 80\%$ (Niigata, M_w 6.5, 24th October 2004) and $\sim 54\%$ (Qeshm Island, M_w 5.8, 28th June 2006). However, for the majority of thrust earthquakes, where the ICMT moment is a significant overestimate with respect to the GCMT value, the relative contribution from aftershocks is small.

For several of the large subduction zone events in this study aftershocks account for much less than half of the estimated moment release during the observed postseismic period. Afterslip on the subduction interface may be responsible for the additional moment release as reported contributions from this phenomenon vary from 60% (*e.g.*, Antofagasta, M_w 8.1, 30th July 1995, Chlieh *et al.*, 2004) to 90% (*e.g.*, Pisco M_w 8.0, 15th August 2007, Perfettini *et al.*, 2010) of the overall moment release. Viscoelastic relaxation has also been suggested as a potential mechanism for postseismic deformation in the south American subduction zone. A total of 17 cm of horizontal trenchward motion

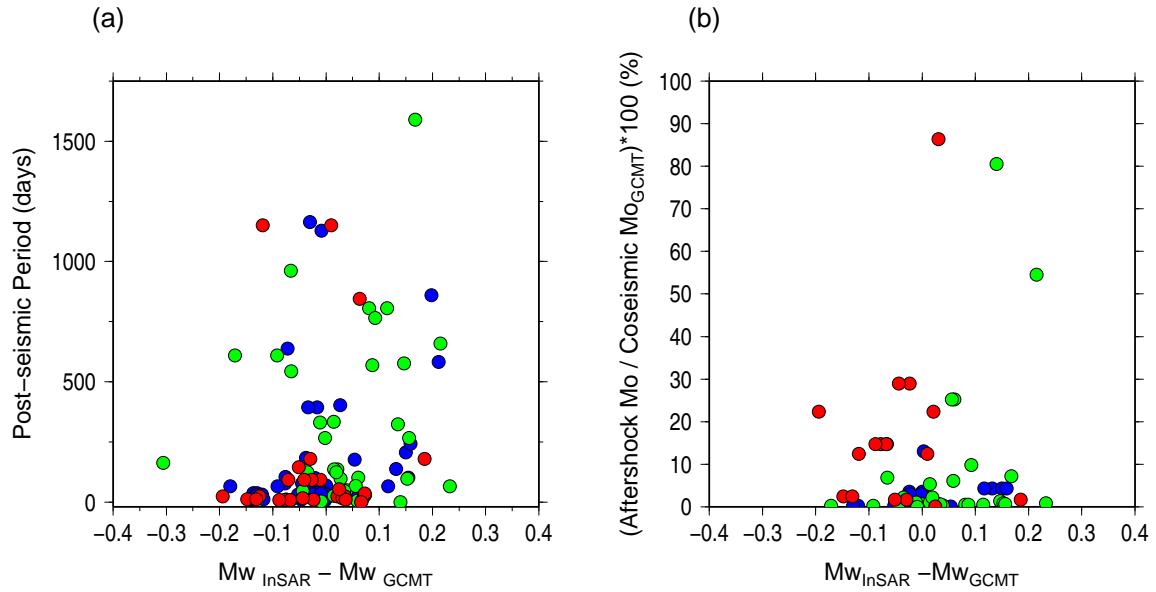


Figure 3.3: Investigating the relationship between M_w , the post-seismic period and the total seismic moment contribution from aftershocks (see text for further explanation), with respect to faulting mechanism. There are 51 strike-slip models, 34 thrust and 29 normal faulting models represented by blue, green and red, respectively. a) The difference in InSAR and GCMT M_w estimates with respect to the post-seismic period. b) The difference between ICMT and GCMT M_w estimates with respect to the seismic moment release due to aftershocks as a fraction of the coseismic moment release reported in the GCMT catalogue.

was observed in the three and a half years following the Arequipa earthquake (M_w 8.5, 23rd June 2001) thought to be due to tensional stresses driving viscoelastic relaxation in the whole crust and the upper mantle (Hergert and Heidbach, 2006). Moving away from the subduction zone setting similarly high levels of afterslip (nearly 95% of the total observed postseismic) were observed in the 1500 days following the Kashmir earthquake (M_w 7.6, 8th October 2005). The total postseismic moment release was $56\% \pm 19\%$ of the coseismic moment release, which is believed to be so high due to the large area affected by afterslip (Jouanne *et al.*, 2011). Therefore postseismic deformation due to afterslip and viscoelastic relaxation is the most likely physical mechanism for this observation because the contribution from aftershocks appears to be too small to account for the surplus moment.

3.3 Centroid Epicentral Location

3.3.1 Comparisons with global seismic catalogues

Centroid epicenters determined using InSAR showed substantial differences to those reported in seismic catalogues. Comparisons with locations in the EHB and ISC catalogues showed very similar results, with an average distance of 11.6 km ($\sigma = 6.9$ km) and 9.3 km ($\sigma = 7.5$ km) between the centroid locations, respectively, compared with 21.0 km ($\sigma = 12.7$ km) for the GCMT catalogue (Figures 3.4 a-c).

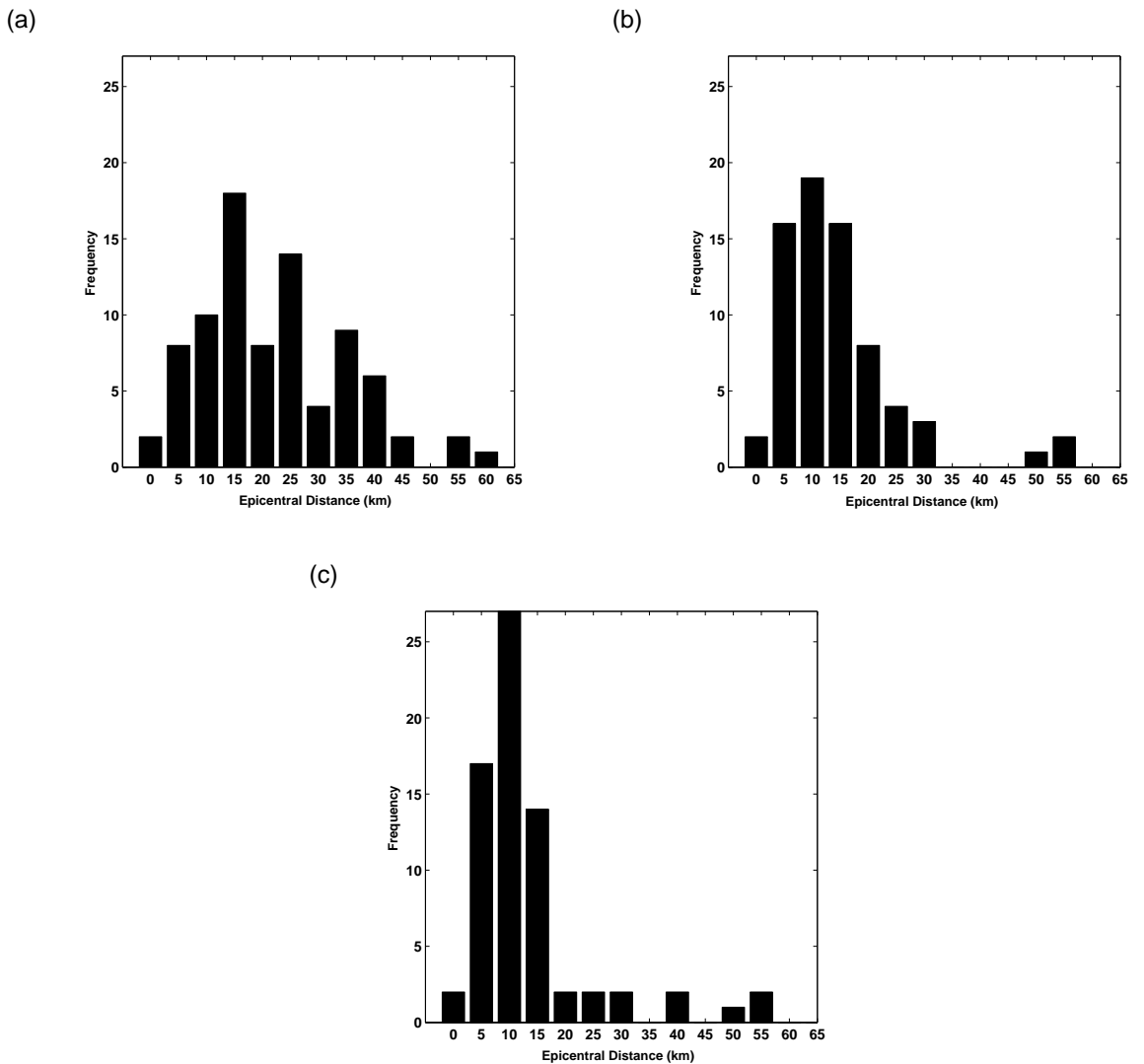


Figure 3.4: a) Distribution of the epicentral distance between GCMT and ICMT centroid locations, where the median distance is 21.0 km ($\sigma = 12.7$ km) for 84 ICMT source models. b) Same as in (a) but for the EHB catalogue for 71 source models. Median is 11.6 km ($\sigma = 6.9$ km). c) Same as in (b) but for the ISC catalogue. Median is 9.3 km ($\sigma = 7.5$ km).

A number of solutions show epicentral distances between InSAR and GCMT larger than 40 km, particularly for subduction zone earthquakes in South America: 2007 Pisco (Pritchard and Fielding, 2008); 1993, 1996, and 1998 northern Chile (Pritchard *et al.*, 2006); and 1996 Nazca Ridge (Salichon *et al.*, 2003). This is probably due to the fact that seismic locations tend to be systematically mislocated in these subduction zones towards the trench (*e.g.* Syracuse and Abers, 2009). However, the InSAR locations might also be systematically located landward due to the lack of InSAR data coverage offshore. For the 1992 Little Skull Mountain earthquake there is an epicentral difference of about 42 km between the GCMT location and that by Lohman *et al.* (2002). This is possibly due to limitations in the GCMT method, as there is a disagreement in location of up to 11 km between different seismic studies (Lohman *et al.*, 2002).

Epicentral distances are smaller for the ISC and EHB catalogues which show narrower distributions with medians of about 9 km and 11 km respectively. For these catalogues all difference in epicentral location are generally smaller than 40 km, except for the 1998 Aiquile earthquake. There is a difference of about 40 km between the ISC epicentral location and the InSAR location obtained by Funning *et al.* (2005a) using a uniform slip model, which is consistent with the damage distribution for that event. It is important to note though that the epicentral distance comparisons for the ISC and EHB catalogues contain 13 fewer comparisons than that for the GCMT. This for two reasons, firstly, at the time of conducting these comparisons solutions for earthquakes after 2007 were not available from the ISC Bulletin. Secondly, we do not carry out comparisons for very large earthquakes ($M_w > 7.7$), which in this case includes the following seven events: Kokoxili (M_w 7.8, 14th November 2001), Antofagasta (M_w 8.1, 30th July 1995), Arequipa (M_w 8.5, 23rd June 2001) and Denali (M_w 7.9, 3rd November 2002), Pisco (M_w 8.1, 15th August 2007), Wenchuan (M_w 7.9 12th May 2008) and Maule (M_w 8.8, 27th February 2010). This is because for such large earthquakes the earthquake centroid (as determined by InSAR) will be different to the rupture's initiation point (reported by ISC and EHB) and thus the comparisons would be inappropriate. The difference in hypocentre and centroid location can provide information on the source rupture length and directivity though, an issue discussed later in section 3.3.4.

We do not find any relationship between the seismic-InSAR epicentral differences

and any other parameters such as seismic moment, earthquake depth, type of earthquake mechanism, type of data used in the InSAR modelling, non-double-couple component of the earthquake and postseismic time elapsed (see Figure A.3 in Appendix A for all these comparisons).

Figure 3.5 shows the mislocation arrows for comparisons with the GCMT, EHB, and ISC catalogues and there is no global trend but there are some regional patterns such as in South America, Morocco, Greece and Turkey (Figure 3.5). The systematic westward bias in locations of subduction zone earthquakes off the coast of south America (Figure 3.6, right) by seismic catalogues has also been observed in several other studies (e.g; Pritchard *et al.*, 2006; Syracuse and Abers, 2009) and is believed to be due to the use of simplified Earth models in seismic inversions. If the 3D variations in the velocity structure of subduction zones are taken into account when inverting seismic data, then the hypocentres can shift by up to 25 km (Syracuse and Abers, 2009).

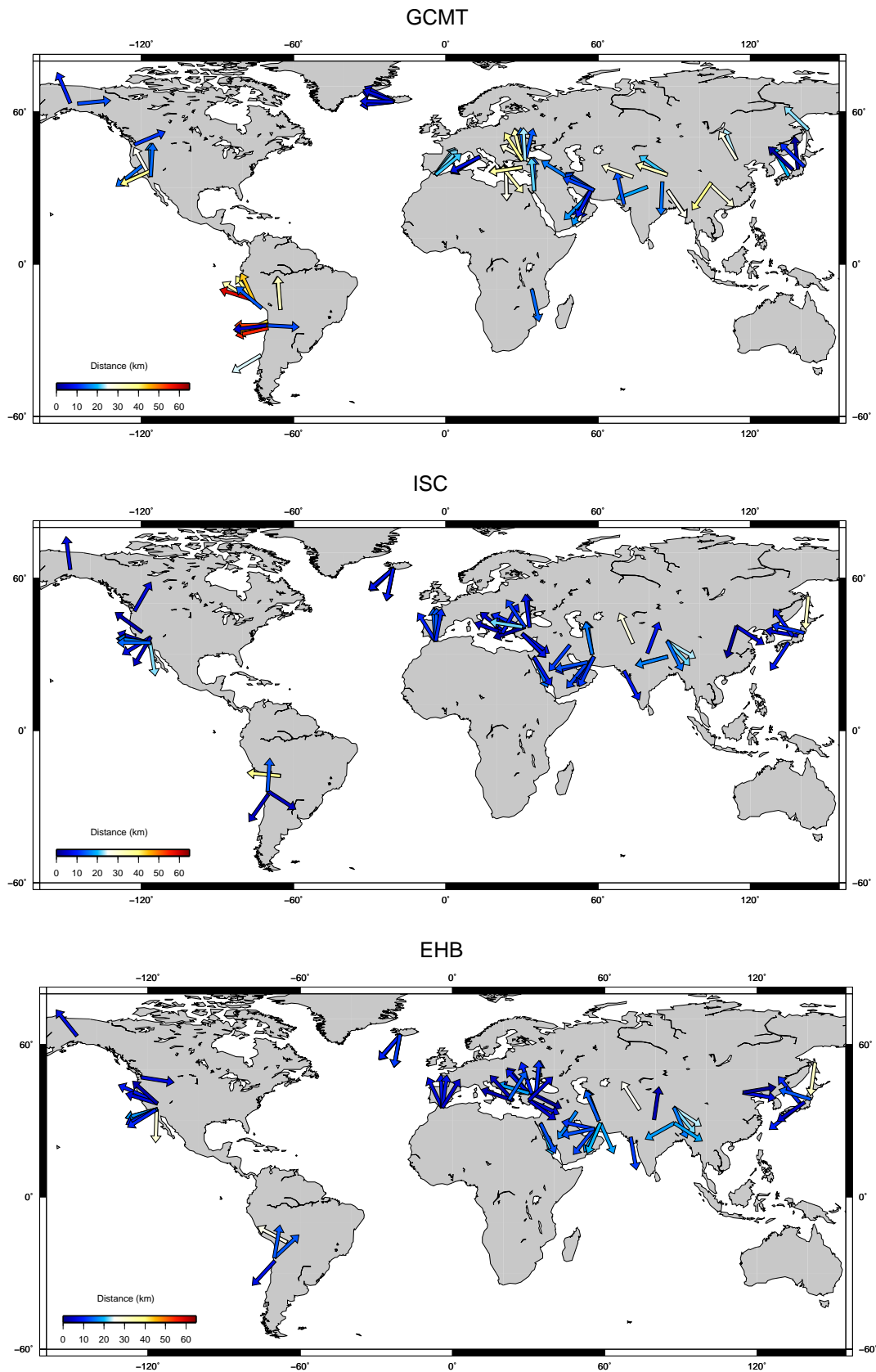


Figure 3.5: (Top) Mislocation arrows between centroid epicentral locations in the GCMT catalogue and those determined in 84 InSAR studies. The starting arrow point corresponds to the InSAR location. (Middle) Same as in (top) but for the ISC seismic catalogue, for 71 epicentral locations determined using InSAR. (Bottom) Same as in (middle) but for the EHB seismic catalogue. The arrows are of constant size and are not to scale; they begin at the InSAR location and point in the direction of the seismic location where the distance in kilometres between the two locations is indicated by the colour of the arrow.

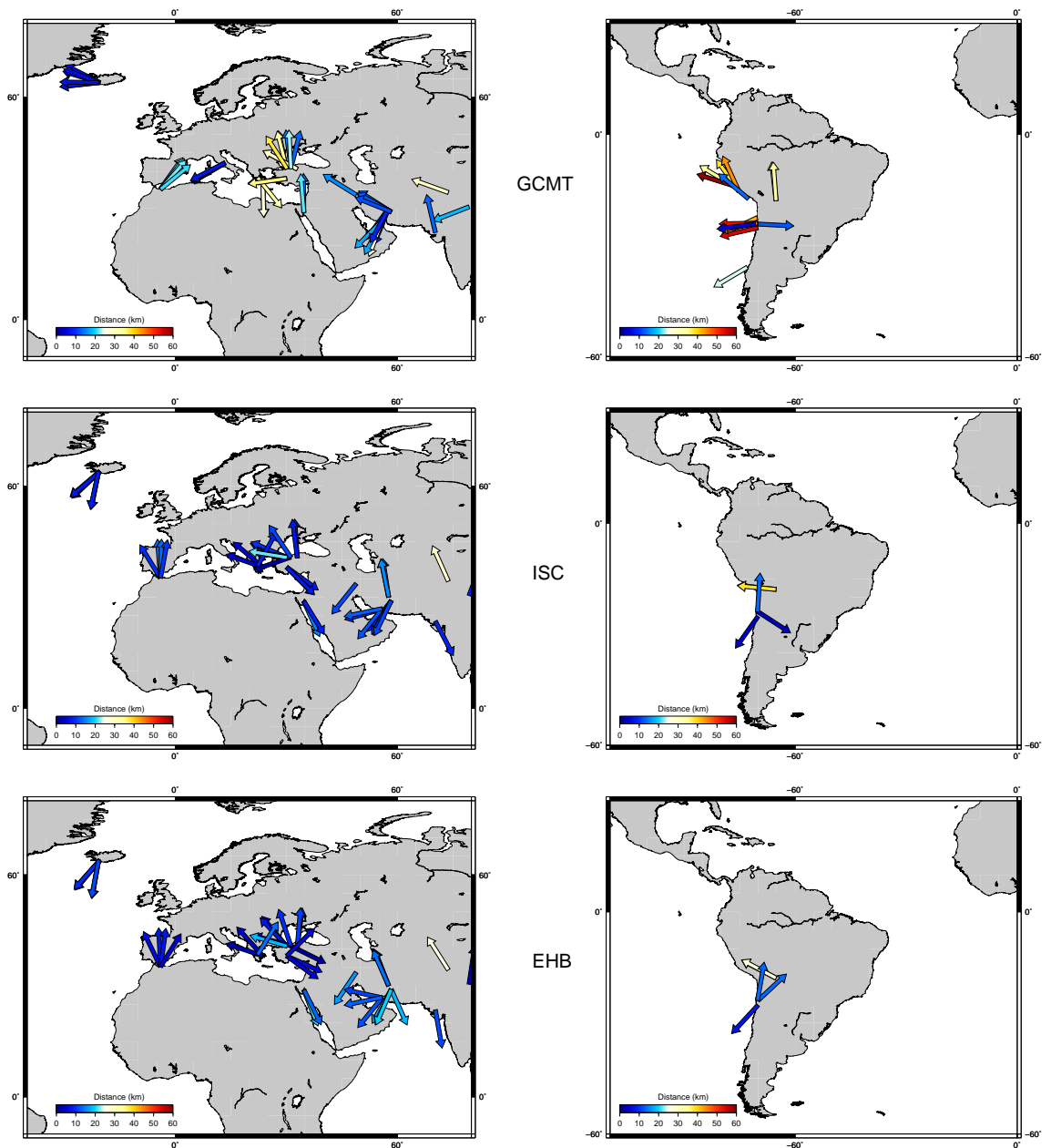


Figure 3.6: Left Mislocation arrows in North Africa, Europe and Middle-East between InSAR epicenters and GCMT (**Top**), ISC (**Middle**), and EHB (**Bottom**) epicenters. **Right** Same as left but for the south America subduction zone.

Ferreira *et al.* (2011) found a similar trend for three events off the coast of Northern Chile in 1993, 1996 and 1998. Four different 3-D Earth models were tested and in some instances the disagreement between InSAR and CMT centroid locations was reduced by up to 40 km. Two forward modelling techniques for the computation of synthetic seismograms were also considered but produced similar results for the same Earth model. However, these events were an isolated case and overall the use of different Earth models

in the GCMT method did little to change the distances between the InSAR and GCMT centroid locations. This suggests that for significant improvements in GCMT centroid locations higher resolution Earth models are needed (Ferreira *et al.*, 2011).

3.3.2 Comparisons with regional catalogues

In Figure 3.7 location comparisons are carried out for earthquakes that appear in regional catalogues, which are only available for 26 events. In general, for the moderate magnitude earthquakes there is better agreement between InSAR centroid location and seismic hypocentre locations from regional catalogues than for global catalogues, with a median difference of ~ 6.3 km compared with 9.2 km and 17.0 km for the ISC and GCMT catalogues, respectively. As expected, this shows that the data from local networks used to determine the hypocentral locations reported in the regional catalogues can improve location determinations. Moreover, the finer-detailed local velocity models used in the inversions for the regional seismic catalogues further improve the accuracy of the locations.

3.3.3 Comparisons with geological information

Commonly, additional geological information can be used when determining a source model from InSAR or seismic data. When the fault ruptures up to the surface this provides a further constraint, and if mapped can then be used in the modelling process (*e.g.*, Rigo *et al.*, 2004). Alternatively, slip measurements observed in the field (*e.g.*, Hao *et al.*, 2009) can be compared with displacements from InSAR data. Considering the fine spatial resolution of InSAR data, it is interesting to compare InSAR and seismically determined earthquake locations with the existing knowledge of geologically mapped surface offsets in an area. Here we focus on two events in Southern California: Hector Mine (M_w 7.1, 16th October 1999) and Landers (M_w 7.3, 28th June 1992). In Figures 3.8 and 3.9, mapped locations of the faults known to have ruptured in the two earthquakes are compared with locations from seismic catalogues and InSAR studies. For Hector Mine (Figure 3.8), the rupture initiated on a strand of the Lavic Lake fault, approximately where the Southern California Seismic Network (SCSN) location is, yet the EHB and ISC hypocentre locations are ~ 18 km to the west of this. A maximum right lateral slip of 5.25 m

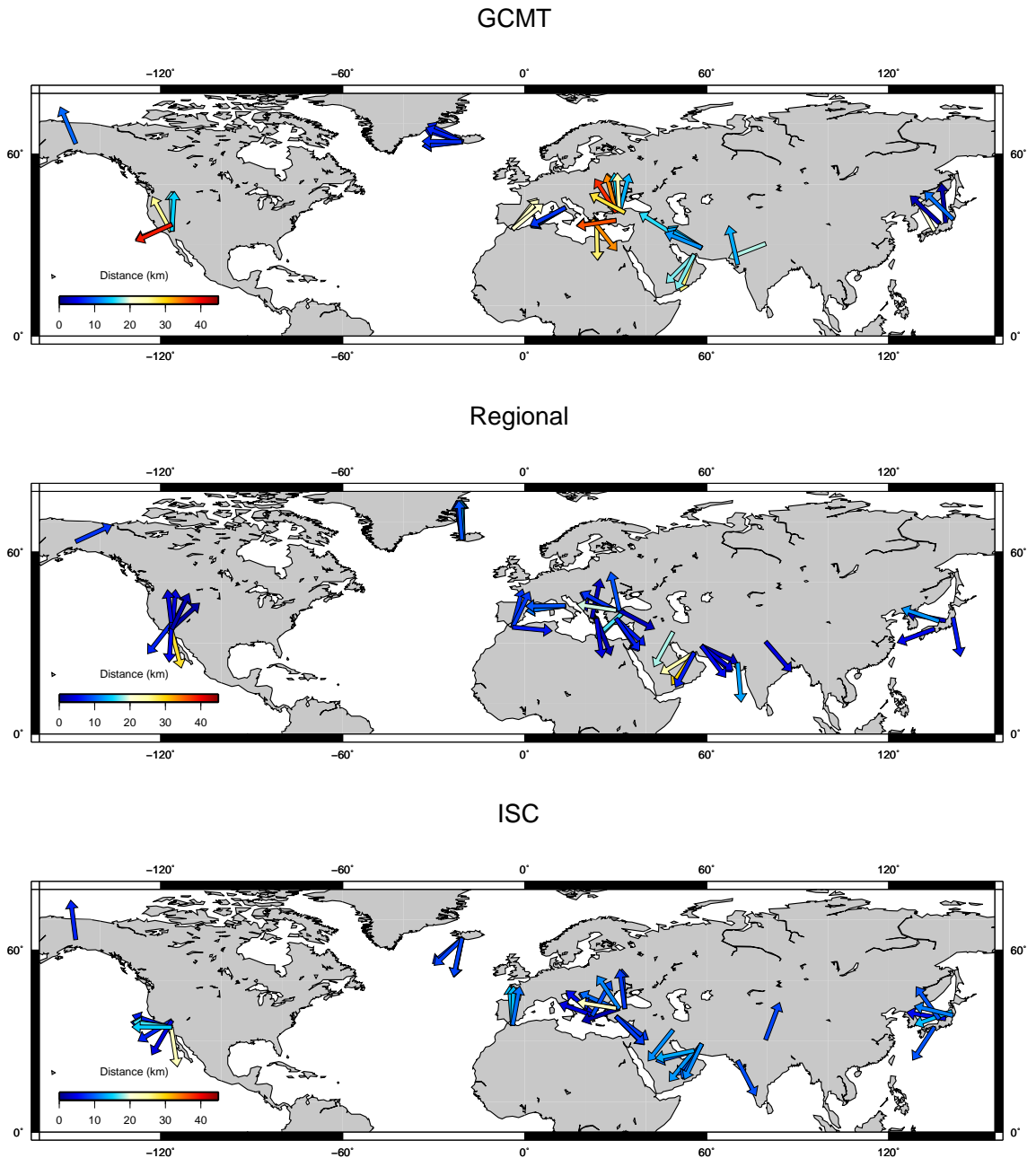


Figure 3.7: Difference between InSAR centroid locations and 48 GCMT (**Top**) solutions, 50 regional seismic solutions (**Middle**; see also section 2.4) and 46 ISC solutions (**Bottom**). The arrows are of constant size and are not to scale; they begin at the InSAR location and point in the direction of the seismic location where the distance in kilometres between the two locations is indicated by the colour of the arrow. The median difference for comparisons with GCMT is 16.96 km ($\sigma = 10.74$ km), for regional catalogues the median is 6.26 km ($\sigma = 6.49$ km), and a median of 9.23 km ($\sigma = 4.07$ km) is obtained for comparisons with the ISC catalogue. It must be noted that all comparisons in this figure are only for earthquakes with regional solutions.

was observed four kilometres south of the epicentre (Treiman *et al.*, 2002), which agrees well with the InSAR centroid locations. The majority of the rupture occurred on the Lavic Lake fault as it propagated north-west, which may explain why the GCMT catalogue centroid estimate is 14–17 km north of the ICMT locations and ~ 9 km from the mapped Lavic Lake fault. Interestingly the ICMT locations are all on the west side of the mapped fault yet for two of the three InSAR solutions (Jónsson *et al.*, 2002; Salichon *et al.*, 2004) the fault dips to the east, in agreement with the solution in the GCMT catalogue. This issue and the slip distribution of the three InSAR solutions are discussed further in section 3.6.1.

The Landers earthquake (Figure 3.9) was larger than the Hector Mine event and involved five different faults with a total rupture length of ~ 80 km (Sieh *et al.*, 1993). The agreement between the location of mapped faults and earthquake locations is better than for Hector Mine. The event is believed to have initiated on the Johnson Valley fault, as indicated by the SCSN location in Figure 3.9, which also shows the ISC and EHB again to the west, by ~ 8 km. The GCMT is the most northerly location, slightly to the east of the Emerson fault, whereas the ICMT location is to the west of the fault zone near the central part of the Homestead Valley fault. This east-west difference in location is in agreement with the fact that the ICMT and GCMT solutions dip in opposite directions. Locations from the other three seismic catalogues suggest that the fault dips to the west rather than the east, in agreement with InSAR. Large offsets of more than 4 m were observed in the field on the Emerson fault in the north (Sieh *et al.*, 1993) and slip distribution models from strong motion data showed more than 6 m of shallow slip on the Camp Rock and Emerson faults (*e.g.* Cohee and Beroza, 1994; Cotton and Campillo, 1995). However, probably due to these large surface displacements, the interferograms are heavily decorrelated near the fault trace, so despite the use of azimuth offsets, the resulting slip distribution from these InSAR data appears to estimate much lower values of slip on the same faults. Consequently the maximum slip is nearer the middle of the rupture length in the InSAR-derived finite fault model (Figure 3.10 b) and the resulting ICMT centroid location is further south than the GCMT location. Furthermore, even though the GCMT location appears consistent with this maximum slip at the northern end of the rupture, $\sim 50\%$ of the moment is still estimated to have been released on the Homestead Valley fault (Cohee and Beroza,

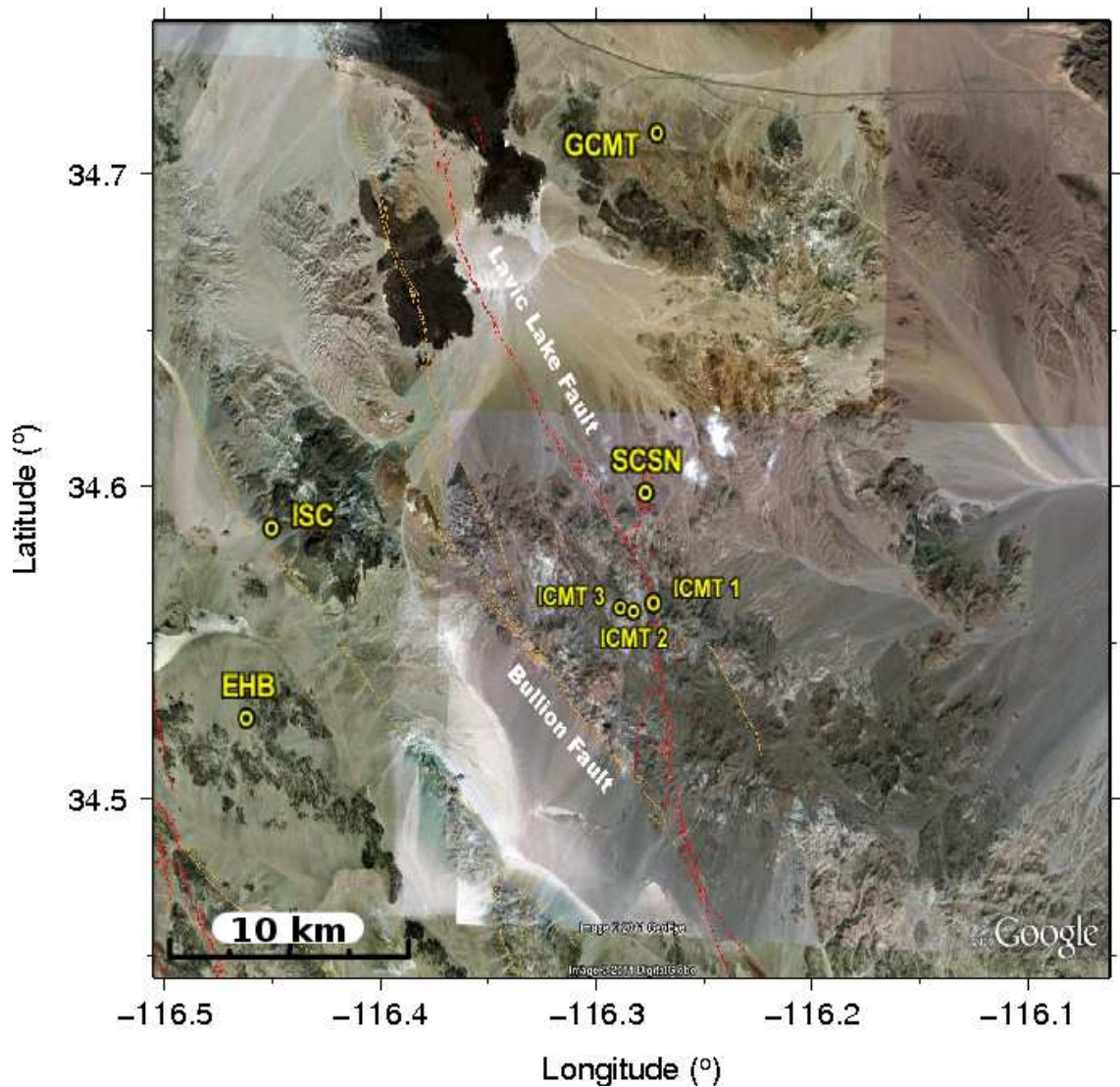


Figure 3.8: Locations from InSAR and seismic data for the Hector Mine earthquake with respect to geological information. ICMT1 refers to the InSAR study of Jónsson *et al.* (2002), ICMT2 refers to Salichon *et al.* (2004) and ICMT3 is Simons *et al.* (2002). SCSN is the hypocentre location from the SCSN catalogue. EHB, ISC and GCMT are the locations from these global catalogues. Mapped fault lines in red correspond to faults that have experienced movement in the past 150 years and the yellow lines are for faults younger than 15,000 years; they were plotted using Quaternary fault maps from the USGS (2011).

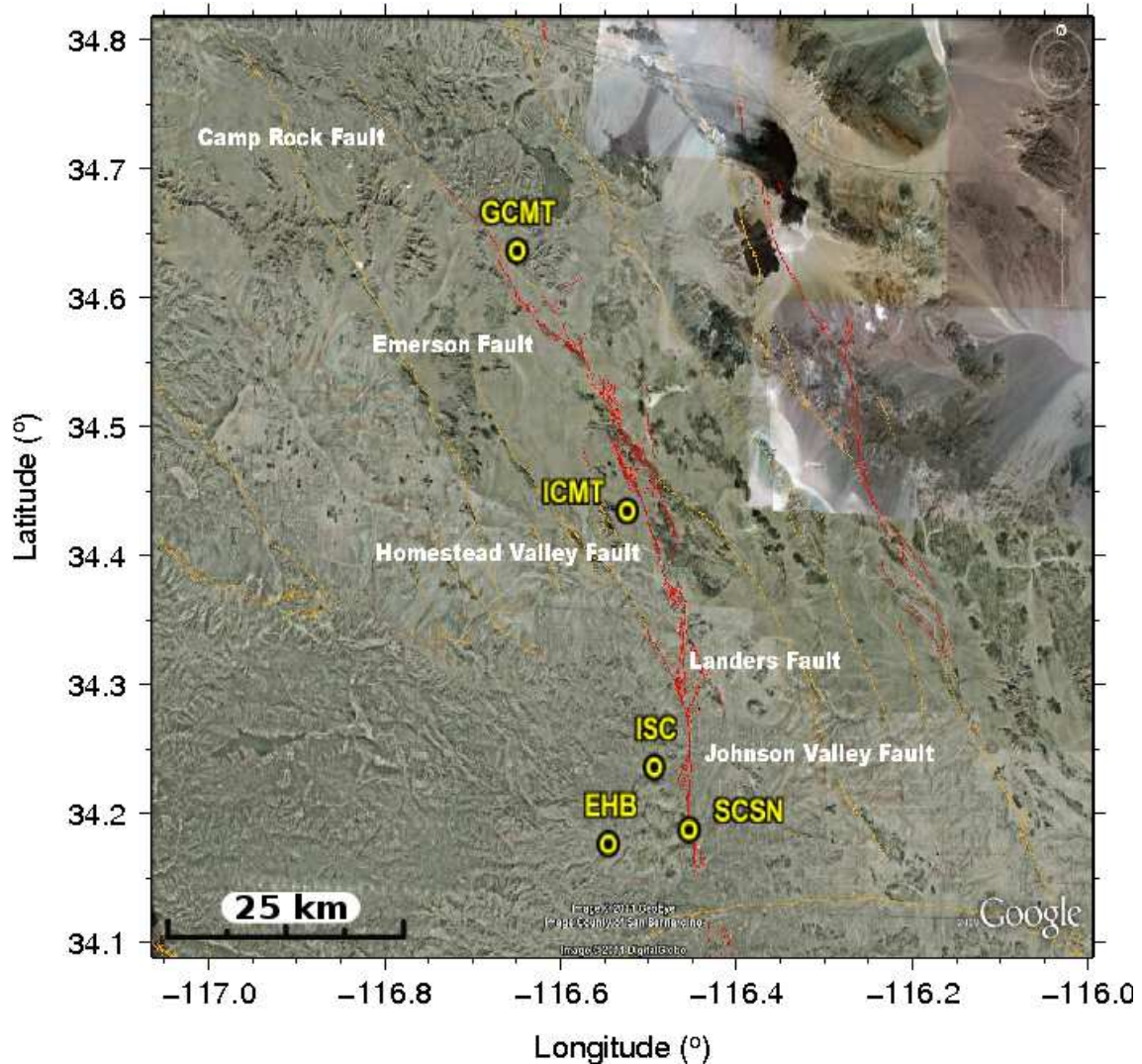


Figure 3.9: Locations from InSAR and seismic data for the Landers earthquake with respect to geological information. ICMT refers to the InSAR study of Fialko (2004). SCSN is the hypocentre location reported in the SCSN catalogue. EHB, ISC and GCMT are the locations from the global catalogues. Mapped fault lines follow the same convention as in Figure 3.8.

1994). Therefore, errors in the assumed Earth model may also be partly responsible for the GCMT location.

Despite this difference between the ICMT and GCMT centroid locations, when compared with hypocentre estimates from various seismic catalogues they both indicate rupture propagation towards the north. This is in agreement with rupture models calculated for this event (*e.g.* Cohee and Beroza, 1994; Wald and Heaton, 1994).

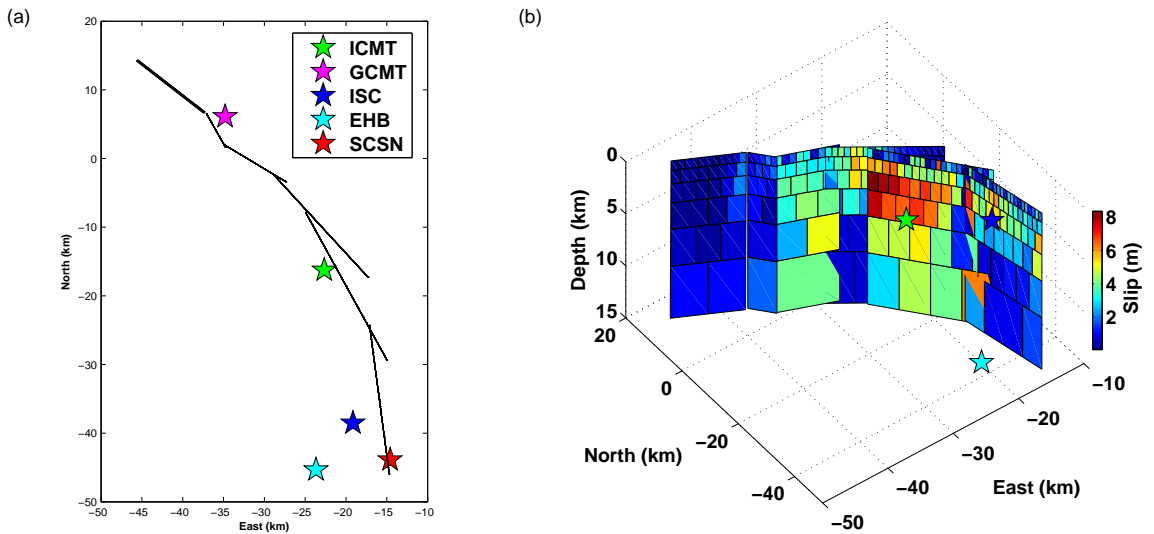


Figure 3.10: Fault trace (a) and 3D view (b) of the subfaults used in the geodetic study of the M_w 7.3 Landers earthquake (Fialko, 2004b), where the ICMT star indicates the centroid location for this model. The remaining stars are locations from the seismic catalogues described in the main text. Stars in (b) follow the same colour scheme as in (a).

3.3.4 Source directivity

Comparisons of hypocentre and centroid locations can provide information regarding the rupture length and directivity. A previous comparison of ISC hypocentre locations and GCMT centroid locations showed that while for earthquakes with $M_w \geq 6.5$ these comparisons provide useful information; for smaller earthquakes the difference between the two can be heavily influenced by location errors, which are likely due to uncertainty in the assumed Earth models (Smith and Ekström, 1997). Taking this into account, Figure 3.11 compares ISC hypocentre locations with GCMT and ICMT centroid locations for events with $M_w \geq 6.5$. It could be argued, considering results shown in Figures 3.4 and 3.5, that for events larger than this, there are still significant errors associated with the locations reported in the GCMT and ISC catalogues. However, the hypocentre-centroid distances being considered here are on average larger than the errors previously found for ISC hypocentre locations; ~ 9 km in this study and ~ 3 – 16 km reported in Syracuse and Abers (2009). Also we are not using the differences between ISC and GCMT or ICMT locations as a means of definitively calculating the rupture length and direction, but rather to qualitatively investigate the consistency of results obtained using different centroid locations. Globally the distances between ISC hypocentres and ICMT and GCMT centroid

locations are similar, with median distances of ~ 32 km and ~ 42 km, respectively. The orientations of hypocentre-centroid vectors show a mixed pattern globally (Figure 3.11), where for some earthquakes there is good agreement between both GCMT and ICMT and with rupture directions from detailed individual studies for some earthquakes. For example, the Denali earthquake (M_w 7.9, 3rd November 2002) shows the largest difference in hypocentre and centroid location (~ 180 km) with the ICMT and GCMT centroids being in agreement with the unilateral south-east rupture models from various seismic and geodetic studies (*e.g.* Velasco *et al.*, 2004; Asano *et al.*, 2005). However, there are significant disagreements for several other events, as will now be discussed.

As one might expect from previous results shown in Figure 3.11, some earthquakes in the south American subduction zone show inconsistency between ICMT and GCMT centroid locations in relation to the ISC hypocentre. One of the largest discrepancies is in relation to three earthquakes in the northern Chile subduction zone: M_w 6.8, 11th July 1993, M_w 6.7, 19th April 1996, and M_w 7.1, 30th January 1998 (NC93, NC96 and NC98 in Figures 8c-d, respectively). The ICMT locations are relatively close to the hypocentre (4–13 km) whereas the GCMT locations are systematically located ~ 50 km to the west (Figures 3.11 c-d). As previously mentioned, this bias is thought to be the result of errors in assumed Earth models so this systematic direction is unlikely to reflect the true rupture directivity.

In the same region there is also disagreement between ISC-ICMT and ISC-GCMT vectors for the Nazca Ridge earthquake (M_w 7.7, 12th November 1996, NR in Figures 3.11 c-d). The ICMT centroid location is twice as far away from the ISC hypocentre than the GCMT, but suggests a directivity in better agreement with the initial south east along-strike rupture propagation reported by (Swenson and Beck, 1999). It must be noted though that for the remaining earthquakes in this region there is general good agreement between reported rupture directivity and the ISC-ICMT and ISC- GCMT location vectors; Antofagasta (M_w 8.1, 30th July 1995, AN), Aiquile (M_w 6.5, 22nd May 1998, AI), Arequipa (M_w 8.1, 23rd June 2001, AR), Pisco (M_w 8.1, 15th August 2007, PI), and Tocopilla (M_w 7.8, 14th November 2007, TO). For example for the Arequipa earthquake (blue arrow, 'AR', in Figures 3.11 c-d) both the GCMT and ICMT centroid locations are consistent with the unilateral south-east rupture direction reported in various seismic and

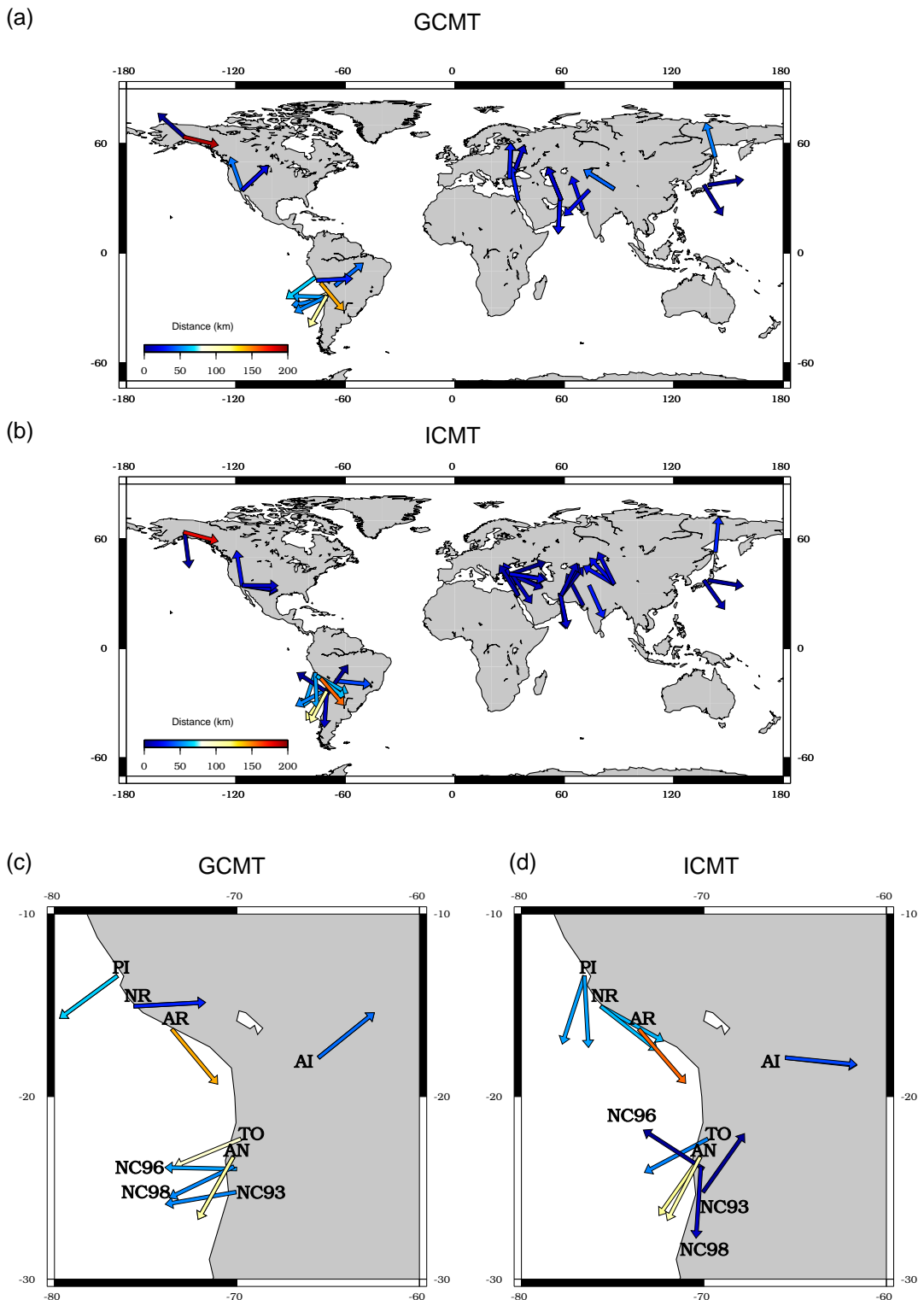


Figure 3.11: Four maps illustrating comparisons between ISC hypocentre locations and GCMT centroid locations (a) and ICMT centroid locations (b) for 28 earthquakes, the ICMT comparisons have more arrows due to multiple InSAR studies for the same earthquake. All the arrows are the same size (not to real scale) and begin at the ISC location and point towards the centroid location where the colour of the arrow indicates the distance between the two locations. c) This is a zoomed in map of ISC hypocentre and GCMT centroid locations for nine earthquakes in the south American region, d) is the same except shows ICMT centroid locations instead. The labels next to each arrow refer to the name of the event where; AI = Aiquile, Bolivia, AN=Antofagasta, Chile, AR=Arequipa, Peru, NC93, NC96, NC98=North Chile Subduction Zone 1993, 1996 and 1998, respectively, NR=Nazca Ridge, Peru, PI=Pisco, Peru, and TO=Tocopilla, Chile. See text for more details.

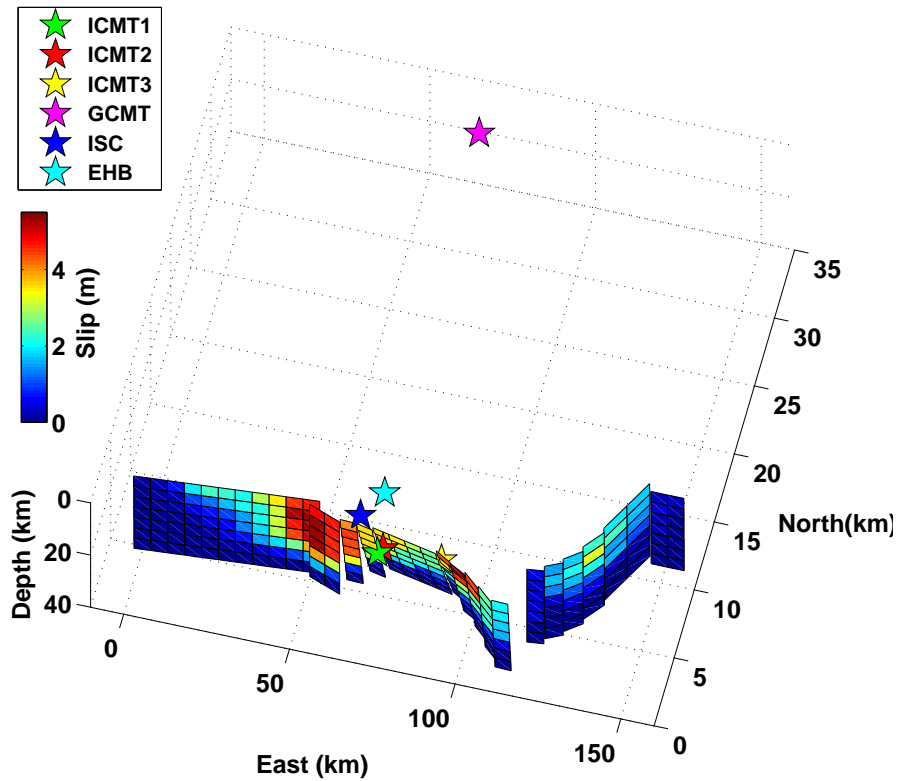


Figure 3.12: Distributed slip model for the Izmit earthquake, from Cakir *et al.* (2003) where ICMT1 indicates the centroid location for this model. ICMT2 and ICMT3 refer to centroid locations from the studies Wright (2000) and Delouis *et al.* (2002), respectively. The remaining locations are from seismic catalogues described in the main text (see figure legend).

geodetic studies (*e.g.* Robinson *et al.*, 2006; Pritchard *et al.*, 2007).

The ISC-ICMT location vectors also appear to disagree significantly with the ISC-GCMT vectors for three events in the North Anatolian fault zone in Turkey. For example, if we consider these locations and a distributed slip model (Figure 3.12) for the Izmit earthquake (M_w 7.5, 17th August 1999, Çakir *et al.*, 2003) the GCMT centroid is a significant distance (~ 30 km) away from the modelled fault planes and in comparison with the ISC and EHB hypocentres could imply a northward rupture propagation. However, the North Anatolian Fault on which this event occurred is not north-south trending and the InSAR-determined centroid locations (ICMT 1–3 in Figure 3.12) are in better agreement with the modelled east-west bilateral rupture propagation from various seismic studies (*e.g.* Yagi and Kikuchi, 2000), particularly ICMT1 (Çakir *et al.*, 2003) and ICMT2

(Wright, 2000) (Figure 3.12). The ICMT3 (Delouis *et al.*, 2002) location is from a distributed slip model which was calculated using GPS and seismic data as well as InSAR, which may explain the more easterly location.

Therefore, although centroid locations from InSAR derived variable slip models for large earthquakes can suffer the same issues as seismically determined locations when they are calculated from an inversion, they can provide valuable independent constraints on the spatial distribution of slip, which is useful for the determination of robust kinematic source models. Even without full kinematic spatio-temporal source inversions the comparison of centroid locations obtained from InSAR slip models with hypocentre locations can also provide important information regarding rupture direction.

3.4 Depth

Accurate earthquake depth values can be difficult to determine routinely for shallow crustal earthquakes. For example, the GCMT technique uses long-period body and surface waves, which cannot accurately determine depths in the upper crust of 15 km or less, thus the depth is often fixed at 12 km. Consequently we use depth estimates reported in the EHB catalogue, which has slightly better depth resolution, but occasionally the source depths for earthquakes shallower than 12 km are also fixed. We do not carry out comparisons for depth values reported in the GCMT catalogue because for most earthquakes in this study the depths are fixed at 12 or 15 km. Moreover, we do not show comparisons with ISC depths, because the results are very similar to those obtained using depths in the EHB catalogue. With the exception of a few outliers, Figure 3.13 shows that differences between InSAR and EHB depths are relatively small, with a median difference on the order of 5 km. The largest difference in depth occurs for the 2005 Qeshm earthquake, where the InSAR depth determined by Nissen *et al.* (2007a) is 39 km shallower than that reported by the EHB catalogue. The same authors also use teleseismic data to determine a depth that is 36 km shallower than that reported by the EHB catalogue; thus, this difference probably results from limitations in the EHB method.

InSAR source inversions commonly determine depths shallower than 12 km. However, it has been observed that InSAR depths are often shallower than those determined from seismic data (see *e.g.*, Feigl, 2002, for a summary). InSAR centroid depths in this

study are ~ 5 km shallower than EHB hypocentre depths (Figure 3.13a). The most likely reason for this is that the resolving power of InSAR data decreases with depth, which is evident from the diagonal trend of the data points in Figure 3.13b showing that differences between InSAR and EHB depths increase with depth.

The bias observed in this study is also consistent with observations that for shallow earthquakes there is a tendency for the rupture to propagate upwards. This is believed to be a result of the inability of an earthquake in a low stress regime to propagate easily into a deeper, higher stress regime, if strength is assumed to increase with depth (Das and Scholz, 1983). Therefore the centroid will be shallower than the hypocentre, hence the observed bias in Figures 3.13a and b. One way of taking the initiation point of the earthquake into account using the InSAR source models in the ICMT database is to consider the maximum depth of the fault model. Comparisons between this value and the EHB hypocentre are shown in Figure 3.13 and there is an evident improvement in the agreement between the two estimates.

Another possible contributing factor to the differences found between the InSAR centroid and EHB hypocentre is the fact that most studies use elastic homogeneous half spaces to model the geodetic data. A half-space is not an exact representation of the medium in which these earthquakes occur. There are large variations in the upper crust therefore the half-space approximation will have the largest influence for shallow earthquakes (Wald and Graves, 2001), and 87% of the earthquakes in our database occurred at depth shallower than 15km.

A finite dislocation in a half-space is a common approach for modelling a fault to explain the observed surface displacement, and the approximation of the earth as a half-space in this context has been the subject of much analysis. Purely theoretical analyses (*e.g.* Savage, 1987, 1998), investigations using geodetic data other than InSAR (*e.g.* Marshall *et al.*, 1991; Eberhart-Philips and Stuart, 1992; Wald and Graves, 2001), and inversions included in this study (Lohman *et al.*, 2002; Lohman and Simons, 2005a) have all found that depths determined in a half-space are 10–30% shallower than those in layered models, in agreement with the findings from this study.

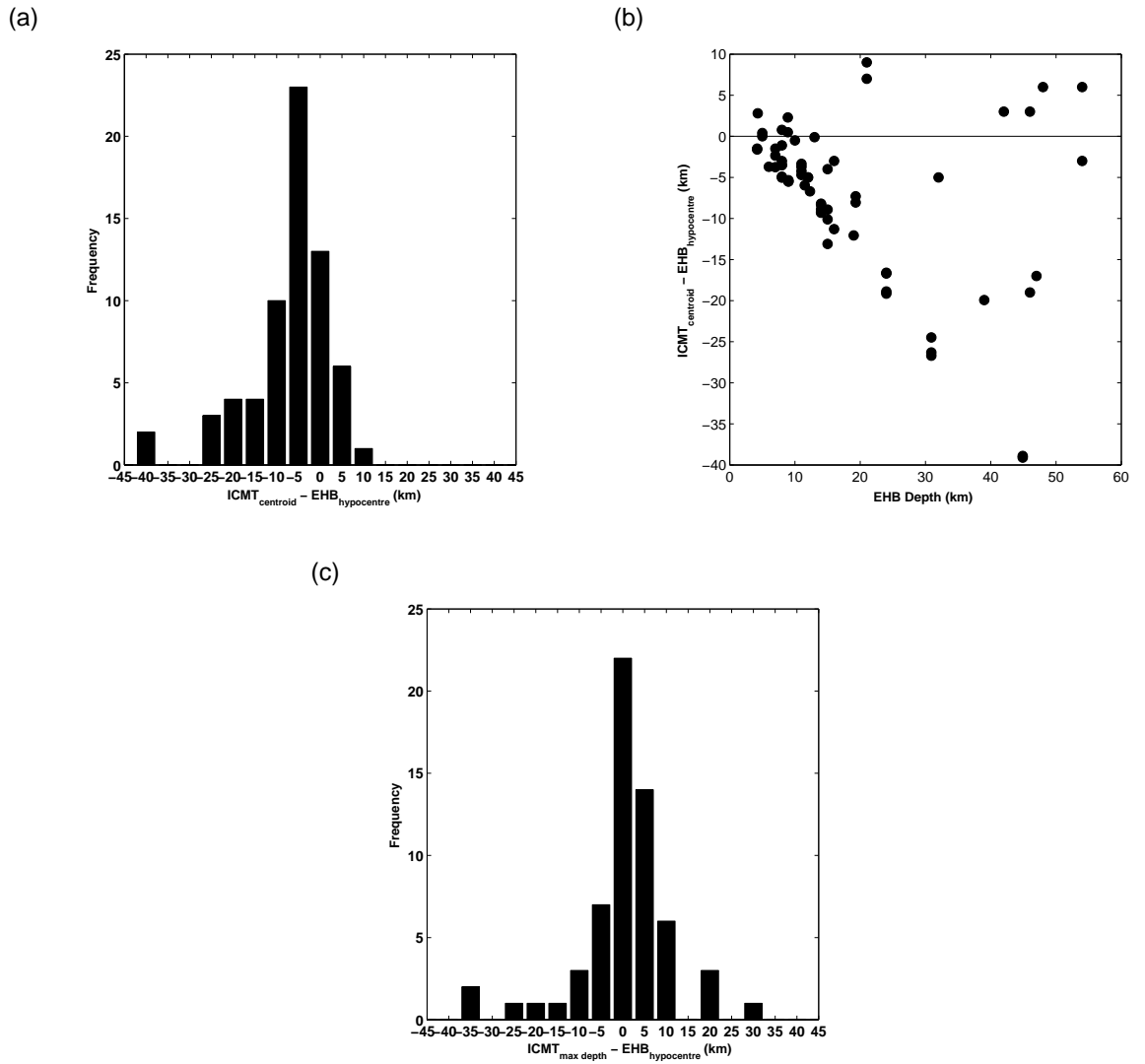


Figure 3.13: a) Distribution of the differences between ICMT centroid depths and EHB hypocentre depths. A negative difference means that the ICMT depth is shallower than the EHB hypocentre depth. The median difference in depth is -5.0 km ($\sigma = 9.6$ km) for 66 ICMT source models. b) Illustrates the differences with respect to increasing depth. c) Distribution of the differences between the maximum depth of the ICMT fault model and EHB hypocentre depths. A negative difference means that the ICMT depth is shallower than the EHB hypocentre depth. The median difference in depth is 2.0 km ($\sigma = 11.0$ km) for 61 ICMT source models.

When considering subduction zones, half-spaces are found to be especially poor representations. Masterlark (2003) investigated the sensitivities of displacement and dislocation predictions to the homogeneous, isotropic, Poisson-solid, half-space assumptions for subduction zone models. The homogeneous assumption was found to produce the largest errors in predictions of surface displacements. Bustin *et al.* (2004) took it one step further, being currently the only study to use a 3D heterogeneous numerical earth model to model InSAR data. They similarly found the depth to be 17% deeper for this more realistic model when compared with a simple half-space.

In recent years there have been some efforts towards the use of layered models in the modelling of InSAR data and when this is considered the trend in depth comparisons between InSAR centroid depths and EHB hypocentre depths changes (Figure 3.14). Despite the smaller dataset, centroid depths from InSAR studies that use layered models are in better agreement with the EHB hypocentre depths, with a median difference of 2.7 km ($\sigma = 8.7$ km) between the two types of estimates, compared with a median difference of -5.0 km ($\sigma = 9.2$ km) when using a homogeneous half-space in the modelling.

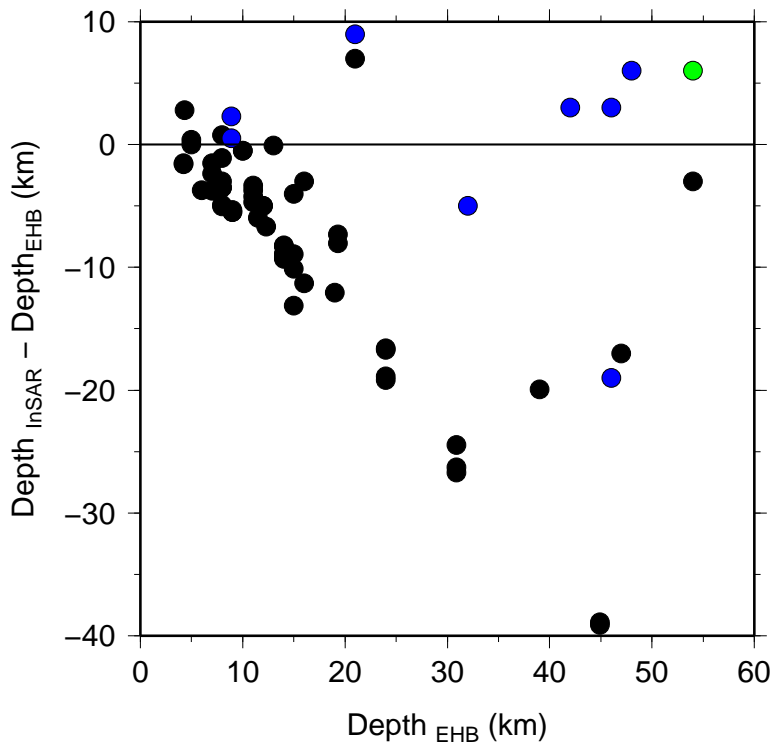


Figure 3.14: A comparison of the differences in depth for parameters based on simple elastic homogeneous half-spaces (black circles), layered half-spaces (blue circles) and one 3-D model (green circle).

Considering the effect of faulting mechanism on the differences in depth (Figure 3.15) there are no evident trends. For the majority of studies, the InSAR centroid depth varies between being 20 km shallower and 10 km deeper than the EHB hypocentre depth. Also there are no systematic trends in particular geographic regions probably because the events in the InSAR database represent a range of inversion methodologies and assumed half-spaces that were used to obtain the source parameters for events in a particular region. Not all of the studies in this region will have used a homogenous elastic half-space and where layered half-spaces are used it is unlikely they will be the same. To investigate regional trends source parameters determined using a uniform inversion technique and assumed half-space are needed. We do not observe any relationship between differences in InSAR and EHB depths and other parameters such as type of data used in the InSAR modelling, type of fault mechanism, earthquake non-double-couple component, and postseismic time elapsed (see Figure A.4 in Appendix A for these comparisons).

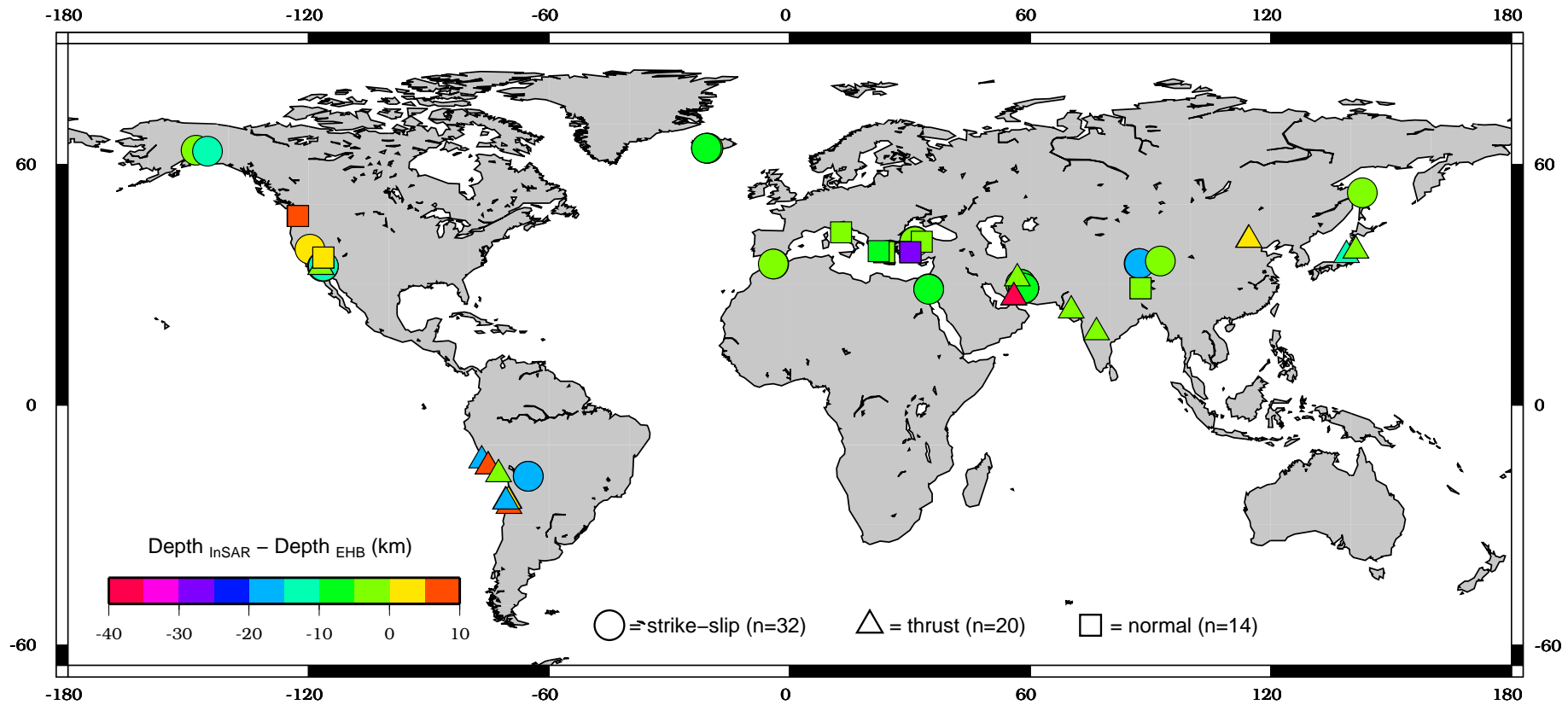


Figure 3.15: Difference between InSAR centroid depths and EHB hypocentre depths with respect to mechanism and fault location, where circles represent 32 strike-slip models, triangles refer to 20 thrust models and 14 squares are normal faulting events. The median difference in depth is similar for all the mechanisms; -5.7 km, -2.7 km and, -3.3 km for strike-slip, thrust and normal faulting, respectively.

3.5 Fault Geometry

Previously little attention has been paid to comparisons between strike, dip and rake fault values determined from the inversion of seismic and InSAR data. It is common for InSAR studies to use solutions from the GCMT catalogue or other seismic solutions as starting values for inversions (*e.g.*, Baer *et al.*, 2008), or even to fix the parameters at these values (*e.g.*, Kontoes *et al.*, 2000). Also, just by visually examining an interferogram, significant constraints can be placed not only on the location but also on the orientation of the fault. This information can be used in the inversions as starting solutions or to fix the fault parameters to reduce the computational cost of the inversions (*e.g.*, Jónsson *et al.*, 2002; Funning *et al.*, 2007). This study does not use strike, dip and rake values that were held fixed in InSAR studies (see Table 2.2).

We find that the strike, dip and rake values tend to agree well between InSAR and seismic models, the majority of the differences being within 20° (Figure 3.16) and median values lying close to 0 for all parameters, being 1.0° , ($\sigma = 12.7^\circ$), 0.0° ($\sigma = 14.6^\circ$), and -5.5° ($\sigma = 16.4^\circ$) for strike, dip and rake, respectively.

Rake shows the widest distribution of differences between InSAR and GCMT solutions. This is largely due to the fact that when inverting InSAR data the rake is poorly constrained if only one track direction is used, as only one component of the deformation is available (*e.g.*, Wright *et al.*, 2004b). Therefore, it is difficult to distinguish between strike-slip and dip-slip motions, leading to poorly constrained rake values in the inversion. The -42° discrepancy in rake for the Noto Hanto earthquake (M_w 6.7, 25th March 2007, Ozawa *et al.*, 2008) is a good example of this, as only descending data from the ALOS satellite were used in the inversion with GPS data. However, Fukushima *et al.* (2008) used data from ascending and descending tracks for this same earthquake, and consequently this discrepancy in rake is reduced to 7° when compared with the GCMT solution.

Furthermore, since the image acquisition geometry of most SAR satellites leads to greater sensitivity to vertical than to horizontal motions, dip-slip motion is typically easier to detect using InSAR. Consequently the displacement seen in an interferogram could be due to a small dip-slip motion or equally due to a much larger strike-slip motion (assuming

that the pattern of surface displacements is rendered sufficiently ambiguous by decorrelation or noise). Therefore, the seismic moment of an event can also vary greatly in an inversion, leading to a tradeoff between rake and moment and other parameters related to seismic moment such as fault dip, slip, length and width (Funning, 2005). Inversions for the Ngamring County, Tibet earthquake (M_w 6.0, 20th March 1993) are a good example of these tradeoffs with a difference of 37.4° between the InSAR and GCMT rake values (Figure 3.16). A significant tradeoff was found between rake and location in the inversion, as well as dip-slip, slip-width, and dip-width tradeoffs (Funning, 2005).

These tradeoff issues can be further complicated by poorly-correlated InSAR data due to the presence of significant atmospheric and topographic effects. Poor data quality also affects other parameters, including strike; for example, the InSAR and GCMT strike solutions disagree by 39° for the Killari, India earthquake (M_w 6.1, 29th September 1993). The interferogram used suffers from significant temporal decorrelation due to land use changes and large areas of vegetation and surface water (Satyabala, 2006).

In addition, the way in which these comparisons have been conducted must be taken into consideration as only solutions from one seismic catalogue are used, but there may be several other published independent seismic solutions, which can differ greatly from the GCMT solutions. For example, even though there is a 34° discrepancy in strike for the Qeshm Island event (M_w 5.8, 28th June 2006) the difference between the study's InSAR solution and their own seismic solution from the inversion of body wave data is halved, to a difference of 17° (Nissen *et al.*, 2007b).

A further difference that is an artefact of the method of comparisons is the 46° discrepancy in strike between InSAR and GCMT estimate for the Al Hoceima earthquake (M_w , 24th February 2004, Tahayt *et al.*, 2009). The InSAR solution is a cross-fault model and a moment-weighted average strike of the two faults has been used for comparisons (as described in section 2.5.1.1), so such an average is not a true representation of the source and not a fair comparison with the GCMT solution, which is a simple point source solution.

Overall strike, dip and rake agree well between InSAR and seismic solutions and this is evident when considering Figure 3.17. There are no clear patterns in terms of the geographical distribution of the differences in fault strike, dip and rake suggesting that InSAR

and seismic data constrain the fault geometry equally well and are relatively insensitive to the assumed Earth model. Although, similar to the depth comparisons (section 3.4), the lack of regional trends could alternatively be due to the use of different inversion techniques and assumed half-space models for events in the same region. This highlights the importance of taking the inversion technique and assumed half-space into account when comparing different source models for the same event. We do not find any relationship between difference in strike, dip and rake and the type of data used in the InSAR modelling. Moreover, we examined the differences in strike, dip and rake as a function of other parameters such as seismic moment, postseismic elapsed time, non-double-couple component of the earthquakes reported in the GCMT catalogue and earthquake depth and did not find any clear relationship (see Figures A.5-A.7 in Appendix A, which show all these comparisons).

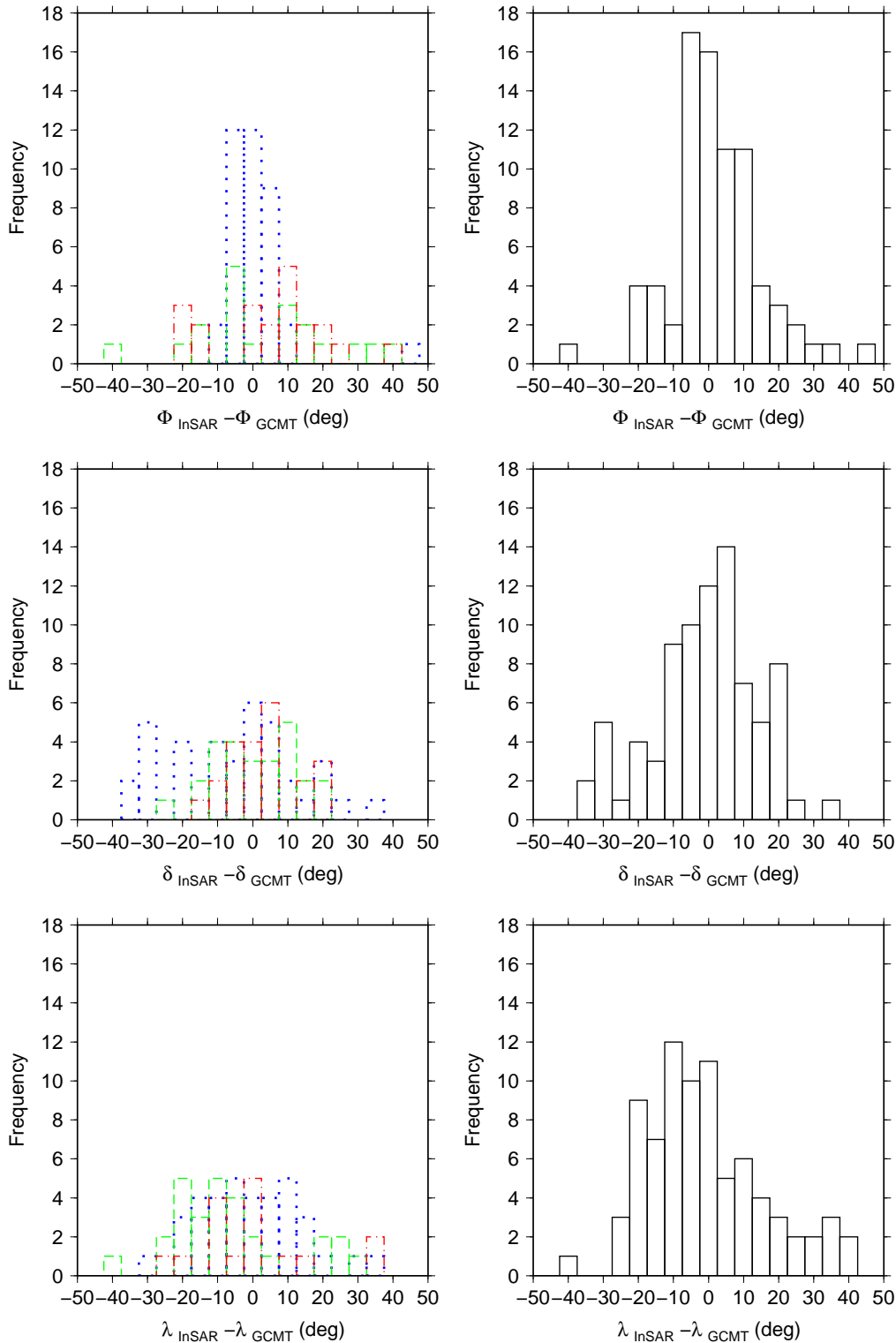


Figure 3.16: Comparison of InSAR and GCMT strike, ϕ (**Top**), dip, δ (**Middle**) and rake, λ (**Bottom**). Figures show the distribution of the difference with respect to mechanism where the blue dotted line corresponds to strike-slip, green dash is thrust and red dash dot refers to normal faulting events. The figures on the right side are the total distribution of all the mechanisms, for 78, 85 and 80 estimates of strike, dip and rake, respectively, where the median and standard deviations for each of the parameters are as follows; $\psi=1.0^\circ$, ($\sigma = 12.7^\circ$), $\delta=0.0^\circ$ ($\sigma = 14.6^\circ$), and $\lambda=-5.5^\circ$ ($\sigma = 16.4^\circ$).

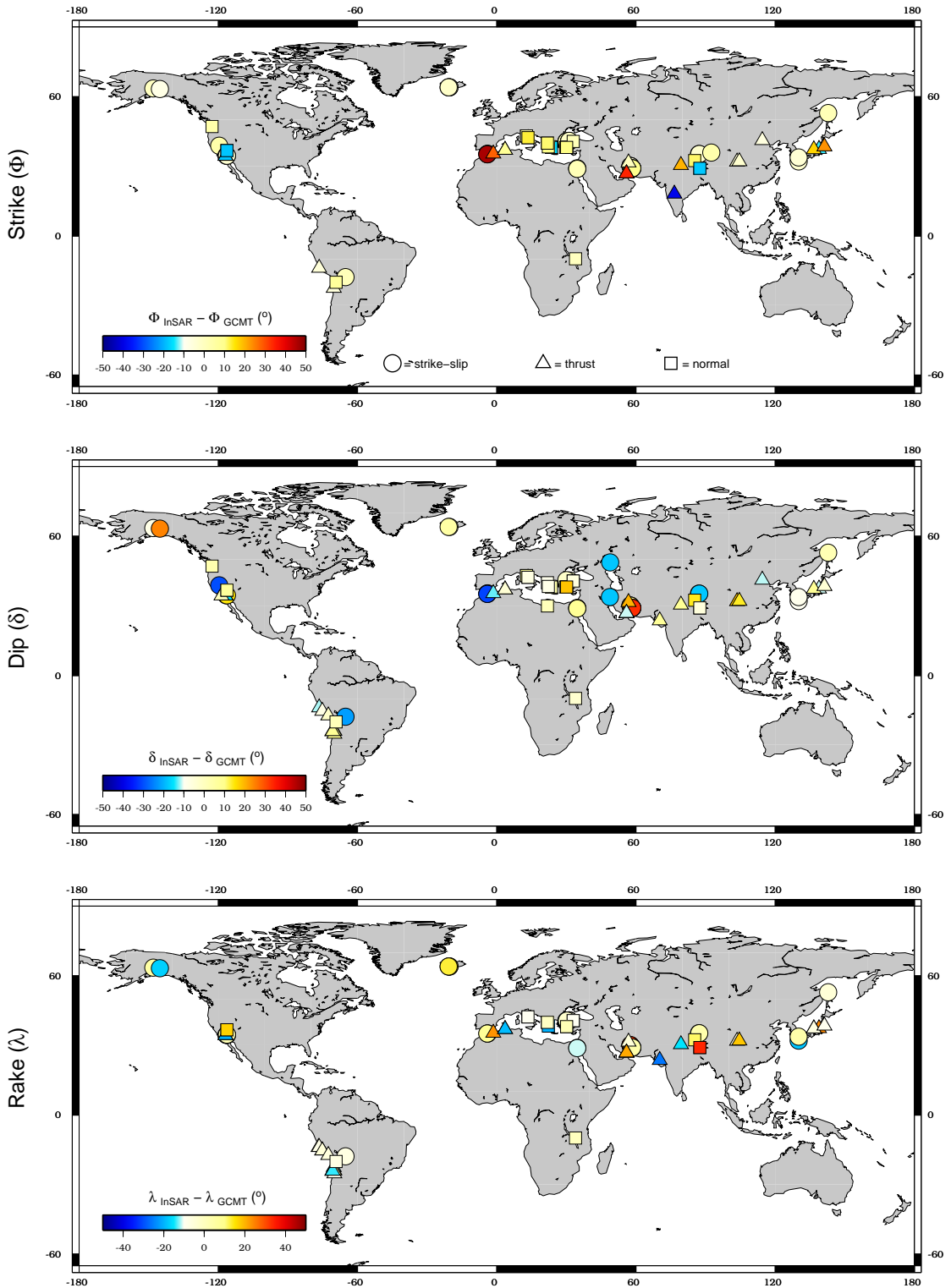


Figure 3.17: Differences, in degrees, between GCMT and InSAR strike (**Top**), dip (**Middle**) and rake (**Bottom**) with respect to mechanism and InSAR location. The notation for each mechanism is the same as in previous figures (strike-slip = circle, triangle = thrust, square = normal).

3.6 Distributed Slip Models

3.6.1 Intraevent variability

During the past three decades there have been several notable earthquakes that have been studied independently by multiple groups using InSAR data. A good example of this is the M_w 7.1 Hector Mine earthquake, previously discussed in section 3.3.3. Figure 3.18 shows three distributed slip models for this event, produced using InSAR data. Models (a) (Jónsson *et al.*, 2002) and (b) (Salichon *et al.*, 2004) have been built using the same InSAR data from ascending and descending tracks from the ERS-1 and ERS-2 satellites, to produce interferograms with measurement periods of 35 days. Model (c) (Figure 3.18c, Simons *et al.* (2002), uses an ascending interferogram covering a longer period of ~ 4 years. The fault geometry is complex for this event and each study uses multiple fault segments, varying from 4 to 9. Despite the varying numbers of segments, the length, width, strike and rake values are consistent across all the models, likely the result of the fact that the trace of the surface rupture is well constrained by the InSAR data.

However, there is some discrepancy in the direction of dip, as mentioned in section 3.3.3. For the ICMT models (a) and (b), and the GCMT solution, the fault is dipping to the west whereas the fault segments dip eastwards in model (c). It must be noted though that when solving for the slip distribution that the dip was held fixed in models (a) and (b). The difference in dip is small because it is near vertical for all models (dip $\approx 82^\circ$). The principal difference between model (c) and the other two is that Simons *et al.* (2002) use a layered half-space, which could be responsible for the variation in dip direction.

As discussed in section 3.4, the use of a layered half-space can reduce the bias towards shallower depths seen in models, that use a homogeneous half-space. Yet even though the peak slip is in the north-west part of the rupture for models (a)-(c), it is shallowest in model (c). Therefore different methods of inversion and model parameterisations could be responsible for the variation in dip and the depth of maximum slip. Furthermore, only one of the interferograms used by Jónsson *et al.* (2002) includes post-seismic deformation due to afterslip in the month following the earthquake. In comparison, both the ascending and descending tracks used in Simons *et al.* (2002) could include postseismic deformation, which could also explain why their estimated geodetic moment is the largest of the three models ($\sim 20\%$ larger than models (a) and (b)).

The slip distribution in model (b) extends ~ 12 km further to the south-west than the other two models, which could be a result of the inclusion of teleseismic data in the inversion, although little change in the spatial pattern of the slip distribution was seen when these additional data were included (Salichon *et al.*, 2004). Very similar InSAR datasets are used in each of the three studies, consequently the variations in the slip distribution models are most likely the result of differences in inversion methods. The relative weighting of the InSAR, GPS and seismic datasets used is of particular importance because it dictates the influence each dataset has on the final inversion result, an issue discussed in chapter 6, as well as *a priori* constraints such as model regularisation (smoothing).

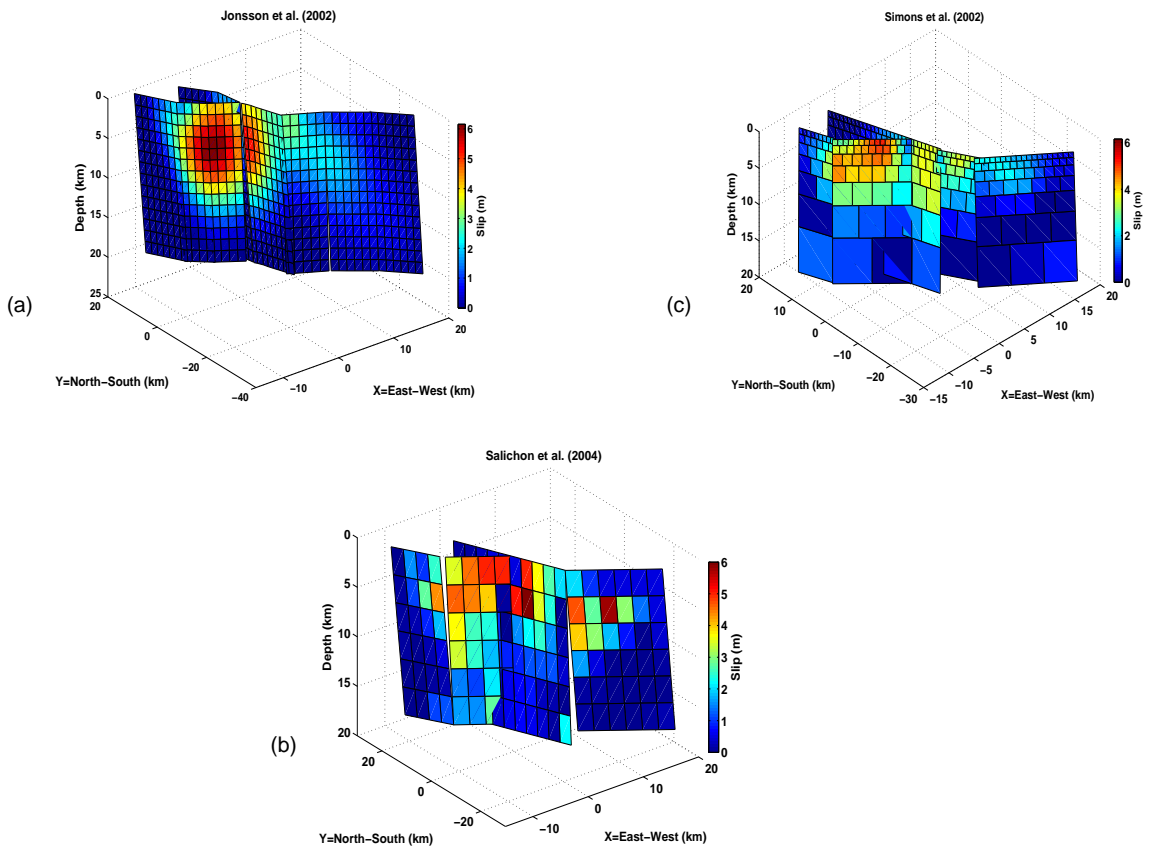


Figure 3.18: Comparison of three distributed slip models for the Hector Mine earthquake (M_w 7.1, 16/10/99). a) Jónsson *et al.* (2002), which is a joint inversion of InSAR and GPS data, b) Salichon *et al.* (2004), which jointly inverted InSAR, GPS and teleseismic data and c) Simons *et al.* (2002), which is a joint inversion of InSAR and GPS data.

3.6.2 Earthquake location

One of the strengths of InSAR data is their spatial resolution, where even just the visual examination of the interferogram can place strong constraints on the location of an earthquake. However, for large magnitude events with long rupture lengths the InSAR-determined centroid location is calculated from a slip distribution, which is the result of an inversion, and consequently suffers the same issues as seismically determined locations that are also determined from an inversion. Here we illustrate differences in location between seismic and InSAR (distributed slip) determinations for the Wenchuan earthquake (M_w 7.9, 12th May 2008). This large, predominantly, thrust event occurred in the Longmen Shan range and was one of the largest intraplate events in recent years, with a very complicated surface rupture that sparked many seismological, geodetic and field studies (*e.g.*, Ghasemi *et al.*, 2010; Li *et al.*, 2010; Liu-Zeng *et al.*, 2010; Zhang and Ge, 2010).

The rupture initiated near Wenchuan and propagated unilaterally to the north-east (*e.g.*, Zhang and Ge, 2010), which is consistent with the NEIC hypocentre estimate (blue star in Figure 3.19) in relation to all the calculated centroid locations (pink star, GCMT location, green, Hao *et al.* (2009), and yellow, Feng *et al.* (2010)). There is a significant offset between the GCMT centroid location and the two estimates from InSAR studies; 38 km and 28 km for Hao *et al.* (2009) and Feng *et al.* (2010), respectively. However, considering the large magnitude of this event and compared with the previous case studies (Landers, Hector Mine and Izmit) the two InSAR estimates are in good agreement with each other, and the differences seen are likely due to the variation in slip distribution. In particular the maximum slip is much lower in the model from Feng *et al.* (2010) (Figure 3.19b) ~ 7 m, compared with ~ 12 m for Hao *et al.* (2009). The latter study also obtains a larger area of higher slip for the hypocentre at the south-west end of the rupture. Both models use similar InSAR data (ALOS data from tracks 471–477), but Hao *et al.* (2009) use measurements of offset observed in the field to help constrain the source model, whereas GPS and InSAR data were used in Feng *et al.* (2010), which may explain the large difference.

There are also large variations in the finite fault models for this event that are calculated using seismic data (*e.g.*, Ji and Hayes, 2008; Liu-Zeng *et al.*, 2009). Generally both

geodetically and seismically determined source models appear to model two large asperities, one near the hypocentre and one ~ 150 km to the north east but the asperity areas and magnitude of slip vary substantially between them. The two InSAR source models do have one or two more subfaults than are used in the seismically derived source models (e.g. Ji and Hayes, 2008) which are in agreement with observed surface ruptures (e.g. Liu-Zeng *et al.*, 2009). The source model from Hao *et al.* (2009) is more consistent with the high peak slip seen in the seismically derived source models and offsets observed in the field (e.g. Liu-Zeng *et al.*, 2009; Nakamura *et al.*, 2010). The large number of varying finite fault models that fit the observed data is potentially due to the complicated nature of the rupture. Despite this complexity, the relative good agreement in centroid location between the two InSAR studies demonstrates the ability of InSAR to constrain the spatial features of the rupture.

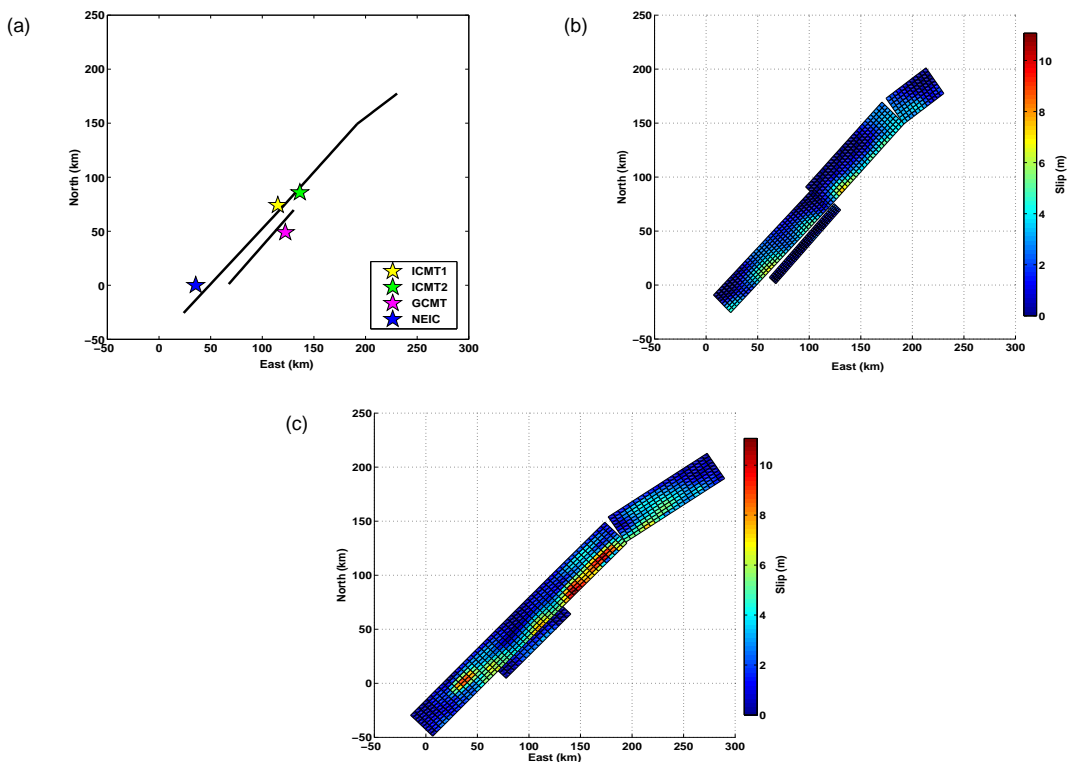


Figure 3.19: a) Fault trace of the distributed slip model for the Wenchuan earthquake from Feng *et al.* (2010), where ICMT1 refers to the centroid location from the same study, ICMT2 is the centroid location from Hao *et al.* (2009), GCMT is the centroid location reported in the GCMT catalogue and NEIC is the hypocenter location from the NEIC Preliminary Determination of Epicenters (PDE) catalogue. b) Plan view of the Feng *et al.* (2010) distributed slip model. c) Plan view of the Hao *et al.* (2009) distributed slip model.

3.7 Discussion

3.7.1 Source parameter validation

Seismic and InSAR data are independent observations of different aspects of an earthquake, therefore with our compilation of source parameters from published InSAR studies, it is possible to validate source parameters from seismic catalogues against an independent dataset. Comparisons between databases compiled using InSAR and seismic catalogues have highlighted certain issues. For example, the comparisons of GCMT and InSAR centroid locations have highlighted limitations in GCMT locations, as well as the influence that the earth model used in CMT inversions has on the location of the events (Ferreira *et al.*, 2011). Conversely, the good agreement between strike, dip and rake values suggests how well both datasets constrain these particular parameters.

Comparisons between InSAR and seismic data can be used to quantify uncertainties in source parameters reported in seismic catalogues or InSAR studies. For example, as previously mentioned, the location from the GCMT catalogue differs on average by about 21 km from the InSAR centroid location. The moment magnitude differs by ~ 0.02 ($\sigma = 0.09$) and fault geometry estimates (strike, dip and rake) by $\sim 0^\circ\text{--}5^\circ$ ($\sigma = 13^\circ\text{--}16^\circ$). In addition, the standard deviations also give an indication of the level of uncertainty associated with the source parameters determined using various inversion techniques using seismic and geodetic data. These uncertainties need to be taken into account when using them to determine the changes in tectonic stress (*e.g.*, Coulomb stress changes; King *et al.*, 1994) in an area, which in turn can be used for assessing seismic hazard.

3.7.2 Earth structure models

Source parameters, whether they are inverted using seismic or InSAR data, are sensitive to the assumed Earth model. Ferreira and Woodhouse (2006) were the first to attempt to quantify the uncertainties in seismic CMT inversions due to inaccurate Earth structure using a variety of Earth models and forward modelling techniques. The global Earth models used in global seismic catalogues currently do not seem to have high enough resolution to locate shallow crustal events accurately (Ferreira *et al.*, 2011). Mellors *et al.* (2004) also found the Earth model to be an influential factor when comparing InSAR and

seismic source parameters. The InSAR-derived source parameters agreed well with those determined from seismic data relocated using a 3-D velocity model, but the agreement was poorer with seismic parameters obtained employing 1-D velocity models.

The assumption of a homogeneous half-space in InSAR data inversions leads to a bias towards shallower depths, but even though a layered half-space is an improvement, it does not solve the problem. The layered or 3-D earth model must be accurate, as found by Cattin *et al.* (1999), who investigated the effect of the inclusion of a lower-rigidity layer in a homogeneous half-space on modelled coseismic surface displacements and the interpretation of source parameters. The horizontal component of displacement was more sensitive than the vertical component to the inclusion of the layer. Horizontal motions could increase by up to 40% using a half-space that incorporates a lower rigidity layer at the surface in comparison with motions determined using a homogenous half-space. If InSAR data from only one SAR track direction is available, then horizontal motions (particularly those in the north-south direction) are already poorly constrained with respect to the vertical component; if in addition the Earth model is incorrect, further errors are introduced.

3.8 Conclusions

Overall, InSAR and seismic data lead to seismic source parameters that agree well concerning the fault geometry and are complementary datasets when jointly inverted. The assumed Earth structure model is an influential factor concerning the quality of the earthquake location and depth. In terms of the moment magnitude, there is general good agreement, with a slight tendency for the InSAR estimates for thrust events to be slightly larger. This is a possible artefact of the events included in the study and also the result of potential deformation from aftershocks, afterslip and viscoelastic relaxation being included in the measurement period, and increased sensitivity to vertical motion. New techniques for the processing and inversion of both InSAR and seismic data are constantly being developed, and particular focus is needed on verifying the accuracy of the assumed earth model and on the accurate quantification of uncertainties.

These issues are further explored in the next chapter, where earthquakes which showed large discrepancies regarding certain source parameters are investigated, particularly in

the context of the assumed Earth structure model.

Chapter 4

Testing InSAR and seismically-determined source models using 1-D and 3-D seismic forward modelling

4.1 Introduction

Chapter 3 highlighted the complementary strengths of InSAR and seismic data. However, for some earthquakes, comparisons of InSAR and seismically-determined source models revealed large discrepancies in estimates of fault geometry, centroid location and/or seismic moment. Moreover, some large differences between multiple source models obtained from seismic, geodetic and/or joint inversions for the same earthquake (*e.g.*, for the M_w 7.5, Izmit and M_w 7.1 Hector Mine events) were also observed. This is in part due to the differing assumptions regarding fault geometry and crustal structure, and also due to different inversion approaches used in the various studies considered. Understanding large discrepancies in earthquake models is a particularly important issue, as robust source parameters are key inputs into, *e.g.*, the dynamic modelling of earthquakes and the calculation of Coloumb stress changes, with strong implications for earthquake physics and seismic hazard assessment.

Forward modelling of source models along with comparisons of the resulting synthetic seismograms with real data is a useful and independent means of investigating which source parameters are well constrained. Advances since the late 1990s in numerical methods for the simulation of seismic waves in a realistic 3-D Earth along with a great increase in computer power have significantly improved seismic forward modelling efforts. Of all numerical methods, the spectral element method (SEM) (Komatitsch and Tromp, 1999, 2002a,b) is particularly attractive, enabling the accurate simulation of full wave propagation in complex 3-D Earth models at the global scale, at a reasonable computational cost. Comparisons of synthetic seismograms calculated using SEM with observed seismic data have been used to test source models for large strike-slip earthquakes such as Denali, Alaska (M_w 7.9, 3rd November 2002, Tsuboi *et al.*, 2003) and Wenchuan, China (M_w 8.0, 12th May, 2008, Nakamura *et al.*, 2010). Moreover, comparisons between real data and SEM synthetics have also been used to establish the robust features of a range of source models for a large subduction zone event offshore northern Sumatra (Konca *et al.*, 2007) and to further refine existing body wave inversion results for the Balleny Islands earthquake (M_w 8.1, 25th March 1998, Hjörleifsdóttir *et al.*, 2009).

In this chapter comparisons are made between observed long period seismic data and theoretical seismograms calculated with the SEM to investigate the following five earthquakes, shown in Figure 4.1:

- Landers, M_w 7.3, 28th June 1992
- Eureka Valley, M_w 6.1, 17th May 1993
- North Chile Subduction Zone, M_w 6.6, 19th April 1996
- Izmit, M_w 7.5, 17th August 1999
- Pisco, M_w 8.1, 15th August 2007

These earthquakes were chosen based on the findings from Chapter 2; they all exhibited large discrepancies for one or more source parameters when comparing solutions from the ICMT database with those from the GCMT catalogue. They occur in a variety of tectonic settings, have a range of magnitudes and have been previously studied through a mix of uniform and variable slip source models. There are discrepancies in centroid location between ICMT and GCMT estimates for all the events, varying from ~ 30 to 60 km

for Izmit and Pisco, respectively. There are also large discrepancies in seismic moment estimates for the two subduction zone events, Pisco and North Chile, and in strike estimates for the Eureka Valley event. GCMT, ICMT and a mixed source parameters for these five earthquakes are used to calculate theoretical seismograms for: (i) a 1-D Earth model (PREM, Dziewonski *et al.*, 1981) using normal mode summation (Gilbert, 1976); (ii) a 3-D Earth mantle—S20RTS (Ritsema *et al.*, 1999)—combined with the global crustal model CRUST 2.0 (Bassin *et al.*, 2000) using the spectral element method. The results of the comparisons between synthetic seismograms and data are then presented and subsequently discussed in terms of the robustness of the source parameters and the influence of the assumed Earth structure.

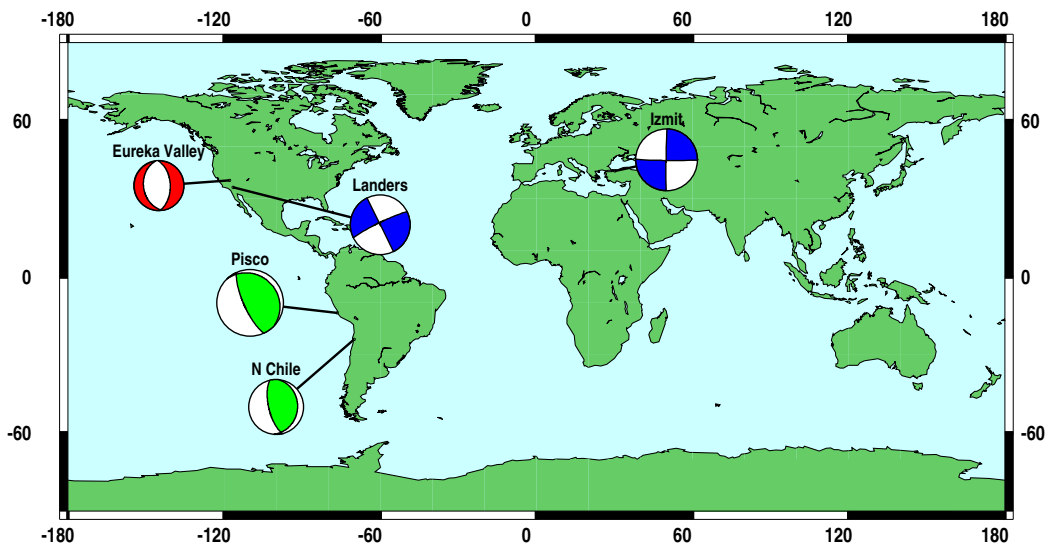


Figure 4.1: Global map showing focal mechanisms and locations for the five events studied, including two strike-slip events (blue), two subduction zone earthquakes (green) and one normal faulting event (red).

4.2 Data and methodology

4.2.1 Data selection and processing

Data for each event were downloaded from IRIS (Incorporated Research Institutions for Seismology) for all available stations on the GEOFON and Global Seismograph Network (GSN) within an epicentral distance of 40–140° of the earthquake. The instrument

response is deconvolved from the data and the horizontal components are rotated into longitudinal and transverse components. Cosine high-and low-pass filters are used to filter for long period surface waves ($T \sim 150\text{s}$) and Butterworth high-and low-pass filters are applied for long period body waves ($T \sim 50\text{s}$). Any noisy stations are removed via visual examination of the data and, following this, 1000 s-long and 250 s-long time windows are manually picked for surface and body waves, respectively.

It must be noted that comparisons of long period body waves are only carried out for the M_w 6.1 Eureka Valley earthquake. For the larger earthquakes – Pisco, Izmit, Landers and North Chile – the source’s duration is similar to the dominant period of the long-period body waves. Therefore, a source time function is needed to be taken into account when modelling these earthquakes. Tests were carried out using a simple boxcar source time function, but this was not sufficiently accurate to account for the time and amplitude shifts seen between the data and synthetics due to the source complexity. Consequently robust body wave comparisons could not be made for these earthquakes. Where possible, comparisons have been made for all three components of motion (vertical, longitudinal and transverse). However, depending on the data quality, this is not always possible for all events and is noted when it is the case.

4.2.2 Normal mode summation

In seismology the displacement due to a seismic source recorded at seismic stations can be represented as the sum of standing waves, or normal modes of the Earth. The association of the normal mode concept with the seismic moment tensor formalism of Gilbert and Dziewonski (1975) motivated many source studies, including the approach used in the GCMT catalogue (*e.g.* Dziewonski *et al.*, 1981). Since then, the normal mode formalism has been widely used for the calculation of exact theoretical seismograms for 1-D Earth models. An in-house modified version of the normal mode summation programme, *apsynah* (J. H. Woodhouse, *pers. comm.*) was used to calculate theoretical seismograms accurate down to a period of 7 s for a 1-D Earth model. It assumes a spherical, non-rotating, elastic and isotropic (SNREI) Earth, in this case the Preliminary Earth Reference Model (PREM, Dziewonski and Anderson, 1981). The SNREI assumption simplifies the calculations such that eigenfunctions for each mode will be constant at the surface and it

is the excitation factors that vary.

4.2.3 Spectral element method

While the normal mode formalism can also be used to calculate synthetic seismograms in 3-D Earth models (*e.g.* Clévéde *et al.*, 2000; Millot-Langet *et al.*, 2003; Romanowicz *et al.*, 2008), in practice its application is complex, time-consuming and cumbersome, particularly when modelling shorter period seismic data. Purely numerical methods, such as the Spectral Element Method (SEM) offer an interesting alternative, enabling the accurate calculation of full waveforms in the presence of complex Earth structure and with reasonable computational time requirements (*e.g.* Capdeville *et al.*, 2003; Chaljub *et al.*, 2003). It is a highly accurate technique for the forward modelling of seismic data, particularly when assuming a 3-D Earth structure, as it is able to take into account free-surface topography and the effects of anisotropy and fluid-solid boundaries on the resulting seismic waveforms (Komatitsch and Tromp, 1999). The technique solves the weak form of the equation of motion on a user-defined mesh consisting of hexahedral elements. The equation is solved by integrating over the volume and absorbing boundary, which is achieved by solving smaller integrals over the volume and surface elements that make up the mesh. The mesh represents the Earth as a cubed-sphere, which is split up into six chunks and the number of elements along the side of each chunk determines the resolution of the resulting synthetics, *i.e.* the period to which they can be calculated down to. For more details see Komatitsch and Tromp (1999).

There are various implementations of the spectral element method; the approach used here is as implemented in the SPECFEM3D Globe package (Komatitsch and Tromp, 1999), which is freely available from Computational Infrastructure for Geodynamics (CIG, <http://www.geodynamics.org/cig/software/specfem3d-globe>). The package allows a wide choice of 3-D Earth models that can be used in the simulations. In this chapter two shear wave mantle models are used—S20RTS (Ritsema *et al.*, 1999) and the more recently updated S40RTS (Ritsema *et al.*, 2011) mantle model. In both cases the crustal model CRUST 2.0 (Bassin *et al.*, 2000) is assumed and 266 elements are assigned to each side of the chunk, which means that the resulting synthetics are accurate down to a period of ~ 15 s.

4.2.4 Quantifying phase, amplitude and waveform misfits

In order to quantify how well the synthetic seismic waveforms match the observed data three types of misfits are calculated between the data and synthetics: phase ($\delta\Psi$), amplitude (δA) and waveform (m^2) misfits. A time window is manually picked on the data and the corresponding time frame is selected for the synthetics. Then, a least-squares algorithm is used to determine the phase shift ($\delta\Psi$, measured in seconds) and amplitude factor (δA) that lead to the best fit between the data and the synthetics. An amplitude factor of 1.0 means that the waveforms match perfectly; if δA is greater than one, the synthetic amplitudes are systematically smaller than the data, and, conversely, if δA is smaller than one, then the synthetic amplitudes are larger than the observations.

The waveform misfit is calculated in a least squares sense (L_2 -norm misfit) using the following equation:

$$m^2 = \frac{(s - d)^2}{d^T d} \quad (4.1)$$

where d refers to the data and s to the synthetics.

4.3 Results

4.3.1 Normal faulting event: Eureka Valley, M_w 6.1, 17th May 1993

This event is the first of two earthquakes studied in this chapter occurring in the Great Basin and Range province and lying within the North American - Pacific plate boundary zone (Figure 4.2). The influence of motion along this plate boundary has recently been suggested to extend as far as 1000 km east into the Great Basin and Range Province (Parsons and Thatcher, 2011), which includes the Walker Lane Belt (WLB) and Eastern Californian Shear Zone (ECSZ). These zones form part of the diffuse transform boundary zone and structures within them accommodate the majority of residual motion not taken up by the San Andreas fault (*e.g.* Atwater, 1970; Dokka and Travis, 1990; Bennett *et al.*, 2003); the central section of the WLB is suggested to accommodate as much as 25% of the relative plate motion (Oldow *et al.*, 2001). The spatial and temporal distribution of the strain accumulation in the WLB and ECSZ is highly heterogeneous and certain regions show large discrepancies between geodetic and geologic strain rates, which could be due

to the diffuse nature of the deformation that is not evident on surficial faults (Foy *et al.*, 2012).

The Eureka Valley earthquake occurred in the WLB and is the only normal faulting event studied in this chapter. It was part of a sequence of earthquakes including the large strike-slip event, Landers (M_w 7.3), investigated in section 4.3.2. It occurred on a buried fault, one of five normal fault zones that lie between the Panamint Valley-Hunter Mountain-Saline Valley fault system and Furnace Creek and Fish Lake Valley faults (Figure 4.3, see Oswald and Wesnousky, 2002).

There are two previous geodetic studies of this earthquake, which are listed in Table 4.1; Massonnet and Feigl (1995); Peltzer and Rosen (1995). In addition, Table 4.1 also includes an InSAR source model determined in this study using the approach outlined in Chapter 2, section 2.2. The source model from this study is used and referred to as the ICMT solution to investigate the 55 km discrepancy in location (see Figure 4.3) and the 30° difference in strike between the geodetic results and those reported in the GCMT catalogue. Both long period surface and body waves are considered.

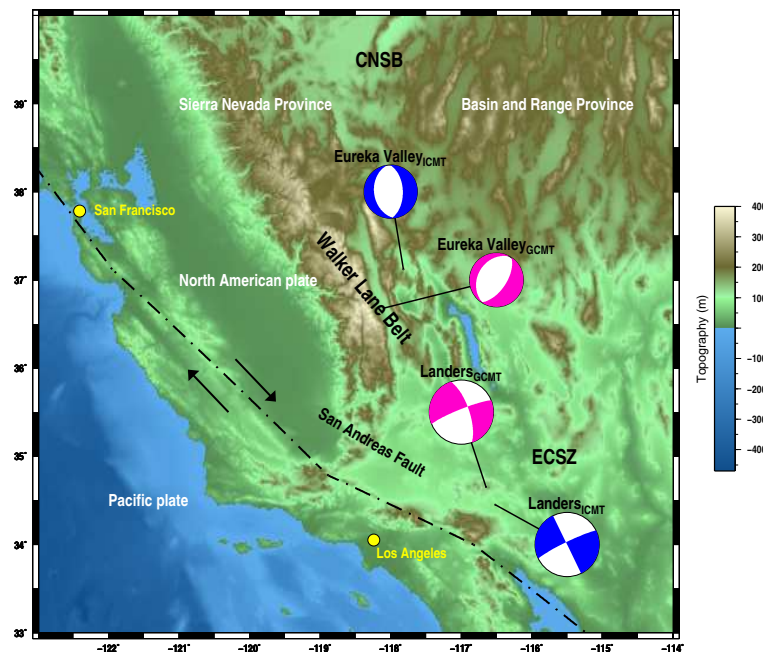


Figure 4.2: a) Californian section of the North American - Pacific plate boundary (dashed black line). Three key zones in this diffuse transform boundary are shown: Central Nevada Seismic Belt (CNSB), Walker Lane Belt (WLB), East Californian Shear Zone (ECSZ). The focal mechanisms for both Californian earthquakes studied in this chapter are also shown, where pink refers to GCMT solutions and blue to ICMT solutions.

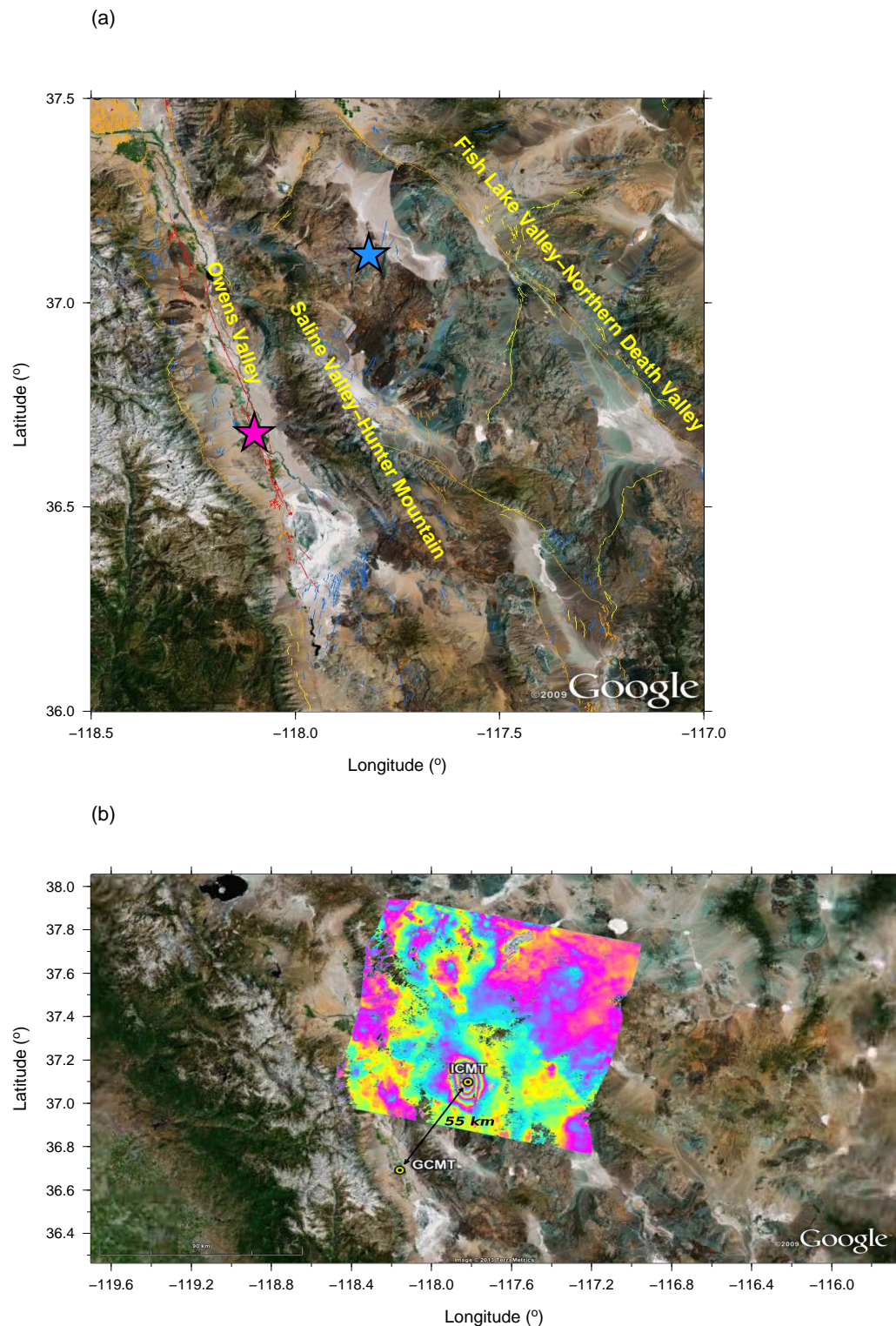


Figure 4.3: a) Tectonic setting in Eureka Valley. Main fault zones in Owen Valley, Saline Valley, Hunter Mountain, Fish Lake Valley, Northern Death Valley are highlighted based on fault maps from the USGS fault database which are coloured according to age; Historic (red), Holocene - Latest Pleistocene (orange), Late Quaternary (yellow) and Quaternary (blue). GCMT and ICMT locations are shown as blue and pink stars, respectively. b) Interferogram in tectonic context to highlight the 55 km discrepancy between the ICMT and GCMT locations, which are shown as yellow circles.

Table 4.1: Summary of source parameters for the Eureka Valley earthquake (M_w 6.1, 17th May 1993) from various studies including Massonet & Feigl (1995), Peltzer & Rosen (1995), this study and the GCMT catalogue. The latitude, longitude and depth refer to the centroid location.

Parameter	Massonet & Feigl	Peltzer & Rosen	This Study	GCMT
Mw	6.10	6.11	6.06	6.1
Mo ($\times 10^{18}$ Nm)	1.70		1.55	1.83
Lat ($^\circ$)	37.111		37.118	36.680
Lon ($^\circ$)	242.206		242.18	241.900
Depth (km)	9.2	13	8.1	15
Strike ($^\circ$)	173.0	7.0	172.0	210
Dip ($^\circ$)	54.0	50.0	37.6	30
Rake ($^\circ$)			-95.2	-93

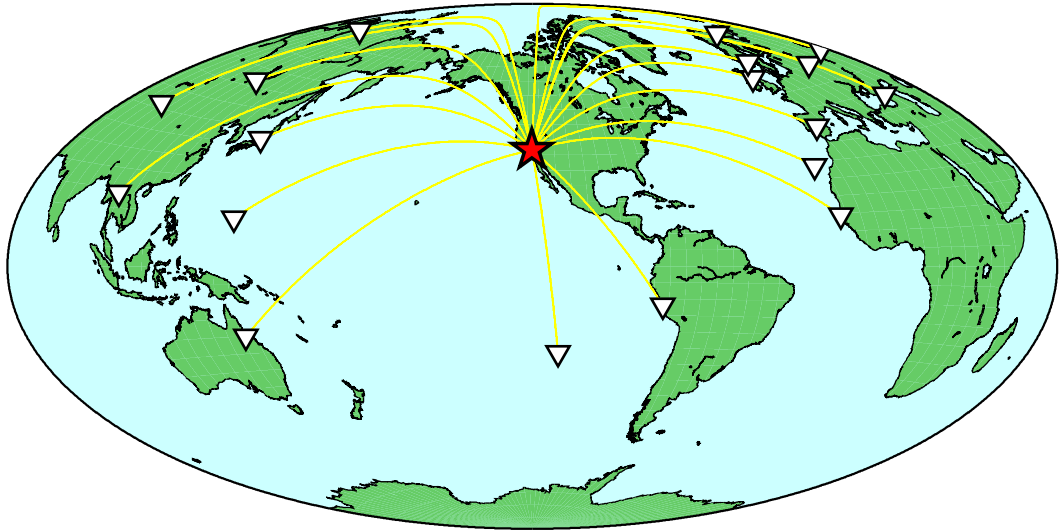


Figure 4.4: Distribution of stations (white triangles) with respect to the M_w 6.1 Eureka Valley earthquake (red star), where the ray paths are shown in yellow.

4.3.1.1 Long Period Surface Waves

Only comparisons for vertical component data from 18 stations are investigated here as the transverse and longitudinal components for the majority of stations are too noisy. Figure 4.4 shows the distribution of stations used in the comparisons. We carry out comparisons between real data and 1-D Earth and 3-D Earth theoretical seismograms for a variety of earthquake source models: (i) ICMT; (ii) GCMT; (iii) GCMT model combined with the ICMT centroid latitude and longitude estimates ($GCMT_{lat/lon}$); and, (iv) GCMT model

combined with the ICMT strike ($\text{GCMT}_{\text{strike}}$).

Initial comparisons of the ICMT and GCMT synthetic waveforms with the data show that synthetics calculated in the 3-D Earth model (S20RTS) fit the data better than those calculated using PREM; there are evident phase shifts when assuming a 1-D Earth structure (see, *e.g.*, stations NNA, ARU, Figure 4.5). Consequently, the waveform misfit for PREM calculations is twice as large as that for synthetics calculated using a 3-D Earth model, with the ICMT solution showing the best overall fit to the observed waveforms ($m^2 = 0.17$; see Table 4.2). In order to investigate whether the poorer fit of the GCMT synthetics is due to the 55 km mislocation of the event, the GCMT latitude and longitude are replaced with those from the ICMT solution (3-D $\text{GCMT}_{\text{lat/lon}}$ in Table 4.2, and Figure 4.5). Compared to the original GCMT solution, there is an improvement in the fit in phase to the data (~ 3 s) resulting in a lower overall misfit ($m^2 = 0.22$), but this remains a poorer fit than that attained with the ICMT solution.

There is also a large difference of 30° in strike between the ICMT and the GCMT solutions, which could also explain the difference in the fit of the synthetics to the data. For moderate magnitude events, visual examination of an interferogram can provide strong constraints on the strike of the fault, as is the case for the the Eureka Valley earthquake (see Figure 4.3b). Therefore, similar to the investigation of location, the GCMT strike (210°) is replaced by the ICMT estimate (172°). However, in this case, the fit to the data deteriorates (Table 4.2, 3-D $\text{GCMT}_{\text{strike}} - m^2 = 0.29$) in comparison with that for the original GCMT solution ($m^2 = 0.24$). Consequently, in addition to strike, the GCMT latitude, longitude are also replaced by the ICMT location, which results in a lower data misfit ($m^2 = 0.23$), but it is still a higher misfit than when only using the ICMT centroid location along with all other GCMT source parameters. Additional tests, including replacing the dip and rake in the GCMT solution also show little improvement in the fit to the observed data. It appears that it is the combination of all the parameters in the ICMT solution which best explain the observed long period surface waves.

It must be noted that 3-D synthetics were also calculated using the recently published S40RTS, an improvement of S20RTS. However, the differences in fit of the synthetics to the data relative to the S20RTS synthetics are relatively small (Table 4.2). Thus, for the remaining earthquakes, only 3-D synthetics calculated using S20RTS are referred to.

Also in some cases the changes/differences in waveforms are very subtle, especially when considering single figure phase shifts for long period surface waves, in which case the values given in the table are more instructive than the figures. This is particularly relevant for the subsequent four earthquakes when investigating the influence of centroid location.

Table 4.2: Summary of average phase ($\delta\Psi$), amplitude (δA) and waveform misfits (m^2) for comparisons between the vertical component (Z) of synthetic and observed surface waves (LPS, $T \sim 150$ s) and body waves (LPB, $T \sim 50$ s) for the Eureka Valley, M_w 6.1, 17th May 1993 event. The number of waveforms, n , used to calculate the average misfits are given in brackets at the top of each column. Parameters in subscript in the first column refer to those that have been replaced by estimates from the other solution (ICMT or GCMT), where location refers to latitude, longitude and depth. The last two lines refer to synthetics calculated using the S40RTS Earth model. The solution highlighted in bold refers to the solution which shows the lowest overall misfit. If the data and synthetics match perfectly then $\delta\Psi = 0.0$, $\delta A = 1.0$ and $m^2 = 0.0$.

Synthetics	LPS Z (n=18)			LPB Z (n=18)		
	$\delta\Psi$	δA	m^2	$\delta\Psi$	δA	m^2
1-D GCMT	18.44	0.90	0.59	2.44	0.96	0.49
1-D ICMT	14.65	0.91	0.45	1.95	1.12	0.44
3-D GCMT	8.72	0.94	0.24	3.73	0.55	1.45
3-D ICMT	6.13	0.98	0.17	1.08	0.84	0.32
3-D GCMT <i>depth</i>	10.73	0.80	0.39	3.11	0.79	0.57
3-D GCMT <i>lat/lon</i>	5.63	0.95	0.22	2.02	0.52	1.05
3-D GCMT <i>location</i>	6.55	0.81	0.34	1.71	0.81	0.38
3-D GCMT <i>strike</i>	11.51	1.11	0.29	2.72	0.54	0.96
3-D GCMT <i>strike/location</i>	7.05	1.10	0.23	1.95	0.54	0.88
3-D GCMT (s40rts)	9.80	0.94	0.26	3.75	0.52	1.45
3-D ICMT (s40rts)	6.47	0.98	0.20	1.10	0.84	0.32

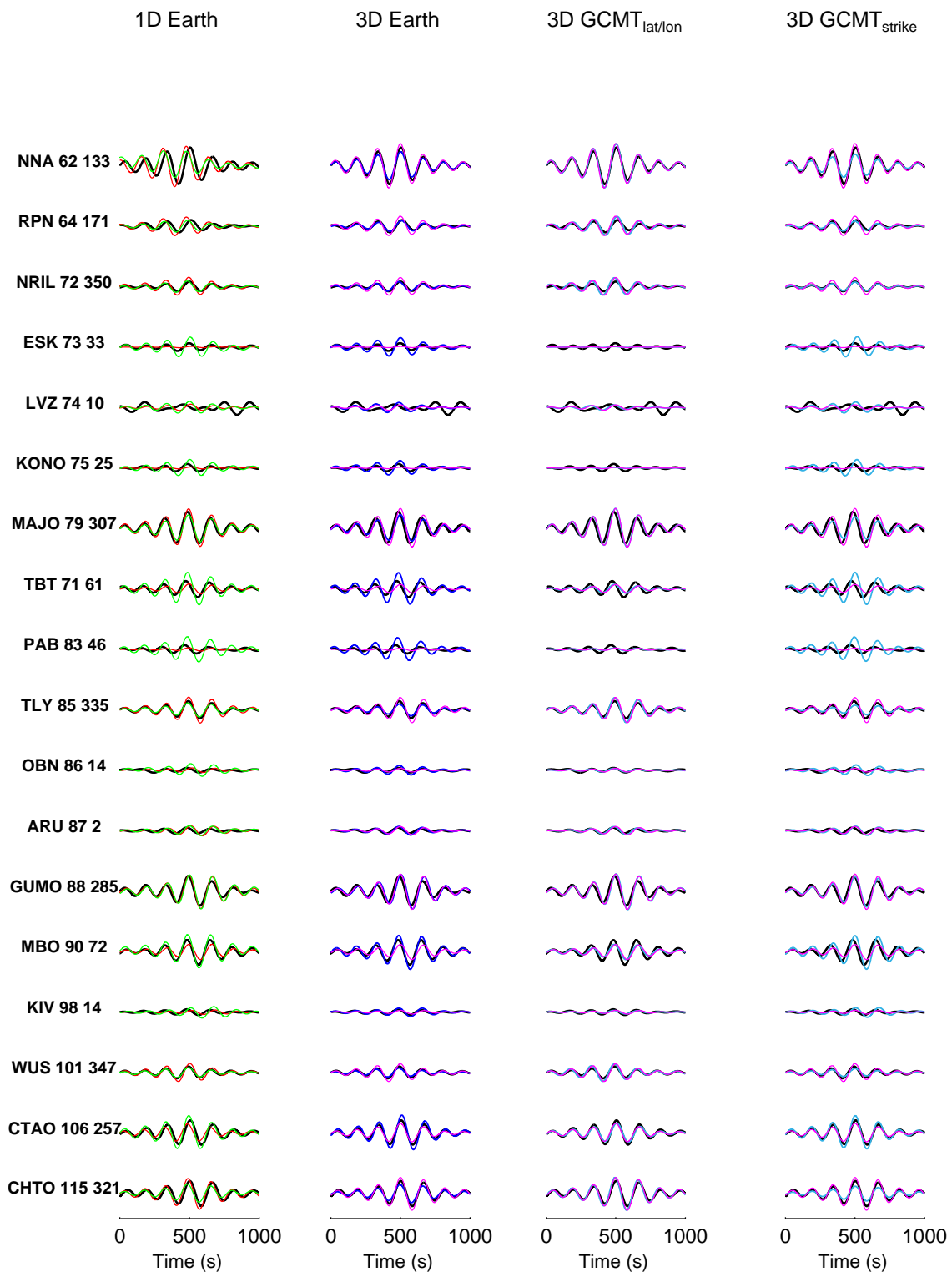


Figure 4.5: Comparisons of observed vertical component surface waves ($T \sim 150$ s) for the M_w 6.1 Eureka Valley earthquake (black) with synthetics calculated in a 1-D Earth (PREM) using GCMT (red) and ICMT (green) source parameters (1-D Earth), and for a 3-D Earth (S20RTS combined with CRUST 2.0) using GCMT (pink) and ICMT (blue) source parameters (3-D Earth). The two right hand side columns compare synthetics calculated in a 3-D Earth using GCMT solutions (pink) where specific GCMT source parameters have been replaced with ICMT estimates (light blue): latitude and longitude (3-D GCMT $_{lat/lon}$) and strike (3-D GCMT $_{strike}$). The waveforms are sorted by epicentral distance (first number after station name) and a range of azimuths (second number) are investigated; this convention is used throughout the waveform comparison figures in this chapter.

4.3.1.2 Long Period Body Waves

As explained previously, Eureka Valley is the only event for which comparisons of long period body waves are possible with the data available. Similar to the long period surface wave comparisons, the ICMT solution combined with a 3-D Earth model leads to the best fit to the data. The fit in phase is better than for long period surface waves ($\delta\Psi = 1.08$ s, 3-D ICMT in Table 4.2) but the amplitude is overestimated ($\delta A = 0.84$) which leads to a slightly higher overall misfit ($m^2 = 0.32$) than for surface waves.

Unexpectedly synthetics calculated using the GCMT solution and assuming a 3-D Earth structure significantly overestimate the amplitude of the P-wave arrival (Figure 4.6, 3-D Earth), leading to a waveform misfit that is more than double that for the 1-D Earth case. The fit to the body waves assuming a 3-D Earth structure is improved if the GCMT latitude and longitude are replaced by the ICMT estimates; specifically, a 1 s reduction in phase misfit results in a better waveform misfit, but it is still significantly large (*i.e.*, greater than 1). The largest improvement is seen if the depth is replaced by the shallower ICMT estimate (8 km); the amplitude fit is much improved and the waveform misfit is reduced to less than 1 ($m^2 = 0.57$; 3-D GCMT_{depth} in Figure 4.6 and Table 4.2). If the ICMT latitude, longitude and depth are all used, then the fit to the data is further improved and the overall misfit is much reduced ($m^2 = 0.38$; see Table 4.2).

Contrary to the surface wave results, if the ICMT strike is used instead of the GCMT value then the fit to the data improves, especially the phase misfit (Table 4.2, 3-D GCMT_{strike}). However, if the ICMT strike is used in combination with the ICMT location then the overall waveform misfit worsens.

Overall, despite investigating various source parameter combinations, theoretical seismograms calculated using the ICMT solution combined with a 3-D Earth lead to the best data fit for both long period surface and body waves.

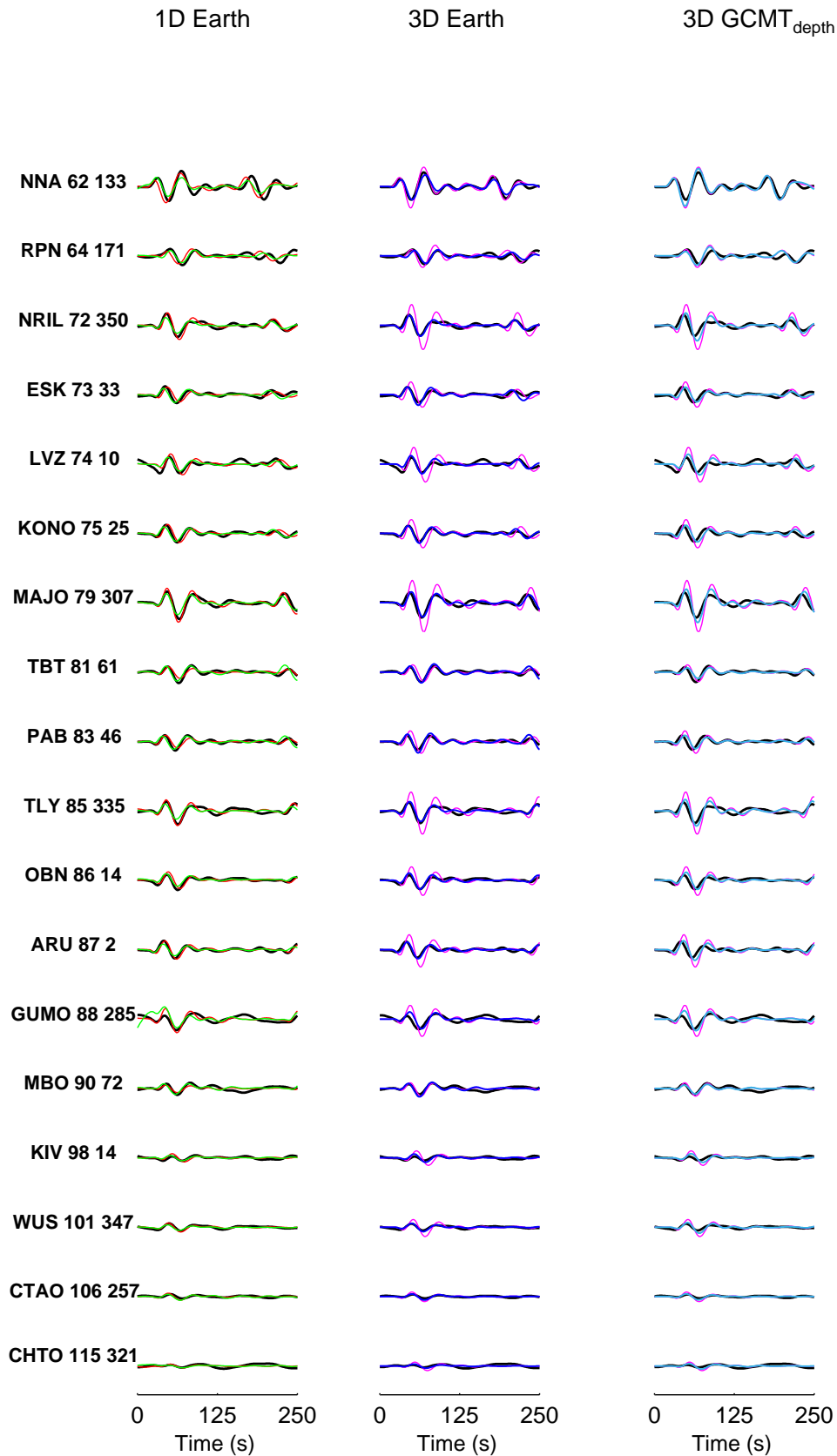


Figure 4.6: Comparisons of real vertical component body waves ($T \sim 50$ s) from the M_w 6.1 Eureka Valley earthquake (black) with synthetics calculated in a 1-D Earth using GCMT (red) and ICMT (green) source parameters (1-D Earth) and a 3-D Earth using GCMT (pink) and ICMT (blue) source parameters. The rightmost column (3-D GCMT_{depth}) compares the GCMT solution (pink) and GCMT solution with the depth replaced by the ICMT estimate (light blue).

4.3.2 Large strike-slip event: Landers, M_w 7.3, 28th June 1992

This was the first large earthquake to be fully investigated using InSAR data and provided a unique opportunity to investigate the rupture process of a large continental strike-slip event (*e.g.* Peltzer *et al.*, 1994; Zebker *et al.*, 1994). The earthquake ruptured five major faults (Johnson Valley, Landers, Homestead Valley, Emerson and Camp Rock faults; see Figure 3.9 in Chapter 3) located in the ECSZ, which is responsible for 15% of the relative plate motion (Sieh *et al.*, 1993). There is variation between multiple existing source rupture models (*e.g.* Cohee and Beroza, 1994; Wald and Heaton, 1994; Cotton and Campillo, 1995; Fialko, 2004b), but the majority suggest an unilateral rupture initiating on the Johnson Valley fault and propagating north-westwards up to Camp Rock and Emerson faults.

There is general good agreement between the ICMT and GCMT source models (see Table 4.3) and both the locations are relatively consistent with the mapped location of the faults thought to have ruptured during the event. However, the GCMT location is towards one end of the rupture and is 25 km further north from the ICMT location (see Figure 3.9). Due to the large magnitude of this event, seismic data from 18 stations (Figure 4.7) and all three components (vertical, transverse and longitudinal) are analysed and all show the same trends unless stated otherwise. Therefore, it must be noted that any misfit values referred to correspond to the vertical component. Any waveform comparisons for additional seismic data components not shown can be found in Appendix B, Figure B.1.

Table 4.3: Summary of source parameters for the Landers earthquake (M_w 7.3, 28th June 1992) from an InSAR study (Fialko, 2004) and the GCMT catalogue. The latitude, longitude and depth refer to the centroid location.

Parameter	Fialko (2004)	GCMT
Mw	7.28	7.30
Mo ($\times 10^{18}$ Nm)	103.0	106.0
Lat ($^{\circ}$)	34.450	34.650
Lon ($^{\circ}$)	-116.517	-116.650
Depth (km)	5.5	15.0
Strike ($^{\circ}$)	154.1	341.0
Dip ($^{\circ}$)	89.9	70.0
Rake ($^{\circ}$)	173.9	-172.0

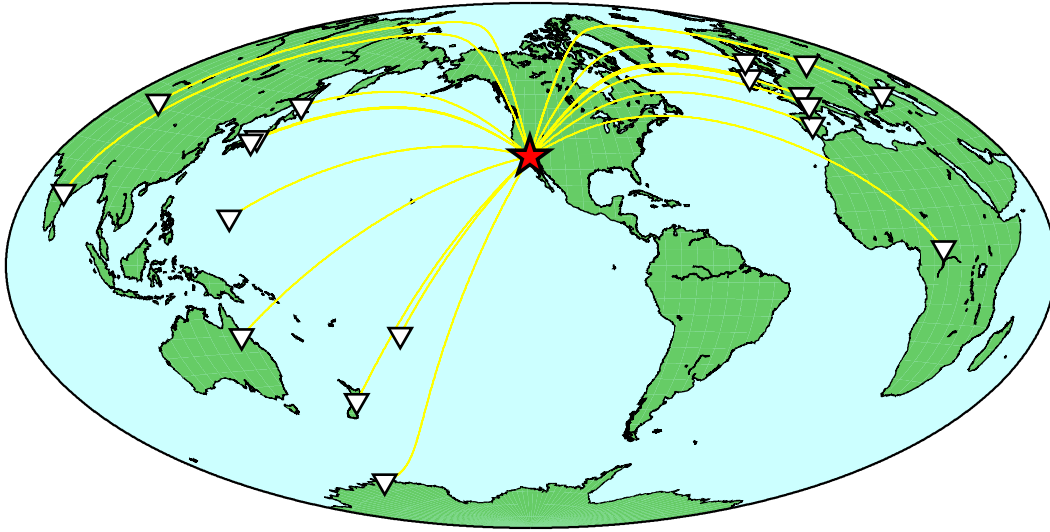


Figure 4.7: Distribution of stations used (white triangles) with respect to the M_w 7.3 Landers earthquake (red star), where ray paths are shown in yellow.

4.3.2.1 Long Period Surface Waves

Theoretical seismograms calculated using the GCMT solution for the 3-D Earth model show the best fit to the data (see, *e.g.*, stations OBN and BNG in Figure 4.8), with an overall waveform misfit value of $m^2=0.16$ (3-D GCMT in Table 4.4). A potential reason for the best fit of the long-period surface waves by the GCMT synthetics could be the fact that the GCMT solution is built using these data. Considering the large discrepancy in centroid location both ICMT and GCMT estimates are tested. Replacing the GCMT value with the latitude and longitude from the variable slip model in Fialko (2004b) results in a worse fit to the data (Table 4.4, 3-D GCMT_{lat/lon}), particularly in phase, where a 2 s increase in misfit is observed. Conversely a 2 s reduction in phase misfit is seen if the GCMT latitude and longitude are used with the ICMT solution (3-D ICMT_{lat/lon} in Figure 4.8, Table 4.4, 3-D ICMT_{lat/lon}).

The depth reported by Fialko (2004b) is also very shallow (~ 5 km) and the GCMT is unable to resolve depths shallower than 12 km. Therefore the GCMT depth is replaced with the estimate from Fialko (2004b) but the fit to the data is reduced (Table 4.4, 3-D GCMT_{depth}). Moreover if the depth in the ICMT solution is increased to 15 km then the fit to the data improves (Table 4.4, 3-D ICMT_{depth}) suggesting that the 5 km estimate may be too shallow. Consequently if the depth, latitude and longitude in the GCMT solution

are replaced by the ICMT estimates this results in the solution which shows the highest overall misfit ($m^2 = 0.27$) of all the source parameter combinations tested (Table 4.4, 3-D GCMT_{location}). Interestingly though if the dip in the GCMT solution is increased to a more vertical angle, as seen in the Fialko (2004b) source model, then the average perfect fit in amplitude is achieved ($\delta A = 1.0$, Table 4.4, 3-D GCMT_{dip}) but there is an increase in phase misfit.

Table 4.4: Summary of average phase ($\delta\Psi$), amplitude (δA) and waveform misfits (m^2) for comparisons between synthetic and observed surface waves ($T \sim 150$ s) for the M_w 7.3 Landers earthquake, where results for the vertical (Z), transverse (T) and longitudinal (L) components are shown. Format is same as in Table 4.2

Synthetics	Z (n=18)			T (n=17)			L (n=16)		
	$\delta\Psi$	δA	m^2	$\delta\Psi$	δA	m^2	$\delta\Psi$	δA	m^2
1-D GCMT	11.66	1.51	0.32	12.30	1.10	0.25	13.38	1.63	0.36
1-D ICMT	14.28	0.92	0.52	12.71	1.07	0.27	14.40	0.96	0.56
3-D GCMT	7.09	1.07	0.16	5.24	1.04	0.08	8.03	1.14	0.14
3-D ICMT	9.85	0.88	0.26	5.57	1.06	0.14	10.08	0.93	0.23
3-D ICMT _{depth}	9.95	1.27	0.22	5.66	1.06	0.14	9.88	1.05	0.21
3-D GCMT _{depth}	7.89	0.97	0.20	5.67	1.04	0.10	8.29	1.03	0.16
3-D GCMT _{lat/lon}	9.12	1.07	0.23	6.09	1.04	0.09	9.77	1.14	0.21
3-D GCMT _{location}	9.40	0.97	0.27	5.96	1.04	0.09	10.02	1.03	0.23
3-D GCMT _{dip}	7.88	1.00	0.20	5.80	1.06	0.13	8.19	1.07	0.16
3-D ICMT _{lat/lon}	7.90	0.87	0.19	5.95	1.05	0.14	7.99	0.93	0.15
3-D GCMT (s40rts)	7.09	1.07	0.16	5.24	1.04	0.08	8.04	1.14	0.14
3-D ICMT (s40rts)	9.85	0.88	0.26	5.57	1.06	0.14	10.09	0.93	0.23

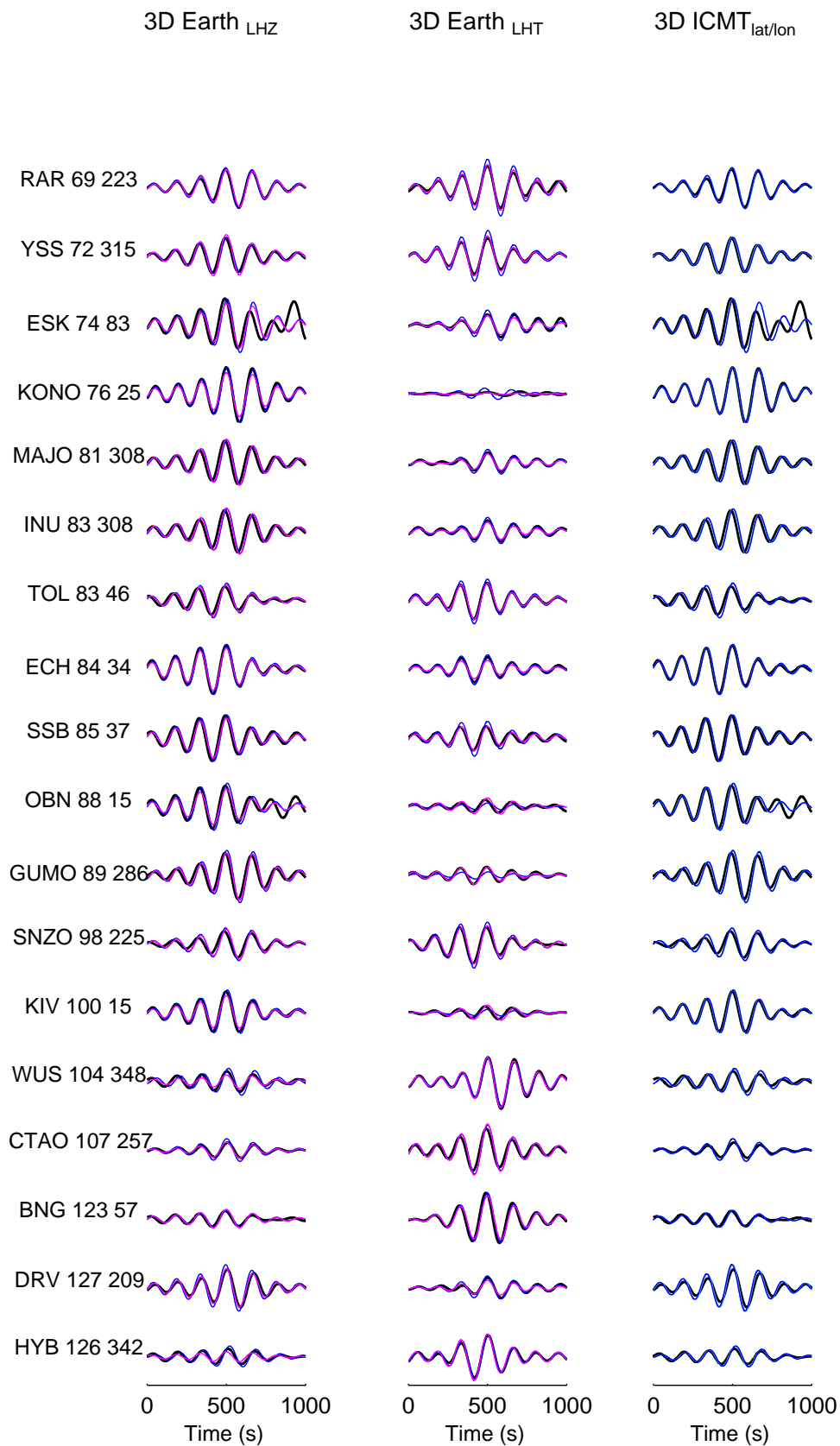


Figure 4.8: Comparisons of observed surface waves for the M_w 7.3 Landers earthquake (black) with synthetics calculated in a 3-D Earth using GCMT (pink) and ICMT (blue) source parameters, for vertical (3-D Earth_{LHZ}) and transverse components (3-D Earth_{LHT}). The rightmost hand side column (3-D Earth ICMT_{lat/lon}) compares ICMT synthetics (blue) with synthetics calculated using ICMT source parameters combined with GCMT centroid latitude and longitude (light blue).

4.3.3 Multiple InSAR Models: Izmit, M_w 7.5, 17th August 1999

On 17th August 1999 the Izmit earthquake ruptured nearly 150 km (*e.g.* Barka *et al.*, 2002; Çakir *et al.*, 2003) of a splay of the North Anatolian Fault (NAF), which separates the Eurasian and Anatolia plates (Fig 4.9). The earthquake occurred in the western end of the NAF where the fault splays into three main sections, north, middle and south. Average slip rates for this region range from 10 mm yr⁻¹ from geological measurements (Polonia *et al.*, 2004; Gasperini *et al.*, 2011b) to 24 mm yr⁻¹ from geodetic measurements (*e.g.*, McClusky *et al.*, 2000), where the northern splay accommodates 70–90% of this relative plate motion (Armijo *et al.*, 2002).

This earthquake was the seventh in a sequence of events migrating east-west on the NAF (Barka, 1996; Stein *et al.*, 1997), 32 years after the most recent earthquake (Mudurnu Valley, M 7.1, 22nd July 1967). It is the only region in the world where this type of seismic behaviour is observed and the Izmit earthquake was the first opportunity where large volumes of data were available, including geodetic and strong motion data. Consequently, there are multiple source models for this event. Similar to the Landers earthquake, the existing studies show a large variation in the slip distribution, partly due to the different datasets used. Specifically, there is debate regarding the termination of the western end of the rupture, with field observations (Barka *et al.*, 2002) indicating that the rupture only reached the eastern side of the Heselk Delta, whereas various geodetic studies, including the solutions investigated here (Wright, 2000; Wright *et al.*, 2001a; Delouis *et al.*, 2002; Çakir *et al.*, 2003), suggest that the rupture extends further into the Sea of Marmara. Recent high resolution bathymetric data suggests that the rupture terminated in between these two locations, in the Darcia Basin (Gasperini *et al.*, 2011a). Thus, understanding the uncertainty surrounding the source parameters for this earthquake is key for interpreting the future seismic hazard in this region, including the risk for city of Istanbul (Barka, 1999; Parsons *et al.*, 2000; Atakan *et al.*, 2002). Here the discrepancy in centroid location between three studies taken from the ICMT database, one uniform slip (Wright, 2000), and two distributed slip models (Delouis *et al.*, 2002; Çakir *et al.*, 2003), and that reported in the GCMT catalogue is investigated. All three InSAR studies are in good agreement, as was seen in section 3.3.4 (Figure 3.12), but the GCMT location lies ~ 30 km north of the InSAR locations.

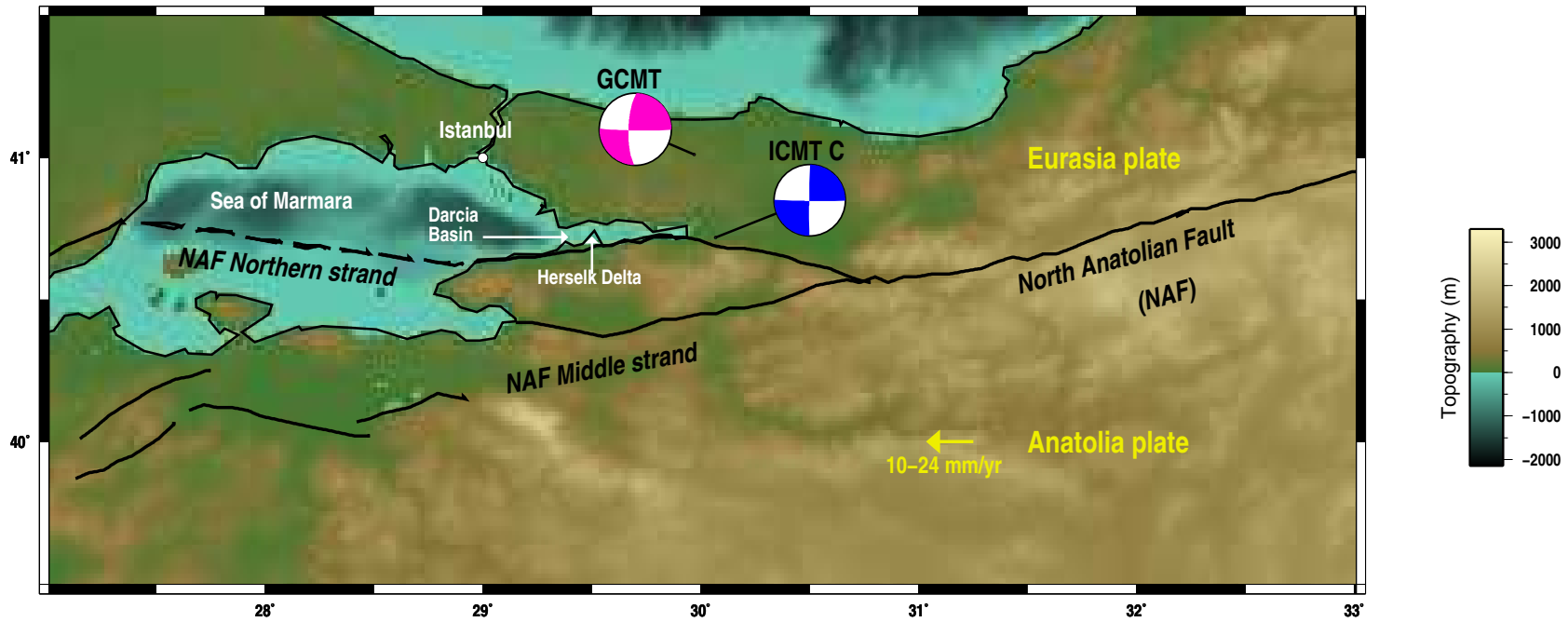


Figure 4.9: Tectonic setting of the Izmit earthquake on the North Anatolian fault (black line), which separates the Eurasia and Anatolia plates in Turkey. The focal mechanism from the GCMT catalogue (pink) and that based on the source model from Çakir *et al.* (2003) (blue) are shown. The fault locations are based on data from (Saroglu *et al.*, 1992) and the files are courtesy of Richard Walters.

Table 4.5: Summary of source parameters for the Izmit, Turkey earthquake (17th August 1999, M_w 7.5) from the GCMT catalogue and three InSAR studies by Çakir *et al.* (2003), Delouis *et al.* (2002) and Wright (2000). Values in bold were fixed during the inversions and the latitude, longitude and depth refer to the centroid location.

Parameter	Çakir <i>et al.</i> (2003)	Delouis <i>et al.</i> (2002)	Wright (2000)	GCMT
M_w	7.50	7.52	7.54	7.60
M_0 ($\times 10^{18}$ Nm)	190.0	240.0	253.6	288.0
Lat ($^\circ$)	40.719	40.724	40.728	41.01
Lon ($^\circ$)	30.067	30.214	30.050	29.97
Depth (km)	6.99	7.90	10.80	17.00
Strike ($^\circ$)	90.7	267.6	271.2	91.0
Dip ($^\circ$)	88.3	85.0	89.7	87.0
Rake ($^\circ$)	178.7	179.6	-173.1	164.0

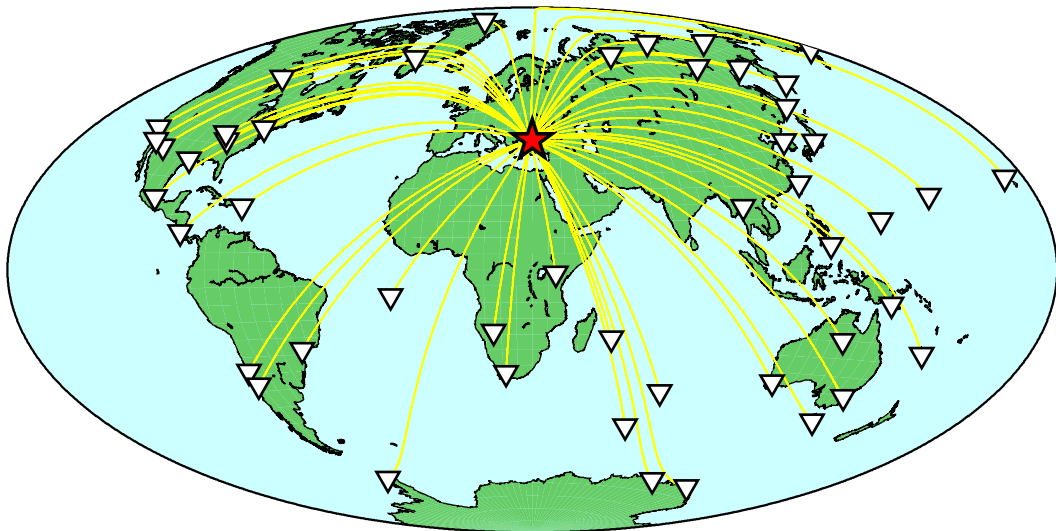


Figure 4.10: Distribution of stations (white triangles) used with respect to the M_w 7.5 Izmit earthquake (red star), where the great circle paths are shown in yellow.

4.3.3.1 Long Period Surface Waves

This event occurred several years after the two previously discussed earthquakes and during that time the density of stations in the global seismic networks increased significantly. Thus, the number of stations used for comparisons here is almost double that used in the previous analyses in this chapter (43 stations are used; see Figure 4.10). We are able to compare waveforms for all three components and the misfit values shown in Table 4.5 correspond to calculations using all the stations; however, for clarity, comparisons only

for the vertical component and for 20 stations are shown (Fig 4.11). Similar to Landers the trends are consistent across all components and the longitudinal and transverse components are shown in Appendix B, Figures B.2 & B.3.

The distributed slip model from Çakir *et al.* (2003) combined with a 3-D Earth model shows the best fit to the observed waveforms (3-D ICMT C in Table 4.6), compared to the GCMT model and to the other InSAR source models. The average phase misfit ($\delta\Psi = 6.7$ s) is slightly larger than the 5.0 s calculated for the GCMT solution, but the amplitude and overall waveform misfit values are smaller, where $\delta A=0.96$ and $m^2=0.18$ (Table 4.6 and Figure 4.11, 3-D Earth). The GCMT solution appears to overestimate the amplitude by approximately 20% ($\delta A = 0.79$), which is potentially due to the larger moment estimate, being the highest value of all solutions (Table 4.5). Replacing the GCMT seismic moment with the estimate from Çakir *et al.* (2003) reduces the amplitudes, and on average they are systematically smaller than the data, with the overall misfit being lower than the original solution from Çakir *et al.* (2003) (see 3-D GCMT_{Mo} in Figure 4.11 and Table 4.6).

To investigate further the poorer fit of the GCMT solution, the centroid latitude and longitude are replaced with those from the ICMT solution (Figure 4.11, 3-D GCMT_{lat/lon}). The resulting fit to the data is worse, with both the amplitude and phase misfit increasing, resulting in an overall waveform misfit of $m^2=0.37$ (Table 4.6, 3-D GCMT lat/lon). This is unexpected as all three ICMT locations are consistent with the geological location of the North Anatolian Fault (NAF) on which the Izmit earthquake occurred and agree with the east-west bilateral rupture observed in various kinematic models, whereas the GCMT location is 30 km north of the fault and suggests a north-south rupture propagation (see section 3.3.4 for further details). If the latitude and longitude in the Çakir *et al.* (2003) solution are replaced with those from the GCMT solution this results in synthetics which show the best fit to the data compared with all the other solutions ($m^2 = 0.14$; see 3-D ICMT_{lat/lon} in Table 4.6 and Figure 4.11).

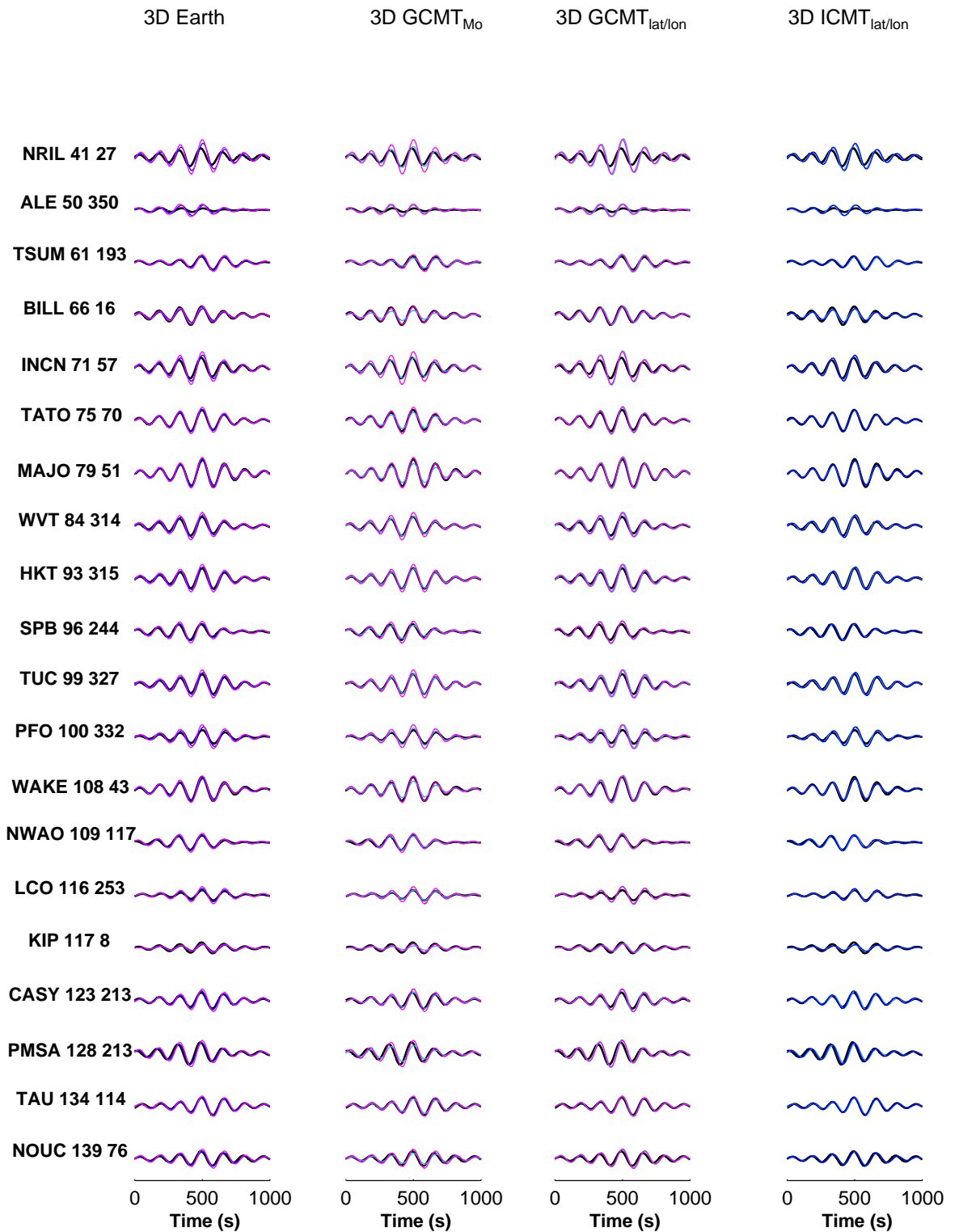


Figure 4.11: Comparisons of the vertical component of observed long period surface waves ($T \sim 150$ s) for the M_w 7.5 Izmit earthquake (black) with synthetics calculated in a 3-D Earth using GCMT (pink) and ICMT C (blue) source parameters (3-D Earth). 3-D GCMT $_{Mo}$ compares GCMT synthetics (pink) with the same solution except that the moment is replaced by the estimate from $\text{\u00c7}akir et al. (2003)$ (light blue). 3-D GCMT $_{lat/lon}$ follows the same format except the light blue synthetics refer to the GCMT solution with the latitude and longitude replaced by estimates also from $\text{\u00c7}akir et al. (2003)$. The far right column compares ICMT synthetics (blue) with the ICMT solution where the latitude and longitude are replaced by those from the GCMT catalogue (light blue).

Table 4.6: Summary of average phase ($\delta\Psi$), amplitude (δA) and waveform misfits (m^2) for comparisons between synthetic and observed surface waves ($T \sim 150$ s) for the M_w 7.5 Izmit earthquake. ICMT C refers to the study by Çakir *et al.* (2003), ICMT D corresponds to the study by Delouis *et al.* (2002) and ICMT W refers to results from Wright (2000). The table headings and format is the same as in Table 4.2.

Synthetics	Z (n=43)			T (n=40)			L (n=41)		
	$\delta\Psi$	δA	m^2	$\delta\Psi$	δA	m^2	$\delta\Psi$	δA	m^2
1-D GCMT	9.98	0.83	0.51	14.47	0.86	0.70	10.79	0.89	0.92
1-D ICMT C	13.05	1.08	0.49	16.14	1.18	0.48	13.75	1.11	0.76
1-D ICMT D	14.77	0.90	0.66	16.90	0.97	0.67	14.29	0.89	0.93
1-D ICMT W	12.79	0.85	0.67	17.24	1.49	0.72	13.52	0.89	0.96
3-D GCMT	5.00	0.79	0.23	5.41	0.73	0.41	5.37	0.86	0.22
3-D ICMT C	6.68	0.96	0.18	8.54	1.00	0.15	7.31	1.05	0.19
3-D ICMT D	7.23	0.79	0.30	5.18	0.78	0.26	7.79	0.86	0.28
3-D ICMT W	6.48	0.76	0.33	5.85	0.78	0.36	7.09	0.83	0.29
3-D GCMT _{Mo}	5.99	1.21	0.15	5.94	1.11	0.12	6.40	1.33	0.19
3-D ICMT_{lat/lon}	5.76	1.01	0.14	5.61	1.04	0.13	6.36	1.11	0.17
1-D ICMT _{lat/lon}	10.07	1.08	0.34	13.92	1.19	0.37	10.79	1.12	0.36
3-D GCMT _{lat/lon}	7.60	0.76	0.37	6.82	0.73	0.49	8.13	0.83	0.26

4.3.4 Large Subduction Zone event: Pisco, M_w 8.1, 15th August 2007

Large subduction earthquakes frequently occur off the coast of South America coast due to the subduction of the Nazca plate beneath the South American plate. Rates of convergence vary with latitude due to the rotation of the Nazca plate relative to the South American craton and increase towards the south (*e.g.* Kendrick *et al.*, 2003), with rates from various studies ranging from 61 mm yr⁻¹ to 68 mm yr⁻¹ (*e.g.* Sella *et al.*, 2002; Kendrick *et al.*, 2003; Vigny *et al.*, 2009).

The south American subduction zone along the coast of Peru can be split into three zones – north, central and south – which exhibit different types of seismic behaviour, mainly due to the latitudinal variation in the trench geometry. The central zone shows the most complex behaviour (Dorbath *et al.*, 1990) and is where the 2007 Pisco earthquake occurred in a seismic gap, and where the previous large event was a tsunami earthquake in 1746 that destroyed the city of Lima. This was followed by 200 years of quiescence and activity resumed in 1940. Geodetic estimates of interseismic moment deficit and coseismic moment release due to the four events since 1940 suggests that this section could have the potential generate an earthquake of M_w 8.5–8.7 (Chlieh *et al.*, 2011).

The Pisco event occurred in an interesting location due to the variation in strike along the rupture length due to a kink in the coastline; Sladen *et al.* (2010) have shown the coseismic slip distribution to follow the coastline. However, there is still a debate regarding the number of asperities involved in the event. Teleseismic studies (Ji and Zeng, USGS, 2007) suggest two sub-events, whereas geodetic studies (Motagh *et al.*, 2008) and models based on multiple geodetic and seismic datasets (Pritchard and Fielding, 2008; Biggs *et al.*, 2009) all suggest a single patch of slip, although it has been argued that at the depths for this earthquake the InSAR data have no power to resolve between one or two asperities (Biggs *et al.*, 2009). A study which used tsunami waveforms as well as InSAR and teleseismic data found that one or two patches both explain the data well and the issue remains unresolved (Sladen *et al.*, 2010). Nevertheless, the South American subduction zone is one of the few places where InSAR data can be used to investigate these types of earthquakes and has proven extremely useful in constraining the spatial slip distribution of the event.

Locations for earthquakes in this region that are reported in the GCMT catalogue are

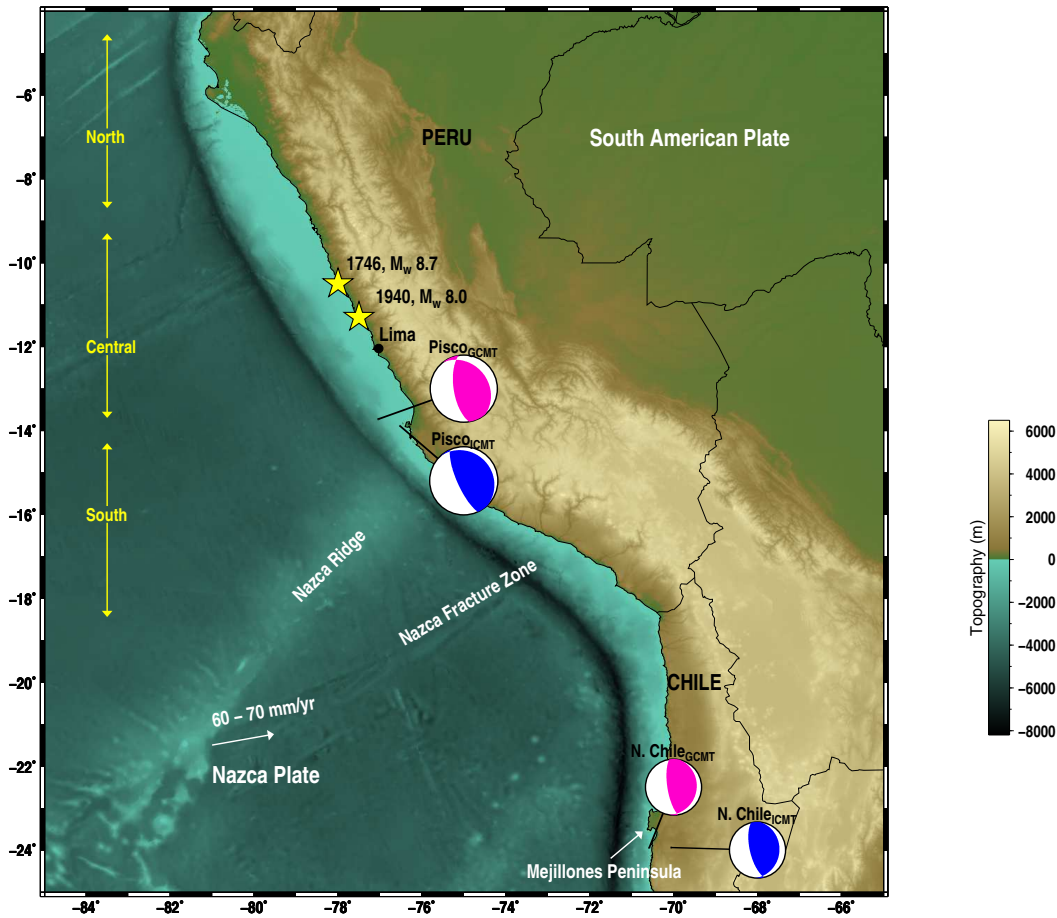


Figure 4.12: Section of the South American subduction zone from -4° S to -25° S, where the north, central and southern zones of the Peru section are shown in yellow. The focal mechanisms of the two subduction zone events studied are shown: Pisco, M_w 8.1 and northern Chile M_w 6.6. The yellow stars denote the locations of two of the largest earthquakes to occur off the coast of Peru. Features of the subduction zone relevant to the earthquakes are highlighted, including the Nazca Ridge and the Mejillones Peninsula, and the trench is highlighted in black.

systematically shifted westwards towards the trench (Chapter 3, section 3.3, and Syracuse and Abers, 2009); in this case there is nearly 60 km between the ICMT and GCMT locations, where the ICMT location is from Pritchard and Fielding (2008). Moreover, the InSAR-determined seismic moment is also nearly twice as large as the moment reported in the GCMT catalogue (see Table 4.7). It should be noted that despite previously referring to several geodetic models for this event (*e.g.* Motagh *et al.*, 2008; Biggs *et al.*, 2009; Sladen *et al.*, 2010) only the model from Pritchard and Fielding (2008) is used in the comparisons. This is because at the time of calculating the synthetics this was the only model for which a full set of source parameters for, including centroid location was available.

Table 4.7: Summary of source parameters for the Pisco, Peru earthquake (M_w 8.1, 15th August 2007) from one InSAR study by Pritchard and Fielding (2008) and from the GCMT catalogue. Values in bold were fixed during the inversion and the latitude, longitude and depth refer to the centroid.

Parameter	Pritchard and Fielding (2008)	GCMT
Mw	8.12	8.0
Mo ($\times 10^{18}$ Nm)	1900.0	1210.0
Lat ($^\circ$)	-13.89	-13.73
Lon ($^\circ$)	-76.52	-77.04
Depth (km)	30.0	33.8
Strike ($^\circ$)	316.0	321.0
Dip ($^\circ$)	16.4	28.0
Rake ($^\circ$)	71.0	63.0

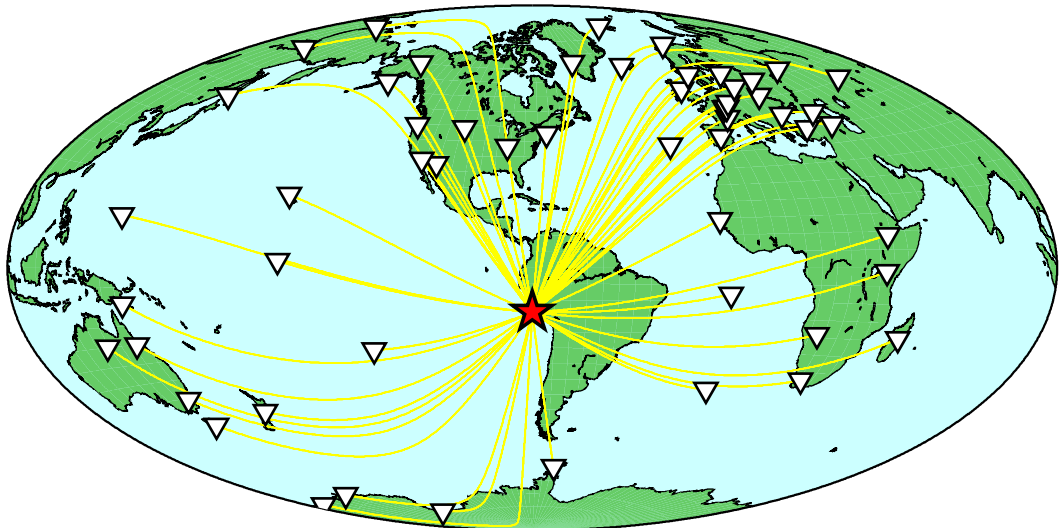


Figure 4.13: Distribution of the seismic stations (white triangles) relative to the M_w 8.1 Pisco earthquake (red star), where ray paths are shown in yellow.

4.3.4.1 Long Period Surface Waves

Three-component long-period surface waves recorded by 57 global stations (see Figure 4.13) are analysed, again trends are consistent across all components and the transverse and longitudinal comparison figures can be found in Appendix B, Figures B.4 & B.5.

The synthetics calculated in a 3-D Earth model using the GCMT solution show the best fit to the data (3-D GCMT, Table 4.8). The amplitude of the ICMT synthetics are systematically too large (see 3-D Earth column in Figure 4.14, *e.g.*, for stations SSB and TAU), which is potentially due to an overestimation of the seismic moment by the

InSAR data. As seen in Chapter 2, for large subduction zone events, deformation due to significant afterslip and viscoelastic relaxation can contaminate the interferogram if it spans a large period of postseismic activity. If the seismic moment in the ICMT solution is replaced with the GCMT estimate, the amplitude misfit is greatly reduced; in fact, for the majority of stations the synthetic amplitudes are systematically too small ($\delta A = 1.06$, 3-D ICMT_{Mo} in Table 4.8) but the overall fit is improved.

Despite the systematic mislocation of the GCMT solutions for events in the south American subduction zone, replacing the latitude and longitude in the GCMT solution with values from the ICMT database does not improve the fit to the data (3-D GCMT_{lat/lon} in Figure 4.14 and Table 4.8). In contrast replacing the ICMT latitude, longitude and seismic moment with the GCMT estimates results in synthetics which fit the data almost as well as the original GCMT solution (3-D ICMT_{lat/lonmo} in Figure 4.14 and Table 4.8).

Table 4.8: Summary of average phase ($\delta\Psi$), amplitude (δA) and waveform misfits (m^2) for comparisons between synthetic and observed surface waves ($T \sim 150s$) for the M_w 8.1 Pisco earthquake. Results for all three components vertical (Z), transverse (T) and longitudinal (L) are shown, and the solution in bold refers to the overall best fitting solution.

Synthetics	Z (n=55)			T (n=48)			L (n=53)		
	$\delta\Psi$	δA	m^2	$\delta\Psi$	δA	m^2	$\delta\Psi$	δA	m^2
1-D GCMT	10.44	0.81	0.32	13.21	0.92	0.61	11.02	0.83	0.37
1-D ICMT	10.92	0.61	0.81	16.17	0.92	0.81	14.32	0.81	0.77
3-D GCMT	5.76	0.91	0.11	6.43	0.80	0.29	5.61	0.93	0.13
3-D ICMT	10.48	0.63	0.80	8.83	0.82	0.59	9.29	0.65	0.64
3-D ICMT _{Mo}	10.69	1.06	0.22	8.83	1.39	0.26	9.28	1.11	0.18
3-D ICMT _{Mo/dip}	7.18	0.73	0.35	8.55	0.94	0.41	6.31	0.76	0.30
3-D GCMT _{lat/lon}	6.98	0.85	0.19	5.74	0.80	0.30	6.75	0.88	0.16
3-D ICMT _{lat/lon mo}	7.08	1.09	0.11	10.96	1.46	0.31	6.48	1.14	0.11

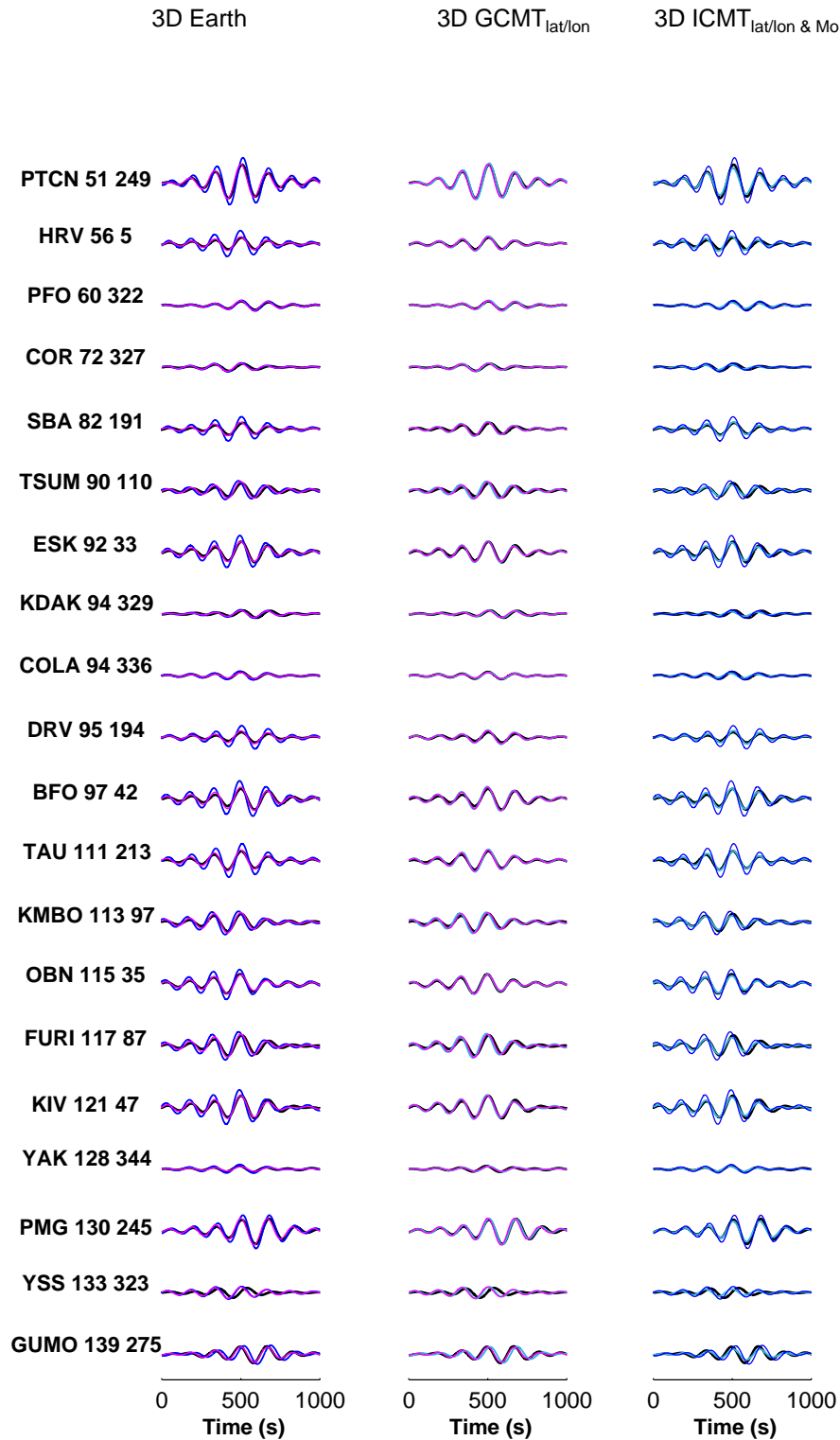


Figure 4.14: Comparisons of the vertical component of observed surface waves ($T \sim 150$ s) for the M_w 8.1 Pisco earthquake (black) with synthetics calculated in a 3-D Earth using GCMT (pink) and ICMT (blue) source parameters (3-D Earth). 3-D $GCMT_{lat/lon}$ shows a comparison of the GCMT solution (pink) with the same solution except that the latitude and longitude are replaced with the location from Pritchard and Fielding (2008) (light blue). The rightmost column (3-D $ICMT_{lat/lon \& Mo}$) compares the ICMT solution (blue) with the ICMT solution where the latitude, longitude and moment have been replaced with the GCMT estimates (light blue).

4.3.5 Small Subduction Zone Event: North Chile Subduction Zone, M_w 6.6, 19th April 1996

This smaller subduction zone event also occurred on the subduction interface between the Nazca and South America plates, which are converging at a rate of 6–6.5 mm yr⁻¹ (Kendrick *et al.*, 2003). In this region the seismogenic zone dips 12–14° to the east and extends from 35–50 km (Allmendinger and Gonzalez, 2010). The earthquake is located just south of the Mejillones Peninsula, which coincides with the location of a suggested barrier to the propagation of megathrust earthquakes such as Tocopilla (M_w 7.7, 14th November 2007) to the north and Antofagasta (M_w 8.1, 30th July 1995) (*e.g.* Loveless *et al.*, 2010). Similar to the Pisco earthquake, the GCMT location is 52 km west of the ICMT location and the InSAR-determined seismic moment is nearly twice that of the GCMT estimate (see Table 4.9).

Table 4.9: Summary of source parameters for the North Chile earthquake (19th April 1996, M_w 6.6) from the GCMT catalogue and from one InSAR study (Pritchard *et al.*, 2006). Values in bold were fixed during the inversion and the latitude, longitude and depth refer to the centroid location.

Parameter	(Pritchard <i>et al.</i> , 2006)	GCMT
M _w	6.7	6.6
M _o (x10 ¹⁸ Nm)	14.00	8.43
Lat (°)	-23.94	-23.95
Lon (°)	-70.06	-70.58
Depth (km)	49.0	50.0
Strike (°)	5.0	11.0
Dip (°)	23.0	19.0
Rake (°)	107.0	109.0

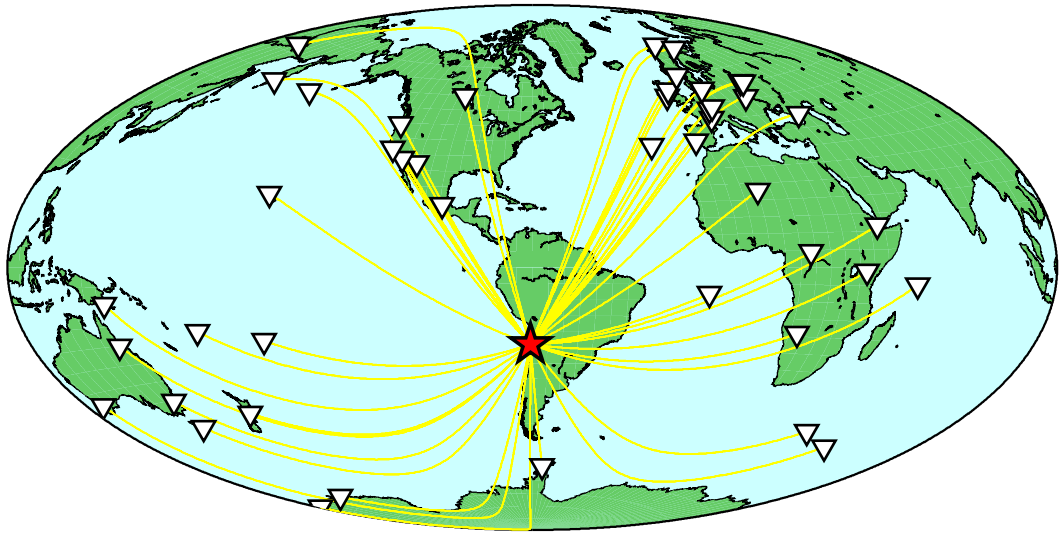


Figure 4.15: Distribution of seismic stations (white triangles) with respect to the M_w 6.6 northern Chile subduction zone earthquake (red star), where the ray paths are highlighted in yellow.

4.3.5.1 Long Period Surface Waves

Figure 4.15 shows the station distribution used in vertical and transverse component surface wave comparisons carried out for this event (Figures showing the transverse component are in Appendix B (Figure B.6). As was the case for Pisco, the synthetics calculated in a 3-D Earth using the GCMT solution show the better fit to the observed data, in comparison with the ICMT solution (Table 4.10, Figure 4.16; see, *e.g.*, stations KIP and ATD). The amplitude of the ICMT synthetics are on average twice as large as the observed waveforms ($\delta A = 0.58$), which is again likely due to the overestimation of the seismic moment in the ICMT solution. Replacing the ICMT moment estimate with the corresponding GCMT value significantly improves the fit in amplitude of the synthetics to the data (3-D ICMT_{*M_o*} in Figure 4.16). Consequently, the waveform misfit is reduced to $m^2=0.15$, less than that of the synthetics calculated using the original GCMT solution ($m^2 = 0.24$; see 3-D ICMT_{*M_o*} and 3-D GCMT rows in Table 4.10).

In contrast to the Pisco earthquake, replacing the latitude and longitude in the GCMT solution with values from the ICMT solution further improves the fit to the data. The phase misfit is reduced by ~ 2 s, the amplitude misfit is slightly worse, but the overall waveform misfit is reduced by half to $m^2=0.12$ (see 3-D GCMT_{*lat/lon*} in Table 4.10 and

Figure 4.16). This combination of the ICMT latitude and longitude and the remaining source parameters taken from the GCMT catalogue results in synthetics which show the overall best fit to the data.

Table 4.10: Summary of average phase ($\delta\Psi$), amplitude (δA) and waveform misfits (m^2) for comparisons between synthetic and observed surface waves ($T \sim 150$ s) for the M_w 6.6 northern Chile earthquake. Both comparisons for the vertical (Z) and transverse (T) components are shown, where the solution highlighted in bold refers to the one which shows the best overall fit to the data.

Synthetics	Z (n=43)			T (n=29)		
	$\delta\Psi$	δA	m^2	$\delta\Psi$	δA	m^2
1-D GCMT	13.17	1.04	0.43	17.06	1.08	0.60
1-D ICMT	10.81	0.56	1.17	11.16	0.70	0.81
3-D GCMT	8.21	1.07	0.24	9.04	1.03	0.31
3-D ICMT	7.65	0.58	0.78	7.41	0.64	0.65
3-D ICMT _{Mo}	7.65	0.97	0.15	7.41	1.06	0.30
3-D GCMT_{lat/lon}	6.70	1.15	0.12	5.92	1.04	0.30

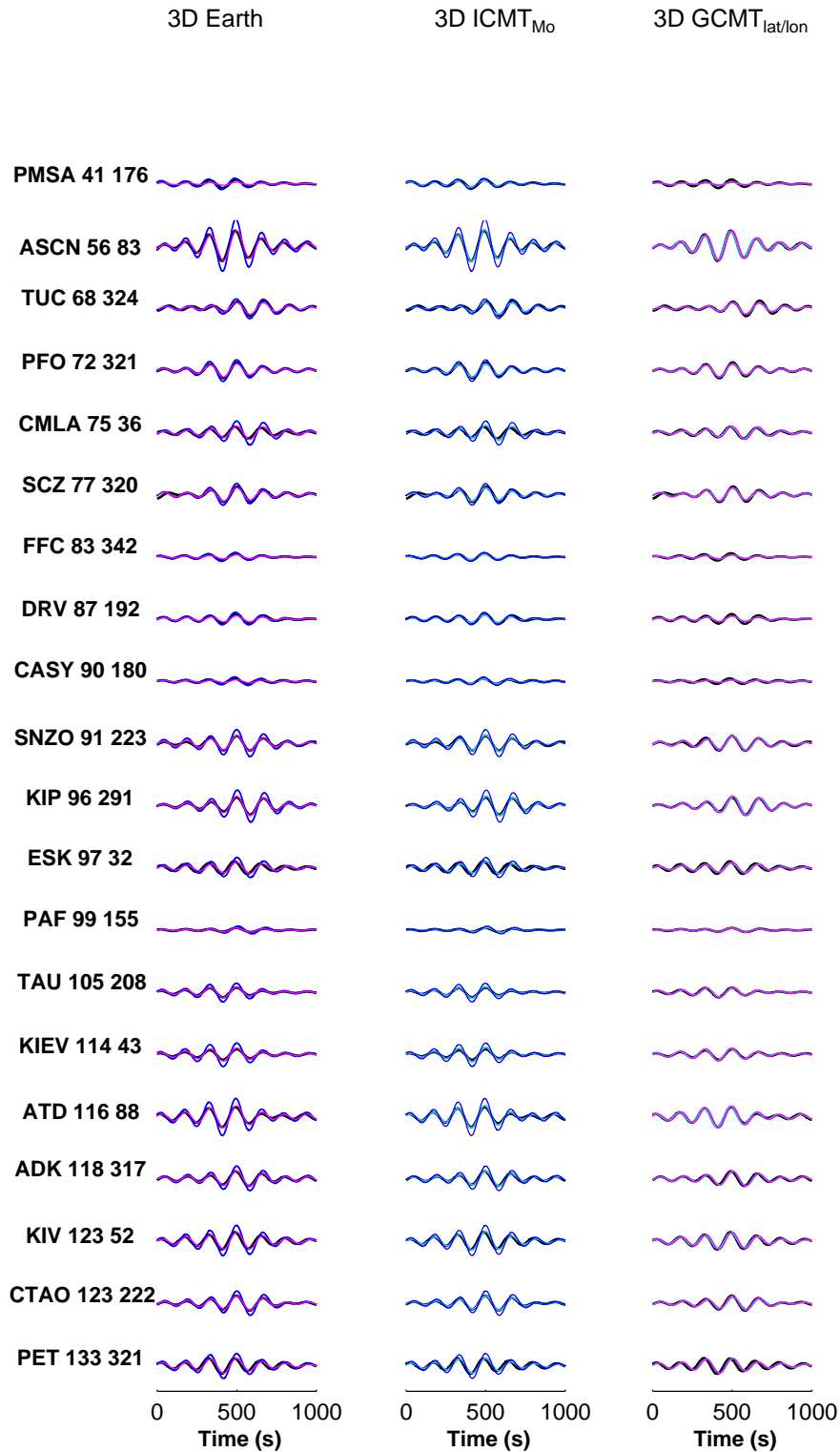


Figure 4.16: Comparisons of observed vertical component surface waves ($T \sim 150$ s) for the M_w 6.6 northern Chile event (black) with synthetics calculated in a 3-D Earth using GCMT (pink) and ICMT (blue) source parameters (3-D Earth). 3d $ICMT_{Mo}$ (middle column) compares ICMT synthetics (blue) with the same solution except that the moment has been replaced with the GCMT estimate (light blue). The right column (3-D $GCMT_{lat/lon}$) compares the GCMT solution (pink) with the GCMT solution where the latitude and longitude are replaced with the estimates from Pritchard *et al.* (2006) (light blue).

4.4 Discussion and Conclusions

There is no overall clear systematic trend when comparing InSAR-and seismically-derived earthquake source models; neither the seismically-determined solutions from the GCMT catalogue nor the InSAR solutions from the ICMT database consistently better explain the observed long period seismic data. For all but one of the events (Eureka Valley) the synthetics calculated using a 3-D Earth model and the GCMT solution initially show the best fit to the data. Further improvements in the fit of the synthetics to the data were achieved by a mix of ICMT and GCMT source parameters, with the centroid location and the seismic moment having often an important control on the misfits.

For the moderate magnitude events (Eureka Valley and northern Chile) replacing the GCMT location with the ICMT latitude and longitude estimates improved the fit of the synthetics to the data. However, for larger magnitude events (Pisco, Landers and Izmit) the ICMT location failed to improve the fit to the data. It has been previously observed that solutions reported in the GCMT catalogue for earthquakes in the south American subduction zone, such as Pisco, are systematically shifted westwards towards the trench (Chapter 2, Pritchard *et al.*, 2006; Syracuse and Abers, 2009). This is thought to be due to the fact that the velocity structure of this subduction zone is not properly taken into account in the Earth model used in the GCMT inversions. Yet despite the strong spatial resolution of InSAR data, using the location from Pritchard and Fielding (2008) does not improve the fit to the data. Also the ICMT location does not improve the fit to the long period surface waves recorded for the Landers earthquake, potentially because it is too far south, as large offsets were observed at the north end of the rupture (Sieh *et al.*, 1993). This meant that the interferograms were extremely decorrelated in this area and hence displacements at this end of the rupture were not well constrained. This highlights the fact that source models from InSAR data suffer the same issues as seismic data whenever the centroid location is determined from a variable slip model, which is the result of an inversion.

Despite the incorrect ICMT location for the Landers earthquake the GCMT location is also probably too far north if 50% of the seismic moment was released at the southern half of the rupture (Cohee and Beroza, 1994). Also, when considering the ICMT and GCMT locations in conjunction with other datasets, such as mapped offsets or strong motion

data, then the InSAR location is in better agreement with these independent constraints than the GCMT location. This is the case for the Izmit earthquake where the GCMT is 30 km north of the NAF, which has been identified as being the locus of the earthquake by geological field observations and geodetic data, and with centroid locations from various InSAR studies all placing the centroid on this fault. Yet using these locations to calculate theoretical seismograms results in a worse fit to the data. Therefore results for the Izmit and Landers earthquakes suggest that errors in the assumed 3-D Earth models are also in part responsible for these observed discrepancies.

Results for the Eureka Valley earthquake provide some indication of the scale of potential errors in the assumed 3-D Earth model used in the forward modelling. The lack of improvement in fit to the long period body waves for the GCMT when using a 3-D Earth model could be due to errors in the source region suggested by the GCMT location. Moreover, this would also be compatible with the significant body wave data fit improvement seen when using the ICMT location. Previous studies have used the results of comparisons between synthetics and observed data to identify errors in the assumed Earth structure at a crustal scale such as in the South-Central Andes (*e.g.* Alvarado *et al.*, 2007) and in the Lesser Antilles (*e.g.* Salichon *et al.*, 2009). There is also the potential to identify errors at the larger mantle scale, as discussed in Tsuboi *et al.* (2003).

The assumed Earth structure is clearly an important consideration when modelling the seismic data and the results from this chapter and the previous one have also highlighted the complementary nature of InSAR and seismic data concerning their spatial and temporal resolution. Moreover, the differences in source models from separate and joint inversions are not only a result of the data but also of the methods used to determine them and the assumptions within them (*e.g.*, Beresnev, 2003). In the following chapter multiple joint inversion approaches are summarised and discussed, and a new joint inversion approach which takes the effects of 3-D Earth structure into account when modelling the seismic data is presented.

Chapter 5

A joint inversion technique for earthquake source parameters

5.1 Introduction

InSAR and seismic data are highly complementary datasets, as is evident from the results in Chapters 3 and 4, and this has prompted the development of many source inversion techniques, which use multiple geodetic and seismic datasets to characterise the earthquake source. Comparisons between InSAR and seismic source models also highlighted the importance of the Earth model used when modelling the seismic data. Almost all existing joint approaches assume a 1-D Earth structure when modelling the various types of seismic data: teleseismic body waves (*e.g.* Ji *et al.*, 2002a), local data (*e.g.* Kaverina *et al.*, 2002), regional data (*e.g.* Lohman *et al.*, 2002) or strong motion data (*e.g.* Hernandez *et al.*, 1999). Wald and Graves (2001) were the first to consider the effects of 3-D Earth structure in the context of joint inversion techniques. Errors in the Earth model can lead to uncertainties in the source parameters, including an overestimation of the seismic moment (*e.g.* Ferreira and Woodhouse, 2006), and the percentage of non-double-couple component (*e.g.* Covellone and Savage, 2012) and can also produce shifts in location (*e.g.* Syracuse and Abers, 2009; Hjörleifsdóttir and Ekström, 2009).

In this chapter a novel joint inversion technique is presented that takes into account the effects of 3-D Earth structure when modelling the seismic data. Existing approaches are discussed first, followed by a description of the data and approach used to calculate the

seismic excitation kernels. An overview of the inversion scheme, including the weighting approach are then presented. Synthetic tests based on real events are carried out to investigate the influence of data noise and 3-D Earth structure in the inversions, and to highlight the benefits of combining the two datasets. Three real case studies in a range of tectonic settings are also investigated where the joint inversion of multiple datasets could be beneficial. For example to resolve large discrepancies between InSAR and seismically-determined source parameters, such as location, using the examples of the Eureka Valley, California (17th May 1993, M_w 6.0), and Aiquile, Bolivia (22nd May 1998 M_w 6.5) events and fault dip angle using the example of Zarand (22nd February 2005, M_w 6.5). For the events in central Iran and in the central Andes in Boliva, robust source models are particularly important as there is still much debate surrounding the tectonic regime and seismic hazard in these regions, that could be informed by accurate earthquake information.

5.2 Existing techniques

The approach used to model the seismic data and the algorithms chosen to search the parameter space are the two key ways in which existing joint inversion techniques differ. Wald and Heaton (1994) were one of the first to combine multiple datasets in order to model a large strike-slip earthquake — Landers (M_w 7.3, 28th June 1992). They used a constrained, damped, linear least-squares inversion approach, which combines teleseismic bodywaves, strong motion data, GPS, and trilateration measurements to determine a slip distribution for the event. Green's functions for the teleseismic P and SH waves are modelled using generalized ray theory, and a frequency wavenumber integration scheme is used for the strong motion data. Ji *et al.* (2002a) took a different approach to modelling the seismic data, in an attempt to include both the high and low frequency features of the seismogram in the inversion. A Meyer-Yamada wavelet transform is applied to the seismic data so the inversion is carried out in the frequency domain, and an objective function is used to guide a simulated annealing algorithm to select the best fitting model (Heat Bath algorithm, Rothman, 1986). The objective function consists of three misfits corresponding to each of the datasets; a combination of L1 and L2 norm are used for the low frequency seismic data, the high frequency data require a correlation function, and the difference between the geodetic data and synthetics is calculated using a sum-squared

residuals. This is one of the most widely used joint inversion approaches (*e.g.* the study of South American subduction zone events, Pritchard *et al.*, 2006). The simulated annealing algorithm has the advantage of no dependency on the starting model and is also used in Delouis *et al.* (2002) where ray theory is used to model the seismic data, and the RMS misfit is used to guide the inversion. As inversions are guided by the misfit to the data it can be useful to observe the misfit over the whole parameter space; this is possible with the Neighbourhood Algorithm (Sambridge, 1998) and it concentrates sampling in the region with lowest misfit. Lohman *et al.* (2002) uses this approach in separate InSAR and seismic inversion which are iterated between multiple times to determine a best fit model for both datasets. The afore-mentioned techniques have so far used local or regional seismic data — Funning (2005) uses long period surface waves, which are forward modelled using normal mode summation and assuming a 1-D Earth model (PREM), and a hybrid downhill Powell-Monte Carlo approach (Clarke *et al.*, 1997) is used to determine the best fitting point source (centroid moment tensor).

Rather than jointly inverting the two datasets, the information can be used separately to constrain source models independently. For example Hernandez *et al.* (1999) used the slip distribution calculated from geodetic measurements as an *a priori* constraint for the modelling of the rupture propagation from strong motion data. Shamir *et al.* (2003) used a kinematic fault model from the inversion of teleseismic bodywaves to forward model surface displacements in the form of a synthetic interferogram. The fault parameters (slip and rake) were then adjusted to achieve the best fit to the observed interferograms. Alternatively fault planes determined from aftershock locations and the inversion of InSAR data can be used to identify which of the faults were involved in the earthquake (*e.g.* Kozani-Grevena, M_w 6.6, 13th May 1995, Resor *et al.*, 2005).

The common theme for most previous joint inversion techniques is that they assume a 1-D Earth structure when modelling the seismic data. The effects of 3-D Earth structure when modelling seismic data, with respect to the joint inversion of seismic and geodetic data has only been considered by Wald and Graves (2001). Green's functions for strong motion data were calculated by forward modelling the strain on a predefined fault structure using a set body force applied at each strong motion station (Graves and Wald, 2001). Synthetic tests with 1-D and 3-D Green's functions revealed that the slip distribution can

be recovered with much higher resolution when a 3-D Earth structure is assumed. Moreover, the addition of geodetic data to the seismic source inversion increased the robustness of the resulting model as it is less sensitive to the Earth structure assumption than seismic data (Wald and Graves, 2001). However, only locally recorded short period seismic data were used and the joint inversion scheme presented here considers long period teleseismic surface and bodywaves.

5.3 Method

5.3.1 Optimisation scheme

A downhill Powell scheme with multiple Monte Carlo starts is used to determine optimal earthquake point source model solutions. Ten source parameters are determined, assuming a pure double-couple source – seismic moment, centroid spatial location (latitude, longitude and depth), fault’s strike, dip, rake, average slip, length and width. The technique is based on an approach originally used for the inversion of geodetic data (Clarke *et al.*, 1997; Wright *et al.*, 1999), which has been modified to include seismic data. The misfit function used in the inversions is a L_2 -norm function involving differences between the observed seismograms \mathbf{d}_S and the theoretical seismograms \mathbf{t}_S , and between observed and theoretical downsampled InSAR displacements (\mathbf{d}_I and \mathbf{t}_I , respectively):

$$m^2 = \alpha_S \frac{(\mathbf{t}_S - \mathbf{d}_S)^T (\mathbf{t}_S - \mathbf{d}_S)}{\mathbf{d}_S^T \mathbf{d}_S} + \alpha_I \frac{(\mathbf{t}_I - \mathbf{d}_I)^T (\mathbf{t}_I - \mathbf{d}_I)}{\mathbf{d}_I^T \mathbf{d}_I}, \quad (5.1)$$

where α_S and α_I are the weights given to the seismic and InSAR data in the inversions, respectively.

Figure 5.1 shows a flowchart illustrating our joint source inversion algorithm. Initial inversions are carried out using the seismic and InSAR data separately, followed by joint data inversions. The Powell algorithm (Press *et al.*, 1992) is used to search the parameter space defined by the input file. The algorithm covaries multiple parameters and for each change theoretical seismograms and LOS displacements are calculated to determine the misfit function. This is used as a penalty function which guides the algorithm until a model leading to a minimum of the misfit function is found. The resulting source model represents a local minimum and depends on the initial estimates used at the start.

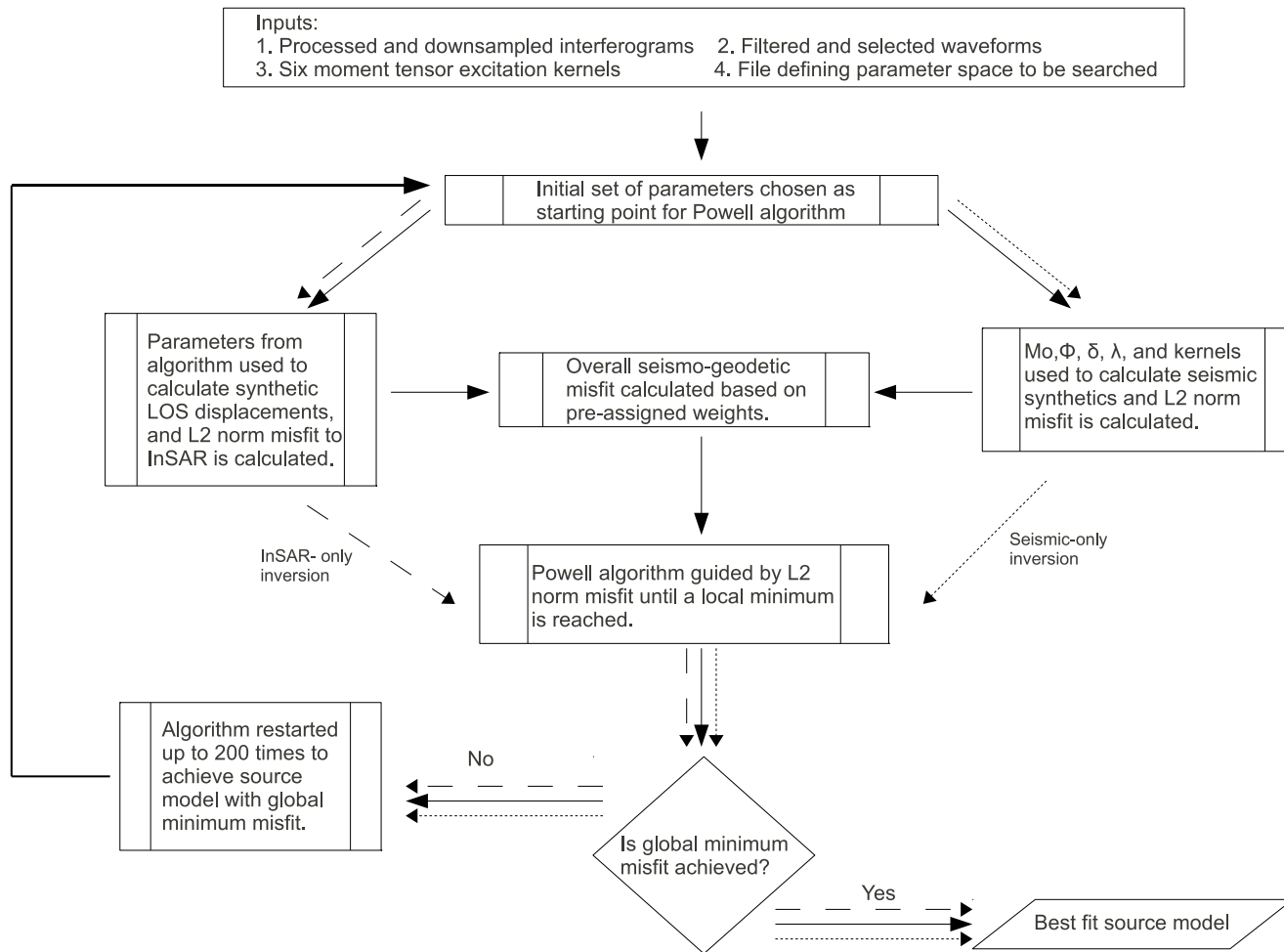


Figure 5.1: Flowchart illustrating the joint inversion approach. Solid arrows show the pathway taken in the joint inversion, dashed and dotted lines show pathways for separate InSAR and seismic inversions, respectively. M_0 , Ψ , δ , and λ refer to the seismic moment, strike, dip and rake, respectively. The global minimum misfit is achieved when 5 of the lowest misfit values within 1×10^{-5} of each other are obtained.

Consequently, the algorithm is restarted up to 200 times using different starting model parameters selected by a Monte Carlo process to determine the source parameters corresponding to the global minimum of the misfit function. The mean misfit values obtained from separate inversions of InSAR and seismic data are used as guides to determine the weights α_S and α_I . If there are multiple seismic or geodetic datasets these are also inverted separately to ensure all features of each dataset are properly taken into account.

Compared to existing earthquake source inversion methods, a novel aspect in this joint inversion technique is that the effects of 3-D Earth structure are fully taken into account when modelling the seismic data, as explained in the following subsection. The InSAR data are modelled using classical elastic dislocation theory (Okada, 1985), assuming uniform slip on a finite fault in a homogeneous half-space ($\mu = 3 \times 10^{10}$ and $\lambda = 3 \times 10^{10}$ Pa) a routine approach widely used in previous studies (*e.g.* Wright *et al.*, 2003; Funning, 2005; Biggs *et al.*, 2006). The use of homogeneous half-space elastic models has been found to be an acceptable approximation in the modelling of geodetic data (*e.g.*, Wald and Heaton 2001), and although it can introduce biases of up to 30% (Chapter 3, section 3.4) for the purposes of this technique a half-space is adequate as a first approximation.

5.3.2 Theoretical seismograms and kernels

The n^{th} component of a seismogram s_n can be represented by the following linear relationship (*e.g.* Gilbert and Dziewonski, 1975):

$$s_n(x, t) = \sum_{i=1}^6 f_i K_i, \quad (5.2)$$

where \mathbf{f} is a vector containing the six independent components of the moment tensor:

$$\mathbf{f} = [M_{rr} \quad M_{\theta\theta} \quad M_{\phi\phi} \quad M_{r\theta} \quad M_{r\phi} \quad M_{\theta\phi}] \quad (5.3)$$

and \mathbf{K} – the excitation kernels – are the partial derivatives of the seismograms with respect to the moment tensor components:

$$K_i = \frac{\partial s_n}{\partial f_i}. \quad (5.4)$$

In this study synthetic seismograms and partial derivatives with respect to the seismic moment tensor are calculated using the spectral element wave propagation package SPECFEM3D Globe (Komatitsch and Tromp, 1999). This is a highly accurate technique, fully taking into account 3-D Earth structure, as well as the effects of gravity, Earth's rotation, attenuation, topography and of the ocean's load on seismic waveforms. A variety of Earth models can be used; in this study the shear wave mantle model S40RTS (Ritsema *et al.*, 2011) is used in combination with the crustal model CRUST 2.0 (Bassin *et al.*, 2000), see Figure 5.2. We calculate 90-min-long theoretical seismograms accurate down to a period of 15 seconds and each run takes approximately six hours using 864 processors on the UK's supercomputer HECToR. Since the earthquakes studied have moderate magnitudes, we model the source time function as a Dirac delta function. This simplified assumption can be used because respectively the source dimension and duration of the earthquakes studied will typically be less than that of the wavelength and period of the seismic data used. In addition, given the high spatial accuracy of InSAR data and the limitations in earthquake locations obtained from long-period seismic data (*e.g.* Ferreira *et al.*, 2011), we use the centroid locations obtained from inversions of InSAR data alone. Thus, the seismic inversion is a linear problem and, for each earthquake, the six moment tensor excitation kernels only need to be calculated once because the kernels are unlikely to vary significantly over the length scale searched in the InSAR part of the inversion.

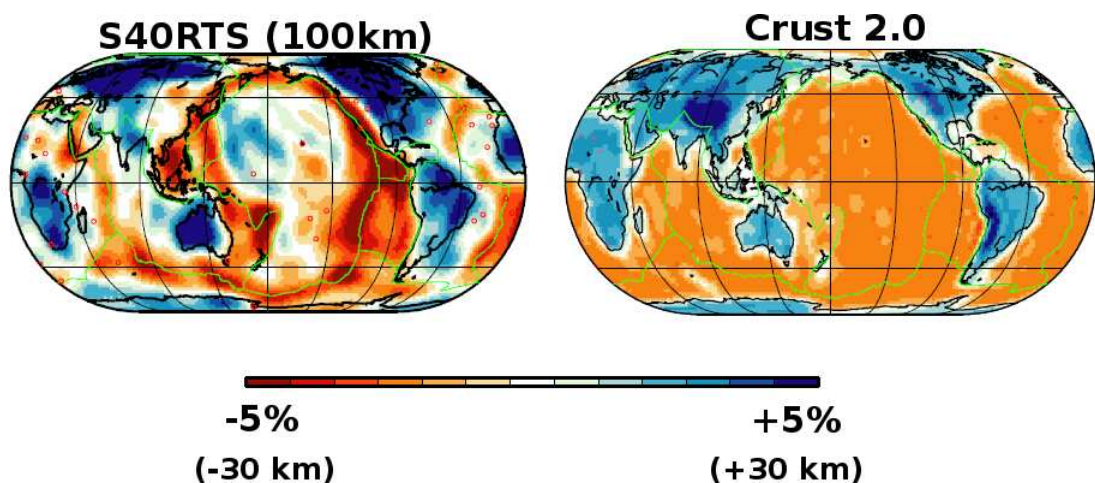


Figure 5.2: The plot on the left shows a horizontal cross section at 100 km depth of the shear mantle model, S40RTS, and CRUST 2.0 is plotted on the right. The colour scale is the same for both figures except for S40RTS it corresponds to 5% perturbations in shear velocity relative to PREM and for CRUST2.0 it illustrates 30 km variations in crust thickness, again relative to PREM. Figures courtesy of Sung-Joon Chang.

An example of excitation kernels calculated for a shallow earthquake ($h=12$ km) located in Northern California and for station TLY in Russia at an epicentral distance of 84.0° and an azimuth of 336.0° is shown in Figure 5.3. Three-component body and surface wave kernels for the 3-D Earth model S40RTS combined with CRUST2.0 (see Figure 5.2) are compared with calculations for the spherically symmetric Earth model PREM (Dziewonski and Anderson, 1981). As expected, the long-period surface wave kernels associated with $M_{r\theta}$ and $M_{r\phi}$ cannot be well constrained as they are small for shallow sources (*e.g.* Dziewonski *et al.*, 1981). In addition, there are substantial differences between PREM and 3-D kernels for both body and surface wave kernels (Figure 5.3).

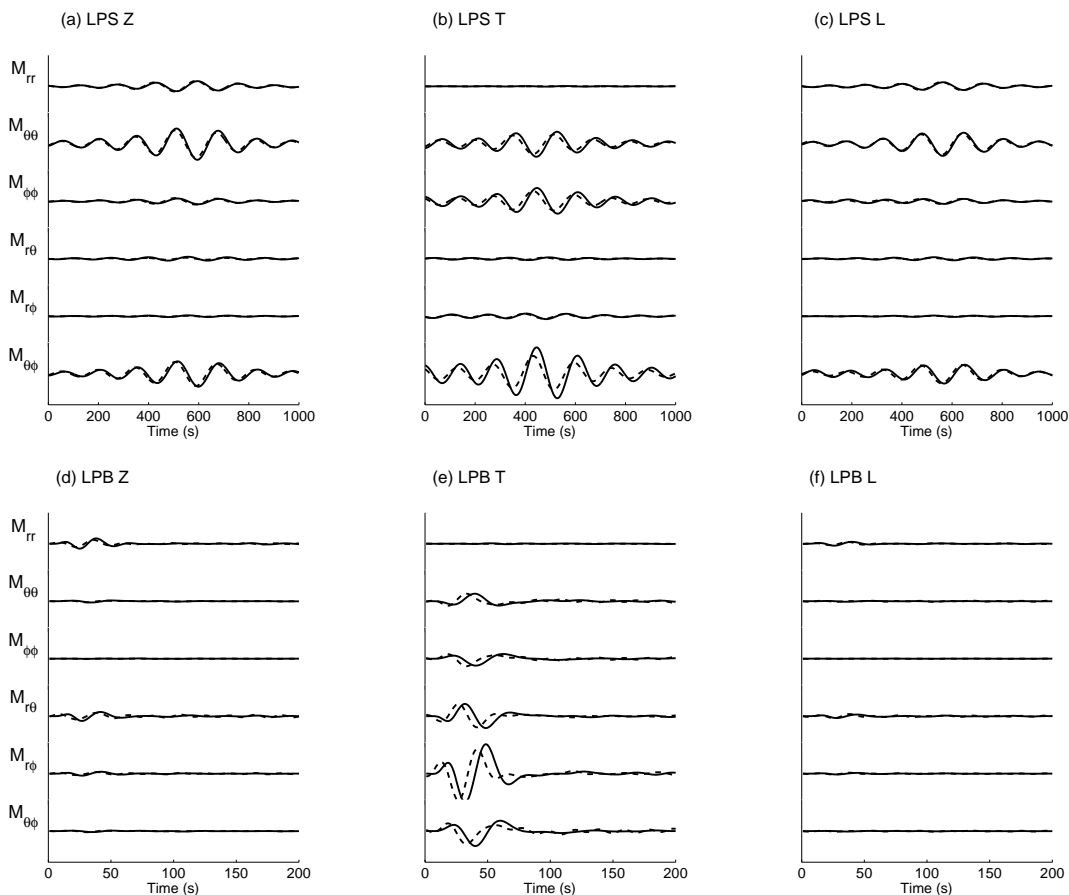


Figure 5.3: Three component excitation kernels calculated using S40RTS combined with CRUST 2.0 (solid black line) in comparisons with kernels calculated using PREM (dashed line) for a source located at latitude 37.092° , longitude -117.930° and 12 km depth for station TLY (Russia). a) - c) Show partial derivatives with respect to the six moment tensor components for long period surface waves and long period body waves are shown in d) - f), and the amplitude scale is uniform for the surface and body wave plots.

5.4 Data

5.4.1 Teleseismic waveform data

Three-component seismic data recorded at stations from the GSN, GEOFON and GEO-SCOPE networks are downloaded from IRIS (Incorporated Research Institutions for Seismology). The horizontal components are rotated into longitudinal and transverse components and all three components are deconvolved for instrument response. Two time windows are used: (i) a window including long period surface waves with a dominant wave period of $T \sim 150$ s (hereafter referred to as LPS) obtained through convolution with the response of an SRO instrument and filtering with cosine high and low pass filters; (ii) a window centered on $T \sim 30$ s body waves (hereafter referred to as LPB), which are band-pass filtered using Butterworth filters.

In order to minimise near-source effects, caustics and multiple orbit overlapping wave trains, we consider stations with epicentral distances in the range 40° – 140° for LPS and 30° – 90° for LPB. The waveforms are visually assessed as a quality control measure and, in order to ensure an even azimuthal distribution of stations. If data from several stations are available in a 5° azimuthal interval, we use the dataset with the best signal-to-noise ratio.

5.4.2 InSAR data

Interferograms used in this study are calculated using SAR images from ENVISAT, ERS-1 and ERS-2 satellites. Whenever possible, both ascending and descending tracks are used for pairs of images with short temporal separations and favorable perpendicular baselines. The images are processed using ROIPAC (Repeat Orbit Interferometry Package, Rosen *et al.*, 2004) and the resulting unwrapped interferograms are downsampled from millions to hundreds of data points using a quadtree decomposition algorithm (*e.g.* Jónsson *et al.*, 2002). A Digital Elevation Model (DEM), *e.g.*, 3 arc second Shuttle Radar Topography Mission (SRTM) data (Farr *et al.*, 2007), is used to correct for topographic effects and to geocode the interferograms.

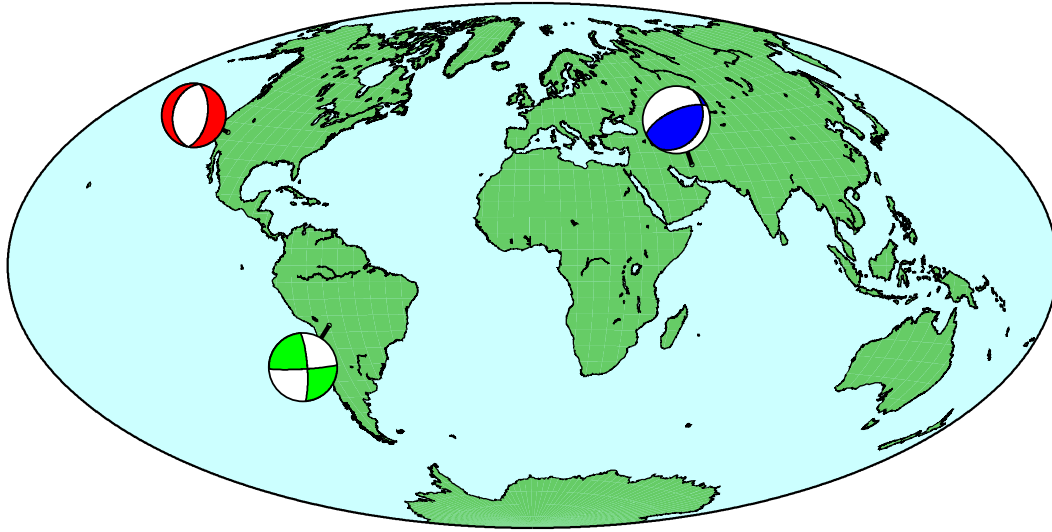


Figure 5.4: Locations and focal mechanisms of the three artificial earthquakes used in this synthetic tests; Normal (red), strike-slip (green), and thrust (blue).

5.5 Synthetic Tests

In this section we carry out synthetic tests to investigate the benefits of joint source inversions in the presence of data noise and of lateral heterogeneity. We consider three fictitious earthquakes of varying magnitude and faulting mechanisms (Figure 5.4) – normal (M_w 6.0), strike-slip (M_w 6.6), and thrust (M_w 6.5) – based on past earthquakes to ensure that the tests are as realistic as possible. Specifically, the input source parameters used to generate the synthetic data are based on previous studies of the following earthquakes: (i) 1993 May 17, M_w 6.1, Eureka Valley (Massonnet and Feigl, 1995; Weston *et al.*, 2012); (ii) 1998 May 22, M_w 6.6 Aiquile, Bolivia (Funning *et al.*, 2005a; Devlin *et al.*, 2012); (iii) 2005 May 22, M_w 6.5 Zarand, Iran (Talebian *et al.*, 2006).

The synthetic interferograms are calculated using elastic dislocation theory (Okada, 1985) assuming uniform slip on a finite-fault in a homogeneous half-space and are down-sampled using quadtree decomposition (*e.g.* Jónsson *et al.*, 2002). Synthetic seismic data are calculated using the spectral element method, as described in section 5.3.2.

Tests are first carried out using purely synthetic data (*i.e.* no noise) for all three faulting mechanisms to verify the technique, and in all the cases the input model is fully recovered in both separate and joint inversions. To add realistic noise to the synthetic seismograms, characteristic real noise recorded at each station during a period of no significant

seismic activity, is filtered for the same periods used for the surface and body waves and is added to the clean synthetics, an approach similar to that used in Hjörleifsdóttir and Ekström (2009). Noisy InSAR data are created using a part of a real interferogram containing no coseismic signal to estimate a 1-D covariance function by averaging the autocorrelation function (Hanssen, 2001). This is achieved by trying to fit an exponential curve of the form, $Ae^{ax} \cos bx$, to the 1-D function in a least squares sense, where A refers to the maximum variance, x the distance between two points in the interferogram, and a and b are positive constants. This is then used to generate a variance-covariance matrix to add random, spatially correlated noise to the clean synthetic data (*e.g.* Wright *et al.*, 2003; Lohman and Simons, 2005a). The data in this case refer to the quadtree forward modelled LOS displacements, which are shown in Figure 5.5 as well as examples of noisy synthetic seismic data. These noisy synthetic datasets are then used as input data following the inversion approach described in section 5.3.1.

In order to estimate uncertainties and investigate tradeoffs between the various source parameters, 100 perturbed noisy synthetic data sets are generated. These 100 data sets are then inverted using the optimisation scheme explained above. While the distributions of the various source parameters can be used to estimate their uncertainties, scatter plots of pairs of source parameters are useful to assess qualitatively the tradeoffs between the parameters.

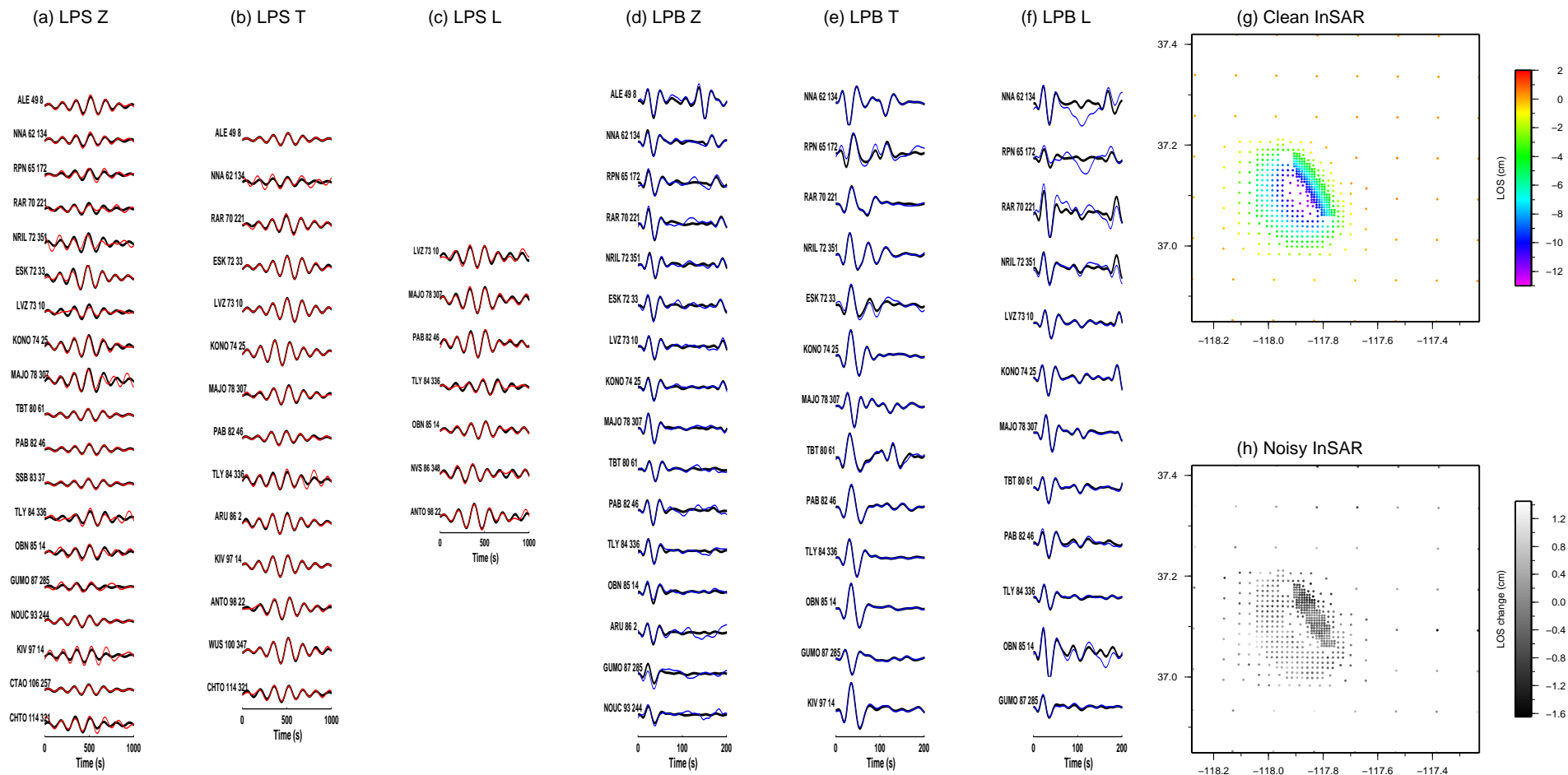


Figure 5.5: Example of the synthetic data used in the tests, where the data shown are for a normal faulting earthquake (M_{w} 6.0, lat: 37.092° , lon: -117.930° , depth: 8 km). a) - f) show the pure synthetics with no noise (black) and synthetic data with characteristic noise added for surface waves (red) and body waves (blue). g) Quadreed synthetic LOS displacements with no noise h) LOS displacements added to those in (g) to perturb the data.

5.5.1 Importance of 3-D Earth structure

To test the effect of the assumed 3-D Earth structure on the inversions, separate and joint synthetic source inversions are carried out for a M_w 6.0 normal faulting earthquake described by the source parameters in the top row of Table 5.1. Source inversions are carried out using two sets of seismic moment tensor excitation kernels. One set is calculated for the 1-D Earth model PREM using normal mode summation (Gilbert, 1976). The second set is calculated using the spectral element method for the 3-D Earth mantle model S40RTS combined with CRUST2.0. For a comparison of the PREM and S40RTS excitation kernels for this event see Figure 5.3. Most notably the P-wave arrivals are earlier and the amplitudes smaller for the PREM kernels (Figure 5.3d-f) and also some of the surface wave amplitudes particularly for the transverse component are smaller than the S40RTS + CRUST 2.0 kernels (Figure 5.3b).

Table 5.1 and the top panel of Table 5.2 show results from separate and joint inversions using PREM and 3-D Earth excitation kernels, respectively. As expected, the seismic-only inversions using the 3-D Earth model show a misfit to the data much lower (more than half) than when using PREM. The joint source inversion results follow the same trend, with the solutions obtained using the 3-D Earth model leading to an improved fit of the seismic and InSAR data (Figure 5.6 b,d,f,i) than results from inversions using PREM excitation kernels (Fig. 5.6 a,c,e,g). Furthermore, in both the 1-D and 3-D Earth model tests the body waves recover the input source parameters more robustly than the surface waves, with the differences between the surface and body wave inversion results being more pronounced when using PREM kernels. In particular, the best fitting fault dip angles from the 1-D inversions are $10\text{-}15^\circ$ steeper than in the input source model. This difference in the recovery of the fault dip is clearly marked out in the tradeoff plots in Figure 5.7, which show the results of 100 inversions with ‘noisy’ datasets plotted as a series of scatterplots between pairs of parameters. Moreover, Figure 5.7 shows that the PREM results are much less tightly clustered in comparison with 3-D Earth inversion results, with stronger tradeoffs than in the 3-D Earth inversions; the fault rake in particular shows a wide distribution of values.








It must be noted though that the 3-D Earth structure assumed in these tests may not necessarily be the correct one, there are still potential errors in the models, as was seen

in Chapter 4 when testing the location for the Izmit earthquake (Figure 4.11). However, S40RTS is still an improvement on PREM which shows a poorer fit to the seismic data (Chapter 4, Figure 4.5), and subsequently the excitation kernels for the three case studies (sections 5.6-5.8) are calculated using S40RTS.

5.5.2 Effect of data noise

In addition to the normal faulting earthquake synthetic tests, Table 5.2 also shows the results from the synthetic tests in the presence of realistic noise for the strike-slip and thrust earthquakes considered. In all cases the joint inversion of InSAR, long period surface and body waves recovers a source model overall closest to the input source model. Strike, dip and rake values from the various separate and joint inversions all vary within $\pm 1^\circ$ from the correct solution. In addition, the deviations from the input model are of about ± 1 km for the fault width and length, and about $\pm 0.2 \times 10^{18}$ Nm for the seismic moment. The results from inversions of 100 sets of perturbed synthetic data and the corresponding tradeoff plots show that for the three earthquakes considered, all the source parameters are better resolved in the joint inversions (red stars in tradeoff plots in Figures 5.8a, 5.9a, 5.10a) than in InSAR-only (blue stars, Figures 5.8a, 5.9a, 5.10a) and seismic-only inversions (pink stars, Figures 5.8b, 5.9b, 5.10b). In these plots, the source parameters from the joint inversions appear as tighter clusters and narrower peaks in these histograms than the results from the separate data inversions. Thus, our new joint inversion technique is shown to reduce the level of tradeoffs in ideal conditions. There is a distinct improvement when determining the rake's fault angle, which shows wide variation in both the separate InSAR and seismic inversions. For all three model earthquakes considered, the moment and dip are also significantly better constrained in the joint inversions, particularly for the normal and strike-slip synthetic test where tradeoffs between the two parameters are evident in the seismic-only inversions (Figures 5.8 and 5.9).

Table 5.1: Summary of source inversion results for a synthetic normal faulting earthquake (M_w 6.0), where the kernels were calculated using PREM. The solution is shown in bold italics, where latitude, longitude and depth refer to the centroid location and parameters fixed during the inversion are shown in bold. LPS refers to long period surface waves and LPB long period body waves.

Study	M_0 ($\times 10^{18}$ Nm)	Lat ($^\circ$)	Lon ($^\circ$)	Depth (km)	Strike ($^\circ$)	Dip ($^\circ$)	Rake ($^\circ$)	Slip (m)	Length (km)	Width (km)	m^2	
<i>Solution</i>	<i>1.76</i>	<i>37.092</i>	<i>-117.930</i>	<i>7.25</i>	<i>155.0</i>	<i>35.0</i>	<i>-89.0</i>	<i>0.3</i>	<i>15.0</i>	<i>13.0</i>	-	
LPS	1.63	37.092	-117.930	12.0	136.5	50.03	-114.7	0.37	15.0	9.8	0.320	
LPB	1.61	37.092	-117.930	12.0	152.8	40.7	-87.8	0.31	15.0	11.5	0.600	
LPS, LPB	1.58	37.092	-117.930	12.0	155.2	40.8	-88.4	0.31	15.0	11.5	0.630	
InSAR, LPS	1.73	37.087	-117.948	7.4	153.6	31.6	-99.1	0.24	17.0	14.02	0.013	
InSAR, LPB	1.88	37.092	-117.930	8.2	153.9	40.4	-90.9	0.31	14.6	14.0	0.013	
InSAR, LPS, LPB	1.84	37.094	-117.930	8.0	153.9	39.7	-92.5	0.30	14.7	13.8	0.008	

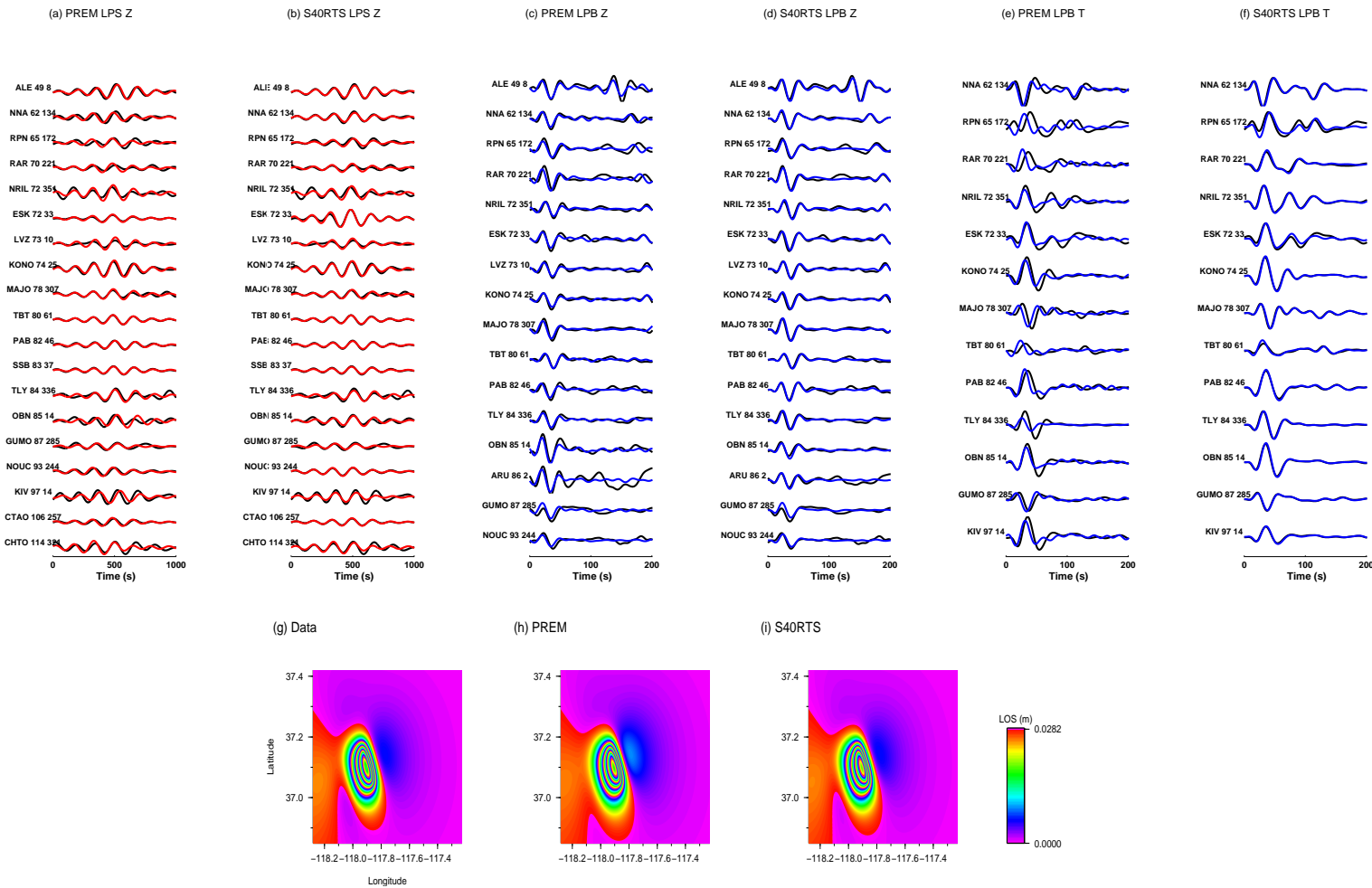


Figure 5.6: Comparison of joint source inversion results calculated using S40RTS combined with CRUST 2.0, and PREM kernels for a synthetic normal faulting event. a) - b) Show the vertical components for long period surface waves, PREM and S40RTS results, respectively. The data are shown in black and synthetics are in red. c)-d) Shows results for body waves, the vertical component and e) - f) the transverse components. g) This is the synthetic interferogram used in both joint inversions which use PREM or S40RTS+CRUST2.0 kernels. h) Interferogram calculated using the results from the joint inversion which uses PREM kernels. i) The same as (h) except the source model from the joint inversion which uses the S40RTS+CRUST2.0 kernels are forward modelled.

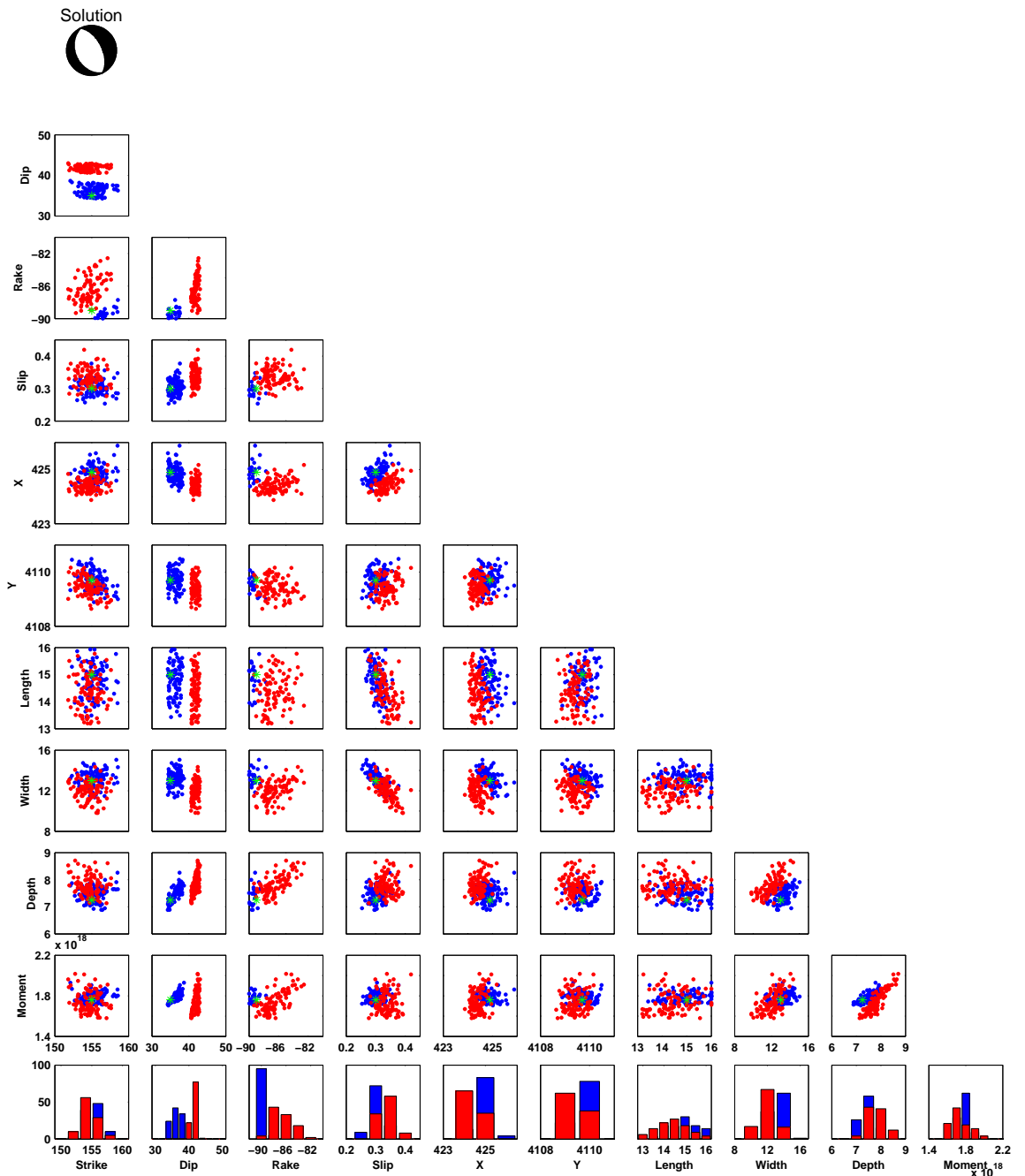


Figure 5.7: Tradeoffs of joint inversions using S40RTS combined with CRUST 2.0 (blue) and PREM (red) excitation kernels for the synthetic normal faulting event, in which synthetic seismograms are computed using S40RTS and CRUST 2.0. The scatterplots show the best fitting source parameters from 100 inversions using 100 datasets which have been perturbed slightly by characteristic noise. Clear positive or negative slopes suggest tradeoffs between the two parameters. Strike, dip and rake are in degrees, Moment is in Nm, slip in m, and length, width and depth in km. X and Y refer to the centroid projected updip to the surface and are given in UTM km rather than degrees to better illustrate the variations. The histograms show the distribution of the inversion results to illustrate the uncertainties for each parameter and the focal mechanism in at the top refers to the input model, the parameters of which are denoted by the green star on the tradeoff plots.

Table 5.2: Summary of results from the three synthetic tests; normal, strike-slip and thrust faulting events. The input models used to calculate the synthetic data are shown in bold italics, where the latitude, longitude and depth refer to the centroid location. Parameters fixed during the inversion are shown in bold. LPS refers to long period surface waves and LPB long period body waves. For the thrust test the subscripts *asc* and *dsc* refer to ascending and descending InSAR data, respectively.

Study	Mo ($\times 10^{18}$ Nm)	Lat ($^{\circ}$)	Lon ($^{\circ}$)	Depth (km)	Strike ($^{\circ}$)	Dip ($^{\circ}$)	Rake ($^{\circ}$)	Slip (m)	Length (km)	Width (km)	m ²	
<i>Solution</i>	<i>1.76</i>	<i>37.092</i>	<i>-117.930</i>	<i>7.25</i>	<i>155.0</i>	<i>35.0</i>	<i>-89.0</i>	<i>0.3</i>	<i>15.0</i>	<i>13.0</i>		
InSAR	1.66	37.095	-117.932	7.28	153.6	36.6	-100.0	0.28	14.6	13.4	0.004	
LPS	1.87	37.092	-117.930	12.0	152.7	31.9	-95.0	0.29	15.0	14.2	0.18	
LPB	1.69	37.092	-117.930	12.0	153.5	34.4	-91.1	0.28	15.0	13.3	0.14	
LPS, LPB	1.73	37.092	-117.930	12.0	154.3	34.6	-90.7	0.29	15.0	13.2	0.29	
InSAR, LPS	1.9	37.091	-117.936	7.64	153.8	36.1	-95.2	0.28	14.8	14.1	0.008	
InSAR, LPB	1.79	37.090	-117.934	7.4	153.9	35.2	-91.9	0.28	14.9	14.2	0.008	
InSAR, LPS, LPB	1.79	37.090	-117.934	7.41	154.0	35.1	-91.9	0.28	14.9	14.2	0.012	
<i>Solution</i>	<i>9.0</i>	<i>-17.903</i>	<i>-65.186</i>	<i>8.4</i>	<i>10.0</i>	<i>80.0</i>	<i>175.0</i>	<i>1.0</i>	<i>20.0</i>	<i>15.0</i>		
InSAR	9.39	-17.904	-65.189	8.4	9.3	82.8	175.2	1.1	19.9	14.9	0.016	
LPS	9.2	-17.903	-65.186	12.0	9.6	73.3	177.0	0.99	20.0	15.4	0.060	
LPB	8.7	-17.903	-65.186	12.0	10.0	79.3	172.0	0.96	20.0	15.0	0.19	
LPS, LPB	8.96	-17.903	-65.186	12.0	9.4	79.2	172.8	0.99	20.0	15.0	0.12	
InSAR, LPS	8.91	-17.905	-65.188	8.1	9.4	81.9	175.0	1.1	19.9	14.3	0.033	
InSAR, LPB	8.67	-17.905	-65.184	8.2	9.3	78.9	174.8	0.98	19.9	14.9	0.034	
InSAR, LPS, LPB	8.90	-17.905	-65.183	8.5	9.3	79.2	174.8	0.97	19.9	15.4	0.041	
<i>Solution</i>	<i>6.43</i>	<i>30.750</i>	<i>56.800</i>	<i>6.6</i>	<i>266.0</i>	<i>67.0</i>	<i>105.0</i>	<i>1.7</i>	<i>12.5</i>	<i>10.1</i>		
InSAR _{dsc}	7.23	30.750	56.798	6.8	266.3	66.5	114.9	1.86	12.5	10.4	0.0005	
InSAR _{asc}	6.48	30.754	56.792	5.6	266.1	58.4	140.0	1.76	13.0	9.5	0.0030	
InSAR _{asc&dsc}	6.74	30.755	57.799	7.0	266.3	66.9	104.6	1.66	12.5	10.8	0.0075	
LPS	6.37	30.75	56.80	12.0	264.3	65.6	105.2	1.67	12.5	10.2	0.11	
LPB	6.13	30.75	56.80	12.0	265.3	69.1	107.6	1.64	12.5	10.0	0.20	
LPS, LPB	6.48	30.75	56.80	12.0	264.8	67.0	104.8	1.71	12.5	10.1	0.21	
InSAR, LPS	5.58	30.746	56.803	5.7	266.4	66.9	104.7	2.04	12.6	7.2	0.0029	
InSAR, LPB	5.71	30.743	56.803	5.7	266.4	68.3	106.1	2.15	12.5	7.1	0.0029	
InSAR, LPS, LPB	6.27	30.750	56.802	6.5	266.3	66.1	105.5	1.71	12.5	9.8	0.0016	

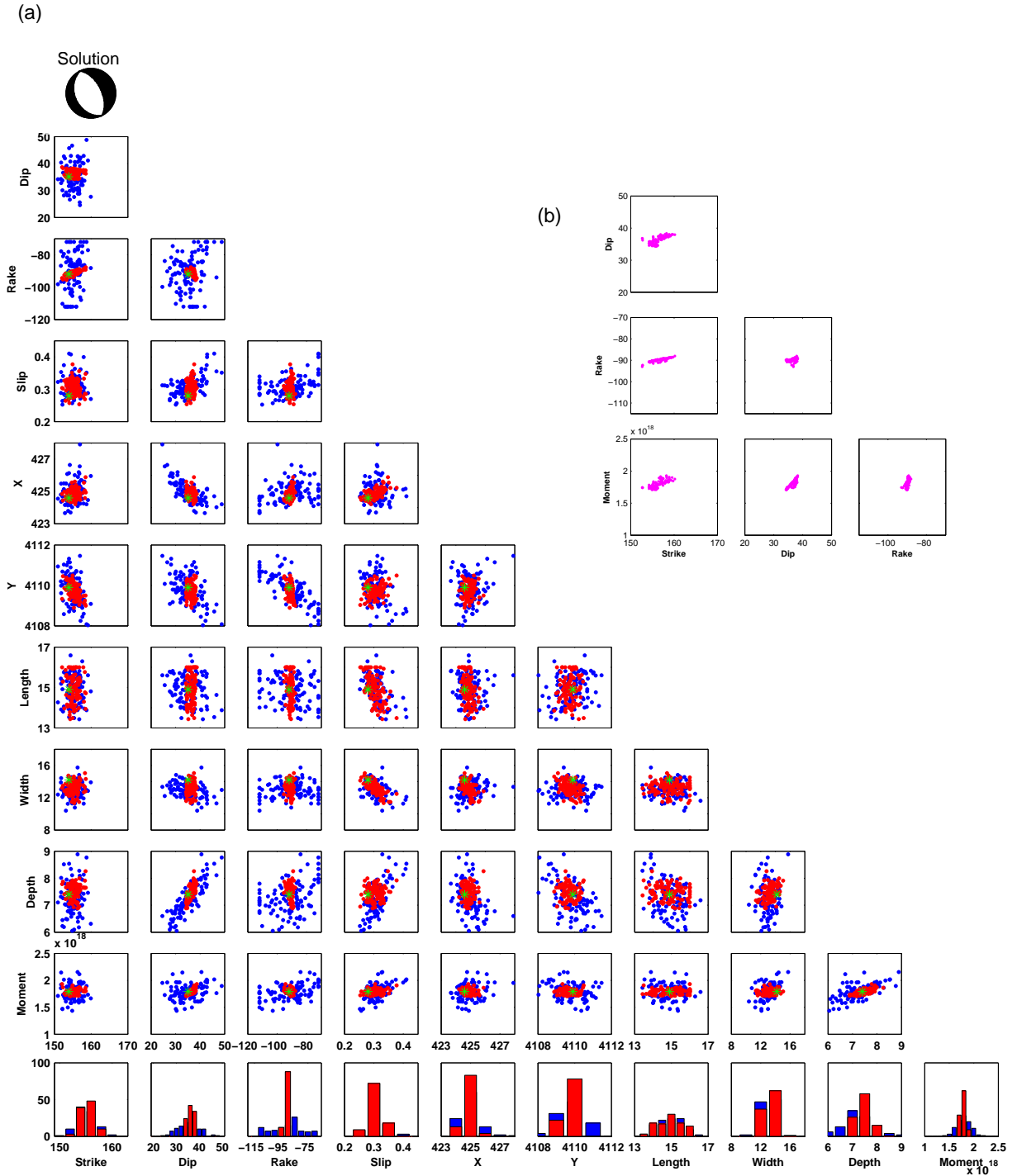


Figure 5.8: a) Tradeoff scatterplots and histograms for the InSAR only inversion (blue) and joint source inversion (red) for a synthetic normal faulting event, where the focal mechanism for the input model is shown at the top. The results were created in the same way and follow the same format as described for Figure 5.7. b) Tradeoff scatterplot for seismic-only inversion for Moment, Strike, Dip and Rake as all other parameters were fixed during the inversion.

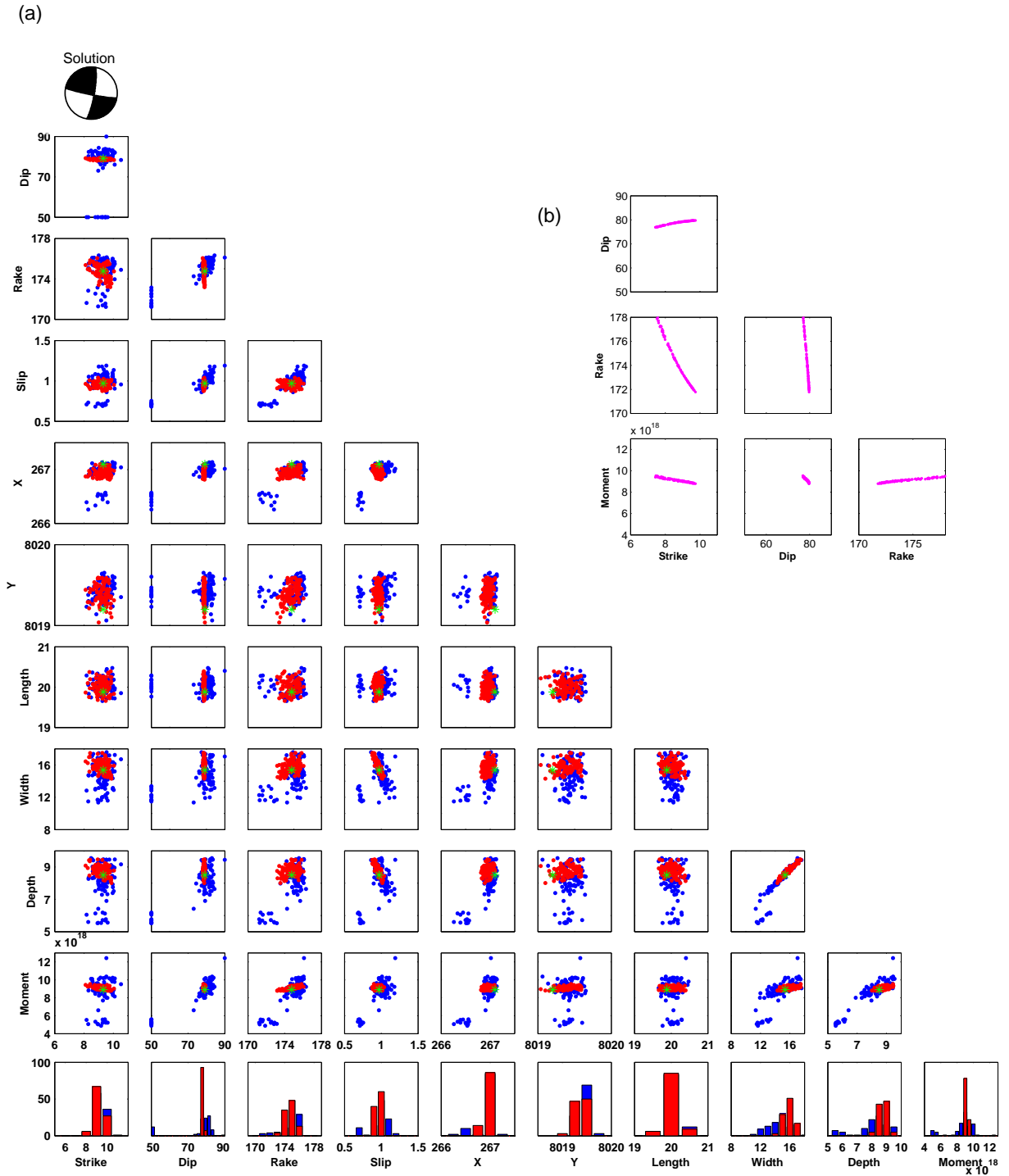


Figure 5.9: a) Tradeoff scatterplots for InSAR only inversion (blue) and joint source inversion (red) for a synthetic strike-slip faulting event, where the focal mechanism from the joint inversion is shown in red at the top. b) Tradeoff scatterplot for seismic-only inversion. The format for a) and b) follow the same as in Figure 5.7.

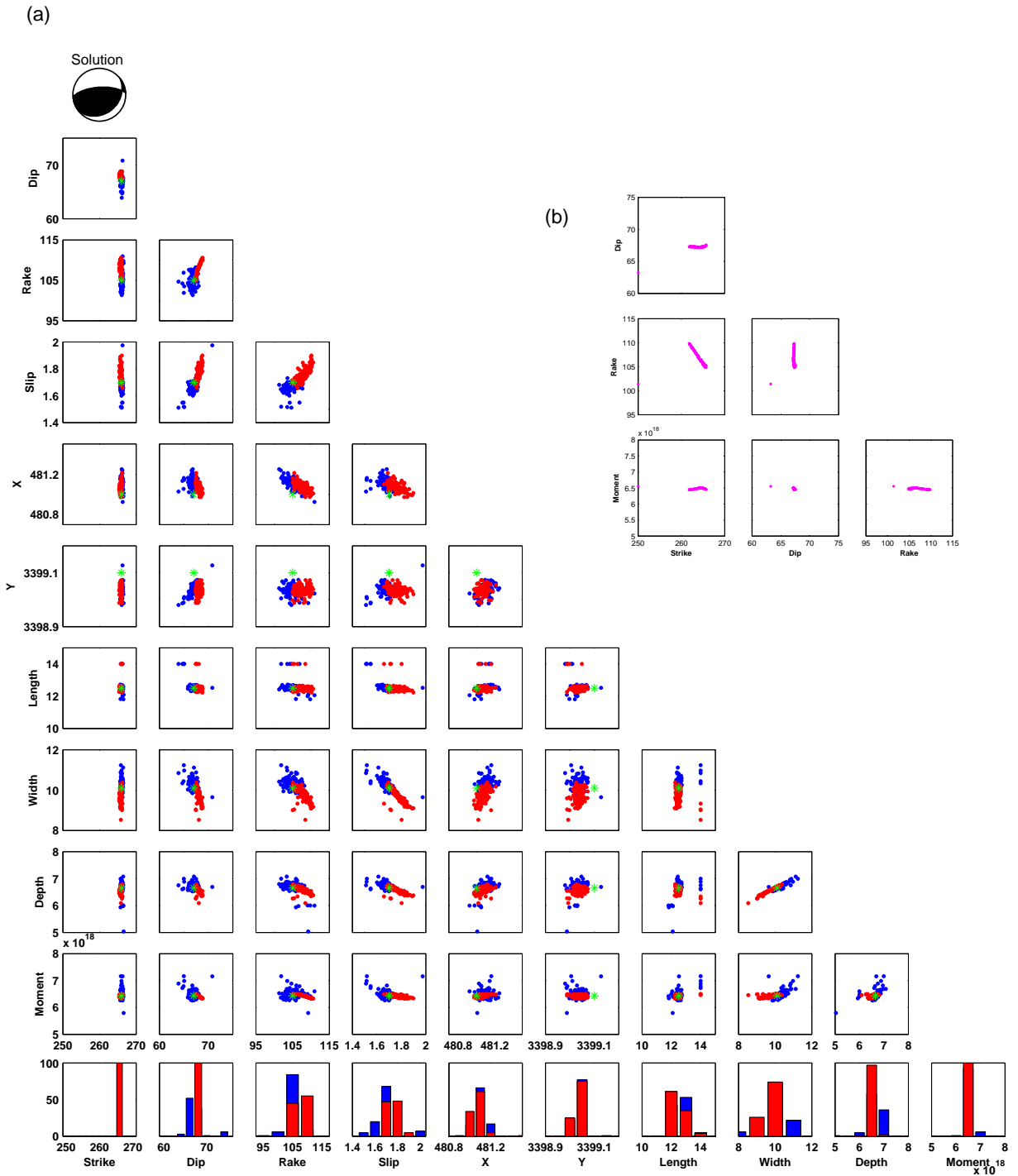


Figure 5.10: a) Tradeoff scatterplots for InSAR only inversion (blue) and joint source inversion (red) for a synthetic thrust faulting event, where the focal mechanism from the joint inversion is shown in red at the top. b) Tradeoff scatterplot for seismic-only inversion. The format for a) and b) follow the same as in Figure 5.7.

5.6 Case Study: Eureka Valley, M_w 6.1, 17th May 1993

The Eureka Valley, California, earthquake was part of a sequence of events including the large strike-slip Landers earthquake (M_w 7.3, 26th June 1992). The Eureka Valley is on the California-Nevada border, within the Basin and Range Province (Figure 5.11). Regional extension plays an important role in driving the deformation within the Pacific-North American plate boundary zone (*e.g.* Atwater, 1970). The event occurred on a buried normal fault which is one of five currently known normal fault zones between the Panamint Valley - Hunter Mountain - Saline Valley fault system and the Furnace Creek and Fish Lake Valley faults (Oswald and Wesnousky, 2002). These fault systems make up part of the Eastern California Shear Zone, which is thought to accommodate the relative motion between the Pacific and North American plates not taken up by the San Andreas fault system, west of the Sierra Nevada (*e.g.* Atwater, 1970).

The Eureka Valley earthquake was a M_w 6.1 normal faulting event, which occurred at 23.20 (GMT) on 17th May 1993. More than 500 aftershocks followed the event (Asad *et al.*, 1999), including three larger than magnitude 4.5 (Massonnet and Feigl, 1995). It was one of the first events to be measured using InSAR (see Table B.6 for existing studies, Massonnet and Feigl, 1995; Peltzer and Rosen, 1995), and the quality of the geodetic data is very high; the coseismic signal is extremely clear due to low levels of noise and high coherence, therefore strong constraints can be placed on the location and strike (see Figure 5.12a). Consequently, this event is partly a test of the efficiency of the new technique. However, there is a large discrepancy of about 55 km between the earthquake's location determined using InSAR (Massonnet and Feigl, 1995) and that reported in the GCMT catalogue, which motivates this case study. By modelling the seismic data using the earthquake's location constrained by InSAR data alone and a different Earth model to the one employed by the GCMT catalogue, this case study investigates whether the two data sets can be reconciled.

A descending interferogram is calculated from two ERS-1 SAR images, spanning 525 days, and is downsampled to 795 points (see Figure 5.12a). The seismic dataset is comprised of data from 17 seismic stations which includes a total of 34 waveforms (18 LPS, 16 LPB; see Figures 5.13 and 5.14).

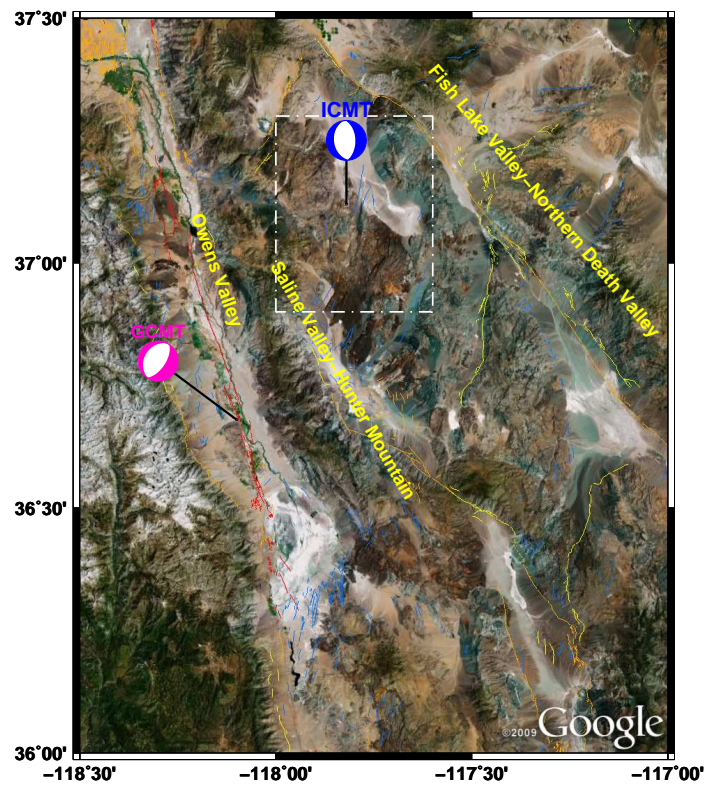
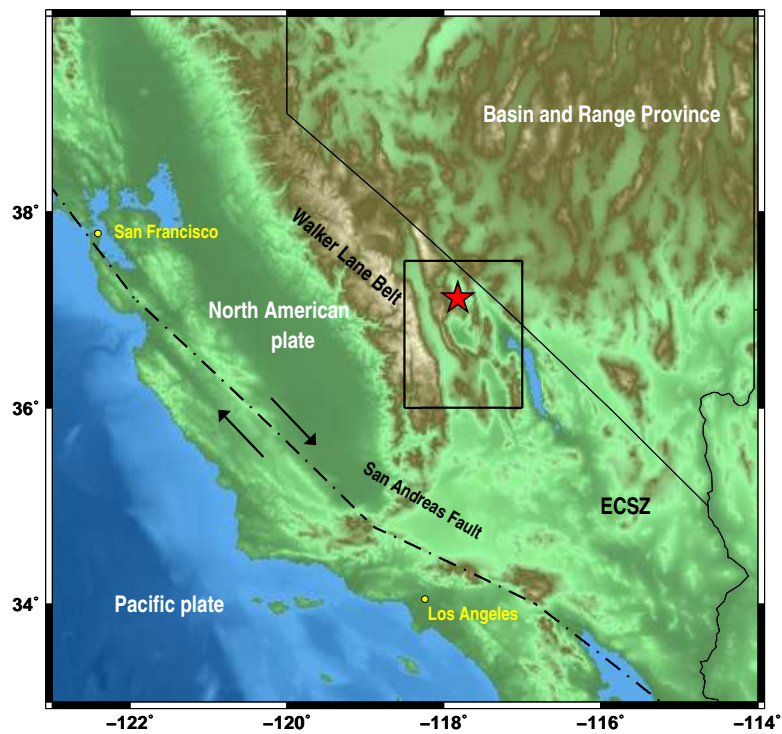












Figure 5.11: Map on the left provides an overview of the overall tectonic setting of northern California, due to the movement of the Pacific and North American plates. The Eureka Valley earthquake is denoted by the red star, and the black square refers to the map on the right, which shows the relevant fault zones (based on USGS fault maps) highlighted in yellow. Focal mechanisms for the event from the GCMT catalogue and results in this study (ICMT) are shown in pink and blue, respectively and the dashed white box corresponds to the area covered by the InSAR data in Figure 5.12. It should be noted that that there are 55 km between the ICMT and GCMT locations.

Table 5.3 shows the results for the individual and joint inversions. The fault strike estimated using long period surface waves is relatively close to that found using InSAR data. However, the best fit strike from the long period body wave inversions favours a fault which strikes $\sim 30^\circ$ more north-westerly. Table 5.3 suggests a potential tradeoff between dip and moment for the long period surface waves, with the dip angle being lower and the seismic moment being larger than in all other inversions. Nevertheless, when all three datasets are combined the resulting moment in comparison with the surface wave inversion, is much reduced (1.2×10^{18} Nm). The dip from the joint inversion is a compromise between the slightly steeper angle suggested by geodetic data and the shallower values preferred by the seismic data. Overall the fit of the joint inversion result to the InSAR data is very good (Figure 5.12 b & c) with no obvious fringes present in the residual interferogram (the difference between the data and forward modelled result). The more north-easterly strike favoured in the body wave inversion is also tested (Figure 5.12 d) and although the shape of the deformation signal is similar to the data the orientation results in a mislocation of the pattern and consequently high residuals (Figure 5.12 e). The joint inversion solution fits the seismic data reasonably well (Figures 5.13 & 5.14). For a few stations there is a slight underestimation of the surface wave amplitudes (*e.g.*, stations NNA, GUMO, CHTO, Figure 5.13 a & b). However, the P-wave arrivals are modelled well in the body wave comparisons (Figure 5.14 a & b). Figure 5.15 shows the tradeoffs between the various source parameters for InSAR-only inversions (blue), seismic-only inversions (pink) and joint inversions (red). There is a slight tradeoffs between strike and rake in the seismic-only inversions (Figure 5.15 b) but the rake is more tightly clustered than in the InSAR-only inversion. The joint inversion results overall are more tightly clustered, in particular for the fault dip angle and slip, but there is a clear tradeoff between fault strike and rake and also strike and latitude. This and how this source model compares with existing ones is discussed in section 5.9.

Table 5.3: Summary of source inversion results for the M_w 6.1 Eureka Valley earthquake. Models from previous studies are listed in the top lines followed by results from this study. The latitude, longitude and depth refer to the centroid location and the misfit value (m^2) refers to an L2-norm misfit. Parameters fixed during the inversion are highlighted in bold. LPS refers to long period surface waves and LPB long period body waves.

Model	Mo ($\times 10^{18} Nm$)	Lat. ($^\circ$)	Lon. ($^\circ$)	Depth (km)	Strike ($^\circ$)	Dip ($^\circ$)	Rake ($^\circ$)	Slip (m)	Length (km)	Width (km)	Misfit m^2	-
Existing studies												
Massonet & Feigl (1995)	1.57	37.11	-117.790	9.2	173.0	54.0		0.43	16.4	7.4		
Peltzer & Rosen (1995)				13.0	187.0	50.0			15.0	16.0		
Asad et al., (1999)					165.0	60.0						
Ichinose et al., (2003)					193.0	48.0	-102.0					
Ritsema & Lay	1.4	37.20	-117.80	10.0	37.0	49.0	-66.0					
GCMT	1.83	36.68	-118.100	15.0	210.0	30.0	-93.0					
This Study												
InSAR	1.60	37.11	-117.79	8.6	173.8	41.4	-87.3	0.36	16.6	9.1	0.011	
LPS	1.93	37.11	-117.79	12.0	181.9	24.0	-122.6	0.26	16.6	14.7	0.090	
LPB	1.15	37.11	-117.79	12.0	212.1	35.0	-71.7	0.22	16.6	10.5	0.220	
LPS, LPB	1.39	37.11	-117.79	12.0	215.3	35.5	-63.9	0.27	16.6	10.3	0.200	
InSAR, LPS	1.39	37.13	-117.78	8.5	173.5	51.3	-113.2	0.66	11.0	6.3	0.051	
InSAR, LPB	1.22	37.11	-117.79	6.7	175.3	34.3	-81.8	0.32	15.2	8.3	0.036	
InSAR, LPS, LPB	1.18	37.11	-117.79	6.7	175.3	35.5	-94.4	0.33	15.0	7.9	0.049	

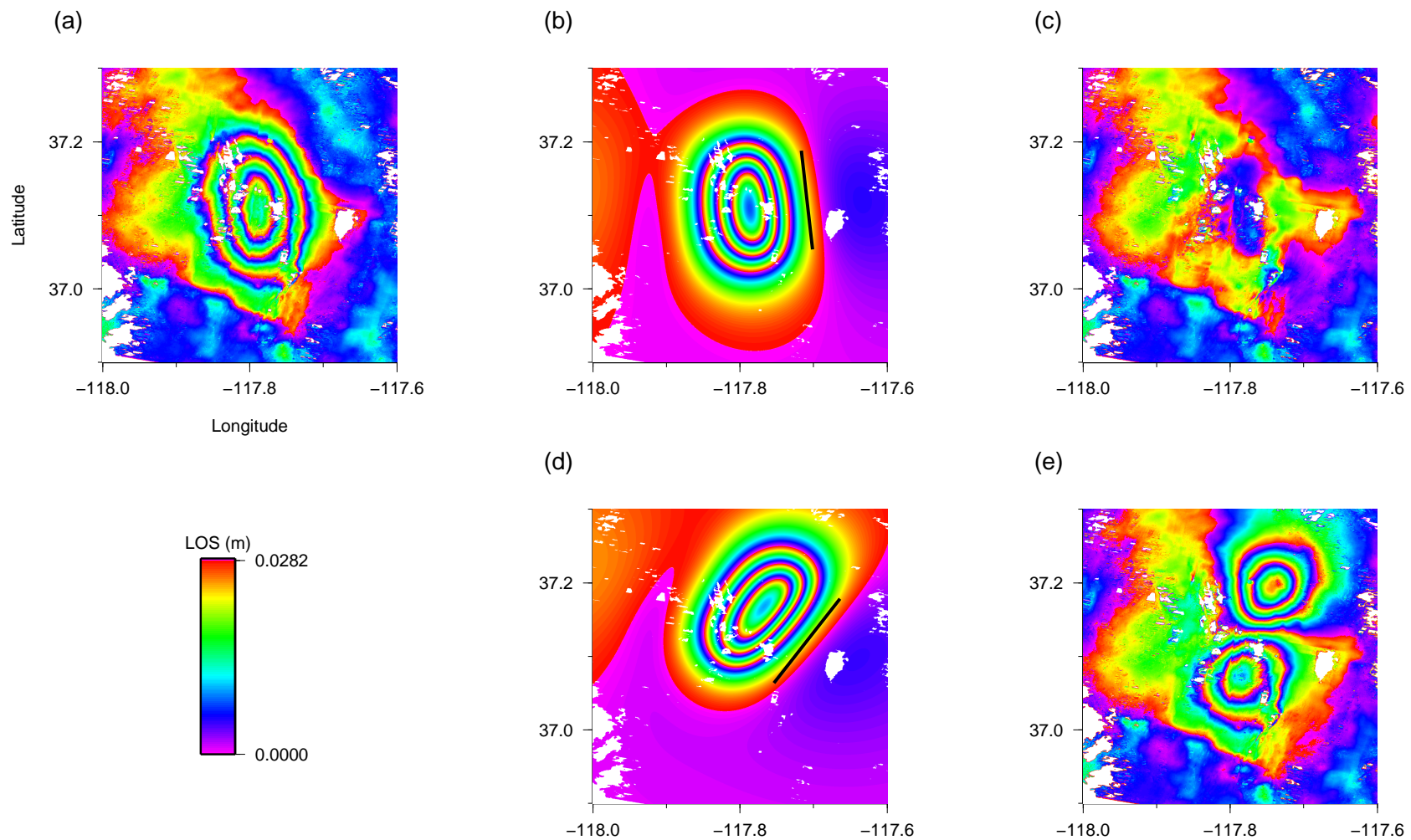


Figure 5.12: a) Descending interferogram calculated from 2 ERS-1 images (01/06/1992 and 08/11/1993, Track 442) b) Forward modelled interferogram using joint inversion result for the M_w 6.1 Eureka Valley earthquake listed in Table 5.3, where the updip projection of the top of the fault to the surface is denoted by the black line c) Residual between interferogram (a) and forward modelled result (b). d) Shows the interferogram calculated using the joint inversion results, except the strike has been replaced with the value from the body wave inversion, which shows large disagreement with the joint inversion result and existing studies (Table 5.3). The black line represent the updip projection of the top of the fault to the surface. e) This is the residual between the model in d) and the data in a), which highlights the poor fit between this model and the data.

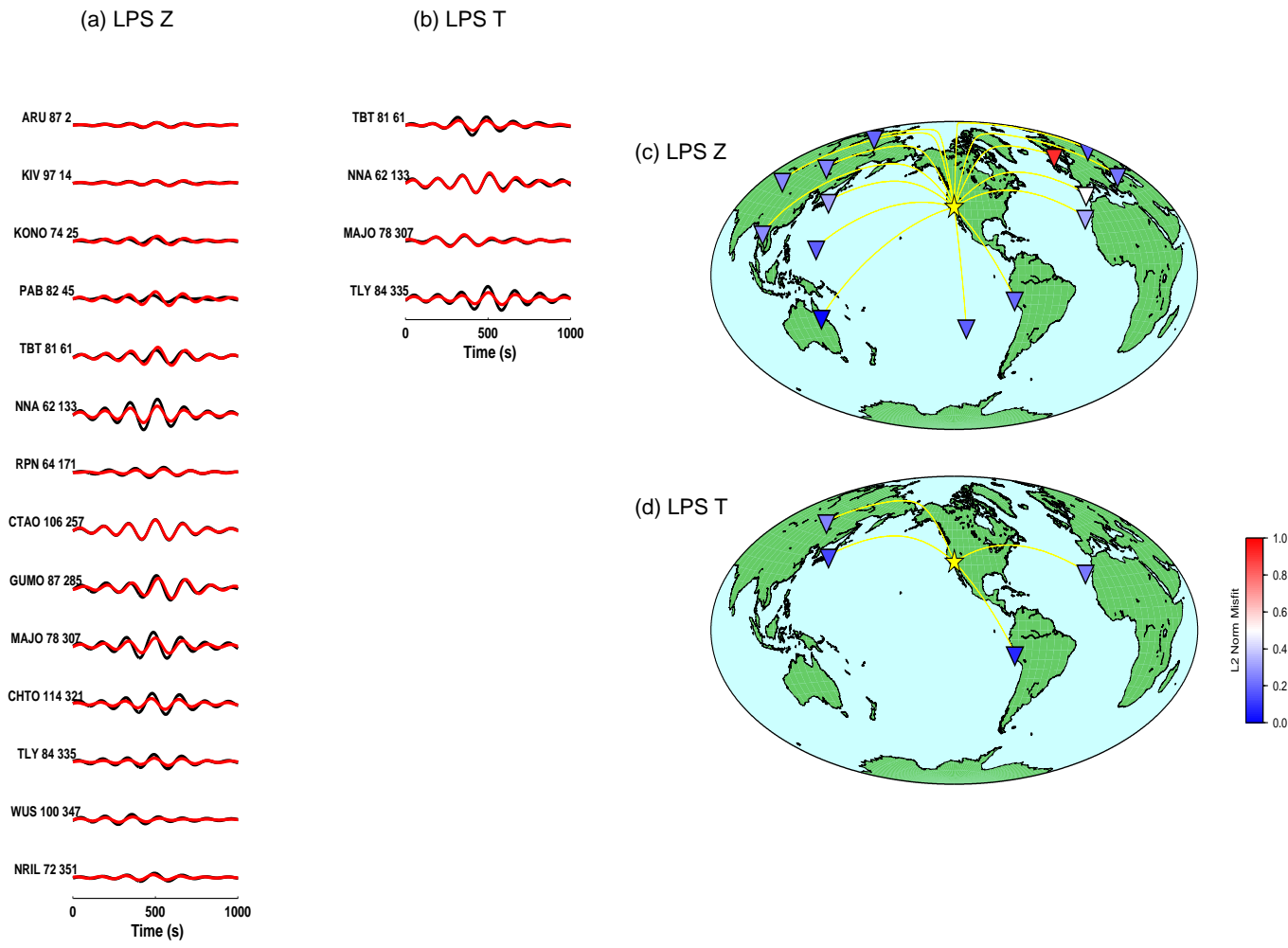


Figure 5.13: a) - b) Fit of joint inversion results for the M_w 6.0 Eureka Valley earthquake (red) to the data (black), filtered for long period surface waves (LPS) where vertical (Z) and transverse (T) components are shown, respectively. The station name, epicentral distance and azimuth are shown next to each waveform. Phase offsets between the modelled and real seismograms could suggest unmodelled heterogeneity in the Earth model used. c) - d) The station distribution and its corresponding misfit to the data for the vertical and transverse components, respectively. Great circle paths are shown in yellow and the yellow star denotes the earthquake location.

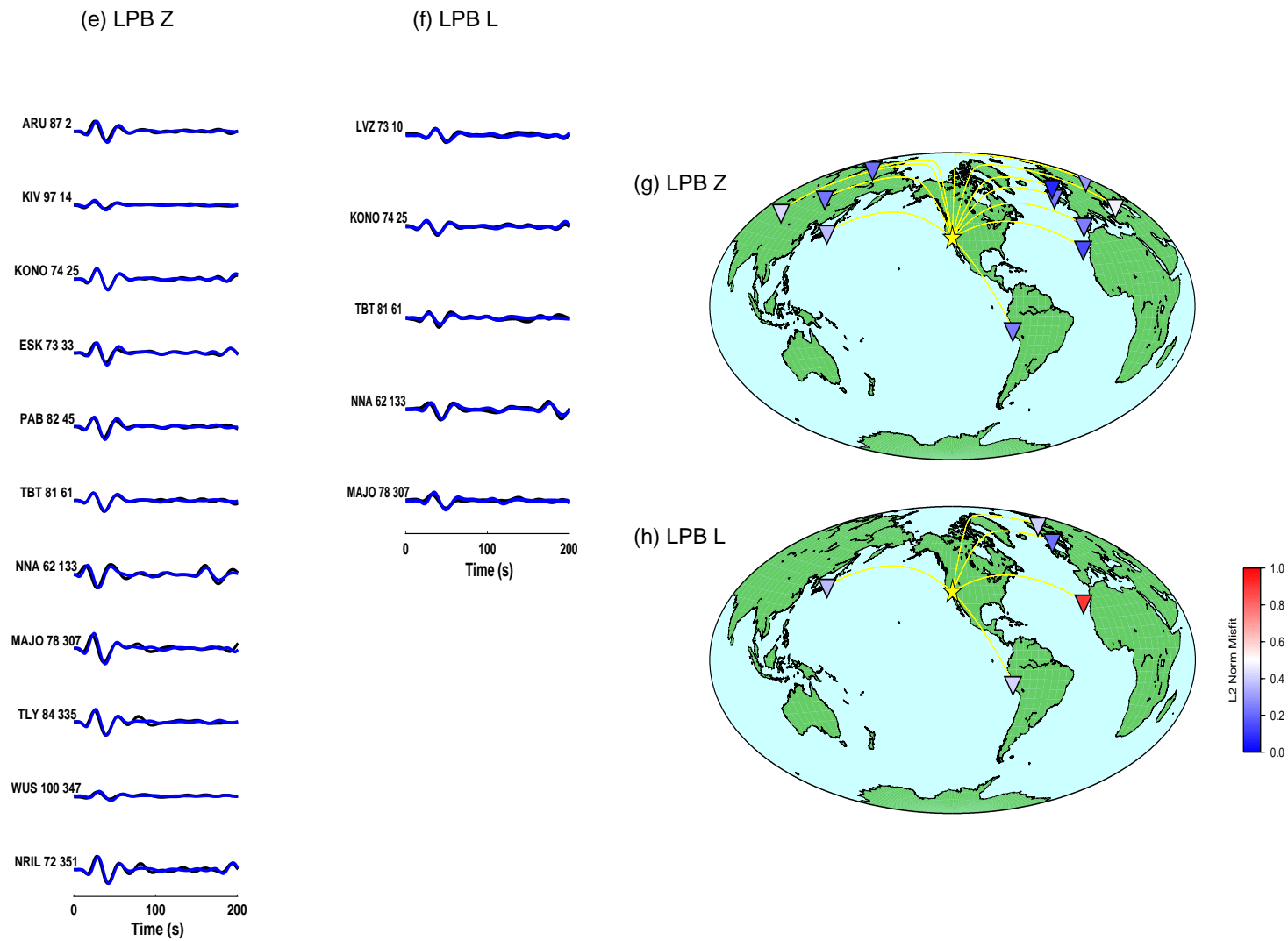


Figure 5.14: a) - b) Fit of joint inversion results for the M_w 6.0 Eureka Valley earthquake (blue) to the data (black), filtered for long period body waves (LPB) where vertical (Z) and longitudinal (L) components are shown, respectively. c) - d) The station distribution and its corresponding misfit to the data for the vertical and longitudinal components, respectively. The format is the same as in Figure 5.13.

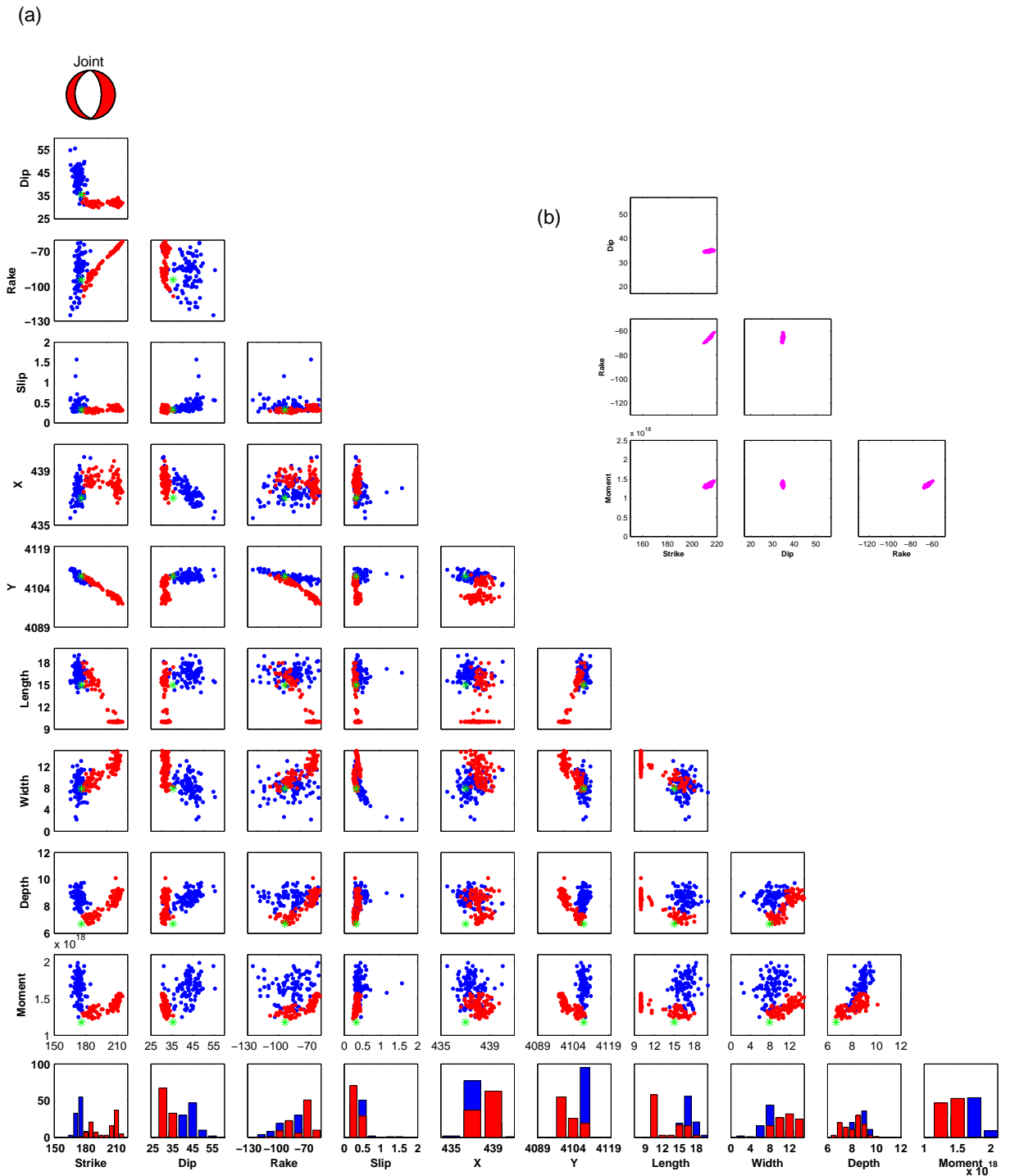


Figure 5.15: a) Tradeoff scatterplots for InSAR only inversion (blue) and joint source inversion (red) for the M_w 6.0 Eureka Valley earthquake, with the focal mechanism from the joint source inversion shown in red at the top. b) Tradeoff scatterplots for seismic only inversion. Format is same as in Figure 5.7.

5.7 Case Study: Aiquile, Bolivia, M_w 6.5, 22nd May 1998

The 1998 Aiquile, Bolivia, earthquake occurred in the Eastern Cordillera section of the Bolivian Andes (Figure 5.16). The central Andes form the widest part of the mountain chain (~ 700 km) and much of the topography reaches elevations of 3-4 km (Lamb, 2000). This section of the Nazca-South American subduction zone is the focus of much research due to the bending of the Bolivian orocline. It is part of the orogenic belt at $\sim 17^\circ$ S, where there is an abrupt change in the horizontal topographic trend, and it is suggested that this is part of mountain range development which initially forms in a linear geometry. Paleomagnetic and velocity gradient studies suggest that this bending has occurred in the last 10 My (*e.g.* Isacks, 1988; Lamb, 2000; Roperch *et al.*, 2000; McQuarrie, 2002). GPS observations have also been interpreted as observations of the bending in real time (over the past two decades) at rates comparable to geological rates (Allmendinger *et al.*, 2005). Presently the convergence of the Nazca-South American plate is accommodated through the movement of the Bolivian Andes towards the continent's interior at 7-10 mm yr⁻¹ (Brooks *et al.*, 2011). It is a complicated region and robust earthquake source models will help us gain insight into the tectonic mechanisms driving the deformation and the resulting changes in the stress regime, important for assessing the seismic hazard.

The M_w 6.6 earthquake struck the mountainous region of Aiquile on 22nd May 1998 at 04.48 (GMT) and resulted in over 100 deaths and caused widespread damage (Funning *et al.*, 2005a). Locations reported in seismic catalogues (GCMT, ISC, EHB, NEIC) and studies with geodetic data (Funning *et al.*, 2005a; Devlin *et al.*, 2012) show a wide variation (Table 5.4), which makes it difficult to identify tectonic structure and mechanism responsible.

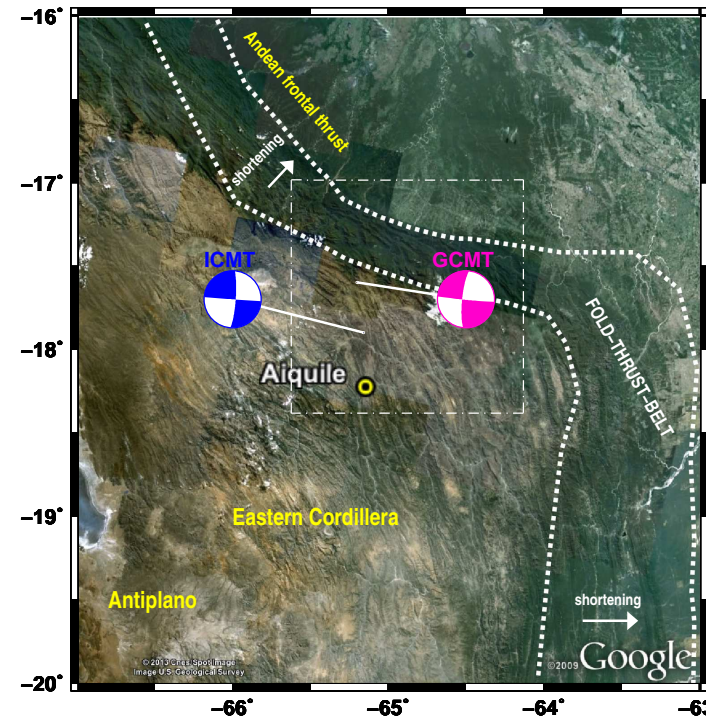
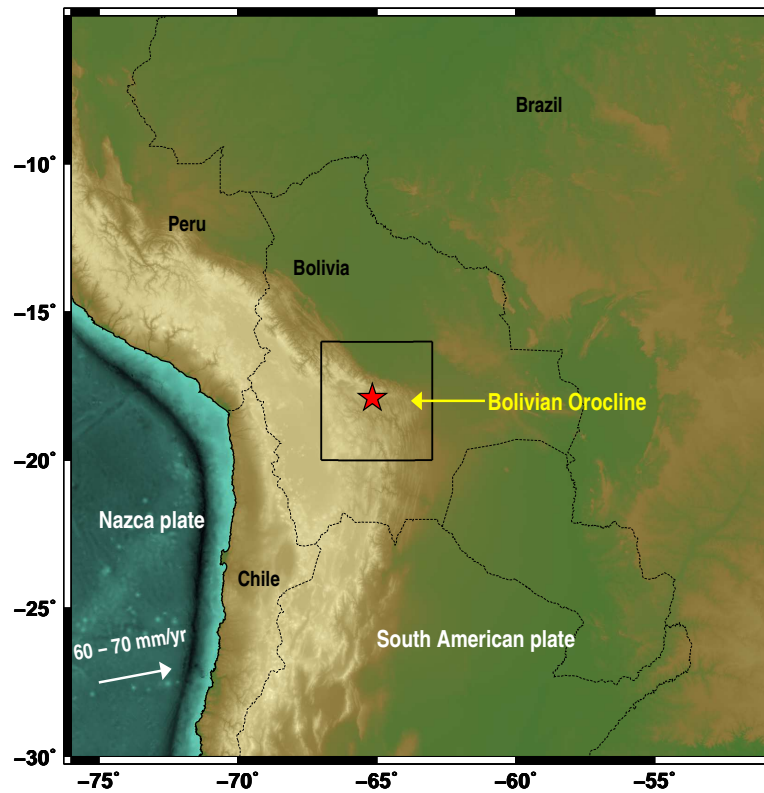



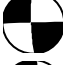










Figure 5.16: Tectonic setting for the M_w 6.6 Aiquile, Bolivia earthquake, denoted by the red star in the map on the left. The black box refers to the figure on the right which shows the focal mechanisms from the GCMT catalogue and this study (ICMT) in pink and blue, respectively. The location of town of Aiquile is shown by the yellow circle and the dashed white box refers to the area covered by the InSAR data shown in Figure 5.19. The high central plateau known as the Antiplano and the more rugged region of the Eastern Cordillera, which reaches heights of 6.5 km (Lamb, 2000) and forms part of the Bolivian Andes, are also highlighted.

The InSAR data for this event are extremely poor due to high levels of noise and poor coherence, and although different studies have found the fault to be near vertical, various InSAR studies and the GCMT catalogue report different dip directions (Funning *et al.*, 2005a; Devlin *et al.*, 2012) and large differences in epicentral location (see Chapter 3). One descending interferogram spanning 821 days is calculated from SAR images taken using the ERS-2 satellite (Figure 5.19 a), this large measurement period is likely partly responsible for the poor quality of the data and could include deformation signals due to events other than the earthquake. Seismic data from 38 stations are used, which results in a total of 86 waveforms (52 LPS, 34 LPB; see Figures 5.17–5.18).

Separate inversions of all three datasets show a general good agreement, favouring a steeply-dipping N-S striking fault (Table 5.4). However, there is a clear moment-dip tradeoff in the surface wave inversion, with the corresponding best fit model having a much shallower dip angle and the largest moment estimate of all inversion results. There is a larger thrust component obtained in the body wave inversion and combining the two seismic datasets results in a vertical fault with pure right lateral strike-slip. A combination of all three datasets introduces a tradeoff between the width and slip; the fault width increases to 18 km and a reduction in slip compensates for this. The fit to the long period surface waves is excellent (Figure 5.17). For long period body waves (Figure 5.18), the data fit is still reasonable, but some phase shifts in P and SH wave arrivals are evident at some stations. Moreover, there is a slight azimuthal trend in the fit of the SH wave synthetics to the data (Figure 5.18e). The InSAR data is fit reasonably well, particularly for the east side of the deformation pattern but there are four residual fringes (Figure 5.19 c) to the south-west. This is partly due to the shorter length of the fault (14 km) which is linked with the tradeoff of the fault size and slip, which in turn influences the dip (Figure 5.20 a). In tests with added realistic noise both separate InSAR and seismic inversions favour a steeper dip of 80° but in the joint inversion this is shifted to 50° , this is partly due to the poor quality of the InSAR data and is an issue which is discussed in section 5.9. Despite this though in the joint inversion the strike and rake are much better constrained.

Table 5.4: Summary of source inversion results for the M_w 6.6 Aiquile earthquake. Format is same as in Table 5.3.

Model	Mo ($\times 10^{18}$ Nm)	Lat. ($^{\circ}$)	Lon. ($^{\circ}$)	Depth (km)	Strike ($^{\circ}$)	Dip ($^{\circ}$)	Rake ($^{\circ}$)	Slip (m)	Length (km)	Width (km)	Misfit	
Existing studies												
InSAR, Funning et al., (2005)	7.7	-17.899	-65.164	7.40	7.0	79.0	171.0	1.1	14.5	15.0		
InSAR, Funning et al., (2005) (ds)	8.44	-17.893	-65.177	7.30	7.0	79.0	171.0	0.6	24.0	18.0		
InSAR, Devlin et al., (2012)		-17.910	-65.153	5.8 \pm 0.2	1.0 \pm 1.0	75.0 \pm 1.0	179.0 \pm 1.0		21.0 \pm 1.0	8.0 \pm 1.0		
Seismic, Devlin et al., (2012)		-17.860	-65.539	11.0	358.0	84.0	179.0					
GCMT	8.44	-17.600	-65.200	15.0	186.0	79.0	-178.0					
This study												
InSAR	7.27	-17.899	-65.165	7.4	7.3	79.1	171.3	1.1	14.6	15.0	0.048	
LPS	9.08	-17.899	-65.165	12.0	4.1	60.4	176.1	1.2	15.0	16.7	0.082	
LPB	6.87	-17.899	-65.165	12.0	1.4	87.6	164.5	1.1	15.0	14.5	0.36	
LPS & LPB	7.7	-17.899	-65.165	12.0	4.6	90.0	180.0	1.2	15.0	14.5	0.193	
InSAR, LPS	7.15	-17.899	-65.173	8.3	3.5	82.7	179.5	1.0	13.7	16.6	0.172	
InSAR, LPB	4.64	-17.911	-65.162	7.23	7.5	75.2	161.1	0.87	11.8	15.0	0.156	
InSAR, LPS, LPB	6.75	-17.901	-65.169	8.9	4.2	81.1	179.8	0.89	14.0	18.0	0.188	

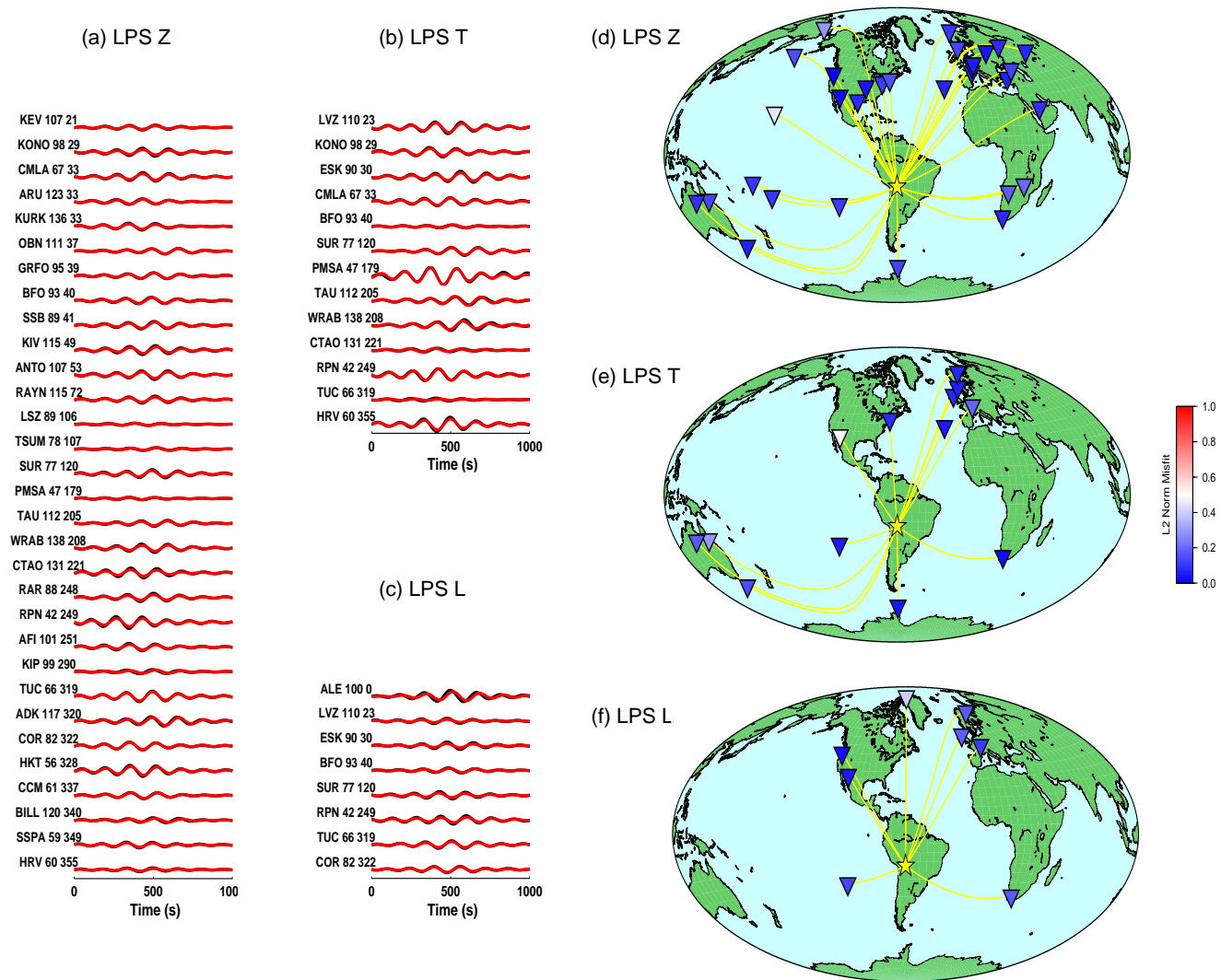


Figure 5.17: a) - c) Fit of joint inversion results for the M_w 6.6 Aiquile earthquake (red) to the data (black), filtered for long period surface waves (LPS) where vertical (Z) transverse (T) and longitudinal (L) components are shown, respectively. The station name, epicentral distance and azimuth are shown next to each waveform. d) - f) Show the station distribution and its corresponding misfit to the data for the vertical, transverse and longitudinal components, respectively. Great circle paths are shown in yellow and the yellow star denotes the earthquake location.

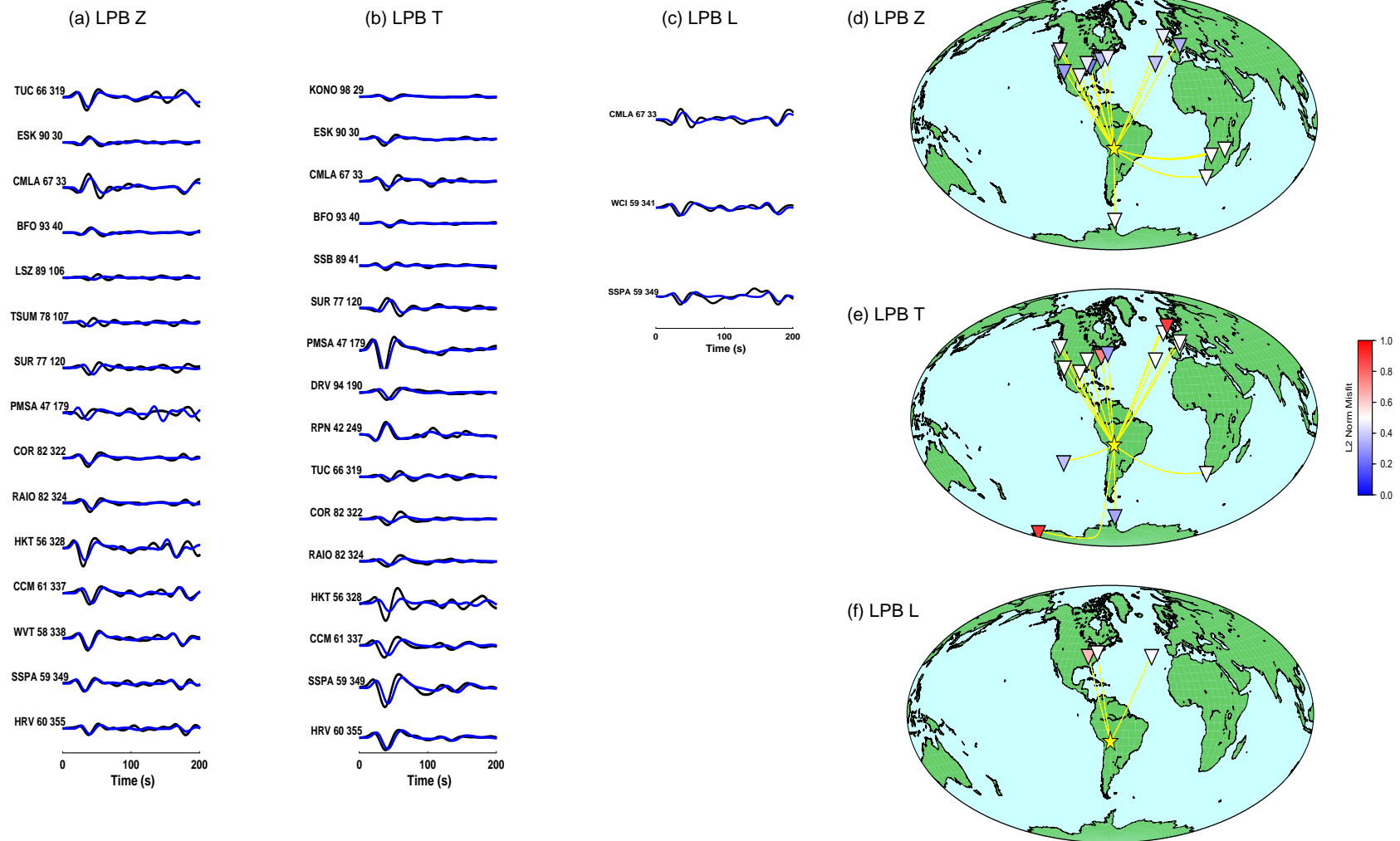


Figure 5.18: a) - c) Fit of joint inversion results for the M_w 6.6 Aiquile earthquake (blue) to the data (black), filtered for long period body waves (LPB) where vertical (Z) transverse (T) and longitudinal (L) components are shown, respectively. The station name, epicentral distance and azimuth are shown next to each waveform. d) - f) The station distribution and its corresponding misfit to the data for the vertical, transverse and longitudinal components, respectively. Great circle paths are shown in yellow and the yellow star denotes the earthquake location.

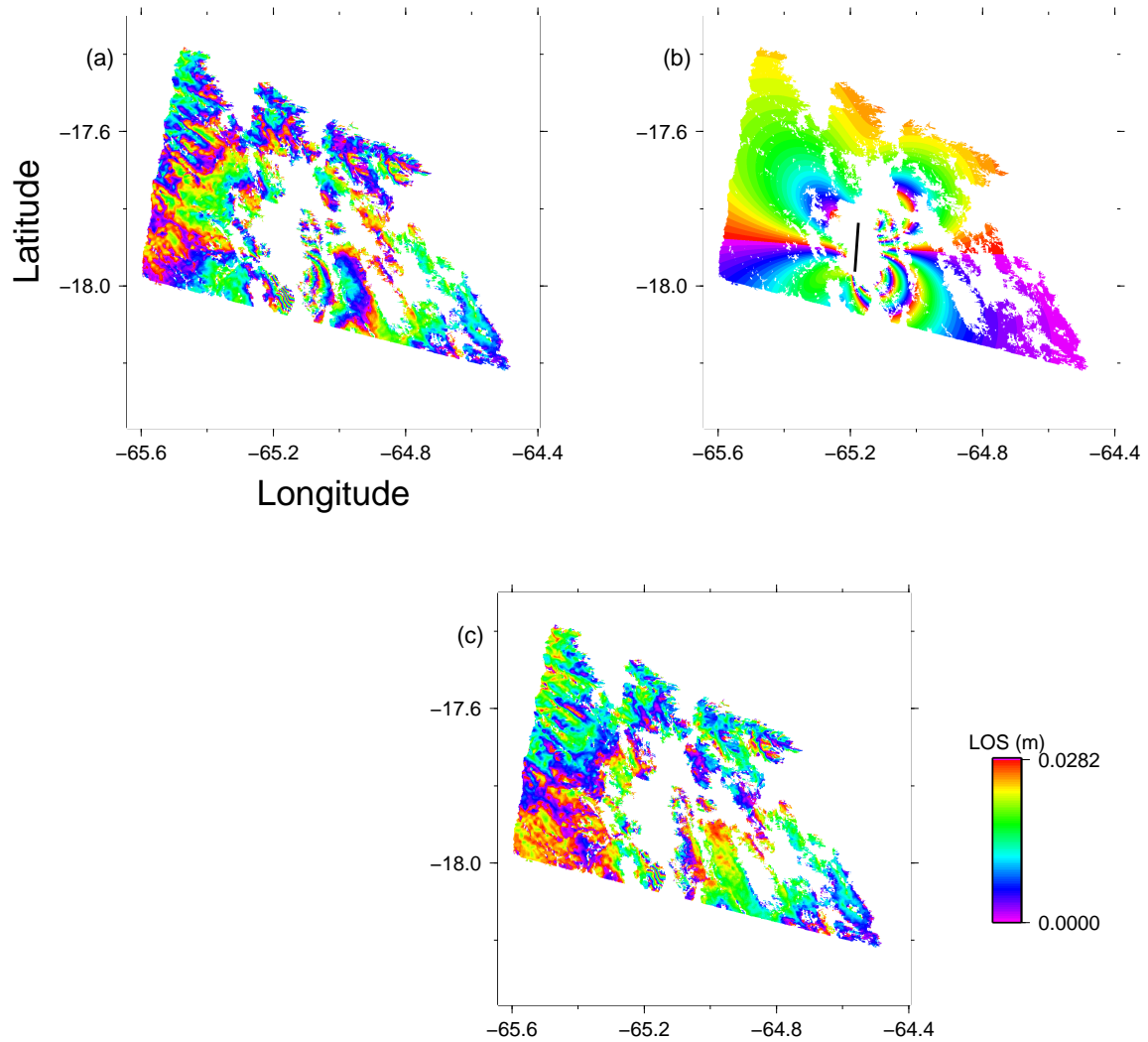


Figure 5.19: a) Descending interferogram calculated from 2 ERS-2 images (11/04/1996 and 30/07/1998, Track 239) b) Forward modelled interferogram using joint inversion result for the M_w 6.6 Aiquile, Bolivia earthquake listed in Table 5.4. The black line represents the updip projection of the top of the fault to the surface. c) Residual between interferogram (a) and forward modelled results (b).

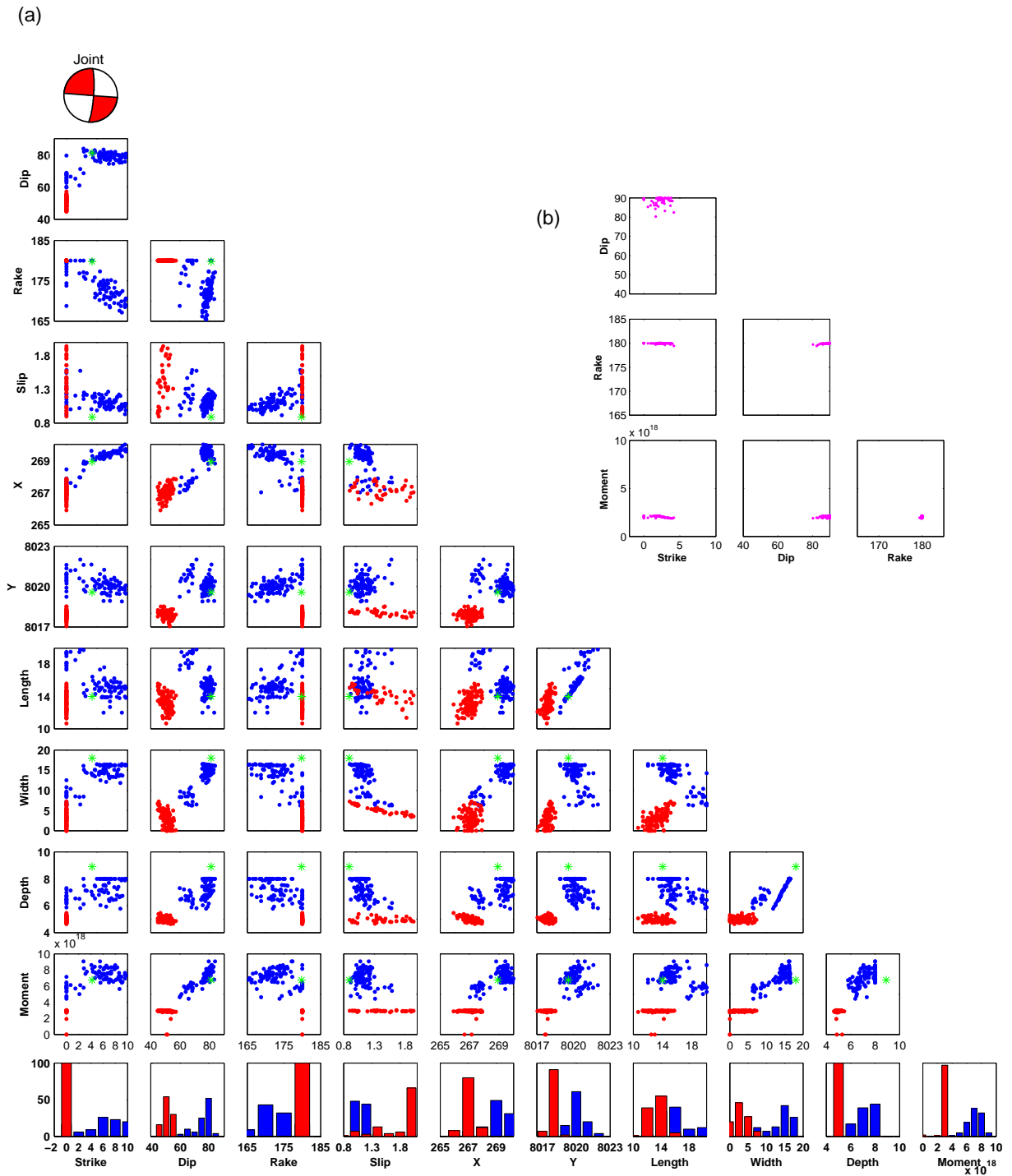


Figure 5.20: a) Tradeoff scatterplots for InSAR only inversion (blue) and joint source inversion (red) for the M_w 6.6, Aiquile earthquake, with the focal mechanism from the joint source inversion shown in red at the top. b) Tradeoff scatterplots for seismic only inversion. Format is same as in Figure 5.7.

5.8 Case Study: Zarand, Iran, M_w 6.5, 22nd February 2005

The 2005 Zarand, Iran earthquake occurred on a previously known fault in the Kerman province in south-central Iran. This region is shortening due to the collision of the Arabian and Eurasian plates (Figure 5.21), which are converging at a rate of $\sim 24 \text{ mm yr}^{-1}$ (Rouhollahi *et al.*, 2012). The fault is part of the Kuhbanan fault zone (Figure 5.21); however, unusually, this reverse event occurred on a fault plane oblique to the edge of the mountain range, as defined by the Kuh-Banan fault (Talebian *et al.*, 2006). Furthermore, the seismic potential of this fault was underestimated due to its unclear geomorphological expression and lack of evidence for recent activity. This is thought to be due to the high levels of erosion as a result of winter rain, snow melt and weak rocks. Triassic-Jurassic sediments mostly comprised of sandstones and shales make up much of the epicentral region (Talebian *et al.*, 2006).

The M_w 6.5 earthquake occurred at 02.25 (GCMT) on the 22nd February 2005, and caused over 500 fatalities (Rouhollahi *et al.*, 2012), only a year after the Bam earthquake which ruptured a blind strike-slip fault further south (*e.g.* Talebian *et al.*, 2004), and resulted in more than 30,000 fatalities (USGS, 2010). These two earthquakes highlight the difficulty of estimating the seismic hazard in this region. Therefore, robust source models are beneficial for gaining insight into the tectonic processes driving the deformation in this region, and consequently to achieve a better understanding of the potential for future earthquakes.

Two interferograms (ascending and descending) calculated using images from ENVISAT were available for this event (Figure 5.22 a & b). However, the signal is very decorrelated near the fault due to steep terrain, possible snow, coseismic ground shaking, and landslides (Talebian *et al.*, 2006). The dip reported by the GCMT catalogue is much shallower than those reported by existing studies (Table 5.5, Talebian *et al.*, 2006; Rouhollahi *et al.*, 2012). This event is the most recent of all the three case studies and the second highest in moment magnitude. A total of 92 seismic waveforms are used (46 LPS, 46 LPB) from 36 stations (see Figures 5.23–5.24).

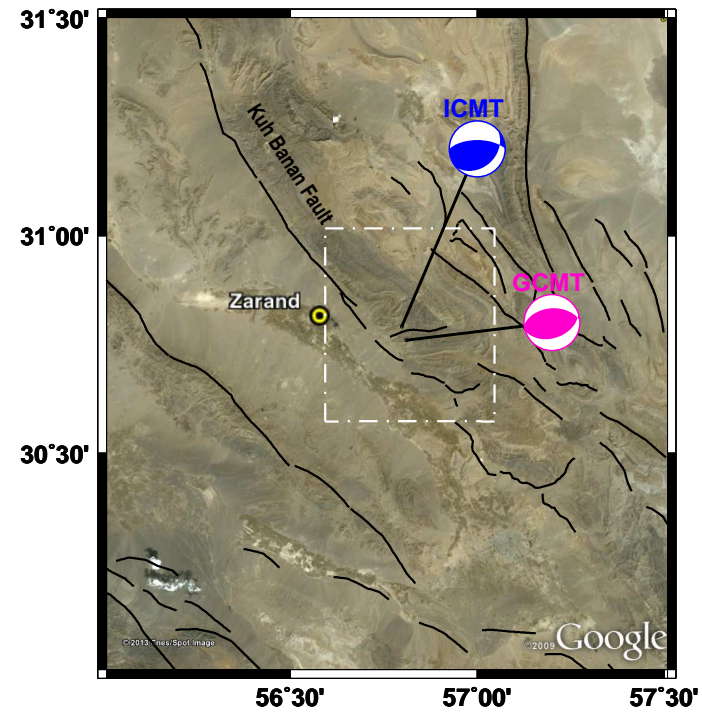
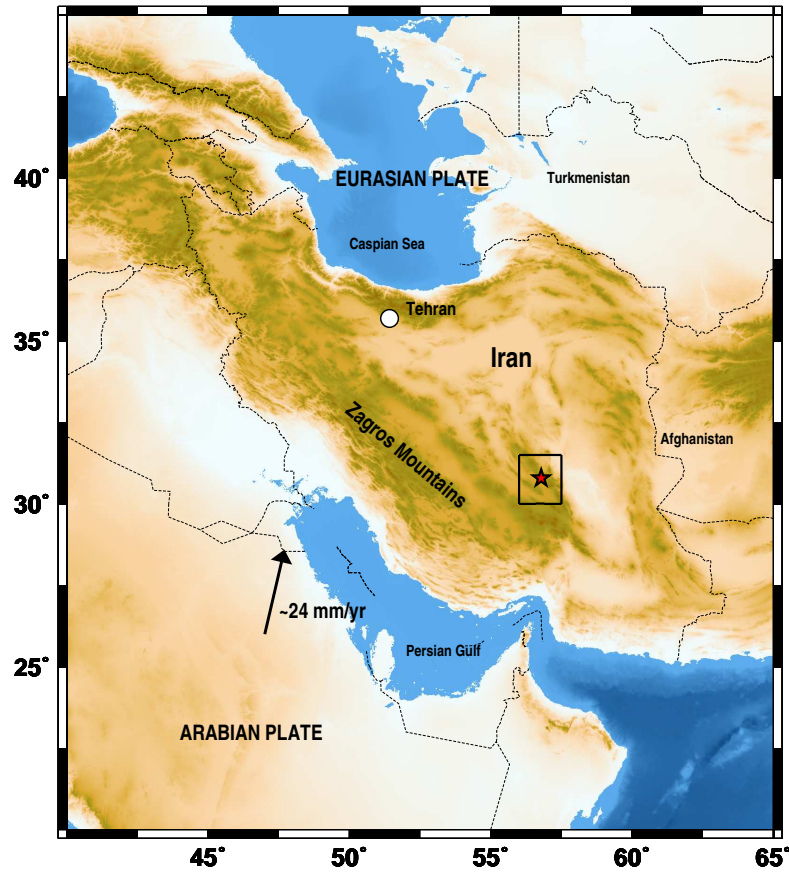















Figure 5.21: Tectonic setting for the M_w 6.5 Zarand, Iran earthquake. Map on the left shows the overall regime due to the collision of the Arabian and Eurasian plates. The earthquake location is denoted by the red star and the black box refers to the figure on the right, where known faults in the region are shown in black, including the Kuh Banan fault zone, locations are from (Walker *et al.*, 2009). The white dashed box refers to the area covered by the two sets of InSAR data shown in Figure 5.22, and the focal mechanisms from the GCMT catalogue and this study (ICMT) are shown in pink and blue respectively.

Table 5.5 shows that separate inversions of the two interferograms result in source parameters which disagree regarding fault geometry, where the ascending data favour a larger right lateral strike-slip component and a much higher moment. The source model from the ascending interferogram shows a higher misfit to the data and hence is given less weight than the descending data in the subsequent joint inversions. The best fit model from the inversion using only body wave data exhibits a strike, dip and rake similar to the InSAR-only solutions, however, the moment is the lowest of all the source models ($M_0 = 3.78 \times 10^{18}$ Nm). The resulting source model from the joint inversion of InSAR and LPS is very similar to that calculated using InSAR and LPB. A joint inversion of InSAR, surface and body waves results in a model which in general fits the seismic data well, particularly the LPS (Figure 5.23), where a slight azimuthal trend in the misfit of the vertical component data is apparent (poorer fit for stations at 90° and 270° , Figure 5.23d). Overall the body wave data fit is good (Figure 5.24), except for a few stations, notably for some SH waves (*e.g.*, for stations DGAR, PAB, TSUM, WRAB in Figure 5.24 b & e). The optimal source model from the joint inversion fits the observed deformation pattern reasonably well, for the descending interferogram. However, there are several fringes in the ascending residual (Figure 5.22 c) and the tradeoff plots in Figure 5.25 clearly show the disagreement in source parameters between the two interferograms, this issue is discussed in section 5.9. The seismic-only inversions (Figure 5.25 b) are relatively tightly clustered, although there is a slight tradeoff in strike and moment. There is an improvement when the two interferograms are jointly inverted with the seismic data, the results (red stars, Figure 5.25) are much more tightly clustered, and the moment, dip and rake are particularly better constrained than in single-data type inversions.

Table 5.5: Summary of source inversion results and existing studies for the M_w 6.5 Zarand earthquake. Format is same as in Table 5.3.

Study	Mo ($\times 10^{18}$ Nm)	Lat ($^{\circ}$)	Lon ($^{\circ}$)	Depth (km)	Strike ($^{\circ}$)	Dip ($^{\circ}$)	Rake ($^{\circ}$)	Slip (m)	Length (km)	Width (km)	m^2	
Existing studies												
Bodywaves, Talebian et al., (2006)	4.9	56.736	30.774	7.93	270	60	104	0.8				
InSAR - Talebian et al., (2006)	6.7			4.8	266	67	105	1.7	12.6	10.4		
Strong motion - Rouhollahi et al. (2012)	7.0				260.0	60.0	104.0		18.0	14.0		
GCMT	5.2	56.800	30.760	12.0	266.0	46.0	124.0					
EHB		56.790	30.710									
This study												
InSAR	6.25	56.792	30.754	3.8	270.9	65.0	107.8	2.23	13.1	7.2	0.018	
InSAR Asc	7.44	56.793	30.805	4.8	264.2	62.5	110.1	2.1	13.8	8.6	0.062	
InSAR Dsc	6.91	56.806	30.799	4.1	273.4	64.6	96.8	2.0	13.4	8.7	0.005	
LPS	8.52	56.797	30.803	12.0	284.2	24.2	136.2	1.1	13.0	20.75	0.100	
LPB	3.78	56.797	30.803	12.0	272.3	55.8	104.9	0.94	13.0	10.3	0.530	
LPS & LPB	5.0	56.797	30.803	12.0	272.9	53.4	110.0	1.2	13.0	10.6	0.426	
InSAR & LPS	6.36	56.804	30.798	3.9	270.4	64.9	103.2	2.1	13.1	7.6	0.029	
InSAR & LPB	6.56	56.805	30.799	4.1	269.0	65.4	94.9	2.1	13.0	7.9	0.041	
InSAR, LPS & LPB	6.50	56.805	30.799	4.1	269.1	65.2	97.03	2.1	13.0	7.9	0.046	

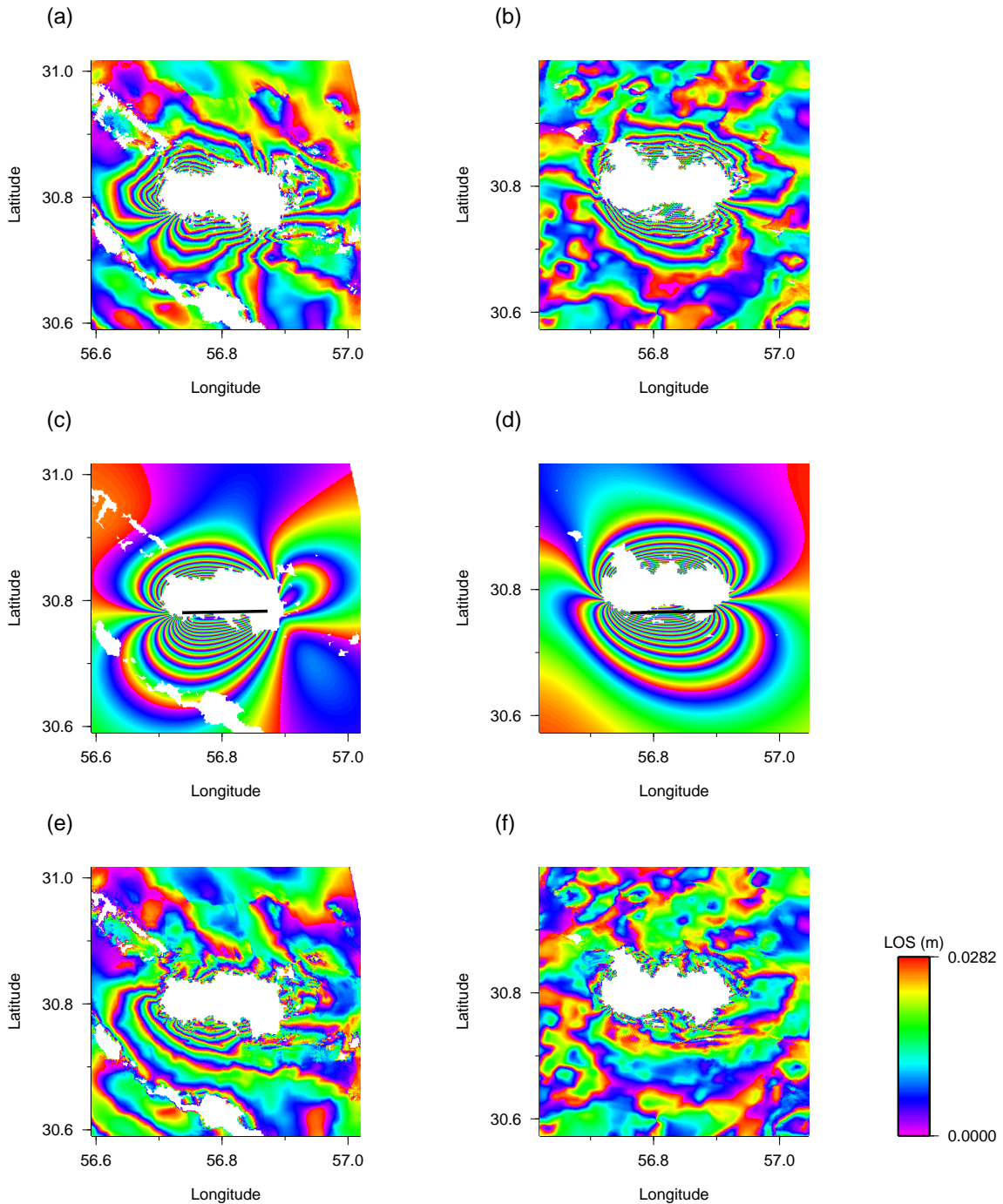


Figure 5.22: Fit of joint inversion results for the M_w 6.5 Zarand earthquake. a) Ascending interferogram calculated using two images from 19/09/04 and 13/03/05, taken on track 285. b) Descending data calculated using images from 17/02/05 and 24/03/05 on track 435. The second row c) and d) are synthetic ascending and descending interferograms, respectively, forward modelled using the joint source inversion result. e) - f) are the residuals for the ascending and descending data and results, respectively.

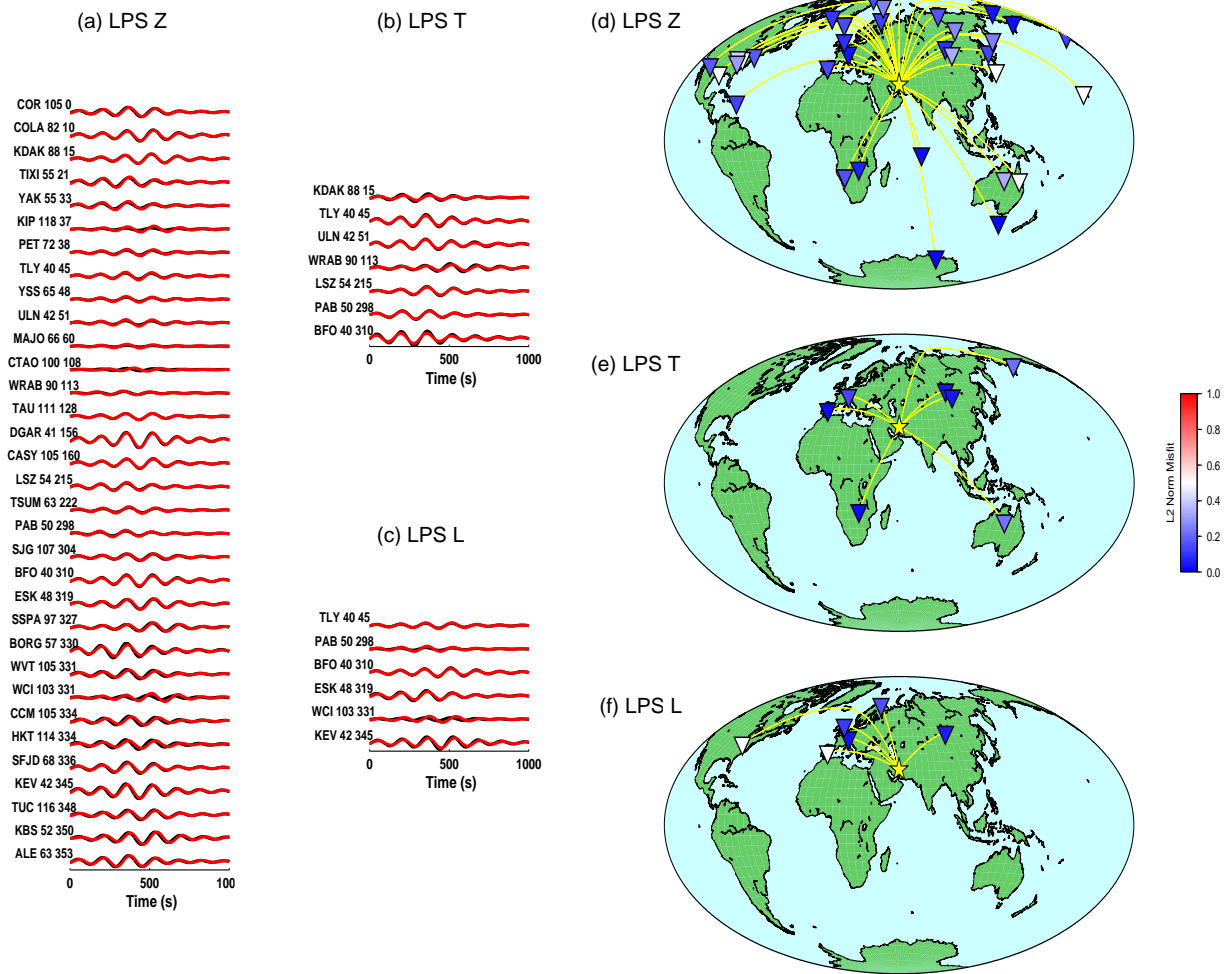


Figure 5.23: a) - c) Fit of joint inversion results for the M_w 6.5 Zarand earthquake (red) to the data (black), filtered for long period surface waves (LPS) where vertical (Z) transverse (T) and longitudinal (L) components are shown, respectively. The station name, epicentral distance and azimuth are shown next to each waveform. d) - f) The station distribution and its corresponding misfit to the data for the vertical, transverse and longitudinal components, respectively. Great circle paths are shown in yellow and the yellow star denotes the earthquake location.

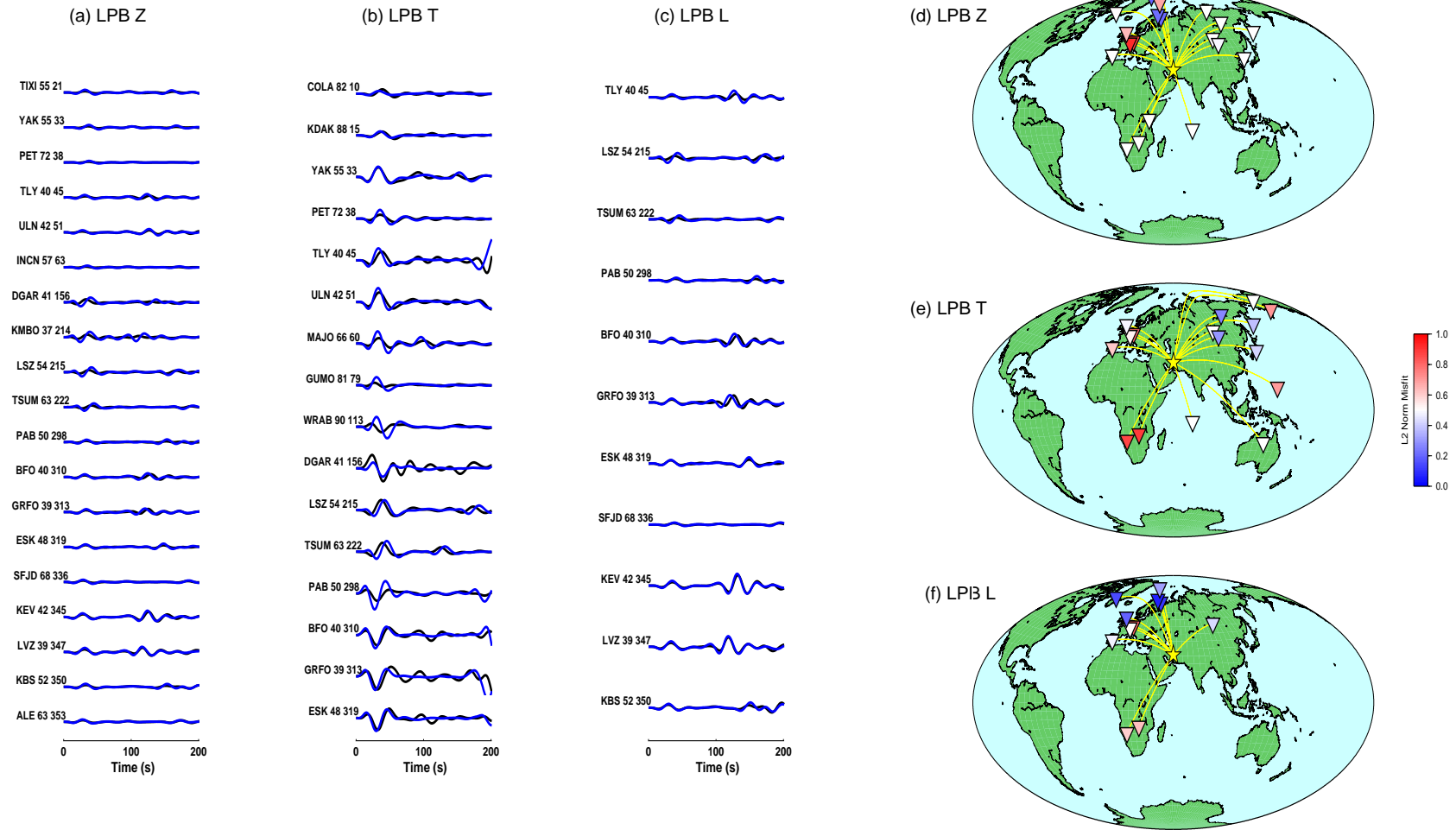


Figure 5.24: a) - c) Fit of joint inversion results for the M_w 6.5 Zarand earthquake (blue) to the data (black), filtered for long period body waves (LPB) where vertical (Z) transverse (T) and longitudinal (L) components are shown, respectively. The station name, epicentral distance and azimuth are shown next to each waveform. d) - f) The station distribution and its corresponding misfit to the data for the vertical, transverse and longitudinal components, respectively. Great circle paths are shown in yellow and the yellow star denotes the earthquake location.

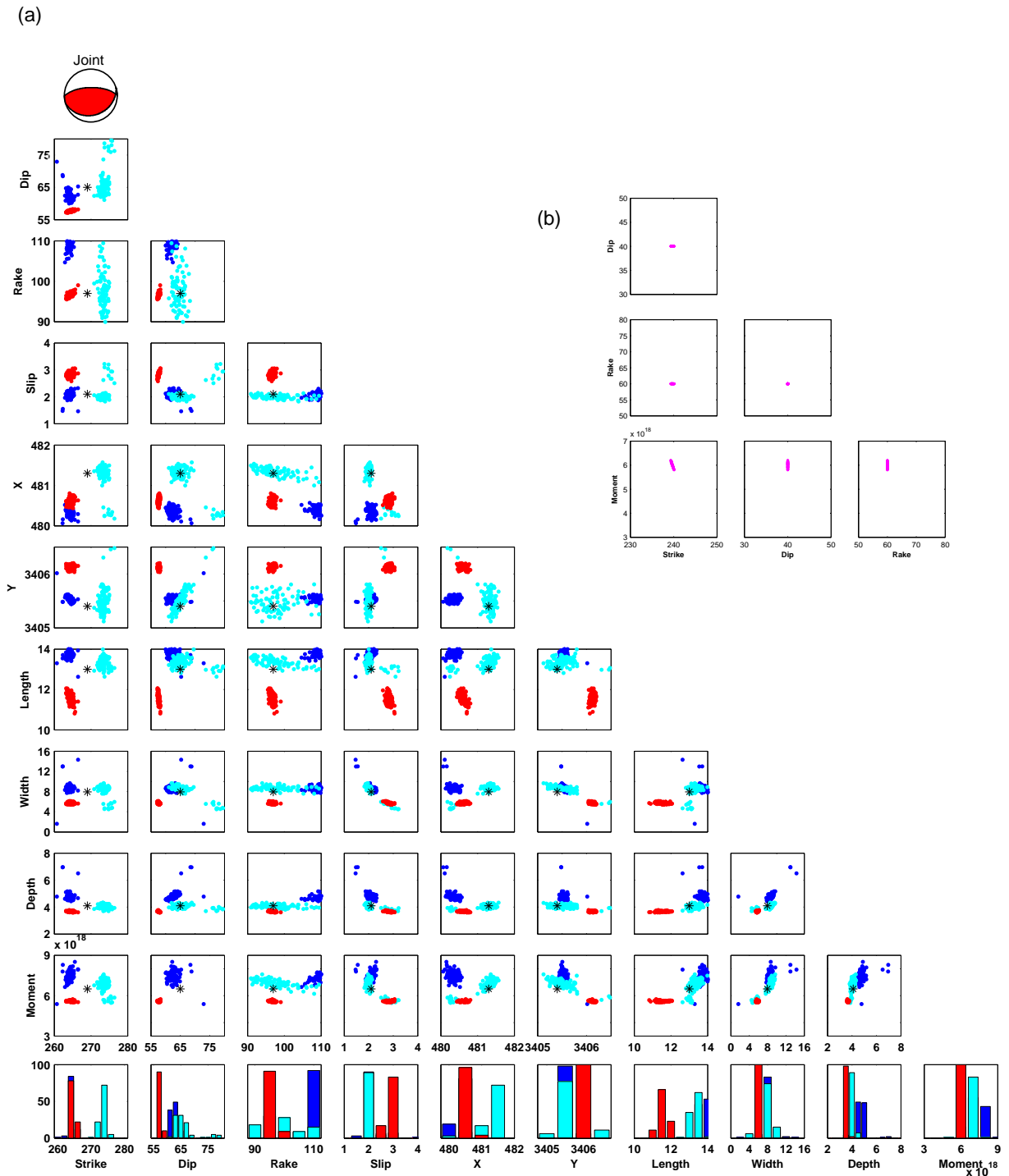


Figure 5.25: a) Tradeoff scatterplots for joint inversion results (red) and InSAR for the M_w 6.5 Zarand earthquake, where separate inversions were carried out using the ascending (cyan) and descending (blue) data and the focal mechanism is shown in red at the top. b) Tradeoff scatterplots for inversion of seismic data. Format is follows that described in Figure 5.7.

5.9 Discussion

The results from both synthetic tests and real data inversions will now be discussed in terms of the data used, fault geometry and centroid location, with particular reference to the effect of incorporating 3-D Earth structure in the modelling of seismic data.

A key consideration in joint inversions is the weighting of each dataset; the results from the analysis of the Zarand earthquake highlight in particular the importance of considering separately the various datasets, even when they are of the same type. Two interferograms from ascending and descending tracks were available for this event and separate inversions of the two datasets led to source parameters with considerable discrepancies, with fault rake exhibiting the largest differences. This type of issue has been previously reported in inversions with synthetic data (*e.g.* Lohman *et al.*, 2002), and it is widely acknowledged that data from both ascending and descending tracks are needed to constrain the rake as the displacements are measured from more than one look direction (*e.g.* Wright *et al.*, 2003). Moreover, the ascending data were acquired at a shallower angle (41°) to the descending data (23°) and consequently are less sensitive to vertical motions than the descending data. This could explain the difference in fault geometry between the two datasets and also the higher misfit of the resulting joint inversion forward model to the ascending data. The poorer fit to the ascending data is also partly explained by unresolved tradeoffs in the joint inversion and the type of misfit and weighting approach used, issues which are discussed later.

Body waves and surface waves also need to be considered separately, mainly due to their varying sensitivity to the Earth structure. Results from synthetic tests using 1-D and 3-D Earth models show that long period surface waves are more sensitive than long period body waves to 3-D Earth structure (Tables 5.1 & 5.2, Figure 5.6). Due to their natural dispersion and sensitivity to shallow structure, long-period surface waves show a stronger frequency dependence regarding changes in phase and amplitude (*e.g.* Zhou *et al.*, 2011). The difference is particularly clear when assuming a 1-D Earth structure, with evident phase shifts in the Rayleigh waves (Figure 5.6 a), although there are also shifts in the arrival of SH waves (Figure 5.6 c). Similar changes in waveforms from comparisons of wave propagation simulations for 1-D and 3-D Earth models have been observed in other studies (*e.g.* Marquering *et al.*, 1998; Furumura *et al.*, 1999).

The changes in waveforms due to Earth structure influence the recovery of resulting source parameters. In this study the fault dip angle is particularly poorly constrained in synthetic tests using the 1-D Earth model, PREM, with results from separate and joint inversions leading to a steeper dip angle than the actual input solution (5-15° steeper). Results from PREM surface wave inversions exhibit the steepest fault dip angle and all other parameters are the furthest from the input solution, yet the surface wave solution leads to a lower misfit to the long period surface waves ($m^2=0.32$) than the long period body waves ($m^2=0.60$). This suggests that errors in the Earth structure and in the retrieved source model compensate each other, leading to an overall good fit to the observed long period surface waves.

Tests with real data have also highlighted the influence of the assumed Earth structure model on the resulting source parameters. Previous geodetic and seismic studies found a large range of values for fault strike for the Eureka Valley earthquake ($\sim 30^\circ$ variation). The results from the InSAR inversion in this study are in agreement with a previous geodetic study by Massonnet and Feigl (1995). Peltzer and Rosen (1995) suggest a more westerly striking fault (strike= 187.0°), which is in agreement with other seismic studies suggesting strike values of 193° (Ichinose *et al.*, 2003) and of 210.0° (GCMT). Interestingly, these seismic studies assume a 1-D velocity structure, whereas an aftershock relocation study using a 3-D velocity model obtains a fault plane with a strike of 165° that is in better agreement with the LPS inversion in this study, which also employs a 3-D Earth structure model. However, the body wave inversion results in this study suggest a strike more in agreement with seismic results that assume a 1-D velocity structure or a very smooth 3-D Earth model. Yet substituting this more north-westerly strike (210°) into the joint inversion result significantly reduces the fit to the interferogram (Figures 5.12d & e). Therefore, considering the shorter period of the body waves ($T \sim 30$ s), this could suggest that smaller scalar heterogeneities, at a local level as in Asad *et al.* (1999), and a global level are at least one factor that needs to be taken into account to improve the modelling of the body waves.

Existing studies for the Eureka Valley earthquake also propose a wide range of dip angles (30° - 60°). Geodetic studies (Massonnet and Feigl, 1995; Peltzer and Rosen, 1995) determine a dip of $\sim 50^\circ$ but there are large discrepancies concerning the seismic studies.

A moment tensor inversion of regional seismic data finds a similar value of 48° (Ichinose *et al.*, 2003) but information from relocated aftershocks suggest a steeper dip (*e.g.* a dip value of 60° by Asad *et al.*, 1999), and the GCMT catalogue reports the shallowest dip of all the existing studies, $\text{dip}=30^\circ$. Another moment tensor inversion study which uses long period regional data obtains a fault which dips at 49° , but in the opposite direction to all other results (Ritsema and Lay, 1995). The dip from the joint inversion results presented here lies in the shallower region of estimates, $\sim 37.0^\circ$, but this fits the data very well and could be due to tradeoffs between the fault geometry, strike and rake (Figure 5.15). The wide variation in fault geometry estimates in existing studies might be due to the complex nature of the event; curvature of the aftershock locations suggests that the fault could be slightly concave (Asad *et al.*, 1999). If this is the case then complex fault geometries are more likely to influence the body waves and could partly explain the poorer fit to these waveforms (Figure 5.14, in comparison with the surface waves (Figure 5.13)).

A similar issue concerning the fault dip angle is highlighted in the results for the Zarand earthquake. InSAR and body wave source inversion results for this earthquake agree well with existing source models (*e.g.* Talebian *et al.*, 2006; Rouhollahi *et al.*, 2012). A slightly shallower dip (55.8°) and lower moment are favoured in this body wave inversion in comparison with body wave results from Talebian *et al.* (2006), but this could be due to the different velocity structures assumed (half-space in Talebian *et al.*, 2006). In addition, we use longer body-wave time series in this study. An inversion of long period surface waves results in a much shallower dip angle (24.2°), shallower than the GCMT result (45.0°), but when combined with the body waves the dip steepens to 55° . This suggests that the shallower GCMT dip could be due to a strong influence of long period surface waves in the inversions. There is significant lateral heterogeneity in the crust and upper mantle in this region as a result of the convergence of two continental plates (*e.g.* Priestley *et al.*, 2012; Hatzfield and Molnar, 2010; Kaviania *et al.*, 2007). Therefore, the lack of inclusion of accurate crustal properties could be responsible for this underestimation of the dip angle. Incorporating accurate crustal properties at the source and receiver could further improve the long period surface wave source inversion results (*e.g.* Hjörleifsdóttir and Ekström, 2009).

Using earthquake locations estimated using InSAR along with a 3-D Earth structure

model is an attempt at trying to resolve these issues surrounding the influence of the assumed Earth structure, including the mislocation of events. Joint inversion results for Eureka Valley and Aiquile have shown that the 40-50 km discrepancies in seismic and geodetic locations can be resolved. Using the locations determined using InSAR in the modelling lead to a good fit to the seismic data in both cases (Figures 5.13, 5.14, 5.17 & 5.18). The seismic data can be reconciled with InSAR-determined locations, including in complex regions such as the central Andes in Bolivia, where accurate earthquake locations and source models are especially important for further understanding their complicated tectonic regime. However, the use of the InSAR location to try and fit the data could be biasing the resulting source models, due to tradeoffs between location and Earth structure. This could also explain some of the variations in source parameters seen for the seismic only inversions in comparison with the InSAR-only and joint inversion results, for example, the shallow dip estimates from the long period surface wave inversions for all three case studies (Tables 5.3, 5.4 & 5.5).

The synthetic tests in the presence of noise carried out in this study clearly showed that the joint inversion technique reduces the level of tradeoffs within model solutions. Moreover, for all three case studies, it is found that the source parameters, particularly fault strike, dip and rake, are more robustly constrained (Figures 5.15, 5.20 & 5.25) in joint inversions using InSAR and seismic data than in separate data inversions, and that both datasets are fit reasonably well. However, the fit to the InSAR data for the Aiquile and Zarand events could be improved. The few fringes of displacement in the residual interferogram for Aiquile (Figure 5.19) could be due to the underestimation of the fault length in the joint inversion, 14 km in comparison with the 24 km and 21 km reported by Funning *et al.* (2007) and Devlin *et al.* (2012), respectively. If a length of 19 km is used instead then a residual interferogram similar to that seen in Funning *et al.* (2007) is obtained. Therefore the length is likely underestimated, and this could be due to the tradeoffs between length, width and slip that are not resolved in the joint inversion. The addition of seismic data may not resolve these tradeoffs because the period of the data used provides little constraint on the length, as the earthquake is a point source with respect the wavelength.

A similar issue is seen for Zarand, where the fit to the ascending data could be improved, there are several residual fringes (Figure 5.22 e) which is partly due to the data being heavily downweighted, with respect to the descending dataset, in the joint inversion. This is based on the high misfit value observed in the InSAR-only inversion, which may be the result of the assumption of uniform slip on one fault, a multi-segment or distributed slip model could improve the fit to this dataset. Talebian *et al.* (2006) suggest a kink in the fault may better explain the ascending data, but argue that this is not consistent with field observations. They do achieve a better fit to the ascending track than that seen in Figure 5.22, and slip shows the largest discrepancy between their model and the one reported here. If the lower slip value from Talebian *et al.* (2006) is used (1.6 m) instead then the number of residual fringes is reduced, thus suggesting that our slip estimate is too high and leads to an over-modelling of the displacement. This high slip value is partly due to a tradeoff with width and length in the joint inversion, when the seismic data are combined with the InSAR data a thinner fault is favoured (Figure 5.25). Moreover, this slip value appears to be originating from the InSAR data, if the separate InSAR inversion results are considered (Table 5.5). Therefore, the weighting and modelling assumptions, seem to explain the resulting high slip value in the joint inversion and consequently the poorer fit to the ascending track.

Fundamentally InSAR and seismic data are two very different datasets which record different aspects related to the earthquake source, and a degradation in fit for both datasets when viewed individually is to be expected, as the inversion is trying to fit both of them. This is partly accounted for by modelling the earthquake using relatively simple and almost equivalent approaches for both datasets; point source approximation for the seismic data and uniform slip on a finite fault with respect to the InSAR data. The misfit function and weighting of the datasets are also important considerations. The results for Zarand highlight the influence of the misfit and weighting approaches on the inversion result. Here an L2-norm misfit is used for all datasets and the weighting is based on results from the separate inversions of the two datasets. This is a relatively simple approach and relies on the assumptions that the model for the separate inversions is best possible model for that dataset, and that the same misfit calculation is appropriate for both datasets. A more complicated misfit function could have been chosen, for example Ji *et al.* (2002a)

use three different approaches to determine the misfit for the geodetic, high and low frequency seismic data (see section 5.2). The misfit to the seismic data can also take into account the fit of each seismic station to the data and the station azimuthal distribution (*e.g.*, Vallée *et al.*, 2011). Furthermore, the weighting of the two datasets could be based on the noise in the datasets (*e.g.*, Sudhaus and Jónsson, 2009) instead of the misfit, and this issue of weighting is discussed in more detail Chapter 6. Overall though the results from both the synthetic tests and the case studies show that the misfit and weighting approaches used are sufficient to effectively combine the InSAR and seismic data, and ways to further improve the joint inversion technique are discussed in the following Chapter.

5.10 Conclusions

A new joint earthquake source inversion technique is presented, which uses InSAR and long-period teleseismic data and takes into account the effects of 3-D Earth structure when modelling the seismic data. Synthetic tests in the presence of data noise and using 1-D and 3-D Earth models highlight the improvement in fault geometry and moment determinations that can be achieved by combining InSAR and seismic data, particularly when using a 3-D Earth model.

This result and the PREM and S20RTS comparisons from Chapter 4 prompted the use of a 3-D Earth model to calculate the seismic excitation kernels. Using the InSAR location to calculate the excitation kernels demonstrates that the two datasets can be reconciled and overall a good fit to both datasets can be achieved. Tradeoffs between fault geometry and moment are reduced in the joint inversions when compared with separate inversion results. Where there are discrepancies between the separate long period surface and body wave inversions, that are not fully resolved in the joint inversion, this could partly be explained by unmodelled lateral heterogeneities in the assumed Earth model. For example, the body wave inversion results for the Aiquile and Eureka Valley earthquakes suggest that improved modelling of these waves at these periods could require the incorporation of smaller scale heterogeneities in current Earth models. Moreover, in regions with high levels of heterogeneity, such as central Iran, realistic crustal properties are important for the robust modelling of surface waves. Consequently, even higher resolution global mantle and crustal models in the future would be beneficial for teleseismic source studies.

Overall this technique illustrates the existing potential to incorporate the effects of 3-D Earth structure and combine the strengths of InSAR and seismic data to determine robust source models.

Chapter 6

Discussion and Conclusions

The findings in this thesis will now be summarised and discussed in the context of the data and inversion approaches used, assumed Earth structures and the influence of these factors on resulting source models, and the consequences for their subsequent interpretation.

6.1 Spatial and temporal resolution

InSAR and seismic data are contrasting datasets regarding their spatial and temporal resolution. InSAR can be seen as a ‘ground truth’ for the location of moderate magnitude earthquakes. As was seen in Chapters 3 and 4, the geodetic location when combined with high-degree seismic tomography models, significantly improved the fit to the observed seismic data. However with the current satellite resources, InSAR data lack temporal resolution, it is impossible to identify the sequence of events which may have occurred in the length of time the interferogram covers and any deformation signals related to the events other than the other earthquake can bias inversions. Afterslip, poroelastic or viscoelastic relaxation if modelled as coseismic deformation could lead to an overestimation of the moment magnitude (Figure 3.3, Chapter 3).

The influence of postseismic deformation and also atmospheric perturbations are key issues, and methods for characterising and removing these are currently being developed, with a particular focus recently on removing phase delays due to the atmosphere. This includes using atmospheric models to simulate the potential phase delay due to water vapour (*e.g.*, Puysegur *et al.*, 2007; Doin *et al.*, 2009; Wadge *et al.*, 2010) and detecting smaller surface displacements with increased accuracy (*e.g.*, Shirzaei, 2013). The effects

of postseismic deformation would be reduced by using interferograms that just cover the very short time period in which the earthquake occurred (~ 20 seconds), currently an unlikely scenario for InSAR but could be possible in the future with real-time GPS. When the SENTINEL-1A satellite is launched in 2013, it will have a repeat orbit of 12 days; once the second satellite is available, the time period between images could be reduced to just six days (Potin, 2011), compared with 35 days for the majority of the ERS-1, ERS-2 and the Envisat missions.

In comparison, seismic data have much better temporal resolution than InSAR, the signal solely due to the earthquake is recorded and for local networks a much higher resolution picture of the propagation of the rupture can be attained, in particular from strong motion sensors, which are able to record the higher amplitude seismic waves more robustly. Recordings from large strike-slip events in the past decade or so, such as the M_w 7.3 Izmit earthquake in 1999 in Turkey and the M_w 7.9, Wenchuan earthquake in China in 2008 have enabled in-depth studies into not only the distribution of slip, but also the propagation of the rupture (*e.g.* Delouis *et al.*, 2002; Zhang *et al.*, 2012). This also includes the observation of supershear rupture, for Izmit (*e.g.* Bouchon *et al.*, 2002).

InSAR in comparison often has better spatial resolution and accuracy; therefore, these two datasets are very complementary. InSAR and seismic data are both powerful tools for constraining the slip distribution; yet, when combined, the InSAR data can further refine the spatial distribution of slip and seismic data are able to constrain the temporal features (*e.g.*, Salichon *et al.*, 2004).

6.2 Weighting the data

Increasingly, InSAR data are being jointly inverted with other types of data, particularly GPS and seismic data. All these datasets when inverted individually can give rise to trade-offs, particularly between dip, rake and moment but, when combined, these tradeoffs can be reduced, as seen in the joint inversion results for the Eureka Valley, Aiquile and Zarand earthquakes in Chapter 5. Moreover, the InSAR inversions for the Zarand earthquake using the ascending and descending tracks highlight the importance of considering each dataset separately before combining them in a joint inversion.

Misfits from these separate inversions are the approach currently used to weight the

contribution of each dataset, but there are numerous approaches to weighting, which are well summarised in Sudhaus and Jónsson (2009). The weights can be equal (*e.g.*, Belabbes *et al.*, 2009) or arbitrary weights can be set (*e.g.*, Delouis *et al.*, 2002). The weights can be based on misfit statistics (*e.g.*, Salichon *et al.*, 2004) or the covariance of each dataset (*e.g.*, Wright *et al.*, 2004a; Sudhaus and Jónsson, 2009). Alternatively, the datasets can be normalized so that the sum of the weights assigned to the individual data points is equal to one and consequently the weights are inversely proportional to the measurement errors (*e.g.*, Fialko, 2004b). A similar approach can be taken if the data are subsampled, and in this case the weights can be related to the area that each of the data points represent (*e.g.*, Simons *et al.*, 2002). A statistical approach can also be adopted to determine the optimal relative weighting, for example the Aike Bayesian Criterion (ABIC) (*e.g.*, Funning, 2005). If the error characteristics in the data are used to weight the datasets they can also be used to propagate the data uncertainties to source parameter uncertainties (Sudhaus and Jónsson, 2009), an issue discussed next.

6.3 Data and source parameter uncertainties

Estimation of the uncertainty or potential errors in earthquake source parameters is an area of increasing focus. Understanding the range of realistic values is important because when using them as inputs for Coulomb stress change calculations (*e.g.*, Woessner *et al.*, 2012), the forward modelling of ground motion (*e.g.*, Imperatori and Mai, 2012) and aftershocks (*e.g.*, Bach and Hainzl, 2012) they can lead to a range of results with significantly different implications or interpretations. Variations in fault geometry and location can significantly impact the results when used in dynamic rupture studies (*e.g.*, Zhang and Chen, 2006; Kaser and Gallovic, 2008; Oglesby *et al.*, 2008). There are multiple sources of uncertainty and error in geodetic, seismic and joint inversions that can influence the resulting source parameters. Incomplete data or errors in the data, the type of model space media and other assumptions made in the modelling process can all introduce uncertainties. Furthermore, as there is no uniform method for processing and modelling both seismic and geodetic data, a blanket approach to assessing the uncertainty cannot be used (*e.g.*, Sudhaus and Jónsson, 2009).

The estimation of uncertainties concerning InSAR data itself, is the subject of much

research, as initially the errors involved with InSAR data were not fully understood, likely the result of the numerous contributing factors of uncertainty that have to be accounted for. There are various methods of quantifying potential errors in the data, one example being to add representative noise to the interferogram and estimate the tradeoffs and uncertainties in source parameters determined from multiple realisations of these ‘noisy’ datasets (*e.g.*, Wright *et al.*, 2003). ‘Noise’ in this case referring to correlated noise due to the atmosphere, rather than thermal noise which is uncorrelated (*e.g.*, Bürgmann *et al.*, 2000). The effect of differences in water vapour content in the troposphere, or of charged particles in the ionosphere between the two SAR acquisition dates is typically spatially correlated. Thus, to simulate the noise in an interferogram accurately it is important to accurately estimate the length scale over which it is correlated (*e.g.*, Lohman and Simons, 2005a).

The influence of noise on the resulting source parameters is an issue investigated by Dawson and Tregoning (2007) where synthetic interferograms were calculated for 84 (M_w 2.4 - 6.7) intraplate earthquakes in Australia and perturbed with characteristic noise. These simulated ‘noisy’ interferograms were then inverted for source parameters which were compared with the original parameters used to produce the simulated interferograms. For earthquakes greater than M_w 5.8 the horizontal component of the epicentral location could be determined to within 0.07 km, the depth within 0.15 km and the strike 0.2° , whereas for smaller events (M_w 5.5) this uncertainty increases to 0.3 km, 0.5 km, and 1.0° , respectively. If we consider the different models for individual events in this study the variability in parameters appears larger than these values, for example strike angle can vary between $1 - 10^\circ$, depth by 1 - 4 km and location by $\sim 2 - 12$ km. This suggests that although noise is a key consideration it is not the most important factor which influences the variability of the inversion solutions. The different methods and assumed Earth models used are also highly influential, this is particularly evident when comparing the range of slip distributions, for the large events Hector Mine and Wenchuan (Figures 3.18 & 3.19), determined using a range of techniques and dataset combinations.

In comparison with noise-related variability, which is a random error, Earth model variability can result in systematic errors which are harder to detect and quantify. This

includes unmodelled lateral heterogeneity in the mantle and crustal models used to calculate seismic synthetics. The comparison of source models determined using datasets which are independent of each other, such as the ICMT and GCMT comparisons in chapter 2, is one way of identifying such errors. Uncertainties for source parameters, such as fault geometry and moment magnitude, reported in seismic catalogues can be independently estimated and systematic mislocations of events identified, such as those in the south American subduction zone (Figure 3.9). On a smaller, individual model scale the uncertainty in the data is one way of quantifying the source parameter uncertainties (Sudhaus and Jónsson, 2009). For events where there are multiple source models, the scatter in source parameters also highlights other sources of systematic error such as the data sampling methods used and the smoothing parameters imposed for distributed slip models. On a smaller, individual model scale the uncertainty in the data is one way of quantifying the source parameter uncertainties (Sudhaus and Jónsson, 2009).

The use of multiple datasets reduces the uncertainty and non-uniqueness in the model parameters, as is evident from the joint inversion results in Chapter 5. However, the differences between ICMT and GCMT source parameters are not significantly reduced if other datasets, such as GPS and seismic data, are used in the InSAR study, as seen in chapter 2. Furthermore, despite the various methods becoming available for the estimation of uncertainties it appears still not to be routine to report the errors in earthquake source parameters.

6.4 Importance of realistic Earth structures

Errors in Earth models can lead to the systematic mislocation of events, for example not properly taking into account the velocity structure of subduction zones. Potentially unmodelled lateral heterogeneities in the upper mantle and crust can also influence the determination of fault geometry, for example the underestimation of the dip for the Zarand earthquake when using long period surface waves (Chapter 5 and Table 5.5).

The poor fit to observed seismic data when using InSAR-determined locations that are in agreement with field observations and the known geology, as is the case for the Izmit earthquake in chapter 3, indicates that improvements are needed in current crustal and mantle models. Locations determined from InSAR data can be useful for identifying

and perhaps even quantifying these errors.

However, InSAR data also suffer issues regarding the assumed modelling medium. Homogeneous half-spaces can lead to biases in depth, Figure 3.13, (*e.g.*, Savage, 1998; Cattin *et al.*, 1999; Wald and Graves, 2001). This is because there are large variations in the upper crust and therefore such homogeneous half-space approximations will have the largest influence for shallow earthquakes, which constitute most of the events in the ICMT database. If depths calculated taking into account layered (*e.g.*, Lohman *et al.*, 2002; Pritchard *et al.*, 2006; Pritchard and Fielding, 2008; Baer *et al.*, 2008) or in one case 3-D structures (Bustin *et al.*, 2004) then this bias is reduced (Figure 3.14).

The Earth model used for the inversion of both InSAR and seismic data is clearly a key consideration for the calculation of robust source parameters, particularly location and depth. However, comparisons between the two types of Earth model used by each dataset are hard to make due to the large difference in scale. For long period seismic data, comparisons between synthetic and observed seismic data for source models in Chapters 3 and 4, and the inversion results in chapter 5, suggest improvements in Earth models on a continental scale and local scale are needed. One way to achieve this could be to use the phase and amplitude misfits for the seismic data for multiple events in the same region to identify and quantify potential structures with anomalously fast or slow seismic velocities, particularly in the upper crust. The homogeneous versus layered half-space issue implies that local-scale structural improvements would be more beneficial for inversions using InSAR data. Currently though the errors in the InSAR location seem to be small enough to be beneficial when combined with seismic data for the determination of more robust locations.

6.5 Conclusions

Since the first InSAR study of an earthquake (Landers, M_w 7.3, 28th June 1992, Massonnet *et al.*, 1993) the interest in the technique has grown and multiple approaches for the processing and modelling of the data have been developed. The first comprehensive global database of InSAR source models, compiled in this study, provides a tool for independently assessing the accuracy associated with source parameters reported in widely used global seismic catalogues. The location shows the largest variation; ~ 20 km for

GCMT catalogue and ~ 10 km for the ISC and EHB Bulletins, with large mislocations (> 30 km) for several earthquakes. InSAR-determined depths are also systematically shallower than those reported in the GCMT catalogue, due to the use of homogeneous half-spaces to model the data and also the fact that hypocentral and centroid depths are compared. However, the moment magnitude and fault geometry show good agreement between the two datasets. Investigations of the large discrepancies, mainly in location and fault geometry, for certain earthquakes highlight the strong spatial resolution of InSAR for locating moderate magnitude events. The lack of improvement in the fit to the seismic data when using the InSAR location for large strike-slip and subduction zone events shows that InSAR data suffer the same issues as seismic data whenever the centroid location is determined from a distributed slip model, which is the result of an inversion. Moreover, the results suggest potential errors in crustal and Earth models for certain regions, for example the North Anatolian fault and the south American subduction zone.

These source parameter comparisons and forward modelling results emphasise the importance of the assumed Earth structure when modelling both datasets, and also their complementary nature. This motivated the development of a joint source inversion technique which takes into account the effects of 3-D Earth structure when modelling the seismic data. Synthetic tests for three events with different faulting mechanisms clearly show the improvement in the fit to the data that can be achieved when using a 3-D Earth model rather than a 1-D Earth model. Also the combination of both InSAR and seismic datasets reduces the parameter tradeoffs and allows the more robust recovery of the source model. These trends are evident when applied to three moderate magnitude earthquakes (M_w 6.0 Eureka Valley, M_w 6.6 Aiquile and M_w 6.5 Zarand) in different tectonic settings. In particular the use of the InSAR location for the Eureka Valley and Aiquile events to calculate the excitation kernels, show that the initial large discrepancies in location between InSAR and seismic data can be resolved. It is evident though, from seismic only and the joint inversion results, that further improvements in existing crustal and mantle models are needed. However, the results demonstrate the combined power of InSAR and seismic data to determine robust source models for moderate to large earthquakes.

With the continued and future investment in satellites, such as Sentinel-1A and ALOS-2, and the deployment of denser global and local seismic networks, this volume of data will allow us to measure earthquakes with higher resolution and accuracy than before. Combined with increased computing capacity it will enable the calculation for more complex and destructive events on a much quicker timescale. The application and development of joint source inversion techniques will prove increasingly useful for characterising earthquakes, which is an important aspect to understanding the seismic hazard in regions with increasing populations at risk.

6.6 Future Work

The past couple of decades have seen exciting developments in the field of earthquake source studies and this trend is set to continue. The volume of data is rapidly expanding, the source inversion techniques and assumed Earth structures used to model the data are constantly developing and this is in part motivated by the significant and continuing advances in computing power. Geodetic data are currently experiencing a rapid expansion with the deployment of more GPS stations, investment in LIDaR (Light Detection and Ranging), and the use of high quality optical images to measure surface displacements. In combination with increased computing power and a better understanding of the errors associated with geodetic data, the automatic processing of these large geodetic datasets, SAR and optical images in particular, could be achieved on a much quicker timescale than before. With regards to seismic data, the deployment of ocean-bottom seismometers (OBS) is helping to fill in gaps in the global seismic network and enables the investigation of deformation mechanisms at plate boundary settings (*e.g.*, Geissler *et al.*, 2010; Sumy *et al.*, 2013). There are also increased efforts to engage public participation in measuring earthquakes, such as the British Geological Survey's 'Seismometers for Schools' program and the 'Quake-Catcher Network' based in Stanford, California, providing more near-source measurements.

In addition, increasingly inventive sources of data are being used to help characterize the earthquake source. This includes the expanding area of seafloor observations, partly due to the rapid expansion of the tsunami warning network following the 2004 Sumatran earthquake. The network is a series of real-time seafloor ocean bottom pressure recorders

deployed around subduction zones, and measurements from these stations have been used to constrain the coseismic slip distribution of large events (*e.g.*, Pisco, Peru, M_w 8.1, 2007, Sladen *et al.*, 2010). Offline versions of the recorders also exist and 12 of these stations have been useful in measuring seafloor displacement due to the M_w 9.0 2011 Tohoku earthquake (Inuma *et al.*, 2012).

Inversion techniques are also becoming more sophisticated. For example the use of finite element modelling to incorporate local 3-D topographic and fault features, when inverting for the coseismic slip distribution (*e.g.*, Volpe *et al.*, 2012). An alternative approach involves the use of sparsity promoting algorithms to simply and rapidly constrain the earthquakes source (*e.g.*, Evans and Meade, 2012; Rodriguez *et al.*, 2012). This approach has been applied to geodetic data, but for seismic data, backprojection imaging is increasingly being used to determine the coseismic slip distribution. It is based on the time reversal of seismic waves and is especially useful for measuring the high frequency radiation resulting from an earthquake (*e.g.*, Yao *et al.*, 2012). The assumed Earth models used to simulate the seismic data and the forward modelling techniques for seismic wave propagation are also becoming increasingly sophisticated due to increased computing power (*e.g.*, SPECFEM 3D Globe Komatitsch and Tromp, 1999). On a local scale ambient noise tomography has proven a powerful tool for the inversion of crustal and upper mantle structures (*e.g.*, Yao *et al.*, 2008; Bensen *et al.*, 2009; Calkins *et al.*, 2011; Kim *et al.*, 2012). For geodetic data the modelling of interseismic deformation using elastic half-spaces can be used to investigate lateral rheological heterogeneities across fault zones (*e.g.*, San Andreas fault, California, Jolivet *et al.*, 2009). Taking all these advances into account, robust earthquake source models which incorporate multiple high quality seismic and geodetic datasets, realistic fault geometries and lateral heterogeneities at all scales will, in the future, be calculated within minutes of an earthquake, providing accurate information for immediate emergency response, perhaps even including the estimation of potential aftershock locations.

Following on from the work presented in this thesis there are also several areas which can be explored, and which will now be discussed in more detail.

6.6.1 ICMT database

The global database of InSAR-determined source models is continuously updated whenever new studies become available, and currently an online archive is being developed so authors are able to submit their own models and the database can be used by the community. As it expands it will improve the means of identifying systematic trends. In particular it is becoming increasingly common that individual earthquakes are studied by multiple independent groups using their own, different, methodologies. Therefore investigating this intraevent variation could prove useful for quantifying the associated uncertainties. Not all the information recorded in the database has been used in this study and there are further comparisons and tests that could be conducted using the database. For example the database could be used as independent dataset to test statistically the significance of the occurrence of earthquakes on previously known faults versus events on unknown faults.

6.6.2 Development of the joint inversion approach

The new technique presented in this study could be further developed in several ways. Firstly, the weighting approach could be improved by using the noise in the datasets to determine relative the weight for each dataset. Secondly, it could be expanded to incorporate other datasets such as known geological information and shorter period seismic data. Also the finite spatial complexity of the source could be taken into account, rather than assuming a point source, which would include using realistic geologic fault shapes for known fault zones such as the San Andreas (*e.g.*, Plesch *et al.*, 2002) and subduction zones (*e.g.*, Hayes *et al.*, 2012). To enable the rapid implementation of the technique (once the second SAR image is obtained) the excitation kernels used to model the seismic data could be pre-calculated at grid points concentrated in zones of particularly high seismic activity. Also multiple Earth models could be used to calculate the kernels, providing another means of estimating the uncertainty in the source model. Moreover, the local crustal structure in the chosen Earth model could be used or for regions where the crustal structure is well known layered half-spaces could be incorporated to model the InSAR data.

6.6.3 Further applications of the joint inversion technique

The variation in source models for the same earthquake and for events in the same tectonic setting is not only due to the different datasets used, but also the inversion technique applied. Therefore, it can be difficult to identify robust parameters to use as inputs for Coulomb stress change calculations, and for further understanding the tectonic regime. Systematic application of the joint inversion technique developed in this thesis to events in different tectonic settings could be beneficial in providing a uniform characterisation of events, useful for assessing the tectonic mechanisms and consequently the seismic hazard in a region.

Appendix A

Additional ICMT and GCMT source parameter comparisons

This appendix contains additional results for the comparisons between ICMT and GCMT source parameters in chapter 3. It includes scatterplots comparing each of the parameters with the other to investigate any trends, but as stated in chapter 3 no trends are apparent (Figures A.1, A.3-A.7). Figure A.2 is a comparison of seismic moment estimate for uniform and distributed slip models.

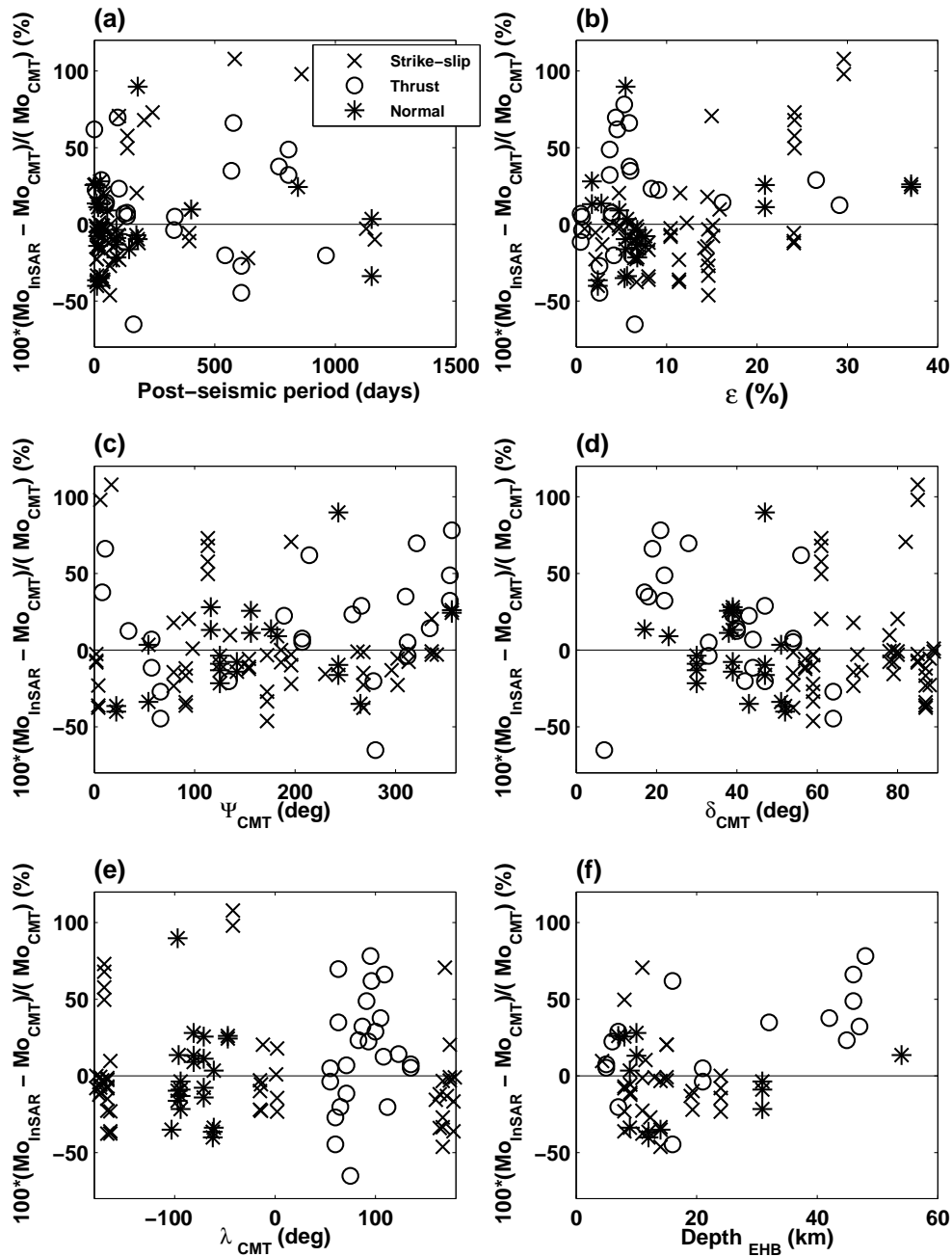


Figure A.1: Difference between InSAR and GCMT seismic moment as a function of (a) Measurement interval of the interferograms; (b) Earthquake non-double-couple component in the GCMT catalog; (c) GCMT fault strike; (d) GCMT fault dip; (e) GCMT fault rake; (f) EHB focal depth.

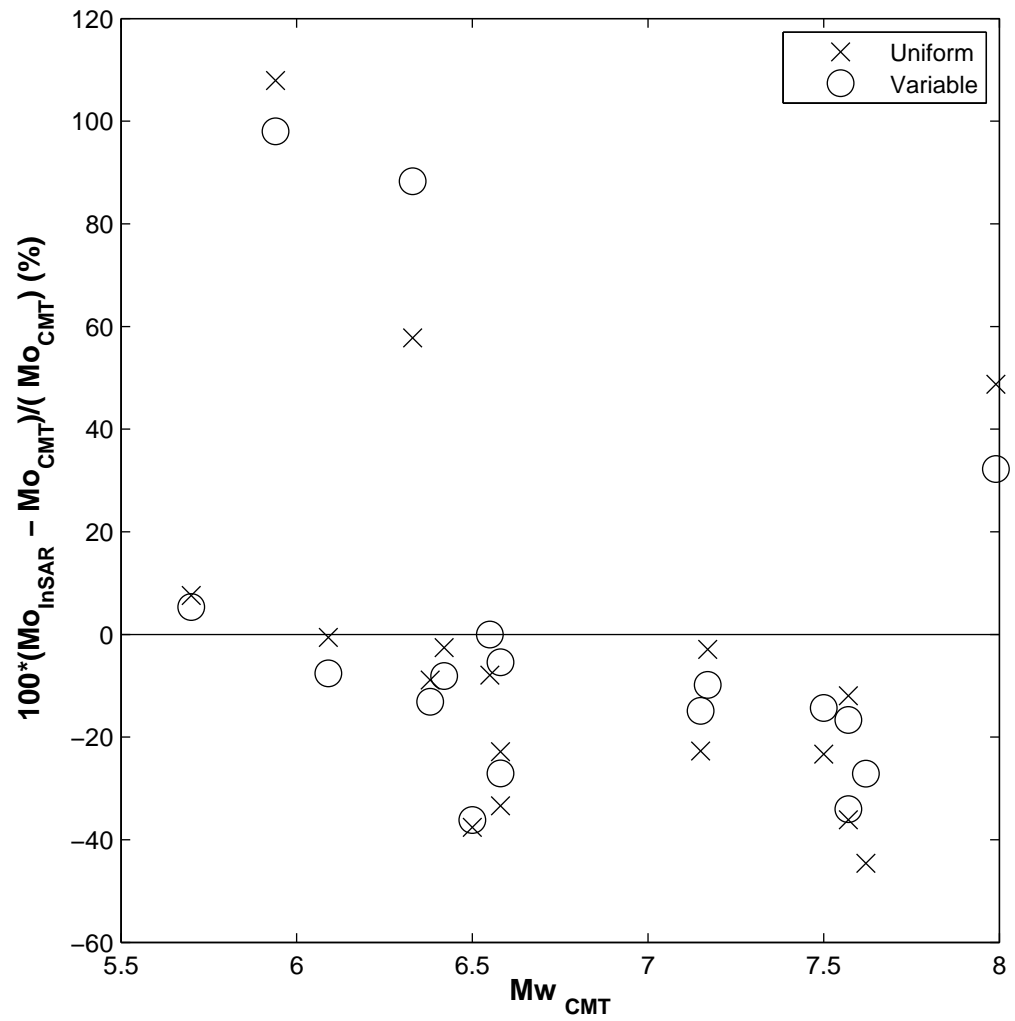


Figure A.2: Comparison of the differences in seismic moment between InSAR and GCMT for earthquakes in the ICMT database for which there are both uniform and variable slip models (17 earthquakes).

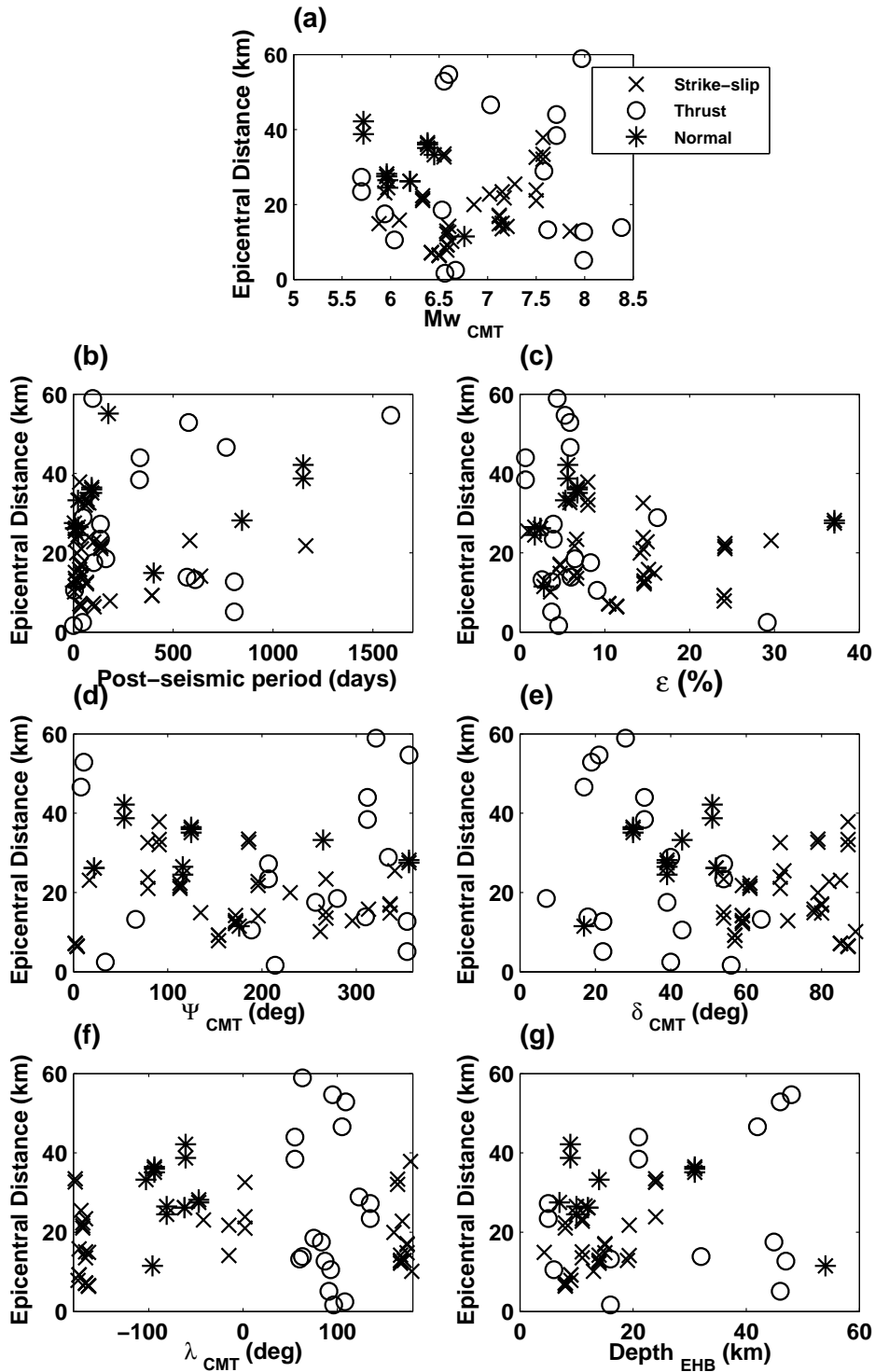


Figure A.3: Difference between InSAR and GCMT centroid locations as a function of: (a) GCMT moment magnitude; (b) Measurement interval of the interferograms; (c) Earthquake non-double-couple component in the GCMT catalog; (d) GCMT fault strike; (e) GCMT fault dip; (f) GCMT fault rake; (g) EHB focal depth.

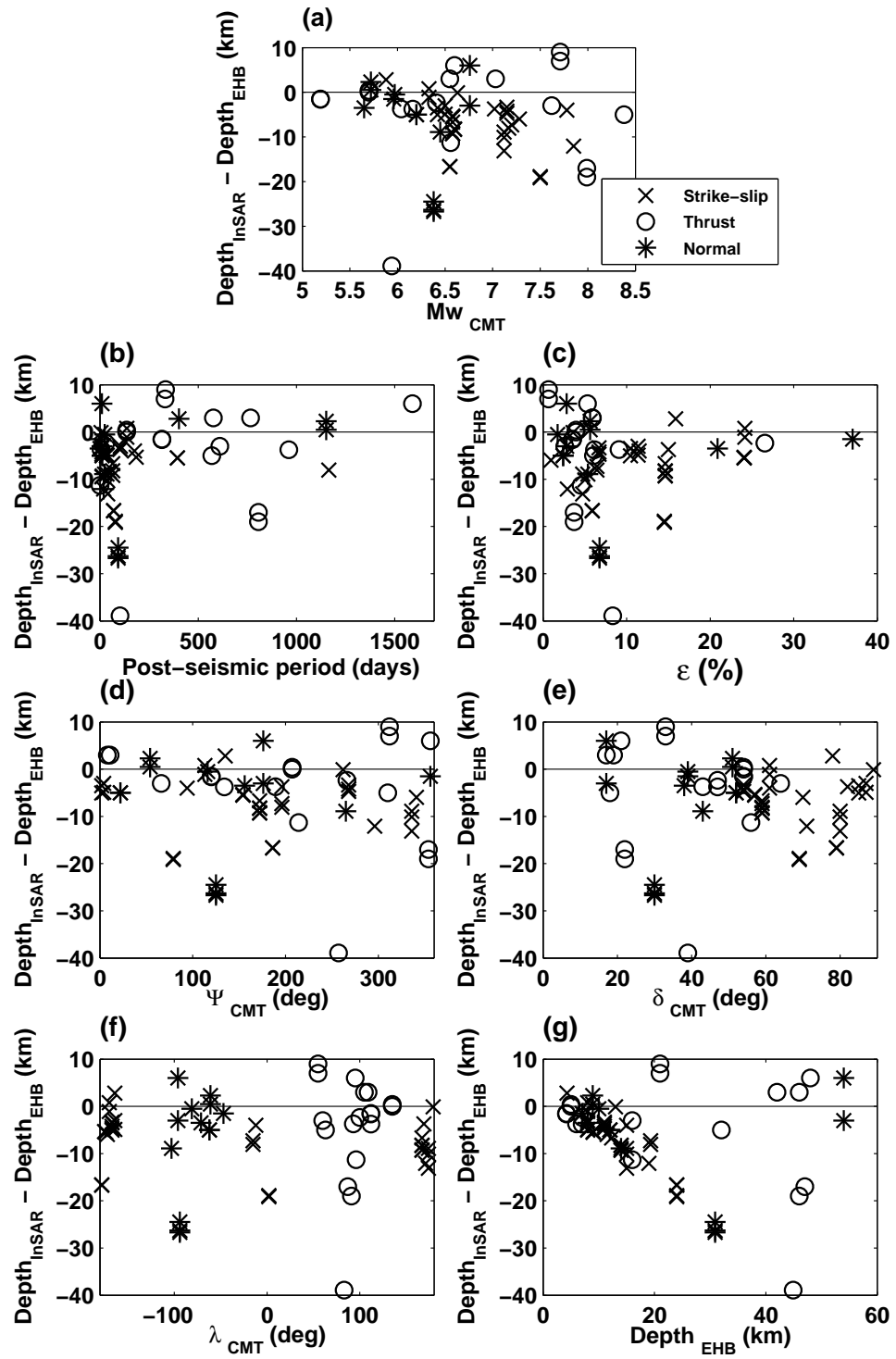


Figure A.4: Same as in Figure A3 but for differences between InSAR and EHB focal depth.

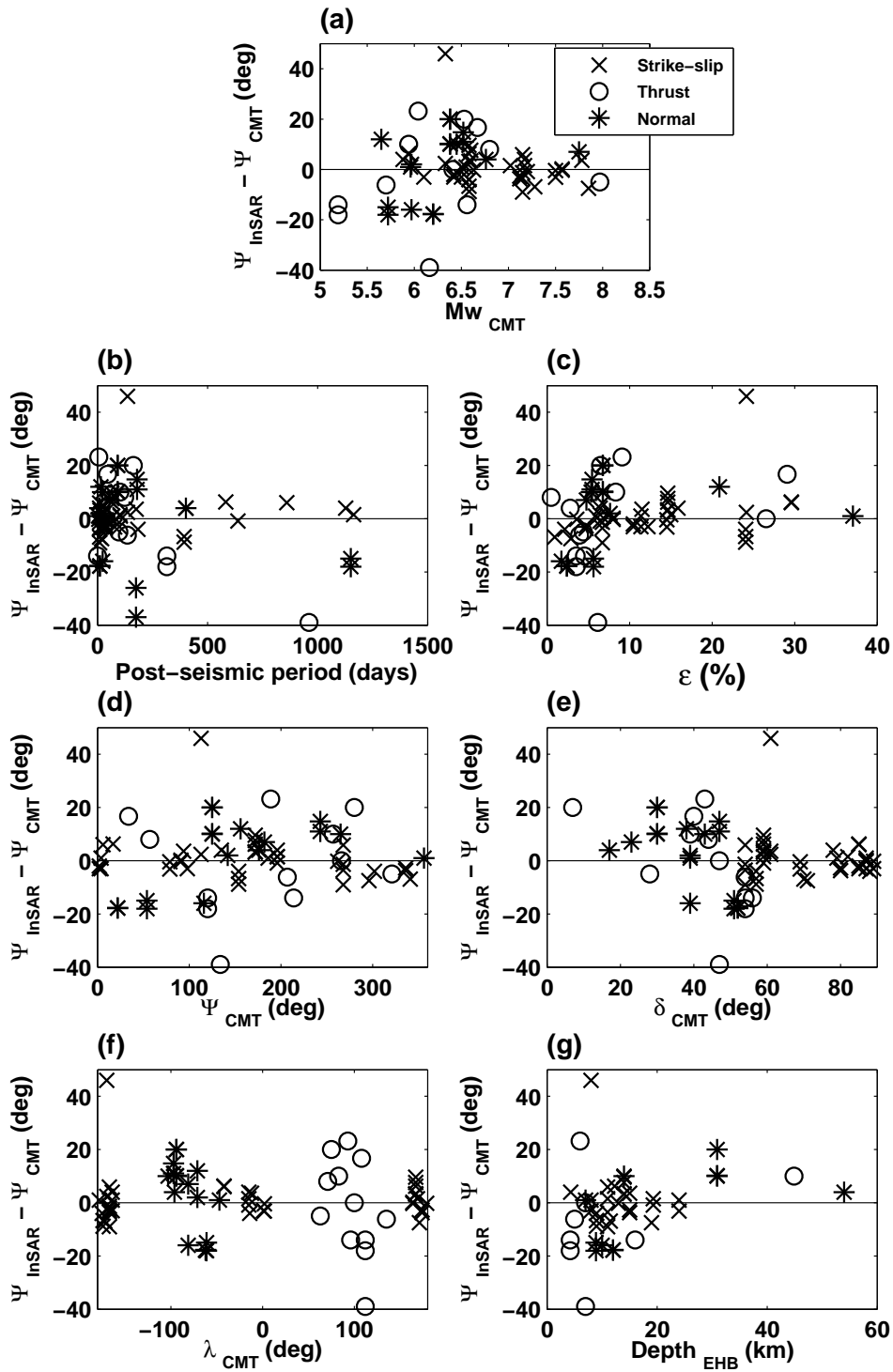


Figure A.5: Same as in Figure A3 for for the fault strike.

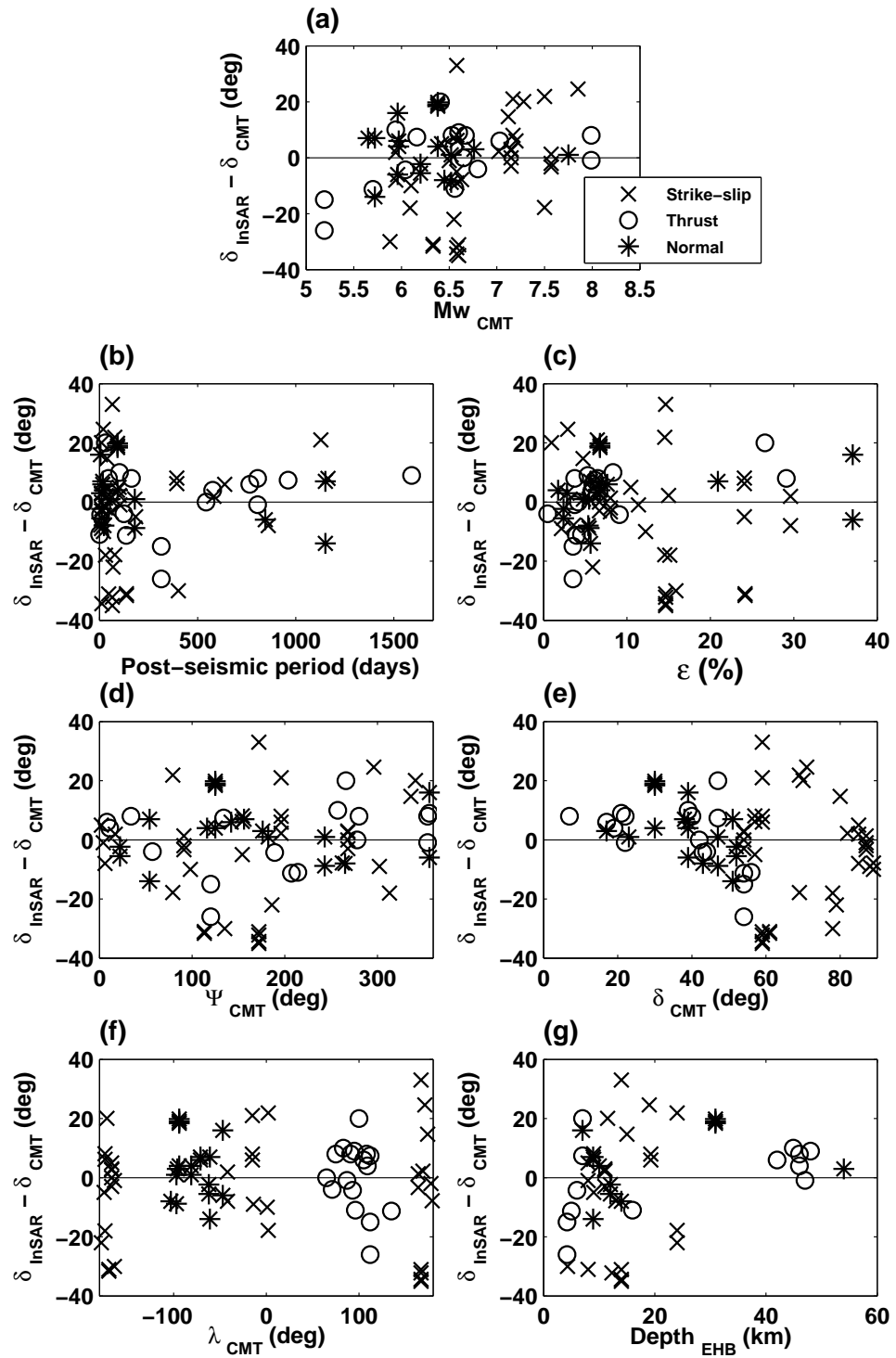


Figure A.6: Same as in Figure A3 but for the fault dip angle.

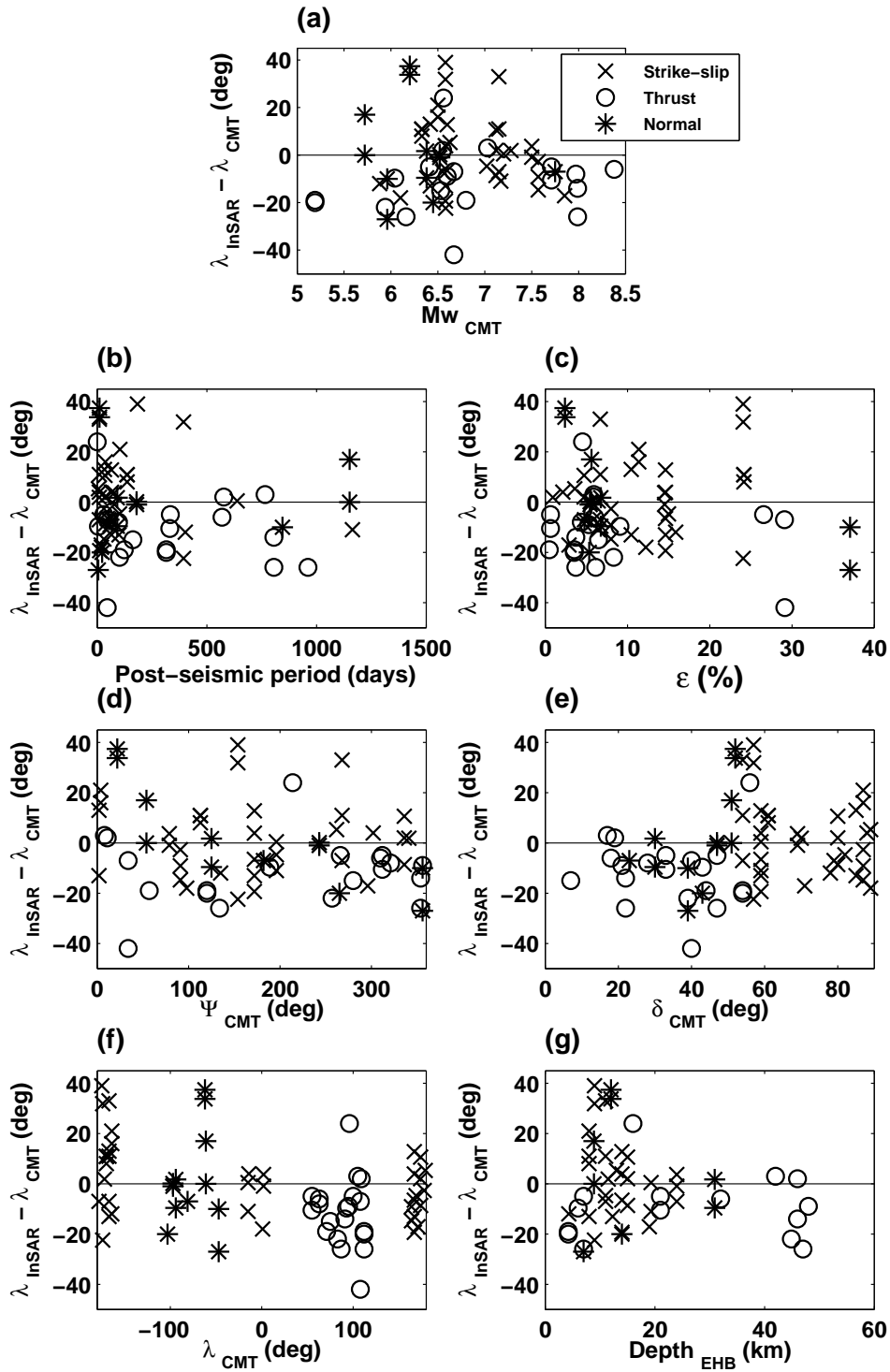


Figure A.7: Same as in Figure A3 but for fault rake.

Appendix B

Additional forward modelling waveform comparisons

This appendix contains additional results from the seismic waveform modelling in chapter 4, and includes comparisons for the transverse and longitudinal components for the Landers (Figure B.1), Izmit (Figures B.2 & B.3), Pisco (Figures B.4 & B.5), and Northern Chile 1996 (B.6) earthquakes.

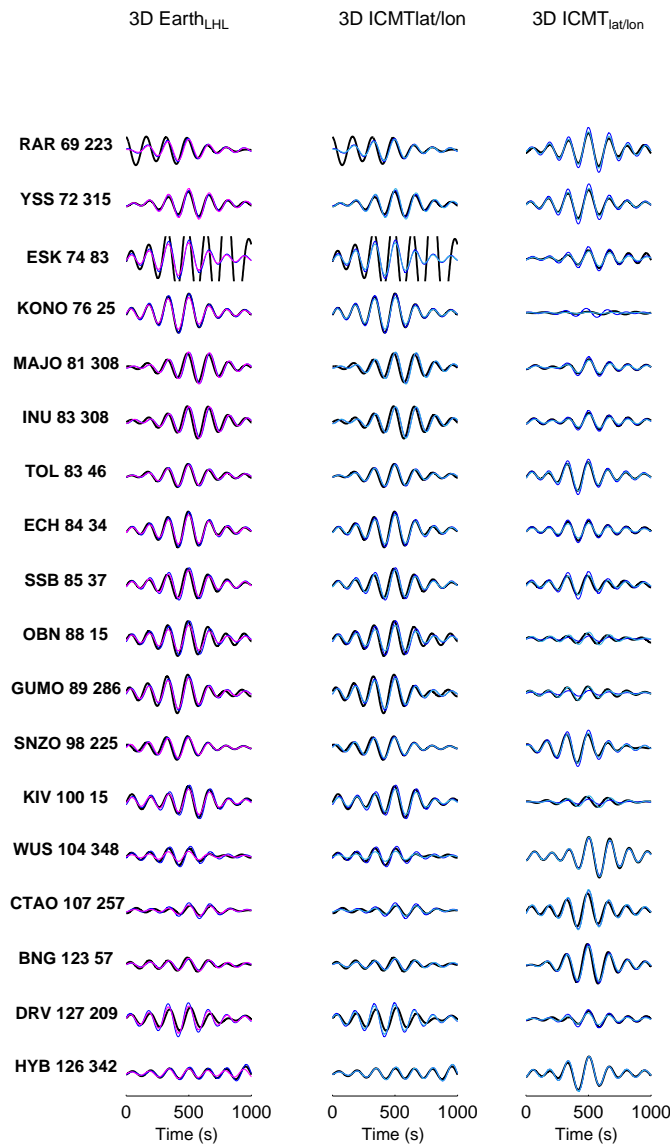


Figure B.1: Additional waveform comparisons for the M_w 7.3 Landers earthquake. Data are shown in black, GCMT in pink, ICMT in dark blue and modified solutions in light blue. Left column compares ICMT and GCMT solutions for the longitudinal component. Middle column compares the original ICMT solution with the latitude and longitude replaced by the GCMT estimates again for the longitudinal component. Right column shows the same as the middle except for the transverse component.

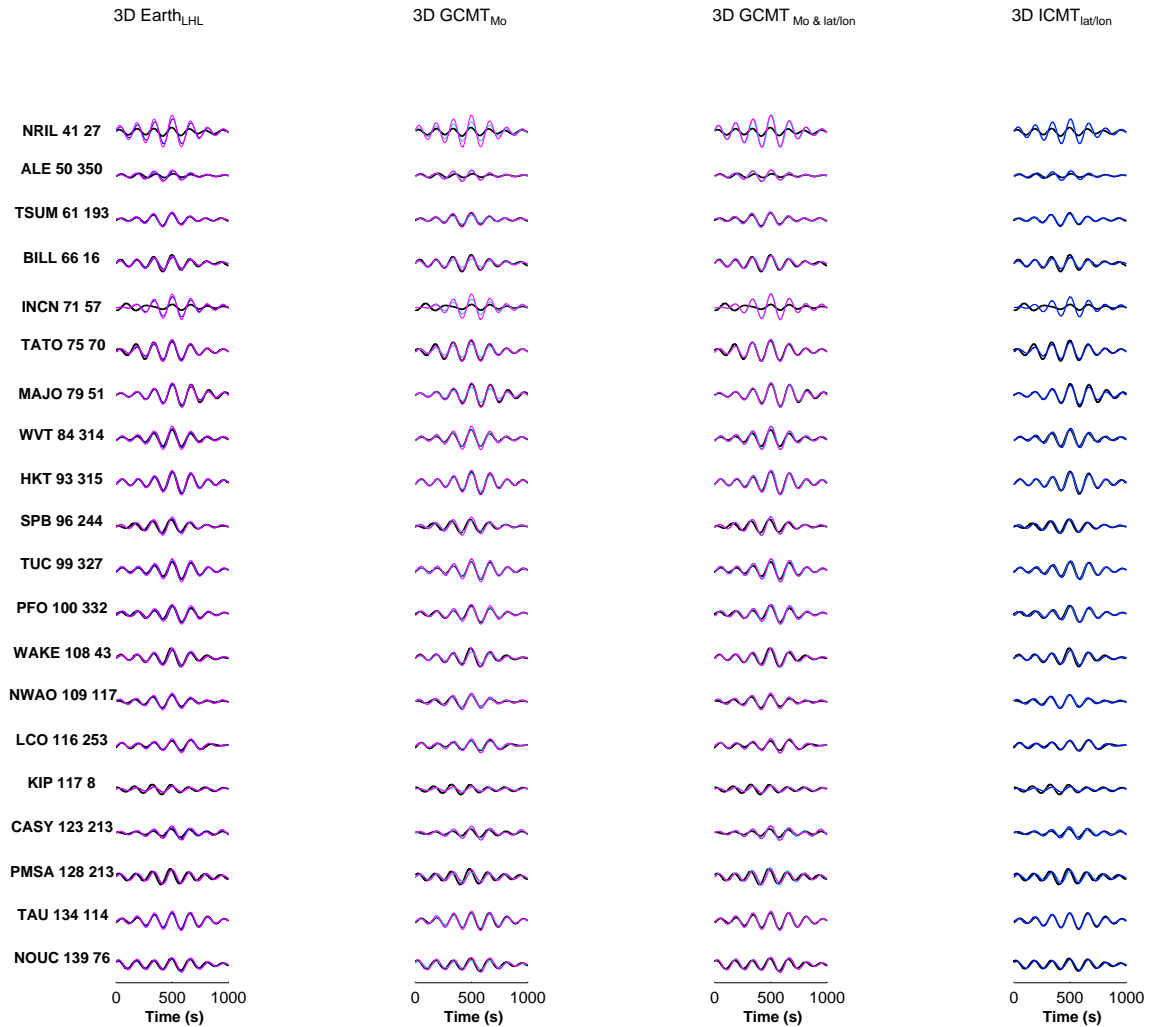


Figure B.2: Additional waveform comparisons (longitudinal component) for the M_w 7.5 Izmit earthquake. Data are shown in black, GCMT in pink, ICMT in blue and modified solutions in light blue. Left column compares the ICMT and GCMT, left middle the GCMT estimate with the moment replaced by that from Cakir et al., (2003). The right middle column compares the GCMT estimate with the latitude and longitude from Cakir et al., (2003). Far right column compares the ICMT solution where the latitude and longitude have been replaced by those reported in the GCMT catalogue.

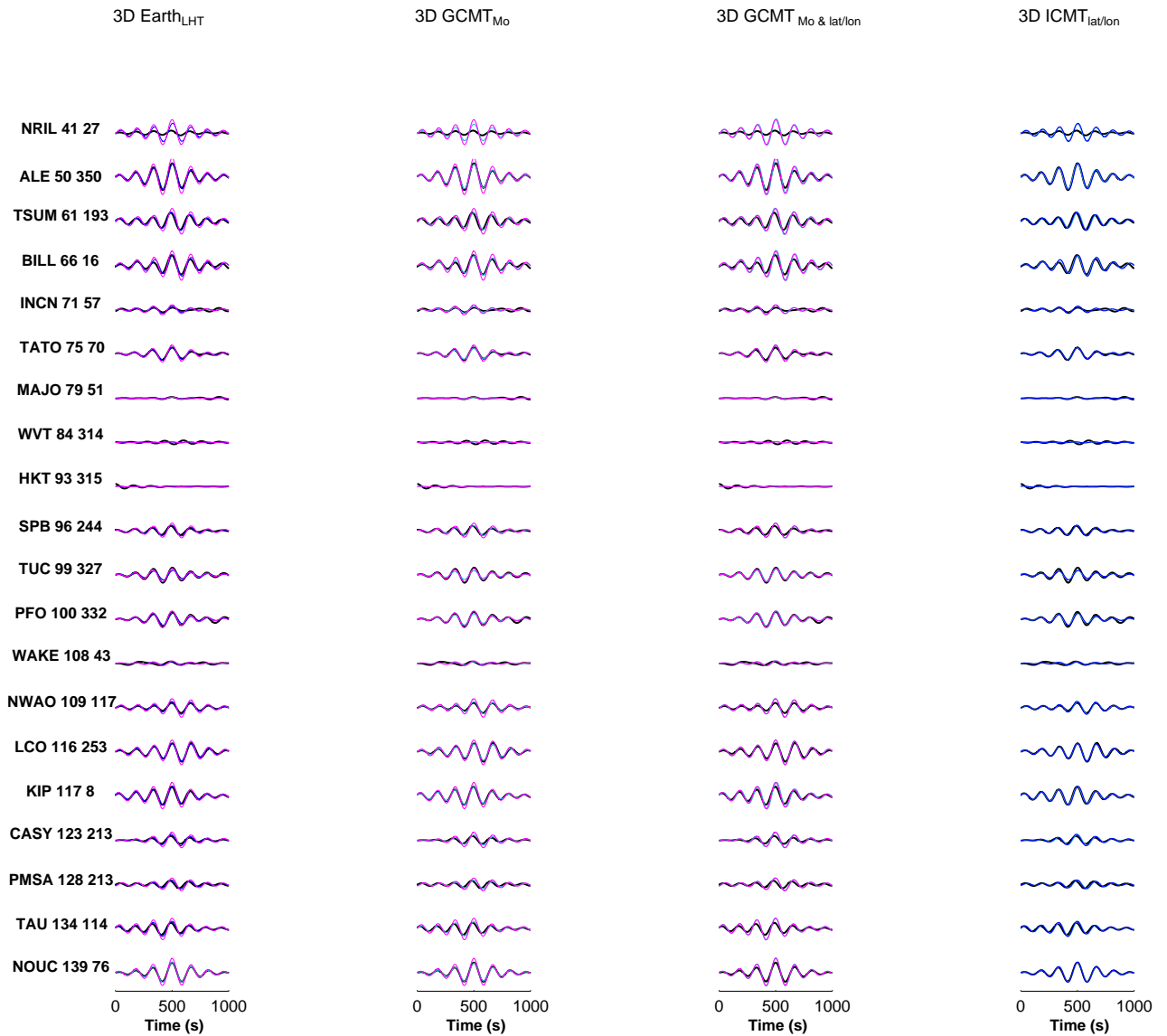


Figure B.3: Additional waveform comparisons for the M_w 7.5 Izmit earthquake. The format is exactly the same as the previous figure, except the transverse component is compared.

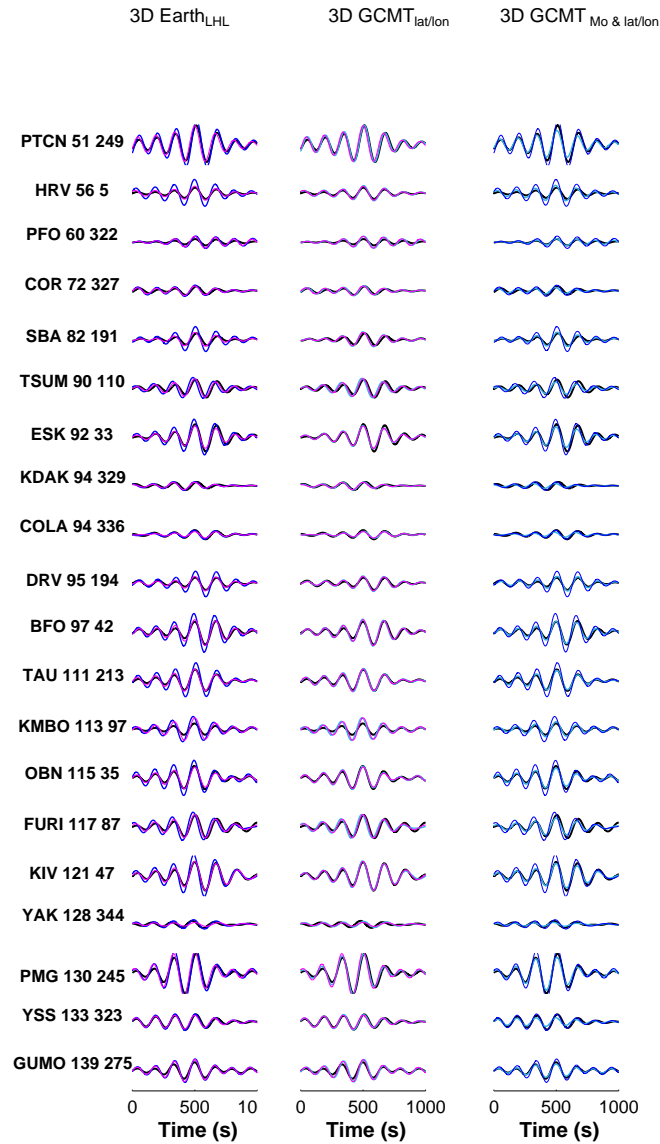


Figure B.4: Additional waveform comparisons (longitudinal component) for the M_w 8.1 Pisco earthquake. Data are in black, GCMT solution in pink, ICMT in blue and modified solutions are highlighted in light blue. Left column compares the GCMT and ICMT estimates. Middle column compares the GCMT solution with the latitude and longitude replaced with those from Pritchard and Fielding (2008). The right column compares the ICMT solution where the latitude, longitude and moment have been replaced with estimates reported in the GCMT catalogue.

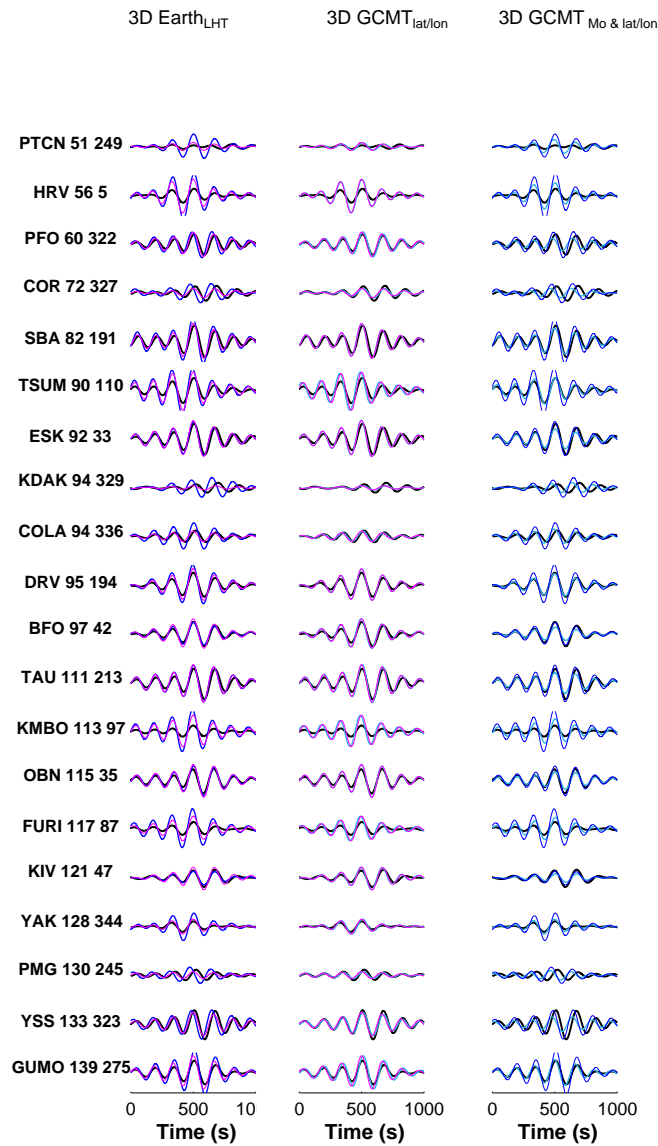


Figure B.5: Additional waveform comparisons for the M_w 8.1 Pisco earthquake. Format is exactly the same as the previous figure except the transverse component is compared.

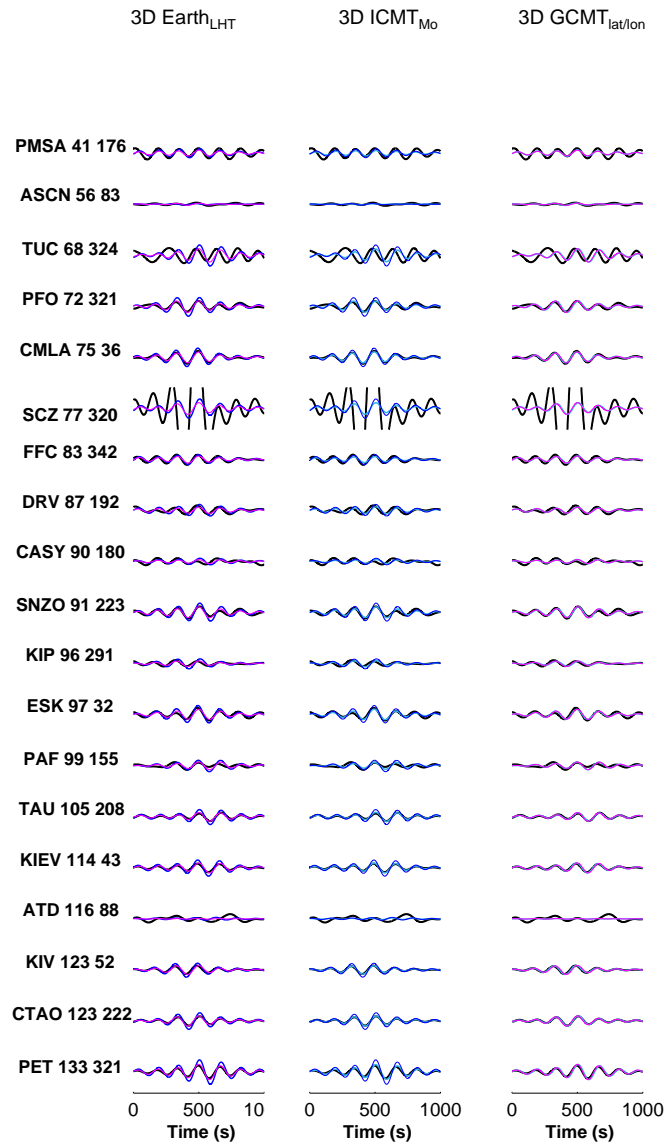


Figure B.6: Additional waveform comparisons (transverse component) for the M_w 6.6 Northern Chile event. Data are in black, GCMT solution in pink, ICMT in blue and modified solutions are highlighted in light blue. Left column compares the GCMT and ICMT estimates, middle column compares the ICMT estimate with the moment replaced by that reported in the GCMT catalogue. The right column compares the GCMT solution where the latitude and longitude have been replaced by that reported in Pritchard et al., (2006).

Appendix C

Technical notes

The CD attached includes the scripts and input files used throughout this thesis and they are described in more detail on the CD, but a brief summary of the contents is listed below. There is also a copy of the joint inversion scheme presented in Chapter 5.

1. ICMT database scripts

This directory includes the scripts that are used to calculate the centroid parameters included in the ICMT database, and there is also a copy of the script used to determine the distance between centroid locations.

2. Seismic data and synthetic calculations

To calculate synthetic seismograms and Green's functions assuming a 1-D Earth an in-house program '*apsynah*' is used and details of how to run it are provided in this directory. To generate the synthetics and Green's functions assuming a 3-D Earth structure the SPECFEM3D Globe package is used and example input files, as well as a brief overview on how to run it are included.

3. Joint inversion code

A copy of the joint inversion code is included, as well as instructions on how to compile it and a brief guide on how to run the programme. The scripts used to generate the input seismic data are included, as a specific format is required. There is also a description of the InSAR data processing, as well as details of the scenes used in the case studies in Chapter 5. Additional scripts which generate 100 sets of noisy seismic data for the tradeoff plots are also included.

References

- Adams, R. D., A. A. Hughes, and D. M. McGregor (1982), Analysis procedures at the International Seismological Centre, *Physics of the Earth and Planetary Interiors*, 30, 85–93.
- Aki, K., and P. Richards (1980), *Quantitative Seismology*, New York: Freeman.
- Akoglu, A. M., Z. Çakir, M. Meghraoui, S. Belabbes, S. O. El Alami, S. Ergintav, and H. S. Akyuz (2006), The 1994-2004 Al Hoceima (Morocco) earthquake sequence: Conjugate fault ruptures deduced from InSAR, *Earth and Planetary Science Letters*, 252, 467–480.
- Allmendinger, R., and G. Gonzalez (2010), Invited review paper: Neogene to Quaternary tectonics of the coastal Cordillera northern Chile, *Tectonophysics*, 495, 93–110.
- Allmendinger, R., R. Smalley, M. Bevis, H. Caprio, and B. Brooks (2005), Bending the Bolivian orocline in real time, *Geology*, 33, 905–908.
- Alvarado, P., S. Beck, and G. Zandt (2007), Crustal structure of the south-central Andes Cordillera and baclaric region from regional waveform modelling, *Geophysical Journal International*, 170, 858–875.
- Ambraseys, N., and J. A. Jackson (1998), Faulting associated with historical and recent earthquakes in the Eastern Mediterranean region, *Geophysical Journal International*, 133, 390–406.
- Amelung, F., and J. W. Bell (2003), Double Spring Flat, Nevada, earthquake (M5.9): Main shock accompanied by triggered slip on a conjugate fault, *Journal of Geophysical Research*, 108(B9), 2433.
- Amelung, F., and S. Day (2002), InSAR observations of the 1995 Fogo, Cape Verde, eruption: Implications for the effects of collapse events upon island volcanoes, *Geophysical Research Letters*, 29, 471–474.
- Armijo, R., B. Meyer, S. Navarro, G. King, and A. Barka (2002), Asymmetric slip partitioning in the Sea of Marmara pull-apart: a clue to propagation processes of the North Anatolian Fault?, *Terra Nova*, 14, 80–86.
- Árnadóttir, T., S. Jónsson, F. Pollitz, W. Jiang, and K. L. Feigl (2005), Postseismic deformation following the June 2000 earthquake sequence in the south Iceland seismic zone, *Journal of Geophysical Research*, 110, B12,308.
- Asad, A., S. Pullammanappallil, A. Anooosheppor, and J. Louie (1999), Inversion of Travel-Time Data for Earthquake Locations and Three-Dimensional Velocity Structure in the Eureka Valley Area, Eastern California, *Bulletin of the Seismological Society of America*, 89(3), 796–810.

- Asano, K., T. Iwata, and K. Irikura (2005), Estimation of Source Rupture Process and Strong Ground Motion Simulation of the 2002 Denali, Alaska, Earthquake, *Bulletin of the Seismological Society of America*, 95, 1701–1715.
- Astiz, L., P. Shearer, and D. Agnew (2000), Precise relocations and stress change calculations for the Upland earthquake in sequence in southern California, *Journal of Geophysical Research*, 105(B2), 2937–2953.
- Atakan, K., A. Ojeda, M. Meghraoui, A. Barka, M. Erdik, and A. Bodare (2002), Seismic Hazard in Istanbul following the 17 August 1999 Izmit and 12 November 1999 Duzce Earthquakes, *Bulletin of the Seismological Society of America*, 92(1), 466–482.
- Atwater, T. (1970), Implications of Plate Tectonics for the Cenozoic Tectonic Evolution of Western North America, *Geol. Soc. Am. Bull.*, 81, 3513–3536.
- Atzori, S., I. Hunstad, M. Chini, S. Salvi, C. Tolomei, C. Bignami, S. Stramondo, E. Trasatti, A. Antonioli, and E. Boschi (2009), Finite fault inversion of DInSAR coseismic displacement of the 2009 L'Aquila earthquake (Central Italy), *Geophysical Research Letters*, 36, L15,305.
- Bach, C., and S. Hainzl (2012), Improving empirical aftershock modeling based on additional source information, *Journal of Geophysical Research*, 117, B04,312.
- Baer, G., G. J. Funning, G. Shamir, and T. J. Wright (2008), The 1995 November 22, Mw 7.2 Gulf of Elat earthquake cycle revisited, *Geophysical Journal International*, 175, 1040–1054.
- Barka, A. (1996), Slip Distribution along the North Anatolian Fault Associated with the Large Earthquakes of the Period 1939 to 1967, *Bulletin of the Seismological Society of America*, 86(5), 1238–1254.
- Barka, A. (1999), Izmit earthquake, *Science*, 285, 1858–1859.
- Barka, A., H. S. Akyuz, E. Altunel, G. Sunal, Z. Çakir, A. Dikbas, B. Yerli, R. Armijo, B. Meyer, J. B. de Chabaliere, T. Rockwell, J. Dolan, R. Hartleb, T. Dawson, S. Christofferson, A. Tucker, T. Fumal, R. Langridge, H. Stenner, W. Lettis, J. Bachhuber, and W. Page (2002), The Surface Rupture and Slip Distribution of the 17 August 1999 Izmit Earthquake (M 7.4), North Anatolian Fault, *Bulletin of the Seismological Society of America*, 92(1), 43–60.
- Bassin, C., G. Laske, and G. Masters (2000), The current limits of resolution for surface wave tomography in North America, *EOS, Trans. Am. Geophys. Un.*, 81, F897.
- Belabbes, S., C. Wicks, Z. Çakir, and M. Meghraoui (2009), Rupture parameters of the 2003 Zemmouri (Mw 6.8), Algeria, earthquake from joint inversion of interferometric synthetic aperture radar, coastal uplift, and GPS, *Journal of Geophysical Research*, 114, B03,406.
- Ben-Menahem, A., and M. Toksoz (1963), Source mechanism from spectrums of long-period surface waves, *Journal of Geophysical Research*, 68(18), 5207–5222.
- Bennett, R., B. Wernicke, N. Niemi, A. Friedrich, and J. Davis (2003), Contemporary strain rates in the northern Basin and Range province from GPS data, *Tectonics*, 22(2), 1008.

- Bensen, G., M. Ritzwoller, and Y. Yang (2009), A 3-d shear velocity model of the crust and uppermost mantle beneath the United States from ambient seismic noise, *Geophysical Journal International*, *177*, 1177–1196.
- Berberian, M., J. A. Jackson, E. Fielding, B. E. Parsons, K. Priestly, M. Qorashi, M. Talebian, R. Walker, T. J. Wright, and C. Baker (2001), The 1998 March 14 Fandoqa earthquake (Mw 6.6) in Kerman province, southeast Iran: re-rupture of the 1981 Sirch earthquake fault, triggering of slip on adjacent thrusts and the active tectonics of the Gowk fault zone, *Geophysical Journal International*, *146*, 371–398.
- Beresnev, I. (2003), Uncertainties in Finite-Fault Slip Inversions: To What Extent to Believe (A Critical Review), *Bulletin of the Seismological Society of America*, *93*(6), 2445–2458.
- Bernard, P., P. Briole, B. Meyer, H. Lyon-Caen, J. M. Gomez, C. Tiberi, C. Berge, R. Cattin, D. Hatzfeld, C. Lachet, B. Lebrun, A. Deschamps, F. and Larroque C. Courboux, A. Rigo, D. Massonnet, P. Papadimitriou, J. Kassaras, D. Diagourtas, K. Makropoulos, G. Veis, E. Papazisi, C. Mitsakaki, V. Karakostas, E. Papadimitriou, D. Papanastassiou, M. Chouliariasis, and G. Stavrakakis (1997), The Ms=6.2, June 15, 1995 Aigion earthquake (Greece): evidence for low angle normal faulting in the Corinth rift, *Journal of Seismology*, *1*, 131–150.
- Beroza, G., and P. Spudich (1988), Linearized inversion for fault rupture behaviour: application to the 1984, Morgan Hill, California earthquake, *Journal of Geophysical Research*, *93*, 6275–6296.
- Berryman, K., Y. Ota, and A. Hull (1989), Holocene paleoseismicity in the fold and thrust belt of the Hikurangi subduction zone, eastern North Island, New Zealand, *Tectonophysics*, *163*, 185–195.
- Biggs, J., E. Bergman, B. Emmerson, G. J. Funning, J. Jackson, B. Parsons, and T. J. Wright (2006), Fault identification for buried strike-slip earthquakes using InSAR: The 1994 and 2004 Al Hoceima, Morocco earthquakes, *Geophysical Journal International*, *166*, 1347–1362.
- Biggs, J., E. Nissen, T. Craig, J. Jackson, and D. P. Robinson (2010), Breaking up the hanging wall of a rift-border fault: The 2009 Karonga earthquakes, Malawi, *Geophysical Research Letters*, *37*, L11,305.
- Biggs, J., D. P. Robinson, and T. H. Dixon (2009), The 2007 Pisco, Peru, earthquake (M8.0): seismology and geodesy, *Geophysical Journal International*, *176*, 657–669.
- Biggs, J., T. J. Wright, Z. Lu, and B. Parsons (2007), Multi-interferogram method for measuring interseismic deformation: Denali Fault, Alaska, *Geophysical Journal International*, *170*, 1165–1179.
- Bondar, I., and D. Storchak (2011), Improved location procedures at the International Seismological Centre, *Geophysical Journal International*, *186*, 1220–1244.
- Bonilla, M., R. Mark, and J. Lienkaemper (1984), Statistical relations among earthquake magnitude, surface rupture length and surface fault displacement, *Bulletin of the Seismological Society of America*, *74*(6), 2379–2411.
- Bouchon, M., M. Toksoz, H. Karabulut, M.-P. Bouin, M. Dietrich, M. Aktar, and M. Edie (2002), Space and time evolution of rupture and faulting during the 1999 Izmit (Turkey) earthquake, *Bulletin of the Seismological Society of America*, *92*(1), 256–266.

- Brooks, B., M. Bevis, K. Whipple, J. Arrowsmith, J. Foster, T. Zapata, E. Kendrick, E. Minaya, A. Echalar, M. Blanco, P. Euillades, M. Sandoval, and R. Smaller Jr (2011), Orogenic-wedge deformation and potential for great earthquakes in the central Andean back arc, *Nat. Geoscience*, 4, 380–383.
- Bürgmann, R., M. Emin Ayhan, E. J. Fielding, T. J. Wright, S. McClusky, B. Aktug, C. Demir, O. Lenk, and A. Turkezer (2002), Deformation during the 12 November 1999 Duzce, Turkey, Earthquake, from GPS and InSAR data, *Bulletin of the Seismological Society of America*, 92(1), 161–171.
- Bürgmann, R., P. A. Rosen, and E. J. Fielding (2000), Synthetic Aperture Radar Interferometry to Measure Earth's Surface Topography and its Deformation, *Annual Reviews Earth and Planetary Sciences*, 28, 169–209.
- Bustin, A., R. D. Hyndman, A. Lambert, J. Ristau, J. He, H. Dragert, and M. Van der Kooij (2004), Fault parameters of the Nisqually Earthquake Determined from Moment Tensor Solutions and the Surface Deformation from GPS and InSAR, *Bulletin of the Seismological Society of America*, 94, 363–376.
- Byerly, P. (1960), Earthquake mechanisms, *Science*, 131, 1493–1497.
- Calkins, J., G. A. Abers, G. Ekström, K. Creager, and S. Rondenay (2011), Shallow structure of the Cascadia subduction zone beneath western Washington from spectral ambient noise correlation, *Journal of Geophysical Research*, 116, B07,302.
- Capdeville, Y., E. Chaljub, J.-P. Vilotte, and J.-P. Montagner (2003), Coupling the spectral element method with a modal solution for elastic wave propagation in global earth models, *Geophysical Journal International*, 152, 34–67.
- Cattin, R., P. Briole, H. Lyon-Caen, P. Bernard, and P. Pinettes (1999), Effects of superficial layers on coseismic displacements for a dip-slip fault and geophysical implications, *Geophysical Journal International*, 137, 149–158.
- Çakir, Z., and A. M. Akoglu (2008), Synthetic aperture radar interferometry observations of the M = 6.0 Orta earthquake of 6 June 2000 (NW Turkey): Reactivation of a listric fault, *Geochemistry, Geophysics, Geosystems*, 9, Q08,009.
- Çakir, Z., J. B. de Chabaliér, R. Armijo, B. Meyer, A. Barka, and G. Peltzer (2003), Co-seismic and early post-seismic slip associated with the 1999 Izmit earthquake (Turkey), from SAR interferometry and tectonic field observations, *Geophysical Journal International*, 155, 93–110.
- Çakir, Z., M. Meghraoui, A. M. Akoglu, N. Jabour, S. Belabbès, and L. Ait-Brahim (2006), Surface Deformation Associated with the Mw 6.4, 24 February 2004 Al Hoceima, Morocco, Earthquake Deduced from InSAR: Implications for the Active Tectonics along North Africa, *Bulletin of the Seismological Society of America*, 96, 59–68.
- Chaljub, E., Y. Capdeville, and J.-P. Vilotte (2003), Solving elastodynamics in a fluid-solid heterogeneous sphere: a parallel spectral element approximation on non-conforming grids, *Journal of Computational Physics*, 187, 457–491.
- Chlieh, M., J. B. de Chabaliér, J. C. Ruegg, R. D. Armijo, R. Dmowska, J. Campos, and K. L. Feigl (2004), Crustal deformation and fault slip during the seismic cycle in the North Chile subduction zone, from GPS and InSAR observations, *Geophysical Journal International*, 158, 685–711.

- Chlieh, M., H. Perfettini, H. Tavera, J.-P. Avouac, D. Remy, J.-M. Nocquet, F. Rolandone, F. Bondoux, G. Gabalda, and S. Bonvalot (2011), Interseismic coupling and seismic potential along the Central Andes subduction zone, *Journal of Geophysical Research*, *116*, B12,405.
- Clark, T., D. Gordon, W. Himwich, C. Ma, A. Mallama, and J. Ryan (1987), Determination of Relative Site Motions in the Western United States Using Mark III Very Long Baseline Interferometry, *Journal of Geophysical Research*, *92*(B12), 12,741–12,750.
- Clark, T., C. Ma, J. Sauber, J. Ryan, D. Gordon, D. Shaffer, D. Caprette, and N. Vandenberg (1990), Geodetic measurement of deformation in the Loma Prieta, California earthquake with very long baseline interferometry, *Geophysical Research Letters*, *17*(8), 1215–1218.
- Clarke, P., D. Paradissis, P. Briole, P. England, B. Parsons, H. Billiris, G. Veis, and J.-C. Ruegg (1997), Geodetic investigation of the 13 May 1995 Kozani - Grevena (Greece) earthquake, *Geophys. Res. Lett.*, *24*(6), 707–710.
- Clévéde, E., C. Megnin, B. Romanowicz, and P. Lognonne (2000), Seismic waveform modeling and surface wave tomography in a three-dimensional Earth: asymptotic and non-asymptotic approaches, *Physics of the Earth and Planetary Interiors*, *119*, 37–56.
- Cohee, B. P., and G. C. Beroza (1994), Slip Distribution of the 1992 Landers Earthquake and Its Implications for Earthquake Source Mechanics, *Bulletin of the Seismological Society of America*, *84*, 692–712.
- Cotton, F., and M. Campillo (1995), Frequency domain inversion of strong motions: Application to the 1992 Landers earthquake, *Journal of Geophysical Research*, *100*, 3961–3975.
- Covellone, B., and B. Savage (2012), A Quantitative Comparison between 1D and 3D Source Inversion Methodologies: Application to the Middle East, *Bull. Seis. Soc. Am.*, *102*(5), 2189–2199.
- Curlander, J. C., and R. McDonough (1991), *Synthetic Aperture Radar systems and the signal processing*, John Wiley and Sons.
- Das, S., and B. Kostrov (1990), Inversion for seismic slip rate history and distribution with stabilising constraints: Application to the 1986 Andrean Islands earthquake, *Journal of Geophysical Research*, *95*(B5), 6899–6913.
- Das, S., and C. Scholz (1983), Why large earthquakes do not nucleate at shallow depths, *Nature*, *305*, 621–623.
- Dawson, J., P. Cummins, P. Tregoning, and M. Leonard (2008), Shallow intraplate earthquakes in western Australia observed by InSAR, *Journal of Geophysical Research*, *113*, B11,408.
- Dawson, J., and P. Tregoning (2007), Uncertainty analysis of earthquake source parameters determined from InSAR: A simulation study, *Journal of Geophysical Research*, *112*, B09,406.
- Decriem, J., T. Árnadóttir, A. Hooper, H. Geirsson, F. Sigmundsson, M. Keiding, B. G. Ofeigsson, S. Hreinsdóttir, P. Einarsson, L. P., and R. A. Bennett (2010), The 2008 May 29 earthquake doublet in SW Iceland, *Geophysical Journal International*, *181*, 1128–1146.

- Delouis, B., D. Giardini, P. Lundgren, and J. Salichon (2002), Joint Inversion of InSAR, GPS, Telesismic, and Strong-Motion Data for the Spatial and Temporal Distribution of Earthquake Slip: Application to the 1999 Izmit Mainshock, *Bulletin of the Seismological Society of America*, *92*, 278–299.
- Delouis, B., P. Lundgren, J. Salichon, and D. Giardini (2000), Joint inversion of InSAR and teleseismic data for the slip history of the 1999 Izmit (Turkey) earthquake, *Geophysical Research Letters*, *27*, 3389–3392.
- Delouis, B., J.-M. Nocquet, and M. Vallée (2010), Slip distribution of the February 27, 2010 Mw = 8.8 Maule earthquake, central Chile, from static and high-rate GPS, InSAR and broadband teleseismic data, *Geophysical Research Letters*, *37*, L17,305.
- Devlin, S., B. Isacks, M. Pritchard, W. Barnhart, and R. B. Lohman (2012), Depths and focal mechanisms of crustal earthquakes in the central Andes determined from teleseismic waveform analysis and InSAR, *Tectonics*, *31*, TC2002.
- Dewey, J., and S. H. Lamb (1992), Active tectonics of the Andes, *Tectonophysics*, *205*, 79–95.
- Doin, M.-P., C. Lasserre, G. Peltzer, O. Cavalie, and C. Doubre (2009), Corrections of stratified tropospheric delays in SAR interferometry: Validation with global atmospheric models, *Journal of Applied Geophysics*, *69*, 35–50.
- Dokka, R., and C. Travis (1990), Role of the eastern California shear zone in accommodating Pacific-North American plate motion, *Geophysical Research Letters*, *17*(9), 1323–1326.
- Dorbath, L., A. Cisternas, and C. Dorbath (1990), Assessment of the size of large and great historical earthquakes in Peru, *Bulletin of the Seismological Society of America*, *80*(3), 551–576.
- Dragert, H., K. Wang, and T. James (2001), A silent slip event on the deeper Cascadia subduction interface, *Science*, *292*, 1525–1528.
- Dziewonski, A. M., and D. Anderson (1981), Preliminary reference Earth model, *Phys. Earth Planet. Inter.*, *25*, 297–356.
- Dziewonski, A. M., T. A. Chou, and J. H. Woodhouse (1981), Determination of Earthquake Source Parameters From Waveform Data for Studies of Global and Regional Seismicity, *Journal of Geophysical Research*, *86*, 2825–2852.
- Dziewonski, A. M., and J. H. Woodhouse (1983), An Experiment In Systematic Study of Global Seismicity: Centroid-Moment Tensor Solutions for 201 Moderate and Large Earthquakes of 1981, *Journal of Geophysical Research*, *88*, 3247–3271.
- Dziewonski, A. M., and R. Woodward (1992), Acoustic Imaging on the planetary scale, *Acoustical Imaging*, *19*, 785–797.
- Eberhart-Philips, D., and W. Stuart (1992), Material heterogeneity simplifies the picture: Loma Prieta, *Bulletin of the Seismological Society of America*, *82*, 1964–1968.
- Ekström, G., M. Nettles, and A. M. Dziewonski (2012), The global CMT project 2004–2010: Centroid-moment tensors for 13,017 earthquakes, *Physics of the Earth and Planetary Interiors*, *200-201*, 1–9.

- Enescu, B., S. Aoi, S. Toda, W. Suzuki, K. Obara, K. Shiomi, and T. Takeda (2012), Stress perturbations and seismic response associated with the 2011 M9.0 Tohoku-oki earthquake in and around the Tokai seismic gap, central Japan, *Geophysical Research Letters*, 39, L00G28.
- Engdahl, E., van der Hilst, R., and R. Buland (1998), Global Teleseismic Earthquake Relocation with Improved Travel Times and Procedures for Depth Determination, *Bulletin of the Seismological Society of America*, 88, 722–743.
- Evans, E., and B. Meade (2012), Geodetic imaging of coseismic slip and postseismic afterslip: Sparsity promoting methods applied to the great Tohoku earthquake, *Geophysical Research Letters*, 39, L11,314.
- Farr, T., P. A. Rosen, E. Caro, R. Crippen, R. Duren, S. Hensley, M. Kobrick, M. Paller, E. Rodriguez, L. Roth, D. Seal, S. Shaffer, J. Shimada, J. Umland, M. Werner, M. Oskin, D. Burbank, and D. Alsdorf (2007), The Shuttle Radar Topography Mission, *Reviews of Geophysics*, 45, RG2004.
- Feigl, K. L. (2002), Estimating Earthquake Source Parameters from Geodetic Measurements, *International Handbook of Earthquake and Engineering Seismology*, 81A, 1–14.
- Feigl, K. L., A. Sargent, and D. Jacq (1995), Estimation of an earthquake focal mechanism from a satellite radar interferogram: Application to the December 4, 1992 Landers aftershock, *Geophysical Research Letters*, 22, 1037–1040.
- Feigl, K. L., and C. H. Thurber (2009), A method for modelling radar interferograms without phase unwrapping: application to the M 5 Fawnskin, California earthquake of 1992 December 4, *Geophysical Journal International*, 176, 491–504.
- Feng, G., E. Hetland, X. L. Ding, Z. Li, and L. Zhang (2010), Coseismic fault slip of the 2008 Mw 7.9 Wenchuan earthquake estimated from InSAR and GPS measurements, *Geophysical Research Letters*, 37, L01,302.
- Ferreira, A., J. Weston, and G. J. Funning (2011), Global Compilation of Interferometric Synthetic Aperture Radar Earthquake Source Models: 2. Effects of 3D Earth Structure, *Journal of Geophysical Research*, 116, B08,409.
- Ferreira, A., and J. H. Woodhouse (2006), Long-period seismic source inversions using global tomographic models, *Geophysical Journal International*, 166, 1178–1192.
- Fialko, Y. (2004a), Evidence of fluid-filled upper crust from observations of postseismic deformation due to the 1992 Mw 7.3 Landers earthquake, *Journal of Geophysical Research*, 109, B08,401.
- Fialko, Y. (2004b), Probing the mechanical properties of seismically active crust with space geodesy: Study of the coseismic deformation due to the 1992 Mw 7.3 Landers (southern California) earthquake, *Journal of Geophysical Research*, 109, B03,307.
- Fitch, T., W. Douglas, W. McCowan, and M. Shields (1980), Estimation of the seismic moment tensor from teleseismic body wave data with applications to intraplate and mantle earthquakes, *Journal of Geophysical Research*, 85(B7), 3817–3828.
- Foy, T., K. Frankel, Z. Lifton, C. Johnson, and M. Caffee (2012), Distributed extensional deformation in a zone of right-lateral shear: Implications for geodetic versus geologic rates of deformation in the eastern California shear zone-Walker Lane, *Tectonics*, 31, TC4008.

- Freed, A. (2005), Afterslip (and only afterslip) following the 2004 Parkfield, California, earthquake, *Geophysical Research Letters*, *34*, L06,312.
- Fujiwara, S., H. Yarai, S. Ozawa, M. Tobita, M. Murakami, H. Nakagawa, and K. Nitta (1998), Surface displacement of the March 26, 1997 Kagoshima-ken-hokuseibu earthquake in Japan from synthetic aperture radar interferometry, *Geophysical Research Letters*, *25*, 4541–4544.
- Fukahata, Y., and T. J. Wright (2008), A non-linear geodetic data inversion using ABIC for slip distribution on a fault with an unknown dip angle, *Geophysical Journal International*, *173*, 353–364.
- Fukushima, Y., T. Ozawa, and M. Hashimoto (2008), Fault model of the 2007 Noto Hanto earthquake estimated from PALSAR radar interferometry and GPS data, *Earth Planets and Space*, *60*, 99–104.
- Funning, G. J. (2005), *Source parameters of large shallow earthquakes in the Alpine-Himalayan belt from InSAR and waveform modelling*, Ph.D. thesis, Faculty of Physical Sciences, University of Oxford.
- Funning, G. J., R. M. D. Barker, S. H. Lamb, E. Minaya, B. Parsons, and T. J. Wright (2005a), The 1998 Aiquile, Bolivia earthquake: A seismically active fault revealed with InSAR, *Earth and Planetary Science Letters*, *232*, 39–49.
- Funning, G. J., B. Parsons, and T. J. Wright (2007), Fault slip in the 1997 Manyi, Tibet earthquake from linear elastic modelling of InSAR displacements, *Geophysical Journal International*, *169*, 988–1008.
- Funning, G. J., B. Parsons, T. J. Wright, J. A. Jackson, and E. J. Fielding (2005b), Surface displacements and source parameters of the 2003 Bam (Iran) earthquake from Envisat advanced synthetic aperture radar imagery, *Journal of Geophysical Research*, *110*, B09,406.
- Furumura, M., B. L. N. Kennett, and T. Furumura (1999), Seismic wavefield calculation for laterally heterogeneous earth models - II . The influence of upper mantle heterogeneity, *Geophys. J. Int.*, *139*, 623–644.
- Gahalaut, K., V. Gahalaut, and J. Kayal (2008), Poroelastic relaxation and aftershocks of the 2001 Bhuj earthquake, India, *Tectonophysics*, *460*, 76–82.
- Gasparini, L., A. Polonia, G. Bortoluzzi, P. Henry, X. Le Pichon, M. Tryon, N. Cagatay, and L. Geli (2011a), How far did the surface rupture of the 1999 Izmit earthquake reach in the Sea of Marmara, *Tectonics*, *30*, TC1010.
- Gasparini, L., A. Polonia, N. Cagatay, G. Bortoluzzi, and V. Ferrante (2011b), Geological slip rates along the North Anatolian Fault in the Marmara region, *Tectonics*, *30*, TC6001.
- Geissler, W., L. Matias, D. Stich, F. Carrilho, W. Jokat, S. Monna, A. IbenBrahim, F. Mancilla, M.-A. Gutscher, V. Salleres, and N. Zitellini (2010), Focal mechanisms for sub-crustal earthquakes in the Gulf of Cadiz from a dense OBS deployment, *Geophysical Research Letters*, *37*, L18,309.
- Ghasemi, H., Y. Fukushima, K. Koketsu, H. Miyake, Z. Wang, and J. G. Anderson (2010), Ground-motion solution simulation for the 2008 Wenchuan. China, earthquake using

- the stochastic finite-fault method, *Bulletin of the Seismological Society of America*, 100, 2476–2490.
- Gilbert, F. (1970), Excitation of normal modes of the earth by earthquake sources, *Geophysical Journal of the Royal Astronomical Society*, 22(223-226).
- Gilbert, F. (1976), The representation of seismic displacements in terms of travelling waves, *Geophysical J. R. astr. Soc.*, 44, 275–280.
- Gilbert, F., and A. M. Dziewonski (1975), An application of normal mode theory to the retrieval of structural parameters and source mechanisms from seismic spectra, *Philosophical Transactions of the Royal Society of London*.
- Godey, A., R. Bossu, J. Guilbert, and G. Mazet-Roux (2006), The Euro-Mediterranean Bulletin: A Comprehensive Seismological Bulletin at Regional Scale, *Seismological Research Letters*, 77, 460–474.
- Gonzalez, P., and J. Fernandez (2011), Drought-driven transient aquifer compaction imaged using multitemporal satellite radar interferometry, *Geology*, 39, 551–554.
- Graves, R., B. Aagaard, K. W. Hudnut, L. Star, J. Stewart, and T. Jordan (2008), Broad-band simulations for Mw 7.8 southern San Andreas earthquakes: Ground motion sensitivity to rupture speed, *Geophysical Research Letters*, 35, L22,302.
- Graves, R., and D. Wald (2001), Resolution analysis of finite fault source inversion using one- and three-dimensional Green's functions 1. Strong motions, *J. Geophys. Res.*, 106(B5), 8745–8766.
- Gray, L. (2011), Using multiple RADARSAT InSAR pairs to estimate a full three-dimensional solution for glacial ice movement, *Geophysical Research Letters*, 38, L05,502.
- Hanssen, R. (2001), *Radar interferometry: data interpretation and error analysis*, Kluwer Academic Publishers, Netherlands.
- Hao, K. X., H. Si, H. Fujiwara, and T. Ozawa (2009), Coseismic surface-ruptures and crustal deformations of the 2008 Wenchuan earthquake Mw 7.9, China, *Geophysical Research Letters*, 36, L11,303.
- Hartzell, S., G. Stewart, and C. Mendoza (1991), Comparison of L1 and L2 norms in a teleseismic waveform inversion for the slip history of the Loma Prieta, California, earthquake, *Bulletin of the Seismological Society of America*, 81(5), 1518–1539.
- Hatzfield, D., and P. Molnar (2010), Comparisons of the kinematics and deep structures of the Zagros and Himalaya and of the Iranian and Tibetan plateaus and geodynamic implications, *Reviews of Geophysics*, 38(RG2005).
- Hayes, G., R. Briggs, A. Sladen, E. J. Fielding, C. Prentice, K. Hudnut, P. Mann, F. Taylor, A. Crone, R. Gold, T. Ito, and M. Simons (2010), Complex rupture during the 12 January 2010 Haiti earthquake, *Nature Geoscience*, 3, 800–805.
- Hayes, G., D. Wald, and R. Johnson (2012), Slab1.0, A three-dimensional model of global subduction zone geometries, *Journal of Geophysical Research*, 117, B01,302.
- Hergert, T., and O. Heidbach (2006), New insights into the mechanism of postseismic stress relaxation exemplified by the 23 June 2001, Mw = 8.4 earthquake in southern Peru, *Geophysical Research Letters*, 33(L02307).

- Hernandez, B., F. Cotton, and M. Campillo (1999), Contribution of radar interferometry to a two-step inversion of the kinematic process of the Landers earthquake, *Journal of Geophysical Research*, *104*, 13,083–13,099.
- Hjörleifsdóttir, V., and G. Ekström (2009), Effects of three-dimensional Earth structure on CMT earthquake parameters, *Physics of the Earth and Planetary Interiors*, *179*, 178–190.
- Hjörleifsdóttir, V., H. Kanamori, and J. Tromp (2009), Modeling 3-D wave propagation and finite slip for the 1998 Balleny Islands earthquake, *Journal of Geophysical Research*, *114*, B03,301.
- Hutton, K., J. Woessner, and E. Hauksoo (2010), Earthquake Monitoring in Southern California for Seventy-Seven Years (1932-2008), *Bulletin of the Seismological Society of America*, *100*, 423–446.
- Ichinose, G., G. Anderson, K. Smith, and Y. Zeng (2003), Source Parameters of Eastern California and Western Nevada Earthquakes from Regional Moment Tensor Inversion, *Bulletin of the Seismological Society of America*, *93*(1), 61–84.
- Iinuma, T., R. Hino, M. Kido, D. Inazu, Y. Osada, Y. Ito, M. Ohzono, H. Tsushima, S. Suzuki, H. Fujimoto, and S. Miura (2012), Coseismic slip distribution of the 2011 off the Pacific Coast of Tohoku Earthquake (M9.0) refined by means of seafloor geodetic data, *Journal of Geophysical Research*, *117*, B07,409.
- IMD (2011), Seismological Activities, <http://www.imd.gov.in/section/seismo/static/welcome.htm>, Last accessed 23/05/11.
- Imperator, W., and M. Mai (2012), Sensitivity of broad-band ground-motion simulations to earthquake source and Earth structure variations: an application to the Messina Straits (Italy), *Geophysical Journal International*, *188*, 1103–1116.
- Isacks, B. (1988), Uplift of the central Andean plateau and bending of the Bolivian orocline, *J. Geophys. Res.*, *93*, 3211–3231.
- Jackson, J., and D. McKenzie (1984), Active tectonics of the Alpine-Himalayan Belt between western Turkey and Pakistan, *Geophysical J. R. astr. Soc.*, *77*, 185–264.
- Jahnke, G., M. Thorne, A. Cochard, and H. Igel (2008), Global SH-wave propagation using a parallel axisymmetric spherical finite-difference scheme, *Geophysical Journal International*, *173*, 815–826.
- Jeffreys, H., and K. Bullen (1940), Seismological Tables, *British Association for the Advancement of Science*, *50*.
- Ji, C., and G. Hayes (2008), Preliminary Result of the May 12, 2008 Mw 7.9 Eastern Sichuan, China Earthquake, <http://earthquake.usgs.gov/earthquakes/eqinthenews/2008/us2008ryan/finite-fault.php>, Last accessed 19/10/08.
- Ji, C., D. Wald, and D. Helmberger (2002a), Source Description of the 1999 Hector Mine, California, Earthquake, Part I: Wavelet Domain Inversion Theory and Resolution Analysis, *Bulletin of the Seismological Society of America*, *92*(4), 1192–1207.
- Ji, C., D. Wald, and D. Helmberger (2002b), Source description of the 1999 Hector Mine, California, earthquake, Part II: Complexity of slip history, *Bulletin of the Seismological Society of America*, *92*(4), 1208–1226.

- Johanson, I., E. J. Fielding, F. Rolandone, and R. B'urgmann (2006), Coseismic and postseismic slip of the 2004 Parkfield earthquake from space-geodetic data, *Bulletin of the Seismological Society of America*, 96(4B), S269–S282.
- Jolivet, R., R. B'urgmann, and N. Houlié (2009), Geodetic exploration of the elastic properties across and within the northern San Andreas Fault zone, *Earth and Planetary Science Letters*, 288, 126–131.
- Jónsson, S., H. Zebker, P. Segall, and F. Amelung (2002), Fault Slip Distribution of the 1999 Mw 7.1 Hector Mine, California, Earthquake, Estimated from Satellite Radar and GPS Measurements, *Bulletin of the Seismological Society of America*, 92, 1377–1389.
- Jouanne, F., A. Awan, A. Madji, A. Pecher, M. Latif, A. Kausar, J. L. Mugnier, I. Khan, and N. A. Khan (2011), Postseismic deformation in Pakistan after the 8 October 2005 earthquake: Evidence of afterslip along a flat north of the Balakot-Bagh thrust, *Journal of Geophysical Research*, 116, B07,401.
- Julian, B. (1983), Evidence for dyke intrusion earthquake mechanisms near Long Valley caldera, California, *Nature*, 303, 323–325.
- Julian, B. (1998), Non-double-couple earthquakes 1. Theory, *Reviews of Geophysics*, 36(4), 525–549.
- Kanamori, H. (1970), The Alaska earthquake of 1964: Radiation of long-period surface waves and source mechanism, *Journal of Geophysical Research*, 75(26), 5029–5040.
- Kanamori, H. (1977), The Energy Release in Great Earthquakes, *Journal of Geophysical Research*, 82, 2981–2987.
- Kaser, M., and F. Galovic (2008), Effects of complicated 3-D rupture geometries on earthquake ground motion and their implications: a numerical study, *Geophysical Journal International*, 172, 276–292.
- Kaverina, A., D. Dreger, and E. Price (2002), The combined inversion of seismic and geodetic data for the source process of the 16 October 1999 Mw 7.1 Hector Mine, California, earthquake, *Bulletin of the Seismological Society of America*, 92(4), 1266–1280.
- Kaviania, A., A. Paul, E. Bourova, D. Hatzfield, H. Pedersen, and M. Mokhtari (2007), A strong seismic velocity contrast in the shallow mantle across the Zagros collision zone, *Geophysical Journal International*, 171, 399–410.
- Kendrick, E., M. Bevis, R. Smalley, B. Brooks, R. Vargas, E. Lauria, and L. Souto Fortes (2003), The Nazca-South America Euler vector and its rate of change, *Journal of South American Sciences*, 16(2), 125–131.
- Kennett, B. L. N., E. R. Engdahl, and R. Buland (1995), Constraints on seismic velocities in the Earth from traveltimes, *Geophysical Journal International*, 122, 108–124.
- Kim, S., A. Nyblade, N. Rhie, C.-E. Baag, and T.-S. Kang (2012), Crustal S-wave velocity structure of the Main Ethiopian Rift from ambient noise tomography, *Geophysical Journal International*, 191, 865–878.
- King, G. C. P., R. Stein, and J. Lin (1994), Static Stress Changes and the Triggering of Earthquakes, *Bulletin of the Seismological Society of America*, 84, 935–953.

- Klinger, Y., R. Michel, and J.-P. Avouac (2000), Co-seismic deformation during the Mw 7.3 Aqaba earthquake (1995) from ERS-SAR interferometry, *Geophysical Research Letters*, 27, 3651–3654.
- Komatitsch, D., and J. Tromp (1999), Introduction to the spectral element method for three-dimensional seismic wave propagation, *Geophysical Journal International*, 139, 806–822.
- Komatitsch, D., and J. Tromp (2002a), Spectral-element simulations of global seismic wave propagation - I. Validation, *Geophysical Journal International*, 149, 390–412.
- Komatitsch, D., and J. Tromp (2002b), Spectral-element simulations of global seismic wave propagation - II. Three-dimensional models, oceans, rotation and self-gravitation, *Geophysical Journal International*, 150, 303–318.
- Konca, A., V. Hjorleifsdottir, T.-R. Song, J.-P. Avouac, D. Helmberger, C. Ji, K. Sieh, R. Briggs, and A. Meltzner (2007), Rupture Kinematics of the 2005 Mw 8.6 Nias-Simeulue Earthquake from the Joint Inversion of Seismic and Geodetic Data, *Bulletin of the Seismological Society of America*, 97(1A), S307–S322.
- Konca, A., S. Leprince, J.-P. Avouac, and D. Helmberger (2010), Rupture process of the 1999 Mw 7.1 Duzce earthquake from joint analysis of SPOT, GPS, InSAR, strong-motion and teleseismic data: A supershear rupture with variable rupture velocity, *Bulletin of the Seismological Society of America*, 100(1), 267–288.
- Kontoes, C., P. Elias, O. Sykioti, P. Briole, D. Remy, M. Sachpazi, and G. and Kotsis I. Veis (2000), Displacement field and fault model for the September 7, 1999 Athens earthquake inferred from ERS2 satellite radar interferometry, *Geophysical Research Letters*, 27, 3989–3992.
- Kubo, A., E. Fukuyama, H. Kawai, and K. Nonomura (2002), NIED seismic moment tensor catalogue for regional earthquakes around Japan: quality test and application, *Tectonophysics*, 356, 23–48.
- Lamb, S. (2000), Active deformation in the Bolivian Andes, South America, *Journal of Geophysical Research*, 105(B11), 25,627–25,653.
- Lasserre, C., G. Peltzer, F. Crampe, Y. Klinger, J. Van der Woerd, and P. Tapponnier (2005), Coseismic deformation of the 2001 Mw = 7.8 Kokoxili earthquake in Tibet, measured by synthetic aperture radar interferometry, *Journal of Geophysical Research*, 110, B12,403.
- Lawson, A. (1908), *The California earthquake of April 18, 1906: Report of the State Earthquake Investigation Commission*, Tech. rep., Carnegie Institution of Washington Publication.
- Lensen, G. (1968), Analysis of Progressive Fault Displacement During Downcutting at the Branch River Terraces, South Island, New Zealand, *Geological Society of America Bulletin*, 79, 545–556.
- Li, X. J., L. Liu, Y. S. Wang, and T. Yu (2010), Analysis of horizontal strong-motion attenuation in the great 2008 Wenchuan earthquake, *Bulletin of the Seismological Society of America*, 100, 2440–2449.

- Li, Z., W. Feng, Z. Xu, P. Cross, and J. Zhang (2008), 1998 Mw 5.7 Zhangbei-Shangyi (China) earthquake revisited: A buried thrust fault revealed with interferometric synthetic aperture radar, *Geochemistry, Geophysics, Geosystems*, 9, Q04,026.
- Li, Z., J.-P. Muller, P. Cross, and E. J. Fielding (2005), Interferometric synthetic aperture radar (InSAR) atmospheric correction: GPS, Moderate Resolution Imaging Spectroradiometer (MODIS) and InSAR integration, *Journal of Geophysical Research*, 110, B03,410.
- Liu-Zeng, J., L. Wen, J. Sun, Z. Zhang, G. Hu, X. Xing, L. Zeng, and Q. Xu (2010), Surface Slip and Rupture Geometry on the Beichuan Fault near Hongkou during the Mw 7.9 Wenchuan Earthquake, China, *Bulletin of the Seismological Society of America*, 100, 2615–2650.
- Liu-Zeng, J., Z. Zhang, L. Wen, P. Tapponnier, J. Sun, X. Xing, G. Hu, Q. Xu, L. Zeng, L. Ding, C. Ji, K. W. Hudnut, and J. van der Woerd (2009), Co-seismic rupture of the 12 May 2008, Ms 8.0 Wenchuan earthquake, Sichuan: East-west crustal shortening on oblique, parallel thrusts along the eastern edge of Tibet, *Earth and Planetary Science Letters*, 286, 355–370.
- Lohman, R. B., and M. Simons (2005a), Locations of selected small earthquakes in the Zagros mountains, *Geochemistry, Geophysics, Geosystems*, 6, Q03,001.
- Lohman, R. B., and M. Simons (2005b), Some thoughts on the use of InSAR data to constrain models of surface deformation: Noise structure and data downsampling, *Geochemistry, Geophysics, Geosystems*, 6, Q01,007.
- Lohman, R. B., M. Simons, and B. Savage (2002), Location and mechanism of the Little Skull Mountain earthquake as constrained by satellite radar interferometry and seismic waveform modelling, *Journal of Geophysical Research*, 107, B6.
- Loveless, J., M. E. Pritchard, and N. Kukowski (2010), Testing mechanisms of subduction zone segmentation and seismogenesis with slip distributions from recent Andean earthquakes, *Tectonophysics*, 495, 15–33.
- Lubis, A., A. Hashima, and T. Sato (2013), Analysis of afterslip distribution following the 2007 September 12 southern Sumatra earthquake using poroelastic and viscoelastic media, *Geophysical Journal International*, 192, 18–37.
- Marquering, H., G. Nolet, and F. A. Dahlen (1998), Three-dimensional waveform sensitivity kernels, *Geophysical Journal International*, 132, 521–534.
- Marshall, G., R. Stein, and W. Thatcher (1991), Faulting geometry and slip from co-seismic elevation changes: The 18 October 1989, Loma Prieta, California, earthquake, *Bulletin of the Seismological Society of America*, 81, 1660–1693.
- Massonnet, D., and K. L. Feigl (1995), Satellite radar interferometric map of the coseismic deformation field of the M = 6.1 Eureka Valley, California earthquake of May 17, 1993, *Geophysical Research Letters*, 22, 1541–1544.
- Massonnet, D., and K. L. Feigl (1998), Radar interferometry and its application to changes in the earth's surface, *Reviews of Geophysics*, 36, 441–500.
- Massonnet, D., K. L. Feigl, H. Vadon, and M. Rossi (1996), Coseismic deformation field of the M = 6.7 Northridge California earthquake of January 17, 1994 recorded by two radar satellites using interferometry, *Geophysical Research Letters*, 23, 969–972.

- Massonnet, D., M. Rossi, C. Carmona, F. Adragna, G. Peltzer, K. Feigl, and T. Rabaute (1993), The displacement field of the Landers earthquake mapped by radar interferometry, *Nature*, *364*, 138–142.
- McCalpin, J. (Ed.) (1996), *Paleoseismology*, vol. 62, Academic Press Inc.
- McClusky, S., S. Bassalanian, A. Barka, C. Demir, S. Ergintav, I. Georgiev, O. Gurkan, M. Hamburger, K. Hurst, H.-G. Hans-Gert, K. Karstens, G. ad King R. Kekkelidze, V. Kotzev, O. Lenk, S. Mahmoud, A. Mishin, M. Nadariya, A. Ouzounis, D. Paradissis, Y. Peter, M. Prilepin, R. Relinger, I. Sanli, H. Seeger, A. Tealab, M. Toksoz, and G. Veis (2000), Global positioning system constraints on plate kinematics and dynamics in the eastern Mediterranean and Causcaus, *Journal of Geophysical Research*, *105*, 5695–5719.
- McGuire, J. (2008), Seismic cycles and earthquake predictability on East Pacific Rise transform faults, *Bulletin of the Seismological Society of America*, *98*(3), 1067–1084.
- McQuarrie, N. (2002), Initial plate geometry, shortening variations, and evolution of the Bolivian orocline, *Geology*, *30*, 867–870.
- Meade, B., and J. Loveless (2009), Predicting the geodetic signature of $M_w \geq$ slow slip events, *Geophysical Research Letters*, *36*, L01,306.
- Mellors, R. J., H. Magistrale, P. Earle, and A. Cogbill (2004), Comparison of Four Moderate-Size Earthquakes in Southern California Using Seismology and InSAR, *Bulletin of the Seismological Society of America*, *94*, 2004–2014.
- Meltzer, A., R. Rudnick, P. Zeitler, A. Levander, G. Humphreys, K. Karlstrom, G. Ekström, R. Carlson, T. H. Dixon, M. Gurnis, P. Shearer, and van der Hilst. R. (1999), USArray Initiative, *GSA Today*, *9*(11), 8–10.
- Mendoza, C., and S. Hartzell (1989), Slip distribution of the 19 September 1985 Michoacan, Mexico, earthquake: near source and teleseismic constraints, *Bulletin of the Seismological Society of America*, *79*, 655–669.
- Meyer, B., R. Armijo, D. Massonnet, J.-B. de Chabaliere, C. Delacourt, J. C. Ruegg, J. Achache, P. Briole, and D. Papanastassiou (1996), The 1995 Grevena (Northern Greece) Earthquake: Fault model constrained with tectonic observations and SAR interferometry, *Geophysical Research Letters*, *23*, 2677–2680.
- Millot-Langet, M., E. Clevede, and P. Lognonne (2003), Normal modes and long period seismograms in a 3D anelastic elliptical rotating Earth, *Geophysical Research Letters*, *30*(5), 1202–1208.
- Motagh, M., J. Klotz, F. Tavakoli, Y. Djamour, S. Arabi, H.-U. Wetzell, and J. Zschau (2006), Combination of Precise Leveling and InSAR Data to Constrain Source Parameters of the $M_w = 6.5$, 26 December 2003 Ba, Earthquake, *Pure and Applied Geophysics*, *163*, 1–18.
- Motagh, M., B. Schurr, J. Anderssohn, B. Cailleau, T. Walter, R. Wang, and J.-P. Vilotte (2010), Subduction earthquake deformation associated with 14 November 2007, M_w 7.8 Tocopilla earthquake in Chile: Results from InSAR and aftershocks, *Tectonophysics*, *490*, 60–68.

- Motagh, M., R. Wang, T. Walter, R. B¹urgmann, E. Fielding, J. Anderssohn, and J. Zschau (2008), Coseismic slip model of the 2007 August Pisco earthquake (Peru) as constrained by Wide Swath radar observations, *Geophysical Journal International*, 174, 842–848.
- Murray, J., and J. Langbein (2006), Slip on the San Andreas fault at Parkfield, California, over two earthquake cycles, and the implications for seismic hazard, *Bulletin of the Seismological Society of America*, 96(4B), S283–S303.
- Murray, M., J. Savage, M. Lisowski, and W. Gross (1993), Coseismic displacements: 1992, Landers, California, earthquake, *Geophysical Research Letters*, 20, 632–626.
- Nakamura, T., S. Tsuboi, Y. Kaneda, and Y. Yamanaka (2010), Rupture process of the 2008 Wenchuan, China earthquake inferred from teleseismic waveform inversion and forward modelling of broadband seismic waves, *Tectonophysics*, 491, 72–84.
- Nishimura, T., S. Fujiwara, M. Murakami, H. Suito, M. Tobita, and H. Yarai (2006), Fault model of the 2005 Fukuoka-ken Seiho-oki earthquake estimated from coseismic deformation observed by GPS InSAR, *Earth Planets and Space*, 58, 51–56.
- Nishimura, T., S. Fujiwara, M. Murakami, M. Tobita, H. Nakagawa, T. Sagiya, and T. Tada (2001), The M6.1 Earthquake triggered by volcanic inflation of Iwate volcano, northern Japan, observed by satellite radar interferometry, *Geophysical Research Letters*, 28, 635–638.
- Nishimura, T., T. Imakiire, H. Yarai, T. Ozawa, M. Murakami, and M. Kaidzu (2003), A preliminary fault model of the 2003 July 26, M6.4 northern Miyagi earthquake, north-eastern Japan, estimated from joint inversion of GPS leveling and InSAR data, *Earth Planets and Space*, 55, 751–757.
- Nissen, E., B. Emmerson, G. J. Funning, A. Mistrukov, B. Parsons, D. P. Robinson, E. Rogozhin, and T. J. Wright (2007a), Combining InSAR and seismology to study the 2003 Siberian Altai earthquakes - dextral strike-slip and anticlockwise rotations in the northern India-Eurasia collision zone, *Geophysical Journal International*, 169, 216–232.
- Nissen, E., M. Ghorashi, J. Jackson, B. Parsons, and M. Talebian (2007b), The 2005 Qeshm Island earthquake (Iran) - a link between buried reverse faulting and surface folding in the Zagros Simply Folded Belt, *Geophysical Journal International*, 171, 326–338.
- Nissen, E., F. Yamini-Fard, M. Tatar, A. Gholamzadeh, E. Bergman, J. R. Elliot, J. A. Jackson, and B. Parsons (2010), The vertical separation of mainshock rupture and microseismicity at Qeshm Island in the Zagros fold-and-thrust belt, Iran, *Earth and Planetary Science Letters*, 296, 181–194.
- Oglesby, D., M. Mai, K. Atakan, and S. Pucci (2008), Dynamic models of earthquakes on the North Anatolian fault zone under the Sea of Marmara: Effect of hypocenter location, *Geophysical Research Letters*, 35, L18,302.
- Okada, Y. (1985), Surface Deformation due to Shear and Tensile Fault in a Half-space, *Bulletin of the Seismological Society of America*, 75, 1135–1154.
- Okada, Y., K. Kasahara, S. Hori, K. Obara, S. Sekiguchi, H. Fujiwara, and A. Yamamoto (2004), Recent progress of seismic observation networks in Japan - Hi-net, F-net, K-NET and KiK-net, *Earth Planets and Space*, 56(xv–xxviii).

- Oldow, J., C. Aiken, J. Hare, J. Ferguson, and R. Hardyman (2001), Active displacement transfer and differential block motion within the central Walker Lane, western Great Basin, *Geology*, *29*, 19–22.
- Olson, A., and R. Apsel (1982), Finite faults and inverse theory with applications to the 1979 Imperial Valley earthquake, *Bulletin of the Seismological Society of America*, *72*, 1969–2001.
- Oswald, J., and S. Wesnousky (2002), Neotectonics and Quaternary geology of the Hunter Mountain fault zone and Salin Valley region, southeastern California, *Geomorphology*, *42*, 255–578.
- Ozawa, S., M. Murakami, S. Fujiwara, and M. Tobita (1997), Synthetic aperture radar interferogram of the 1995 Kobe earthquake and its geodetic inversion, *Geophysical Research Letters*, *24*, 2327–2330.
- Ozawa, S., H. Yarai, M. Tobita, H. Une, and T. Nishimura (2008), Crustal deformation associated with the Noto Hanto Earthquake in 2007 in Japan, *Earth Planets and Space*, *60*, 95–98.
- Ozawa, T., S. Nishimura, Y. Wada, and H. Ohkura (2005), Coseismic deformation of the Mid Niigata prefecture Earthquake in 2004 detected by RADARSAT/InSAR, *Earth Planets and Space*, *57*, 423–428.
- Parks, M., J. Biggs, P. England, T. Mather, P. Nomikou, K. Palamartchouk, X. Papanikolaou, D. Paradissis, B. Parsons, D. Pyle, C. Raptakis, and V. Zacharis (2012), Evolution of Santorini Volcano dominated by episodic and rapid fluxes of melt from depth, *Nature Geoscience*, *5*, 749–754.
- Parsons, T., E. Field, M. Page, and K. Milner (2012), Possible earthquake rupture connections on mapped California faults ranked by calculated coulomb linking stresses, *Bulletin of the Seismological Society of America*, *102*(6), 2667–2676.
- Parsons, T., and W. Thatcher (2011), Diffuse Pacific-North American plate boundary: 1000 km of dextral shear inferred from modelling geodetic data, *Geology*, *39*, 943–946.
- Parsons, T., S. Toda, R. Stein, A. Barka, and J. Dieterich (2000), Heightened Odds of Large Earthquakes Near Istanbul: An Interaction-Based Probability Calculation, *Science*, *288*, 661–664.
- Pathier, E., E. J. Fielding, T. J. Wright, R. Walker, B. E. Parsons, and S. Hensley (2006), Displacement field and slip distribution of the 2005 Kashmir earthquake from SAR imagery, *Geophysical Research Letters*, *33*, L20,310.
- Pedersen, R., S. J. Jónsson, T. Árnadóttir, F. Sigmundsson, and K. L. Feigl (2003), Fault slip distribution of two June 2000 Mw6.5 earthquakes in South Iceland estimated from joint inversion of InSAR and GPS measurements, *Earth and Planetary Science Letters*, *213*, 487–502.
- Pedersen, R., F. Sigmundsson, K. L. Feigl, and T. Árnadóttir (2001), Coseismic interferograms of two Ms = 6.6 earthquakes in the South Iceland Seismic Zone, June 2000, *Geophysical Research Letters*, *28*, 3341–3344.

- Peltzer, G., K. W. Hudnut, and K. L. Feigl (1994), Analysis of coseismic surface displacement gradients using radar interferometry: new insights into the Landers earthquake 1992, *Journal of Geophysical Research*, 99(B10), 21,971–21,981.
- Peltzer, G., and P. Rosen (1995), Surface Displacement of the 17 May 1993 Eureka Valley, California, Earthquake Observed by SAR Interferometry, *Science*, 268, 1333–1336.
- Perfettini, H., J.-P. Avouac, H. Tavera, A. Kositsky, J.-M. Nocquet, F. Bondoux, M. Chlieh, A. Sladen, L. Audin, D. L. Farber, and P. Soler (2010), Seismic and aseismic slip on the Central Peru megathrust, *Nature*, 465, 78–81.
- Peyrat, S., J. Campos, J.-B. de Chabaliere, A. Perez, S. Bonvalot, M.-P. Bouin, D. Legrand, A. Necessian, O. Charade, G. Patau, E. Clevede, E. Kausel, P. Bernard, and J.-P. Vilotte (2006), Tarapaca intermediate-depth earthquake (Mw 7.7, 2005, northern Chile): A slab-pull event with horizontal fault plane constrained from seismologic and geodetic observations, *Geophysical Research Letters*, 33, L22,308.
- Peyret, M., J. Chery, Y. Djamour, A. Avallone, F. Sarti, P. Briole, and M. Sarpoulaki (2007), The source motion of 2003 Bam (Iran) earthquake constrained by satellite and ground-based geodetic data, *Geophysical Journal International*, 169, 849–865.
- Peyret, M., F. Rolandone, S. Dominguez, Y. Djamour, and B. Meyer (2008), Source model for the Mw 6.1, 31 March 2006, Chalan-Chulan Earthquake (Iran) from InSAR, *Terra Nova*, 20, 126–133.
- Pezzo, G., C. Tolomei, S. Atzori, S. Salvi, E. Shabanian, O. Bellier, and Y. Farbod (2012), New kinematic constraints of the western Doruneh fault, northeastern Iran, from interseismic deformation analysis, *Geophysical Journal International*, 190, 622–628.
- Plesch, A., J. Shaw, C. Benson, W. Bryant, S. Carena, M. Cooke, J. Dolan, G. Fuis, E. Gath, L. Grant, E. Hauksson, T. Jordan, M. Kamerling, M. Legg, S. Lindvall, H. Magistrale, C. Nicholson, N. Niemi, M. Oskin, S. Perry, G. Planansky, T. Rockwell, P. Shearer, C. Sorlien, P. Suss, J. Suppe, J. Treiman, and R. Yeats (2007), Community Fault Model (CFM) for Southern California, *Bulletin of the Seismological Society of America*, 97(6), 1793–1802.
- Plesch, A., J. Shaw, J. Dolan, L. Grant, E. Hauksson, M. Kamerling, M. Legg, S. Lindvall, C. Nicholson, T. Rockwell, C. Sorlien, and R. Yeats (2002), SCEC 3D Community Fault Model for Southern California, *EOS, Trans. Am. Geophys. Un.*, 83(47), S21A–0966.
- Polonia, A., P. Gasperini, A. Amorosi, E. Bonatti, G. Bortoluzzi, N. Cagatay, L. Captondi, M.-H. Cormier, N. Gorur, C. McHugh, and L. Seeber (2004), Holocene slip rate of the North Anatolian Fault beneath the Sea of Marmara, *Earth and Planetary Science Letters*, 227, 411–426.
- Pondrelli, S., A. Morelli, G. Ekström, S. Mazza, E. Boschi, and A. M. Dziewonski (2002), European-Mediterranean regional centroid-moment tensors: 1997-2000, *Physics of the Earth and Planetary Interiors*, 130, 71–101.
- Pondrelli, S., S. Salimbeni, A. Morelli, G. Ekström, L. Postpischl, G. Vannucci, and E. Boschi (2011), European-Mediterranean Regional Centroid Moment Tensor catalog: Solutions for 2005-2008, *Physics of the Earth and Planetary Interiors*, 185, 74–81.
- Potin, P. (2011), Sentinel-1 Mission Overview, *Sentinel-1 Mission Overview*, p. Last Accessed 26/04/11.

- Prawirodirdjo, L., R. McCaffrey, D. Chadwell, Y. Bock, and C. Subarya (2010), Geodetic observations of an earthquake cycle at the Sumatra subduction zone: Role of interseismic strain segmentation, *Journal of Geophysical Research*, *115*, B03,414.
- Press, W., S. Teukolsky, W. Vetterling, and B. Flannery (1992), *Numerical Recipes in C: The Art of Scientific Computing*, 2nd edn., Cambridge University Press.
- Priestley, K., D. McKenzie, and J. Barron (2012), The Zagros core: Deformation of the continental lithospheric mantle, *Geochemistry, Geophysics, Geosystems*, *13*(Q11014).
- Pritchard, M., and E. J. Fielding (2008), A study of the 2006 and 2007 earthquake sequence of Pisco, Peru, with InSAR and teleseismic data, *Geophysical Research Letters*, *35*, L09,308.
- Pritchard, M. E., C. Ji, and M. Simons (2006), Distribution of slip from 11 Mw \geq 6 earthquake in the northern Chile subduction zone, *Journal of Geophysical Research*, *111*, B10,302.
- Pritchard, M. E., E. O. Norabuena, C. Ji, R. Boroschek, D. Comte, M. Simons, T. H. Dixon, and P. A. Rosen (2007), Geodetic, teleseismic, and strong motion constraints on slip from recent southern Peru subduction zone earthquakes, *Journal of Geophysical Research*, *112*, B03,307.
- Pritchard, M. E., and M. Simons (2004), An InSAR-based survey of volcanic deformation in the southern Andes, *Geophysical Research Letters*, *31*, L15,610.
- Pritchard, M. E., M. Simons, P. A. Rosen, S. Hensley, and F. H. Webb (2002), Co-seismic slip from the 1995 July 30 Mw = 8.1 Antofagasta, Chile, earthquake as constrained by InSAR and GPS observations, *Geophysical Journal International*, *150*, 362–376.
- Puysegur, B., R. Michel, and J.-P. Avouac (2007), Tropospheric phase delay in interferometric synthetic aperture radar estimated from meteorological model multispectral imagery, *Journal of Geophysical Research*, *112*, B05,419.
- Randall, M., and L. Knopoff (1970), The mechanism at the focus of deep earthquakes, *Journal of Geophysical Research*, *75*(26), 4965–4976.
- Reid, H. (1910), *The mechanics of the earthquake*. In: *The California earthquake of 18 April, 1906: Report of the State Earthquake Investigation Commission*, Tech. Rep. 2, Washington: Carnegie Institution.
- Relinger, R. (1984), Coseismic and Postseismic Vertical Movements Associated with the 1940 M7.1 Imperial Valley, California, Earthquake, *Journal of Geophysical Research*, *89*, 4531–4537.
- Resor, P. G., D. D. Pollard, T. J. Wright, and G. C. Beroza (2005), Integrating high-precision aftershock locations and geodetic observations to model coseismic deformation associated with the 1995 Kozani-Grevena earthquake, Greece, *Journal of Geophysical Research*, *110*, B09,402.
- Resor, P. G., D. D. Pollard, T. J. Wright, and G. C. Beroza (2007), Correction to Integrating high-precision aftershock locations and geodetic observations to model coseismic deformation associated with the 1995 Kozani-Grevena earthquake, Greece”, *Journal of Geophysical Research*, *112*(B11).

- Rigo, A., J.-B. de Chabali er, B. Meyer, and R. Armijo (2004), The 1995 Kozani-Grevena (northern Greece) earthquake revisited: an improved faulting model from synthetic radar interferometry, *Geophysical Journal International*, 157, 727–736.
- Ritsema, J., A. Deuss, H. van Heijst, and J. H. Woodhouse (2011), S40RTS: a degree-40 shear-velocity model for the mantle from new Rayleigh wave dispersion, teleseismic traveltimes and normal-mode splitting function measurements, *Geophysical Journal International*, 184(3), 1223–1236.
- Ritsema, J., and T. Lay (1995), Long-period regional wave moment tensor inversion for earthquakes in the western United States, *Journal of Geophysical Research*, 100(B7), 9853–9864.
- Ritsema, J., H. van Heijst, and J. H. Woodhouse (1999), Complex shear wave velocity structure imaged beneath Africa and Iceland, *Science*, 286, 1925–1928.
- Robinson, D. P., S. Das, and A. B. Watts (2006), Earthquake Rupture Stalled by a Subducting Fracture Zone, *Science*, 312, 1203–1205.
- Rodr iguez, I., M. Sacchi, and Y. Gu (2012), Simultaneous recovery of origin time, hypocentre location and seismic moment tensor using sparse representation theory, *Geophysical Journal International*, 188, 1188–1202.
- Roering, J., L. Stimely, B. Mackey, and D. A. Schmidt (2009), Using DInSAR, airborne LiDAR, and archival photos to quantify landsliding and sediment transport, *Geophysical Research Letters*, 36, L19,402.
- Romano, F., A. Piatanesi, S. Lorito, and K. Hirata (2010), Slip distribution of the 2003 Tokachi-oki Mw 8.1 earthquake from joint inversion of tsunami waveforms and geodetic data, *Journal of Geophysical Research*, 115, B11,313.
- Romanowicz, B., M. Panning, Y. Gung, and Y. Capdeville (2008), On the computation of long period seismograms in a 3-D earth using normal mode based approximations, *Geophysical Journal International*, 175, 520–536.
- Roperch, P., M. Fornari, G. Herail, and G. Parraguez (2000), Tectonic rotations within the Bolivian Altiplano: Implications for the geodynamic evolution of the Central Andes during the late Tertiary, *Journal of Geophysical Research*, 105, 795–820.
- Rosen, P. A., S. Hensley, I. R. Joughin, F. K. Li, S. N. Madsen, E. Rodr iguez, and R. M. Goldstein (2000), Synthetic Aperture Radar Interferometry, *Proceedings of the IEEE*, 88(3).
- Rosen, P. A., S. Hensley, and G. Peltzer (2004), Updated Repeat Orbit Interferometry Package Released, *EOS*, 85, 47.
- Rothman, D. (1986), Automatic estimation of large residual statics corrections, *Geophysics*, 51, 337–346.
- Rouhollahi, R., M. Ghayamghamian, F. Yaminpard, P. Suhadole, and M. Tatar (2012), Source process and slip model of 2005 Dahuiyeh-Zarand earthquake (Iran) using inversion of near-field strong motion data, *Geophysical Journal International*, 189, 669–680.
- Ryder, I., B. Parsons, T. J. Wright, and G. J. Funning (2007), Post-seismic motion following the 1997 Manyi (Tibet) earthquake: InSAR observations and modelling, *Geophysical Journal International*, 169, 1009–1027.

- Salichon, J., B. Delouis, P. Lundgren, D. Giardini, M. Costantini, and P. Rosen (2003), Joint inversion of broadband teleseismic and interferometric synthetic aperture radar (InSAR) data for the slip history of the $M_w = 7.7$, Nazca ridge (Peru) earthquake of 12 November 1996, *Journal of Geophysical Research*, *108*, B2, 2085.
- Salichon, J., A. Lemoine, and H. Aochi (2009), Validation of Teleseismic Inversion of the 2004 M_w 6.3 Les Saintes, Lesser Antilles, Earthquake by 3D Finite-Difference Forward Modelling, *Bulletin of the Seismological Society of America*, *99*(6), 3390–3401.
- Salichon, J., P. Lundgren, B. Delouis, and D. Giardini (2004), Slip History of the 16 October 1999 M_w 7.1 Hector Mine Earthquake (California) from the Inversion of InSAR, GPS, and Teleseismic Data, *Bulletin of the Seismological Society of America*, *94*, 2015–2027.
- Salvi, S., S. Stramondo, M. Cocco, M. Tesauro, I. Hunstad, M. Anzidei, P. Briole, P. Baldi, E. Sansosti, G. Fornaro, R. Lanari, F. Doumaz, A. Pesci, and A. Galvani (2000), Modeling coseismic displacements resulting from SAR interferometry and GPS measurements during the 1997 Umbria-Marche seismic sequence, *Journal of Seismology*, *4*, 479–499.
- Sambridge, M. (1998), Geophysical inversion with a neighbourhood algorithm - I. Searching a parameter space, *Geophysical Journal International*, *138*, 479–494.
- Saroglu, F., O. Emre, and I. Kuscü (1992), Active Fault Map of Turkey 1992, *General Directorate of Mineral Research and Exploration (MTA), Eskisehir Yolu, 06520, Ankara, Turkey*.
- Satyabala, S. P. (2006), Coseismic ground deformation due to an intraplate earthquake using synthetic aperture radar interferometry: The M_w 6.1 Killari, India, earthquake of 29 September 1993, *Journal of Geophysical Research*, *111*, B02,302.
- Satyabala, S. P., and R. Bilham (2006), Surface deformation and subsurface slip of the 28 March 1999 $M_w = 6.4$ west Himalayan Chamoli earthquake from InSAR analysis, *Geophysical Research Letters*, *33*, L23,305.
- Savage, J. (1987), Effect of Crustal Layering Upon Dislocation Modeling, *Journal of Geophysical Research*, *92*, 10,595–10,600.
- Savage, J. (1998), Displacement field for an edge dislocation in a layered half-space, *Journal of Geophysical Research*, *103*, 2439–2446.
- Schaefer, J., E. Boschi, and E. Kissling (2011), Adaptively parameterized surface wave tomography: methodology and a new model of the European upper mantle, *Geophysical Journal International*, *186*, 1431–1453.
- Scharroo, R., and P. Visser (1998), Precise orbit determination and gravity field improvement for the ERS satellites, *Journal of Geophysical Research*, *103*, 8113–8127.
- Schmidt, D. A., and R. Bürgmann (2006), InSAR constraints on the source parameters of the 2001 Bhuj earthquake, *Geophysical Research Letters*, *33*, L02,315.
- Sella, G., T. H. Dixon, and A. Mao (2002), REVEL : A model for recent plate velocities from space geodesy, *Journal of Geophysical Research*, *107*(B4), 2081.

- Serpelloni, E., L. Anderlini, and M. Belardinelli (2012), Fault geometry, coseismic-slip distribution and Coulomb stress change associated with the 2009 April Mw 6.3, L'Aquila earthquake from inversion of GPS displacements, *Geophysical Journal International*, 188, 473–489.
- Shamir, G., G. Baer, and A. Hofstetter (2003), Three-dimensional elastic earthquake modelling based on integrated seismological and InSAR data: the Mw = 7.2 Nuweiba earthquake, gulf of Elat/Aqaba 1995 November, *Geophysical Journal International*, 154, 731–744.
- Shirzaei, M. (2013), A Wavelet-based Multitemporal DInSAR Algorithm for Monitoring Ground Surface Deformation, *IEEE Geoscience and Remote Sensing Letters*, 10(3), 456–460.
- Shuler, A., and G. Ekström (2009), Anomalous earthquakes associated with Nyiragongo Volcano: Observations and potential mechanisms, *Journal of Volcanology and Geothermal Research*, 181, 219–230.
- Sieh, K. (1978), Prehistoric Large Earthquakes Produced by Slip on the San Andreas Fault at Pallett Creek, California, *Journal of Geophysical Research*, 83(B8), 3907–3939.
- Sieh, K., L. Jones, E. Hauksoo, K. Hudnut, D. Eberhart-Philips, T. Heaton, S. Hough, K. Hutton, H. Kanamori, A. Lilje, S. Lindvall, S. F. McGill, J. Mori, C. Rubin, J. A. Spotila, J. Stock, H. K. Thio, J. A. Treiman, B. Wernicke, and J. Zachariassen (1993), Near-Field Investigations of the Landers Earthquake Sequence, April to July 1992, *Science*, 260(5105), 171–176.
- Simons, M., Y. Fialko, and L. Rivera (2002), Coseismic Deformation from the 1999 Mw 7.1 Hector Mine, California, Earthquake as Inferred from InSAR and GPS Observations, *Bulletin of the Seismological Society of America*, 92, 1390–1402.
- Sladen, A., H. Tavera, M. Simons, J.-P. Avouac, A. Konca, H. Perfettini, L. F. E. Audin, F. Ortega, and R. Cavagnoud (2010), Source model of the 2007 Mw 8.0 Pisco, Peru earthquake: Implications for seismogenic behaviour of subduction megathrusts, *Journal of Geophysical Research*, 115, B02,405.
- Smith, G. P., and G. Ekström (1997), Interpretation of earthquake epicenter and CMT centroid locations, in terms of rupture length and direction, *Physics of the Earth and Planetary Interiors*, 102, 123–132.
- Stein, R., A. Barka, and J. Dieterich (1997), Progressive failure on the North Anatolian fault since 1939 by earthquake stress triggering, *Geophysical Journal International*, 128, 594–604.
- Steketee, J. (1958), On Volterra's dislocations in a semi-infinite elastic medium, *Canadian Journal of Physics*, 36(2), 192–205.
- Stich, D., D. Baumont, and J. Morales (2005), Source analysis of the Mw 6.3 2004 Al Hoceima earthquake (Morocco) using regional apparent source time functions, *Journal of Geophysical Research*, 110, B06,306.
- Stramondo, S., M. Tesauro, P. Briole, E. Sansosti, S. Salvi, R. Lanari, M. Anzidei, P. Baldi, G. Fornaro, A. Avallone, M. F. Buongiorno, G. Franceschetti, and E. Boschi (1999), The September 26, 1997 Colfiorito, Italy, earthquakes: modelled coseismic surface displacement from SAR interferometry and GPS, *Geophysical Research Letters*, 26, 883–886.

- Sudhaus, H., and S. Jónsson (2009), Improved source modelling through combined use of InSAR and GPS under consideration of correlated data errors: application to the June 2000 Kleifarvatn earthquake Iceland, *Geophysical Journal International*, *176*, 389–404.
- Sumy, D., J. Gaherty, W.-Y. Kim, T. Diehl, and C. J.A. (2013), The mechanisms of earthquakes and faulting in the Southern Gulf of California, *Bulletin of the Seismological Society of America*, *103*(1), 487–506.
- Sun, J., Z. Shen, X. Xu, and R. B'urgmann (2008), Synthetic normal faulting of the 9 January 2008 Nima (Tibet) earthquake from conventional and along-track SAR interferometry, *Geophysical Research Letters*, *35*, L22,308.
- Swenson, J. L., and S. L. Beck (1999), Source Characteristics of the 12 November 1996 Mw 7.7 Peru Subduction Zone Earthquake, *Pure and Applied Geophysics*, *154*, 731–751.
- Syracuse, E. M., and G. A. Abers (2009), Systematic biases in subduction zone hypocenters, *Geophysical Research Letters*, *36*, L10,303.
- Tahayt, A., K. L. Feigl, T. Mourabit, A. Rigo, R. Reilinger, S. McClusky, A. Fadil, E. Berthier, L. Dorbath, M. Serroukh, F. Gomez, and D. Ben Sari (2009), The Al Hoceima (Morocco) earthquake of 24 February 2004, analysis and interpretation of data from ENVISAT ASAR and SPOT5 validated by ground-based observations, *Remote Sensing of the Environment*, *113*, 306–316.
- Talebian, M., J. Biggs, M. Bolourchi, A. Copley, A. Ghassemi, M. Ghorashi, J. Hollingsworth, J. Jackson, E. Nissen, B. Oveisi, K. Priestly, and A. Saiidi (2006), The Dahuiyeh (Zarand) earthquake of 2005 February 22 in central Iran: reactivation of an intramountain reverse fault, *Geophysical Journal International*, *164*, 137–148.
- Talebian, M., E. J. Fielding, G. J. Funning, M. Ghorashi, J. Jackson, H. Nazari, B. Parsons, K. Priestley, P. A. Rosen, R. Walker, and T. J. Wright (2004), The 2003 Bam (Iran) earthquake: Rupture of a blind strike-slip fault, *Geophysical Research Letters*, *31*, L11,611.
- Tobita, M., S. Fujiwara, S. Ozawa, P. A. Rosen, E. J. Fielding, C. L. Werner, M. Murakami, H. Nakagawa, K. Nitta, and M. Murakami (1998), Deformation of the 1995 North Sakhalin earthquake detected by JERS-1/SAR interferometry, *Earth Planets and Space*, *50*, 313–325.
- Tong, X., D. T. Sandwell, and Y. Fialko (2010), Coseismic slip model of the 2008 Wenchuan earthquake derived from joint inversion of interferometric synthetic aperture radar, GPS and field data, *Journal of Geophysical Research*, *115*, B04,314.
- Treiman, J. A., K. J. Kendrick, A. Bryant, T. K. Rockwell, and S. F. McGill (2002), Primary Surface Rupture Associated with the Mw 7.1 16 October 1999 Hector Mine Earthquake, San Bernardino County, California, *Bulletin of the Seismological Society of America*, *92*, 1171–1191.
- Trifunac, M. (1974), A three-dimensional dislocation model for the San Fernando, California, earthquake of February 9, 1971, *Bulletin of the Seismological Society of America*, *64*, 149–172.

- Tsai, Y.-B., and K. Aki (1970), Source mechanism of the Truckee, California, earthquake of September 12 1966, *Bulletin of the Seismological Society of America*, 60(4), 1199–1208.
- Tsuboi, S., D. Komatitsch, C. Ji, and J. Tromp (2003), Broadband modeling of the 2002 Denali fault earthquake on the Earth Simulator, *Physics of the Earth and Planetary Interiors*, 139, 305–312.
- USGS (2010), Earthquake information for 2003, <http://earthquake.usgs.gov/earthquakes/eqarchives/year/2003/>, Last accessed 27/04/13.
- Vallée, M., J. Charley, A. Ferreira, B. Delouis, and J. Vergoz (2011), SCARDEC: a new technique for the rapid determination of seismic moment magnitude, focal mechanism and source time functions for large earthquakes using body-wave deconvolution, *Geophysical Journal International*, 184, 338–358.
- Vannuccii, G., and P. Gasperini (2003), A database of revised fault plane solutions for Italy and surrounding regions, *Computer & Geosciences*, 29, 903–909.
- Velasco, A. A., C. J. Ammon, F. J., and K. Pankow (2004), Rupture Directivity of the 3 November 2002 Denali Fault Earthquake Determined from Surface Waves, *Bulletin of the Seismological Society of America*, 94, S293–S299.
- Vigny, C., A. Rudloff, J. C. Ruegg, R. Madriaga, J. Campos, and M. Alvarez (2009), Upper plate deformation measured by GPS in the Coquimbo gap, *Physics of the Earth and Planetary Interiors*, 175, 86–95.
- Volpe, M., A. Piersanti, and D. Melini (2012), Complex 3-D Finite Element modelling of the 2009 April 6 L'Aquila earthquake by inverse analysis of static deformation, *Geophysical Journal International*, 188, 1339–1358.
- Wadge, G., G. Mattioli, and R. Herd (2006), Ground deformation at the Soufriere Hills Volcano, Montserrat during 1998-2000 measured by radar interferometry and GPS, *Journal of Volcanology and Geothermal Research*, 152, 157–173.
- Wadge, G., M. Zhu, R. J. Holley, I. N. James, P. A. Clark, C. Wang, and M. J. Woodage (2010), Correction of atmospheric delay effects in radar interferometry using a nested mesoscale atmospheric model, *Journal of Applied Geophysics*, 84, 537–546.
- Wald, D., and R. Graves (2001), Resolution analysis of finite fault source inversion using one- and three-dimensional Green's functions 2. Combining seismic and geodetic data, *Journal of Geophysical Research*, 106, 8767–8788.
- Wald, D., and T. Heaton (1994), Spatial and temporal distribution of slip for the 1992 Landers, California earthquake, *Bulletin of the Seismological Society of America*, 84, 668–691.
- Walker, R., P. Gans, A. M.B., J. Jackson, M. Khatib, N. Marsh, and M. Zarrinkoub (2009), Late Cenozoic volcanism and rates of active faulting in eastern Iran, *Geophysical Journal International*, 177, 783–805.
- Wallace, L., and J. Beavan (2006), A large slow slip event on the central Hikurangi subduction interface beneath the Manawatu region, North Island, New Zealand, *Geophysical Research Letters*, 33, L11,301.

- Walters, R. J., J. R. Elliot, N. D'Agostino, P. C. England, I. Hunstad, J. A. Jackson, B. Parsons, R. J. Phillips, and G. Roberts (2009), The 2009 L'Aquila earthquake (central Italy): A source mechanism and implications for seismic hazard, *Geophysical Research Letters*, *36*, L17,312.
- Walters, R. J., R. J. Holley, B. Parsons, and T. J. Wright (2011), Interseismic strain accumulation across the North Anatolian Fault from Envisat InSAR measurements, *Geophysical Research Letters*, *38*, L05,303.
- Wang, H., C. Xu, and L. Ge (2007), Coseismic deformation and slip distribution of the 1997 Mw7.5 Manyi, Tibet, earthquake from InSAR measurements, *Journal of Geodynamics*, *44*, 200–212.
- Weston, J., A. Ferreira, and G. J. Funning (2011), Global Compilation of InSAR Earthquake Source Models: 1. Comparisons with Seismic Catalogs, *Journal of Geophysical Research*, *116*, B08,408.
- Weston, J., A. Ferreira, and G. J. Funning (2012), Systematic comparisons of earthquake source models determined using InSAR and seismic data, *Tectonophysics*, *532*, 61–81.
- Williams, C., T. Arnadottir, and P. Segall (1993), Coseismic Deformation and Dislocation Models for the 1989 Loma Prieta Earthquake Derived From Global Positioning System Measurements, *Journal of Geophysical Research*, *98*(B3), 4567–4578.
- Woessner, J., S. Jónsson, H. Sudhaus, and C. Baumann (2012), Reliability of Coulomb stress changes inferred from correlated uncertainties of finite-fault source models, *Journal of Geophysical Research*, *117*, B07,303.
- Wright, T. J. (2000), *Crustal Deformation in Turkey from Synthetic Aperture Radar Interferometry*, Ph.D. thesis, Faculty of Physical Sciences, University of Oxford.
- Wright, T. J., E. Fielding, and B. Parsons (2001a), Triggered slip: observations of the 17 August 1999 Izmit (Turkey) earthquake using radar interferometry, *Geophysical Research Letters*, *28*(6), 1079–1082.
- Wright, T. J., Z. Lu, and C. Wicks (2003), Source model for the Mw 6.7, 23 October 2002, Nenana Mountain Earthquake (Alaska) from InSAR, *Geophysical Research Letters*, *30*, 1974.
- Wright, T. J., Z. Lu, and C. Wicks (2004a), Constraining the Slip Distribution and Fault Geometry of the Mw 7.9, 3 November 2002, Denali Fault Earthquake with Interferometric Synthetic Aperture Radar and Global Positioning System Data, *Bulletin of the Seismological Society of America*, *94*, 175–189.
- Wright, T. J., B. Parsons, and E. Fielding (2001b), Measurement of interseismic strain accumulation across the North Anatolian Fault by satellite radar interferometry, *Geophysical Research Letters*, *28*(10), 2117–2120.
- Wright, T. J., B. E. Parsons, J. A. Jackson, M. Haynes, E. J. Fielding, P. C. England, and P. J. Clarke (1999), Source parameters of the 1 October 1995 Dinar (Turkey) earthquake from SAR interferometry and seismic bodywave modelling, *Earth and Planetary Science Letters*, *172*, 23–37.
- Wright, T. J., B. E. Parsons, and Z. Lu (2004b), Toward mapping surface deformation in three dimensions using InSAR, *Geophysical Research Letters*, *31*.

- Yagi, Y., and M. Kikuchi (2000), Source rupture process of the Kocaeli, Turkey, earthquake of August 17 1999, obtained by joint inversion of near-field data and teleseismic data, *Geophysical Research Letters*, 27, 1969–1972.
- Yao, H., C. Beghein, and van der Hilst. R. (2008), Surface wave array tomography in SE Tibet from ambient seismic noise and two-station analysis - II. Crustal and upper-mantle structure, *Geophysical Journal International*, 173, 205–219.
- Yao, H., P. Shearer, and P. Gerstoft (2012), Subevent location and rupture imaging using iterative backprojection for the 2011 Tohoku Mw 9.0 earthquake, *Geophysical Journal International*, 190, 1152–1168.
- Yu, E., and P. Segall (1996), Slip in the 1868 Hayward earthquake from the analysis of historical triangulation data, *Journal of Geophysical Research*, 101, 16,101–16,118.
- Zebker, H., P. A. Rosen, R. M. Goldstein, G. A., and C. L. Werner (1994), On the derivation of coseismic displacement fields using differential radar interferometry: the Landers earthquake, *Journal of Geophysical Research*, 99(B10), 19,617–19,634.
- Zhang, G., M. Vallée, X. Shan, and B. Delouis (2012), Evidence of sudden rupture of a large asperity during the 2008 Mw 7.9 Wenchuan earthquake based on strong motion analysis, *Geophysical Research Letters*, 39, L17,303.
- Zhang, H., and X. Chen (2006), Dynamic rupture on a planar fault in three-dimensional half-space - II. Validations and numerical experiments, *Geophysical Journal International*, 167, 917–932.
- Zhang, H., and Z. Ge (2010), Tracking the rupture of the 2008 Wenchuan earthquake by using the relative back-projection method, *Bulletin of the Seismological Society of America*, 100, 2551–2560.
- Zhou, Y., Q. Liu, and J. Tromp (2011), Surface wave sensitivity: mode summation versus adjoint SEM, *Geophysical Journal International*, 187, 1560–1576.